DESIGN AND FABRICATION OF MICRO END MILLS FOR THE MACHINING OF DIFFICULT-TO-CUT MATERIALS

A DISSERTATION SUBMITTED TO

THE GRADUATE SCHOOL OF ENGINEERING AND SCIENCE

OF BILKENT UNIVERSITY

IN PARTIAL FULFILLMENT OF THE REQUIREMENTS FOR

THE DEGREE OF

DOCTOR OF PHILOSOPHY

IN

MECHANICAL ENGINEERING

By

Samad Nadimi Bavil Oliaei

August 2016

Design and Fabrication of Micro End Mills for the Machining of Difficult-to-cut Materials

By Samad Nadimi Bavil Oliaei

August 2016

We certify that we have read this dissertation and that in our opinion it is fully adequate, in scope and in quality, as a dissertation for the degree of Doctor of Philosophy.

Yiğit Karpat(Advisor)

İlker Temizer

Mehmet Ali Güler

Can Çoğun

Orkun Özşahin

Approved for the Graduate School of Engineering and Science:

Levent Onural
Director of the Graduate School

ABSTRACT

DESIGN AND FABRICATION OF MICRO END MILLS FOR THE MACHINING OF DIFFICULT-TO-CUT MATERIALS

Samad Nadimi Bavil Oliaei
Ph.D. in Mechanical Engineering
Advisor: Yiğit Karpat
August 2016

Micromilling is a cost-effective method of fabricating miniaturized components with complex, three-dimensional features made from difficult-to-cut materials. Micro-cutting tools are exposed to harsh conditions during machining of such materials, which leads to short tool life and thus affects the economics of the process.

The aim of this thesis is to develop a systematic approach to the design and fabrication of high-precision micro-cutting tools. Machining characteristics of three different difficult-to-cut materials–stainless steel, titanium alloy, and silicon–have been investigated using experimental techniques. The results reveal the importance of interaction between tool micro geometry and work material mechanical properties. This observation leads to the development of tailored micro-end mills which are designed and fabricated based on the requirements of the specific machining task.

This study also examines in detail built-up edge, an important but usually overlooked issue in micromachining of ductile materials, which affects the process forces, tool wear, and tool deflections. The protective effect of built-up edge has been exploited by creating micro-dimples on the tool surface using electrical discharge machining. Its positive influence on tool performance has been demonstrated. As for the micromachining of silicon, the flow of cut material around the cutting edge is paramount in tool design. A novel tool design for machining of silicon has been proposed and its effectiveness has been validated through experiments.

It has been shown that the selection of proper process parameters together with tailored tool design may increase the productivity of micromachining and improve surface quality and dimensional accuracy of micro-scale parts.

Keywords: Micromilling, Micro cutting tool, Titanium, Polycrystalline diamond, Ductile mode machining.

ÖZET

KESİLMESİ ZOR MALZEMELERİN İŞLENMESİ İÇİN MİKRO FREZELEME TAKIMLARININ TASARIM VE ÜRETİMİ

Samad Nadimi Bavil Oliaei
Makine Mühendisliği, Doktora
Tez Danışmanı: Yiğit Karpat
Ağustos 2016

Mikro frezeleme üç boyutlu karmaşık yüzey özelliklerine sahip işlenmesi zor malzemelerden minyatür komponentlerin üretilmesi için kullanılan düşük maliyetli bir işlemdir. Bu işlemde kullanılan mikro kesici takımlar işlenmesi zor malzemelerin kesilmesi sırasında oluşan kötü şartlara maruz kalmakta, takım ömrü azalmakta bu da işlemenin ekonomisini olumsuz etkilemektedir.

Bu tezin amacı yüksek hassasiyette mikro kesici takım tasarım ve üretilmesi için sistematik bir yaklaşım geliştirmektir. İşlenmesi zor olarak bilinen paslanmaz çelik, titanyum alaşımı, silikon gibi üç değişik malzemenin işlenme karakterleri deneysel olarak incelenmiştir. Sonuçlar mikro takım geometrisi ve iş malzemesi mekanik özellikleri arasındaki ilişkinin önemini ortaya koymuştur. Bu gözlem sonucunda işlemenin isterlerine bağlı olarak tasarlanan özel mikro takımların üretimi gündeme gelmiştir.

Bu çalışmada, sünek malzemelerin mikro işlemesi esnasında önem arz eden, kesme kuvvetlerini, takım aşınmasını ve takım eğilmesini etkileyen, fakat çoğunlukla göz ardı edilen, kesici takıma talaş yapışması konusu detaylı olarak incelenmiştir. Talaşın yapışmasının takım üzerindeki koruyucu etkisi, tel erozyon operasyonu ile takımın ön yüzeyinde oluşturulan mikro-çukurlar vasıtası ile arttırılmış, iki ve üç boyutlu frezeleme operasyonları ile kesici takım ömrü üzerindeki olumlu etkisi gösterilmiştir. Özellikle silikonun işlenmesi esnasında, kesici kenar etrafındaki talaş akışının takım tasarımı üzerindeki önemi ortaya konulmuştur. Silikonun işlenmesi için yenilikçi bir takım geliştirilmiş, yapılan deneylerle işleme üzerindeki etkinliği geçerlenmiştir.

Yapılan çalışmalar sonucunda doğru işleme parametrelerinin seçilmesi ve işleme uygun özel takım tasarımları ile mikro frezeleme işleminde üretkenlik ve işlenen parça yüzey kalitesi ve hassasiyetinde artış elde edilebileceği gösterilmiştir.

Anahtar sözcükler: Mikro frezeleme, Mikro kesici takım, Titanyum, Çok kristalli elmas, Sünek işleme modu.

Acknowledgement

First of all, I would like to express my gratitude to my advisor, Associate Prof. Yiğit Karpat for the continuous support of my Ph.D study, for his patience, motivation, and distinguished knowledge. His guidance helped me in all the time of research and writing of this thesis. Besides my advisor, I would like to appreciate the rest of my thesis committee, Associate Prof. İlker Temizer and Prof. Mehmet Ali Güler, for their insightful comments and suggestions.

I would also like to thank "The Scientific and Technological Research Council of Turkey" (TÜBİTAK) for supporting my work under the project number of 110M660. My sincere thanks also goes to Dr. Şakir Baytaroğlu and Mr. Mustafa Kilic for their helps in preparing experimental setups of this study.

It is a great pleasure to thank my friends at Middle East Technical University and Bilkent University, Dr. Ali Karimzadeh, Dr. Rouhollah Khodadust, Dr. Rahim Jafari, Dr. Ramez Kian, Mr. Mohammad Tofighi, Mr. Kamyar Kargar, Mr. Erman Gözü, Mr. İsmail Uyanık and Mr. Mustafa Reşit Bulut for the invaluable and wonderful times we shared.

Last but not least, I would like to thank my parents and my dear wife Parisa for their support throughout the course of my PhD study and my life in general.

Contents

1 Introduction **1**

2 Micro-tool Fabrication by EDM-based Processes **10**

2.1 Introduction 10

2.2 Principles of Electrical Discharge Machining (EDM) 13

2.3 EDM-based Fabrication Processes 15

2.3.1 Block-EDM Process 15

2.3.2 Rotary Disk EDM Process 16

2.3.3 Wire Electro-discharge Grinding (WEDG) 17

2.4 Some Applications of On-machine Fabrication of Micro-end Mills . . 18

2.4.1 Experimental Setup for On-machine Fabrication of Micro-tools 18

2.4.2 Fabrication of D-shaped Cylindrical End Mills 20

2.4.3 Fabrication of Micro-ball End Mills by Block-EDG 21

2.4.4 Fabrication of Micro-ball End Mills by WEDG 22

2.4.5 Fabrication of Lollipop Micro-end Mills by Block-EDG . . . 24

2.5 Micro-tool Fabrication by Wire Electrical Discharge Machining (WEDM) 26

2.5.1 Materials 29

2.5.2 Experimental Setup 30

2.5.3 Design of Experiments 31

2.5.4 Effect of WEDM Process Parameters on KERF 33

2.5.5 Effect of WEDM Process Parameters on Surface Roughness . 40

2.5.6 Measurement of Surface Roughness 41

2.5.7 Material Removal Rate 44

2.5.8 Analysis of the Results 45

3 An Investigation of Micromilling using Conventional Micro End Mills 52
3.1 Introduction 52
3.2 Size Effects in Micromilling 55
3.3 Minimum Uncut Chip Thickness 57
3.4 Experimental Investigations on Micromilling of Stavax Stainless Steel 60
3.4.1 Experimental Setup for Pocket Micromilling Experiments . . 63
3.4.2 Investigating the Influence of Process Parameters 65
3.4.3 Influence of Tool Wear on Micromilling Forces and Surface Roughness 80
3.4.4 Effect of Tool Wear on Micromilling Forces 83
3.4.5 Effect of Tool Wear on Machined Microchannel Accuracy . . 90
3.4.6 Tool Deflection Modeling by Finite Element Analysis 92
3.4.7 Finite Element Simulation-based Analysis of Tool Deflection . 95
3.4.8 Analytical Modeling of Conventional Micro End Mill Deflections 100
3.4.9 Tool Life 104
3.5 Micromilling Experiments on Ti6Al4V 106
3.5.1 Experimental Setup for Micromilling Experiments on Ti6Al4V 107
3.5.2 Experimental Micromilling Tests on Ti6Al4V 108
3.5.3 Investigation of the Micromilling Forces 109
3.5.4 Investigation of Micro End Mills after Micromilling Tests . . 114

4 An Investigation of BUE Formation in Micro-cutting of Ti6Al4V 122
4.1 Introduction 122
4.2 Experimental Procedure 126
4.2.1 Fabrication of Cutting Edge Micro-geometry 126
4.2.2 Experimental Setup for Orthogonal Micro-cutting Tests . . . 128
4.2.3 Investigation of BUE after Micromachining Experiments . . 130
4.2.4 Force Measurements during Micro-scale Machining of Ti6Al4V 137
4.2.5 Effect of BUE on Surface Roughness 140
4.3 Finite Element Simulation Model of Micro Scale Machining with the Presence of Built-up Edge 143
4.4 Analysis of Stable Built-up Edge Formation at Micro Scale Machining 144

4.4.1 Finite Element Simulation Model of Micro Scale Machining with the Presence of Built-up Edge 146
4.4.2 The Influence of Friction Models on FE Simulations 150

5 A Micro End Mill Design Methodology for Ti6Al4V Micromachining 161
5.1 Introduction 161
5.2 Design of Micro End Mills 163
5.3 Fabrication of Micro End Mills 164
5.4 Preliminary Micromilling Experiments with Tailored Micro End Mills 168
5.5 Micromilling Experiments for BUE Investigations 173
5.6 Effect of BUE on Tool life 178
5.7 Relationship between BUE and Burr Formation 180
5.8 Analysis of the Effect of Deflection on Surface Roughness 182
5.9 Analytical Modeling of Tool Deflection for Tailored Micro-end Mills . 184
5.9.1 Moment of Inertia of the Cutting Portion 186
5.9.2 Moment of Inertia of the Transition Portion 187
5.9.3 Moment of Inertia of the Tapered Portion 188
5.9.4 Moment of Inertia of the Shank Portion 189
5.10 Analytical Model of Tailored Micro End Mill Deflection 189
5.11 Design Optimization of Tailored Micro End Mills Considering BUE Formation 190
5.11.1 Finite Element Modeling of Deflections and Stresses 192
5.11.2 Verification of the Finite Element Model of Tool Failure . . . 193
5.11.3 Comparison between Finite Element and Analytical Model of Tailored Micro End Mill Deflection 197
5.11.4 Graphical Optimization of Tailored Micro-End Mills Based on Finite Element Method 198
5.12 Analytical Optimization of Tailored Micro-End Mills Based on Finite Element Method 201

6 Fabrication of PCD Micro Tools for Ductile Mode Machining of Silicon 208
6.1 Introduction 208
6.2 Ductile Mode Machining 209
6.3 Application of PCD Tools in Machining of Brittle Materials 212

6.4 Defining PCD Micro End Mill Geometry 213
6.5 Fabrication of PCD Micro End Mills by WEDM Process 217
6.5.1 Mechanism of Material Removal in EDM of PCD 217
6.5.2 Fabrication of PCD Tools 219
6.6 Experimental Setup and Plan for Micromilling Tests 221
6.7 Influence of Tool Geometry on Tool Wear 222
6.8 Design and Fabrication of Novel PCD Micro End Mill 225
6.9 Fabrication of Mechanical Planarization Tools 231
6.9.1 Radially Patterned Mechanical Planarization Tools 231
6.9.2 Mechanical Planarization Tools with Micro-pyramid Lattice Structure 236

7 Conclusions **249**

List of Figures

1.1 Micro-parts fabricated by different microfabrication processes 4

2.1 Micro-tools fabricated by EDM-based techniques 12
2.2 Working Principles of EDM 13
2.3 (a) Stationary block-EDM method, (b) Block EDG method, (c) Rotary disk EDM process 15
2.4 (a) Schematic representation of WEDG, (b) WEDG steps to fabricate micro tools 17
2.5 Experimental setup for on-machine fabrication of micro end mills . . 19
2.6 Fabrication of D-shaped flat end cylindrical micro end mill using a combination of block-EDG and WEDG 20
2.7 Fabricated D-shaped flat end cylindrical micro end mills 21
2.8 Micro-ball end mill fabrication by modified block-EDG process . . . 21
2.9 The designation used for wire diameter compensation 23
2.10 Micro ball end mills fabricated through WEDG process: (a) PCD tool (b) WC tool 23
2.11 Measured cutting edge radius of micro-ball end mills 24
2.12 Fabrication of lollipop micro end mill by Block-EDG process 25
2.13 Lollipop end mill fabricated through block-EDG process 26
2.14 Schematic representation of WEDM process and KERF 27
2.15 EDS analysis of the WC-Co material used for micro end mills 30
2.16 (a) WEDM experimental setup, (b) Schematic representation of work-piece fixing method 31
2.17 Part designed with different feature sizes 35
2.18 WEDMed part with different feature sizes 36

2.19 Percent error as a function of machined feature size 36
2.20 A WC part with stepwise variable thickness 37
2.21 KERF measurement on WC part 37
2.22 Sequence of processing operations to extract areal surface roughness paramaters 42
2.23 Pre-processing steps applied to a WEDMed surface to extract areal surface roughness parameters 44
2.24 Main effect plot for the mean value of KERF, Sa and MRR 47
2.25 Main effect plot for the S/N ratio for KERF, Sa and MRR 50

3.1 Different cutting scenarios based on uncut chip thickness 57
3.2 Minimum uncut chip thickness in micromilling 59
3.3 Experimental setup used in Stavax micromilling experiments 64
3.4 The measured diameter of 30 up-sharp micro end mills 65
3.5 CAM simulation of circular pocket milling operation 66
3.6 Different plunging strategies 67
3.7 Effect of different plunging methods on tool wear 68
3.8 SEM images of the wear zone on the tool 68
3.9 Milling forces for the case of pre-drilled hole 69
3.10 Comparison of milling forces in 'Z' direction: (top) pre-drilled hole, (middle) trochoidal, (bottom) drilling with ramping 69
3.11 Comparison of cutting tool edge wears 71
3.12 Laser topography images of worn cutting edges 72
3.13 Optical images of tool profiles: (a) up-sharp tool and (b) worn tool . . 73
3.14 (a) Average effective diameters at the end of each pocket milling and (b) variation of average flank wear length as a function of pocket number 74
3.15 (a) Relative tool diameter reduction criterion and (b) comparison of flank wear length after machining tests 75
3.16 Wear volume comparison 76
3.17 Surface roughness measurement setup and surface of the micro-milled circular pocket 77
3.18 Machined surface of first and last pockets for different experiments . . 78
3.19 3D surface topography of the micro-milled surface (100x magnification) 79
3.20 Surface roughness as a function of experimental conditions 79

3.21 Experimental setup for slot micromilling tests 81
3.22 Surface roughness of the machined microchannels using worn micro end mills 81
3.23 Surface roughness of the machined microchannels: (a) Ra value and (b) Rz value 82
3.24 Powder-like chips get rubbed on the machined surface 83
3.25 Force signals obtained during slot micromilling experiments 84
3.26 Average cutting forces in X and Y directions as a function of feed values 85
3.27 Comparison of: (a) cutting force coefficients and (b) edge force coefficients 87
3.28 Cross-sectional area of micro end mill and edge radius (Experiment #2) 88
3.29 Two different cases of edge wear identified from experiments: (a) worn tool used in experiment #8 and (b) worn tool used in experiment #4 . 89
3.30 Two different wear mechanism identified from experiments (initial edge radius (r_i) is smaller than final edge radius (r_f)) 89
3.31 Schematic representation of slicing using μ-WEDM 90
3.32 Corner radius of the machined microchannels using worn micro end mills 91
3.33 Measured corner radius for different micro end mills 91
3.34 Experimental setup used for tool deflection measurements 93
3.35 Force applied to the cutting tool during deflection test 94
3.36 Meshed model of the micro end mill 95
3.37 Comparison between measured and simulated tool deflections 96
3.38 Maximum deflection of the tool tip for end mill of experiment #5 at $\theta = 126°$ 96
3.39 Total displacements for: (a) up-sharp and (b) tool used in RI-3, (c) tool used in RI-5 and (d) tool used in RI-10 when machining with feed at 8 μm/tooth 98
3.40 (a) Trace left by the tool at the point of failure as measured on workpiece and (b) force measurements at the instant of tool breakage . . . 99
3.41 Total displacements for: (a) up-sharp and (b) tool used in RI-3, (c) tool used in RI-5 and (d) tool used in RI-10 when machining with a feed rate of 8 μm/tooth 99

3.42 Schematic representation of the equivalent micro end mill 101
3.43 Comparison between finite element and analytical tool deflection models 104
3.44 Tool life variation with experiments 105
3.45 Experimental setup for runout measurements 107
3.46 Measured spindle runout 108
3.47 (a) Scanning electron microscope image of the tool, (b) Edge radius measurement using laser scanning microscope 109
3.48 Measured micromilling forces for the micromilling case with 0.4 mm diameter at 40 μm depth of cut 111
3.49 The relationship between uncut chip thickness and cutting forces . . . 112
3.50 Average forces for different uncut chip thicknesses 113
3.51 The relationship between uncut chip thickness and peak-to-valley of first set of micromilling experiments 113
3.52 Statistical distribution of peak forces at a depth of cut of 40 μm 114
3.53 Measured micromilling forces for the micromilling case with 0.4 mm diameter at 80 μm depth of cut 115
3.54 Statistical distribution of peak forces for the second set of experiments 116
3.55 Peak-to-valley forces for the micromilling case with 0.4 mm diameter at 80 μm depth of cut 117
3.56 Ratio of peak forces as a function of feed rate 117
3.57 Edge condition after micromilling 118
3.58 Edge condition after micromilling of Ti6Al4V using tools of different diameters 118

4.1 Schematic of wire-EDM processing to obtain required rake and clearance angles 126
4.2 Edge radius measurement of the insert, before and after edge preparation 127
4.3 Investigation of the tool surface after wire EDM: (a) SEM image, (b) Surface topography of the rake face 127
4.4 The experimental setup used for micro orthogonal cutting tests 128
4.5 (a) Microstructure of Ti6Al4V (b) A typical chip produced during micro turning experiments 129

4.6 SEM images of the cutting edges after machining tests: (a) 0.2 μm, (b) 0.4 μm, (c) 0.6 μm 131
4.7 (a) Scanning electron microscope image of the BUE region and corresponding EDS map, (b) EDS spectrum analysis of the built-up edge zone on the rake face, (c) EDS spectrum analysis of the tool surface, (d) Color map of the Ti and C elements on the BUE 132
4.8 EDS analysis of the surface underneath BUE 133
4.9 3D edge profile measurements. Left column 7°, right column 14° clearance angle. Uncut chip thickness from top to bottom 0.4, 0.6, 0.8, and 1 μm. Cutting speed is 62 m/min. 134
4.10 Increasing BUE tip length with increasing uncut chip thickness: (a) 0.4, (b) 0.6, (c) 0.8, and (d) 1 μm 135
4.11 2D edge profile measurements at cutting speed of 62 m/min 135
4.12 (a) 2D edge profile corresponding to 14° clearance angle at 0.4 μm uncut chip thickness after 2 min of continuous machining, (b) Tip length of BUE after 9 minutes of continuous machining (62 m/min cutting speed) 136
4.13 Force vs. time measurements. Left column 7°, right column 14° clearance angle. Uncut chip thickness from top to bottom 0.4, 0.6, 0.8, and 1 μm 137
4.14 Mean values of: (a) thrust and (b) cutting forces as a function of cutting speed 138
4.15 Mean values of cutting and thrust forces at 62 m/min cutting speed for cutting edges 139
4.16 Laser topography images of the surfaces machined at 62 m/min cutting speed at: (a) 0.4 μm uncut chip thickness, (b) 1 μm uncut chip thickness, (c) 0.8 μm uncut chip thickness at 78 m/min (with 300 height magnification) 141
4.17 Surface roughness analysis as a function of cutting speed: (a) Ra, (b) Rz 142
4.18 Built-up edge formation at 0.8 μm uncut chip thickness 145
4.19 Cutting tool parameters in the presence of stable BUE 145
4.20 Modified geometry of the cutting edge including BUE used in finite element simulations 147

4.21 Influence of coefficient of friction on the chip formation at uncut chip thickness of 1 μm and cutting speed of 62 m/min 150
4.22 Force predictions versus time obtained from finite element simulation model for uncut chip thickness of 1 μm at 62 m/min 151
4.23 Force predictions as a function of coefficient of friction for different uncut chip thicknesses 152
4.24 Force predictions for different uncut chip thickness values for: (a) Cutting speed of 47 m/min, (b) Cutting speed of 62 m/min 153
4.25 Comparison of force measurement and predictions for friction factor of 0.95 at cutting speed of: (a) 47 m/min, (b) 62 m/min 154
4.26 Hybrid friction model used in the finite element simulation with the presence of BUE 155
4.27 Finite element simulations of chips for hybrid friction model 156
4.28 Finite element predictions at different μ and m values for an uncut chip thickness of 1 μm at cutting speed of 62 m/min 157
4.29 Comparison of force measurement and predictions for hybrid friction conditions (Coulomb friction of 0.2 and shear factor of 0.8) at cutting speed of: (a) 47 m/min, (b) 62 m/min 158

5.1 Geometry of the designed single edge cutting tool 163
5.2 Design parameters of the tool 164
5.3 WEDM setup used for micro end mills fabrication 165
5.4 Schematic representation of micro end mill fabrication process 165
5.5 Fabricated single edge WC micro end mills 166
5.6 (a) SEM image of a WEDMed surface, (b) EDS analysis of WEDMed surface 167
5.7 3D topography and top view of the cutting tools: (a) rough WEDMed tool, (b) finish WEDMed tool 168
5.8 Schematic representation of micromilling experiments 169
5.9 (a) Chipped cutting edge (Rough WEDMed-CA=14°), (b) Worn tool (Finish WEDMed-CA=14°) 169
5.10 SEM image of the BUE formed in a finish WEDMed-CA=7° 170

5.11 RMS of the resultant force: (a) Conventional micro end mill, (b) Finish WEDMed-CA=14°, (c) Finish WEDMed-CA=7°, (d) Rough WEDMed-CA=7° 171
5.12 Edge rounding observed in conventional micro end mill 172
5.13 Measurement of average BUE height by 3D laser scanning microscope 174
5.14 Average BUE height for tools having different length of cuts 175
5.15 Normalized resultant forces for tools having different length of cuts . 176
5.16 Surface roughness of the machined microchannels 176
5.17 Arithmetic mean roughness values for the machining conditions of Table 5.2 177
5.18 SEM image of BUE after machining 80 microchannels 178
5.19 EDS analysis of: (a) bulk tool material, (b) Underneath of the BUE . . 179
5.20 Measured cutting forces for: (a) First microchannel, (b) Second microchannel, (c) 40th microchannel, (d) 80th microchannel 180
5.21 SEM image of the burrs formed under experimental conditions of Table 5.2 for Lc=200 μm 181
5.22 Measure burr height and width under experimental conditions of Table 5.2 182
5.23 Effect of length of cut on surface roughness 183
5.24 Tool partitioning for deflection calculations 185
5.25 Concentrated force applied to a position of $\frac{a_p}{2}$ from tool tip 186
5.26 Cross-section of the cutting portion 187
5.27 Cross-section of the transition portion 188
5.28 Cross-section of the tapered portion 188
5.29 Geometry of the designed single edge cutting tools 191
5.30 Finite element model of the conventional 0.4 mm cutting tool 193
5.31 Cutting force data at the point of failure recorded for: (a) Conventional 0.4 mm micro end mill, (b) finish WEDMed, (c) rough WEDMed . . 194
5.32 Results of first principal stress and tool deflection for a conventional 0.4 mm micro end mill 195
5.33 Finite element model of tailored micro end mill 196
5.34 FEM results of tailored micro end mill: (a) deflection, (b) first principal stress, (c) broken micro end mill 196

5.35 Calculated deflection for a cutting tool with specifications given in Table 5.3 . . . 197
5.36 Calculation of critical transition radius and corresponding deflection . 199
5.37 Variation of deflection and first principal stress as a function R_{Tr} for different γ values . . . 200
5.38 Variation of: (a) deflection and (b) first principal stress as a function R_{Tr} and γ . . . 202
5.39 (a) Fabricated tailored micro end mill with optimum design parameters (b) Machined microchannels using tailored micro end mill with optimum geometry . . . 204
5.40 Micromilling forces for different microchannels machined by the tailored micro end mill with optimum geometry . . . 204
5.41 Surface roughness of the machined microchannels using tailored micro end mill with optimum geometry . . . 205
5.42 Stable BUE after micromilling for 130 microchannels . . . 205

6.1 Schematic representation of ductile-to-brittle transition . . . 210
6.2 PCD micro end mill designs with 6 teeth . . . 214
6.3 Different radially patterened PCD square end mill geometries . . . 215
6.4 Schematic representation of material removal in EDM of PCD at: (a) High energy regime, (b) Low energy regime . . . 217
6.5 Surface roughness of PCD machined at low energy EDM regime . . . 218
6.6 Setup used for testing concentricity of PCD tools . . . 219
6.7 PCD cutting edge obtained at low discharge energies . . . 220
6.8 Micromilling experimental setup to test PCD micro end mills . . . 221
6.9 Tool wear of PCD observed at cutting edges . . . 222
6.10 Chip formation during machining of silicon using different edge geometries . . . 223
6.11 Measured forces during machining of silicon using different edge geometries . . . 224
6.12 Solid model and 3D topography of the proposed micro end mill . . . 225
6.13 Micro end mill conditions after dry machining of silicon . . . 226
6.14 Cutting forces for three different micro end mill geometries . . . 227
6.15 Rubbing marks observed at the bottom of circular micro end mill . . . 228

6.16 Micro end mill conditions after dry machining of silicon 229
6.17 Experimental setup for wet machining of silicon 230
6.18 Variation of surface roughness as a function of feed rate and depth of cut for proposed geometry 230
6.19 Radially patterned PCD mechanical planarization tools 232
6.20 Solid model of the proposed radially patterned PCD mechanical planarization tools 233
6.21 Fabricated radially patterned PCD mechanical planarization tools . . . 233
6.22 Edge radius of PCD mechanical planarization tool 233
6.23 Machined pockets using different tools and different pocket milling strategies 234
6.24 Surface roughness of machined silicon as a function of feed rate and depth of cut 235
6.25 Surface roughness of silicon machined by PCD tools 236
6.26 Fabrication steps for tools with micro-pyramid lattice structure 237
6.27 Fine patterned planarization tool 238
6.28 Coarse patterned planarization tool 238
6.29 (a) Accumulation and clogging of silicon at the center of the cutting tool, (b) Surface deterioration due to the rubbing of clogged silicon material 239
6.30 μ-EDM hole drilling of PCD tools 240
6.31 3D close-up view of the hole drilled PCD tool 240
6.32 Micro-grinding experimental setup 241
6.33 Chips produced as a result of ductile mode machining of silicon . . . 242
6.34 Different cutting regimes when machining silicon using different machining parameters 243
6.35 Measured Sa values for ductile mode machined silicon surfaces under different experimental conditions 244
6.36 Machining of 10×10 mm area using a fine patterned planarization tool at: (a) 70% radial immersion, (b) 5% radial immersion 245
6.37 Schematic representation of post-processing using mechanical planarization tools to remove subsurface damage layer 245

6.38 Post-processing using mechanical planarization tools to remove sub-surface damage layer 246
6.39 Wear and breakage of the edges of fine patterned PCD tool 246

List of Tables

1.1 Classification of microfabrication techniques. 3

2.1 Properties of the dielectric fluid (EDMfluid 108 MP-S) 19
2.2 Thermo-physical properties of WC and Co 27
2.3 Material properties of 90WC-10Co 29
2.4 Taguchi's L27 experimental conditions. 34
2.5 Results of mean and standard deviation for KERF measurements at different thicknesses. 39
2.6 ANOVA for KERF at different thicknesses. 40
2.7 Experimental results for a constant thickness of 500 μm 45
2.8 ANOVA results for 'Sa' and MRR 46
2.9 S/N ratio of KERF, 'Sa' and MRR for all experiments 48
2.10 Selection of optimum levels for KERF based on S/N ratio 49
2.11 Selection of optimum levels for 'Sa' based on S/N ratio 49
2.12 Selection of optimum levels for MRR based on S/N ratio 49

3.1 Chemical composition of Stavax ESR stainless steel 65
3.2 Mechanical properties of Stavax ESR stainless steel 65
3.3 Experimental conditions for investigating the relationship between radial immersion and feed rate (N=15000 RPM, ap=0.16 mm). 70
3.4 Experimental conditions for slot micromilling tests with worn tools . . 80
3.5 Experimental set for investigating tool life 105
3.6 Experimental conditions for micromilling of Ti6Al4V 109

4.1 Experimental conditions of orthogonal micro-turning tests. 130
4.2 EDS analysis of surface on the tool 133

4.3 BUE parameters obtained under different machining conditions. . . . 146
4.4 The coefficients of the material model 149
4.5 Friction definitions in the hybrid model. 155

5.1 Specifications of the fabricated tailored single-edge micro end mills . 166
5.2 Experimental conditions used for BUE studies 174
5.3 Micro end mill geometric specifications 190
5.4 A comparison between FEM and analytical model for different γ and R_{Tr} values. 198
5.5 Critical transition radius and corresponding deflections for different neck taper angles (L_c=800 μm) 199
5.6 Coefficients for deflection equation. 203
5.7 Coefficient of the first principal stress equation. 203

6.1 μ-WEDM parameters used for PCD tool fabrication 220
6.2 μ-EDM hole drilling parameters. 239
6.3 Silicon micro-grinding experimental conditions 242

Chapter 1

Introduction

Nowadays, there is an emerging global trend toward miniaturization of systems, equipment and devices almost in every field of science, engineering and technology. Therefore, miniaturization in the fabrication industry and manufacturing systems is not exception from this global trend. Since the world competitive market is experiencing an increasing demand for miniaturized products to increase design flexibility, to dwindle energy consumption and to achieve higher degree of accuracy, concepts like “small equipment for small parts”, “micro-factories for micro-scale products ” and “scaled-down manufacturing systems” are becoming more and more apparent [1, 2].

The miniaturization trend is today demanding the production of higher functionality structural and mechanical components with significantly decreased manufactured features in the range of a few to a few hundred microns for applications in the aerospace, automotive, optics, electronics, medicine, biotechnology, communications, defense and avionics, to name a few [3, 4, 5]. Specific applications for micro-scale parts include microchannels for lab-on-a-chip devices [4], micro heat exchangers as compact devices for heat transfer enhancement [6], miniaturized gas analysis systems [7], micro-scale rate integrating gyroscopes for navigation systems in aircrafts and guided weapons [8, 9], micro-pumps for flow-controlled delivery in micro-fluidic systems [10], micro-nozzles for high-temperature jets [3] and etc.

There are numerous key advantages of miniaturization from both manufacturer and costumer perspectives, including portability (which reduces the risk of sample contamination and problems due to mishandling for users of analytical devices), disposability, heat transfer enhancement due to high surface to volume ratios, lower cost of raw material and reduced power consumption [2, 11].

The starting of miniaturization trend can be traced back to the revolutionary talk of Nobel Laureate Richard Feynman at California Institute of Technology in 1959, which can be considered as the cornerstone of a scientific field which is now known as micro/nanotechnology. With his famous paper in 1960 entitled "There's Plenty of Room at the Bottom", with no doubt, he revolutionized the industry and the vision of scientists and researchers about creating a microscopic world. At that time, he mentioned the fabrication of micro-scale components using scaled-down processes and machines as a great challenge of the researchers [12].

To create microscopic world, and to bring Feynman's vision into practice, various microfabrication techniques have been developed already and people are continuously adding new and efficient techniques to the edifice of microfabrication to bring some fictitious and fantastic designs of the human-being into reality. The developed techniques for the fabrication of micro parts can be classified according to different criteria. In general, they can be divided into two groups [13]: micro-system technologies (MST) which are also known as mask-based, MEMS-based or IC fabrication techniques, and micro-engineering technologies (MET) in which tool-based micromachining techniques are major part of it. Subdivisions for each group can be seen in Table 1.1. Figure 1.1 illustrates examples of micro parts produced by different microfabrication techniques.

Micro-system technologies are widely used to fabricate micro/nano-structures with a resolution in the range of a few 10 nm and with methods based on scanning probe microscopy (SPM) the achievable resolution limit extends to the atomic scale [29]. The most important limitations of micro-system technologies are their quasi-three dimensional nature, meaning that they have only the ability to produce 2D and 2 1/2 D features (planar and quasi-planar geometries). Therefore, they mostly suffer from lack of control and accuracy in third dimension, which makes them very poor in generating

Table 1.1: Classification of microfabrication techniques.

Type of Technology	**Process Category**	**Principle**	**Nature of the process**	**Example**
Micro-engineering Technologies (MET)	Mechanical Processes	Force	Subtractive	Micro-engraving [13] Micro-turning [14] Micromilling [15] Micro-grinding [16] Micro Ultrasonic Machining (MUSM) [17]
		Plastic deformation	Subtractive	Punching [18]
			Near-net-shape process	Microforming [19]
	Energy Assisted Processes	Melting/ Vaporization	Subtractive	Micro-electrical Discharge Machining (EDM) [14] Laser Beam Machining (LBM) [13] Electron Beam Machining [13]
		Ablation	Subtractive	LBM (Excimer, Ultra-fast laser) [13]
		Dissolution	Subtractive	Electro-chemical Machining (ECM) [20]
	Micro-replication Techniques	Replication	Near-net-shape process	Hot-embossing [21] Micro-injection molding [22]
		Solid free-form fabrication (SFF) or Rapid prototyping (RP)	Additive	Selective laser sintering (SLS) [23] Stereolithography [24] Metal-jets [25]
		Recomposition	Additive	Electroforming [26]
	Hybrid Processes	Combination of mechanisms	Mainly subtractive	Combined μ-EDM /μ-ECM [27] Combined -EDM/ MUSM [28]
Microsystem Technologies (MST)	MEMS Based Processes	Photo-lithography Wet-and-dry etching Thin film deposition LIGA SPM-based techniques [29] Other special technologies		

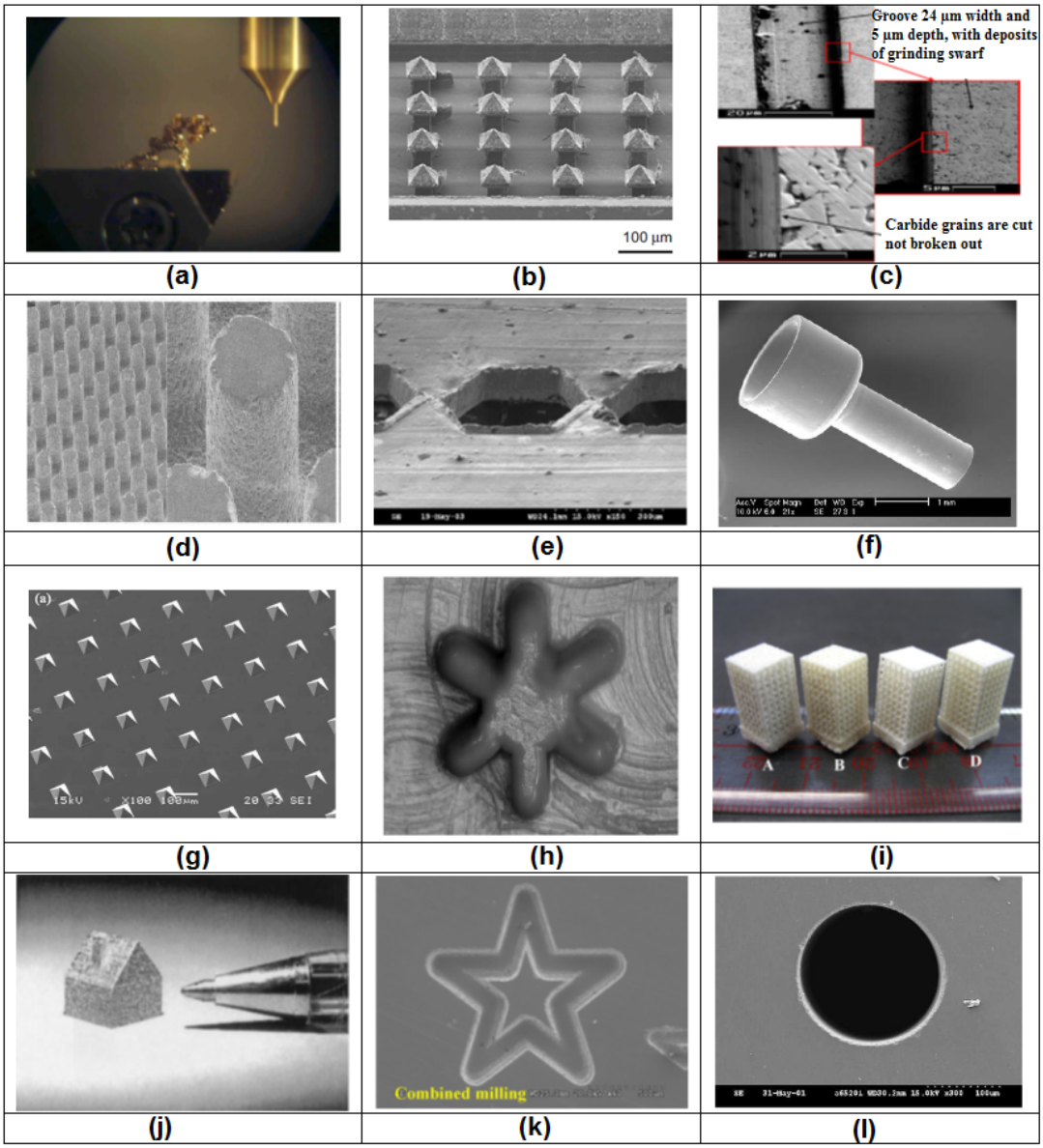

Figure 1.1: Micro-parts fabricated by different microfabrication processes: (a) A 2 mm shaft (µ-turning) [14], (b) Array of microbarbs (Micromilling) [15], (c) Microstructures in carbide (Micro grinding) [16], (d) Micro-cylinders of 280 µm diameter and 600 µm depth on Si (MUSM) [17], (e) hexagonal micro holes (Punching) [18], (f) A micromotor shaft (Microforming) [19], (g) Hot-embossed micro-array [21], (h) Micro-gear in ABS (Micro injection molding) [22],(i) Nano-composite scaffolds (SLS) [23], (j) Micro house model (Metal jet process) [25], (k) Five-pointed star (µ-EDM /µ-ECM) [27], (l) micro-hole in borosilicate glass (µ-EDM/USM) [28].

sculptured (free-form) surfaces. Hence, these processes are preferred for features with low aspect ratios. It should be mentioned that among different MEMS based techniques, deep X-ray lithography using synchrotron radiation beam (LIGA process) can produce three dimensional sub-micron structures with very high form accuracy. However, LIGA processes require special expensive facilities, and it is limited to relatively small thicknesses [14].

Although, IC based techniques has been well developed and implemented for processing of silicon and silicon-like materials, they have a very limited applications in processing wide spectrum of other engineering materials such as metals, polymers, composites and etc. The ever increasing application of these materials in MEMS and other industries and the needs for their processing, together with the limitations and challenges in utilizing MEMS based techniques, have led to the development of tool-based micro-fabrication techniques.

Tool-based micro-fabrication techniques encompass a large variety of processes, some of them have been developed by scaling down of conventional machining processes such as micro-turning, micromilling and micro-drilling. These processes are known as mechanical micromachining processes. There are other processes, which are based on non-traditional machining technologies such as micro-electrical discharge machining (μ-EDM), micro-electro-chemical machining (μ-ECM) or a combination of these processes known as hybrid processes, such as EDM/ECM, ultrasonic assisted EDM (US/EDM)and etc. [14].

The focus of this thesis is on two groups of tool-based micro-fabrication processes i.e. micro-mechanical machining and EDM-based machining methods, which are widely used at micro-system design and manufacturing center of Bilkent University for the fabrication of different micro-components from variety of engineering materials.

The purpose of mechanical micromachining processes is to remove the unwanted materials from workpiece using micro-cutting tools. These micro-cutting tools, which have a defined geometry and cutting edges are able to produce complex 3D geometries in the order of 10 μm to 10 mm from different engineering materials [30]. EDM-based

techniques can be used for different applications, including fabrication of micro-molds for micro-injection molding applications, micro-hole drilling on difficult-to-machine materials and for micro-tool fabrication. In this thesis, EDM-based techniques are mainly used for micro-tool fabrication purposes.

Tool-based micromachining processes not only eliminate the requirements for very expensive clean room facilities but also leave a smaller environmental footprint by completely eliminating chemical materials such as etching solutions and etc. [31]. However, there are several challenges associated with these processes which should be explored before they can be successfully implemented in industrial scale for fabrication of miniaturized components.

The successful implementation of mechanical micromachining processes as a reliable and efficient method of fabricating miniaturized parts, requires an in-depth understanding of various phenomena involved in the process, including mechanism of material removal, tool wear and tool deflections, the interaction between cutting tool and workpiece material at micro-scale, the nature of cutting force and evolution of micro-part surface topography. The knowledge about all these phenomena is necessary to fabricate micro-parts satisfying required dimensional and geometrical tolerances, and surface quality requirements. This knowledge cannot be obtained without doing fundamental research in this field having a well control on different elements contributed to the outputs of micromachining.

One important element of micro-cutting which highly influences process outputs is the micro-cutting tool. The geometry and surface quality of the micro-tool has a direct influence on the process. Therefore, one aim of this theses is to produced engineered micro-tools with a defined geometry, edge radius and surface finish for micro-cutting studies. The other factor of major contribution, is the workpiece material. In order to better understand the interaction between cutting tool and workpiece at micro-scale cutting, materials having different characteristics in terms of ductility are selected. For ductile materials the objective was to determine minimum uncut chip thickness, while for brittle materials the objective was to select a combinations of process parameters to have ductile mode machining without introducing damage to the machined surface.

Objectives

The main objective of this thesis is to better understand the mechanism of micro-scale cutting by using engineered cutting tool geometries, and determine a combination of machining process parameters and cutting tool geometry to produce high precision micro-features on difficult-to-cut materials such as Stavax ESR stainless steel, titanium alloy Ti6Al4V and silicon. The following specific objectives are defined to achieve these goals:

- Improving the understanding about the mechanics of micromachining, especially the tool-material interaction issues through experimental, analytical, and computational models.
- Investigating the possibility of using various electrical discharge machining techniques to fabricate tailored micro cutting tools.
- Experimental investigation of the effect of different WEDM process parameters on performance measures of WEDM for high precision micro tool fabrication.
- Design and fabrication of optimized tailored micro end mills for the machining of difficult-to-cut materials such as stainless steel, titanium alloy Ti6Al4V and silicon.
- Developing a design methodology for tailored micro end mills.
- Finding appropriate process parameters for ductile mode machining of silicon.

Organization of Thesis

This thesis is organized in seven chapters. Chapter 2 is devoted to the micro-tool fabrication by EDM-based processes. In this chapter EDM process and its application for micro-tool fabrication is discussed with an emphasize on WEDM process. Effect of WEDM process parameter on performance measures of WEDM process is studied

through the technique of design of experiments, analysis of variance and S/N ratio. The most significant parameters and their optimum levels are determined.

Chapter 3 deals with experimental investigations of micromilling of Stavax stainless steel and Ti6Al4V. The influence of process input parameters such as cutting speed, depth of cut, feed per tooth, radial immersion percentage, and plunging method on process outputs during circular pocketing operation of Stavax is discussed. Tool wear, machining forces and surface roughness measurements are considered to identify the relationships between process inputs and outputs. The presence of built-up edge (BUE) during micromilling of Ti6Al4V is highlighted.

In Chapter 4, the influence of built-up edge on process forces, surface quality and minimum uncut chip thickness (MUCT) during micro machining of Ti6Al4V is investigated. Cutting edges with small edge radii are fabricated to match the requirements of micro-scale cutting through the use of WEDM process. The uncut chip thickness values were set to be less than the edge radius to create micro-scale machining conditions. Cutting edges and machined surfaces were investigated after the tests to reveal the influence of built-up edge on process outputs. Attempt has been made to do the finite element simulation of micro scale orthogonal machining considering the influence of built-up edge formation, where the edge of the cutting tools is replaced with an equivalent edge, after careful observation of the stable built-up edges obtained during micro turning experiments.

In Chapter 5, the findings in the previous chapter is extended to the micromilling process. Tailored micro end mills have been designed, fabricated and tested for micromilling of Ti6Al4V with geometries emanating from engineered tools used in orthogonal cutting experiments. The effect of BUE on the process outputs of micromilling has been studied using developed tailored single edge micro end mills. A systematic approach is used to obtain an optimum cutting tool geometry to reduce tool deflections during machining.

Chapter 6 investigates the influence of polycrystalline diamond micromilling tool geometry while machining silicon. Micromilling tools with hexagonal and circular array patterns are produced using micro-WEDM. The influence of micromilling tool

geometry and machining process parameters on the tool wear and surface quality is studied. A novel cutting tool geometries are designed and fabricated for ductile mode machining of silicon.

The final chapter provides a summary of the results of this thesis. The scientific accomplishments in this thesis are also highlighted in this chapter along with the recommended future works.

Chapter 2

Micro-tool Fabrication by EDM-based Processes

2.1 Introduction

Micro tools are the most flexible part of any micro-cutting system, and they have the lowest stiffness in whole micro cutting process chain. They are considered to be the main drawbacks of the mechanical micro machining process in terms of tool wear, tool size, tool dimensional accuracy and tool deflection [32] .

There exist variety of conventional micro end mills with diameters in the order of tens of microns in the market. For instance NS Tool Co. produces square micro end mills with diameters starting form 100 μm. A common feature of all available conventional micro tools is their identical geometry obtained by scaling down of macro-scale end mills. A similar situation exist in the academic side of research in the area of micro-tool design and fabrication, and only limited researches reported in this area, where simple geometries are fabricated and used for micromachining without too much attention into geometric optimization of cutting tools to achieve better tool performance. Therefore, design and fabrication of new cutting tool geometries based on the knowledge of interaction between cutting tool and workpiece at micro-scale is a

challenging task. Successful implementation of mechanical micromachining for high precision manufacturing purposes requires high performance, high precision cutting tools with optimized geometries specifically designed based on the requirements of certain machining task. To fulfill all these requirements novel cutting tool geometries and high efficient and accurate fabrication methods are always a requirement.

In contrast to industry which uses grinding as a main manufacturing process of micro end mills, the researchers are mainly focused on non-traditional machining processes to fabricate micro end mills. Two main groups of non-traditional machining processes used in micro-tools fabrication are focused ion beam machining (FIB) and methods based on electro-discharge erosion (EDM-based). Example of application of FIB for micro tool fabrication can be seen in a study conducted by Adams et al. [33]. They reported fabrication of 25 μm diameter micro end mills with 2, 4 and 5 cutting edges in tungsten carbide. They obtained a small edge radius of 0.1 μm. Vasile et al. [34] also used FIB to produce micro end mills of 25 μm diameter in high speed tool steel. Besides FIB, techniques based on discharge erosion are used by various researchers to fabricate micro tools with different sizes and geometries. Figure 2.1 illustrates examples of micro-cutting tools developed by various researches and fabricated by one of the EDM-based techniques.

Comparing FIB and EDM-based techniques, it can be found that FIB technique is considerably more expensive and slower than EDM, but very sharp edges can be machined by means of FIB [35]. However, this small edge radius generated in materials such as tungsten carbide can be easily chipped or will be transformed into a larger radius at the initial stage of the cutting process. Since most of the micro-machined parts require features larger than 100 μm, and sharp edges created on tungsten carbide (WC) or polycrystalline diamond (PCD) will be easily worn at the early stage of the machining, resulting in a larger edge radii, this study is focused on the use of EDM-based techniques in micro-tool fabrication .

In this chapter, after a brief introduction to the principle of EDM process, on-machine micro-tool fabrication techniques are introduced and successfully implemented for fabricating various micro end mills from WC and PCD. When using on-machine fabrication methods, since micro-tools are fabricated on the same spindle

which is also used in machining operations, this makes it possible to achieve the required accuracy by eliminating the errors due to tool runout and tool holding system.

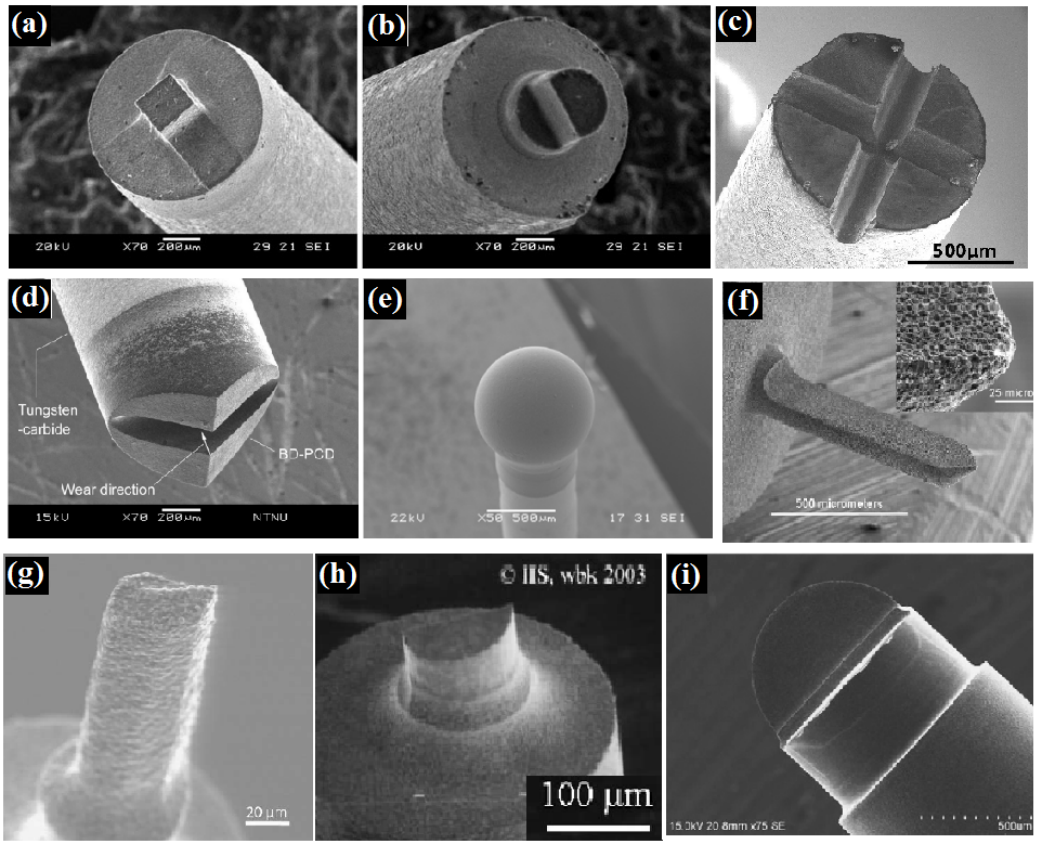

Figure 2.1: Micro-tools fabricated by EDM-based techniques: (a) Square-micro end mill [36], (b) D-shaped micro end mill [36], (c) Micro-tool with two perpendicularly crossed microgrooves [37], (d) micro-tool with double-negative back rake angle [38], (e) spherical micro tool [39], (f) conical tipped micro tool [40], (g) helical shaped micro tool [41], (h) half-polygonal micro end mill [42], (i) half-cut hemisphere micro end mill [43].

In the second part of this chapter, wire electro-discharge machining of WC has been studied in detail in terms of the effect of WEDM process parameters on surface roughness, MRR and cutting width (KERF). Controlling the surface roughness of fabricated micro-tools is important since it directly affects the tribological behavior of the cutting tools during machining. Understanding of KERF in WEDM process is of significant importance, since without having a knowledge about KERF, it is not possible to produce high precision cutting tools. The findings in this part are used in the subsequent

chapters of this thesis to have a full control on the dimensional accuracy and surface quality of the fabricated engineered tool geometries.

2.2 Principles of Electrical Discharge Machining (EDM)

Material removal in EDM process is based on the eroding effect of successive electrical discharges (sparks) due to melting and vaporizing workpiece material. Figure 2.2 schematically illustrates the process of material removal in EDM.

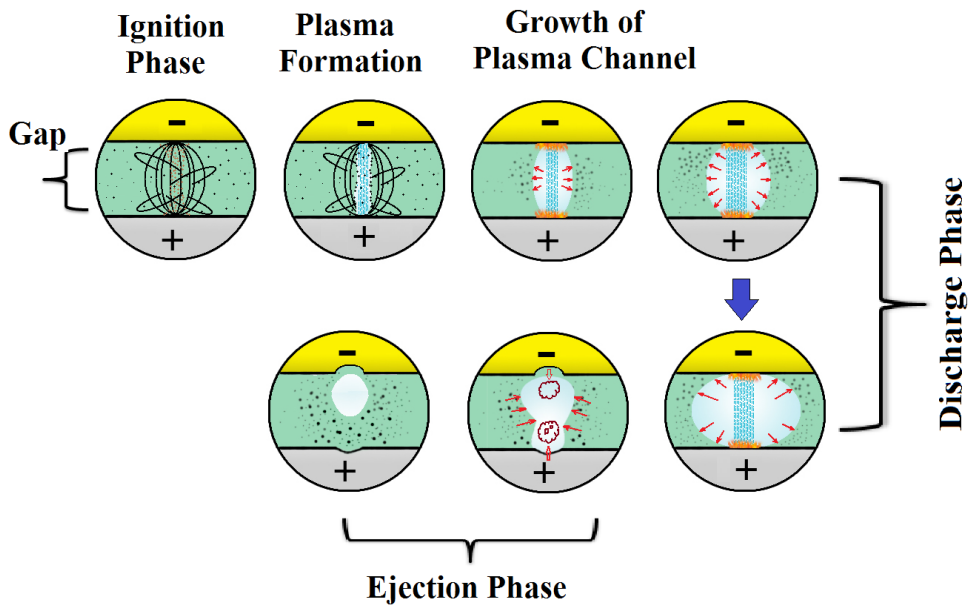

Figure 2.2: Working Principles of EDM.

In this process, when a DC electric pulse reaches to the electrode and workpiece (known as ignition voltage), a strong electric field develops in the gap (separation between electrode and workpiece filled with dielectric fluid). The movement of electrons towards the workpiece starts under the influence of this intense electric field (breakdown initiation). Accelerated electrons collides to the natural species in the dielectric medium causing the creation of an electron avalanche [44]. The distortion in the electric field and streamers development towards both electrodes results in established

discharges, which are known as arc discharges based on discharge duration and current density.

According to Lee [45] the electron emission from the cathode is due to secondary, thermionic and field emissions. Under the conditions of EDM discharges, where there exist strong temperature and electrical field, according to Thomas-Fermi theory the emission process is strongly dependent on both fields[46]. In addition to the electron emission phenomenon, since there is always some microscopic contaminants suspended in the dielectric fluid with diameter in the same order as gap width and surface roughness of the workpiece, these suspended contaminants will also be attracted by the electric field and will concentrate at the strongest point of the field. As a result, a high conductive bridge known as plasma channel forms across the gap.

At the initial stage, the plasma channel has a uniform growth followed by a faster growth phenomena. As a result, much energy will be deposited in the brightly lit plasma column connecting electrode and workpiece. At this point both temperature and pressure rapidly increases in the plasma channel, generating a spark. At the point of spark contact small amount of material melts and vaporises from the electrode and the workpiece. A bubble composed of gaseous byproducts of vaporization rapidly expands outwards from the spark channel. When the pressure of the expanded bubble drops below atmospheric pressure, the bubble collapse occurs and liquid jets penetrate into the bubble. This liquid jet strikes into the generated molten crater and ejects molten material [47]. At the end of pulse duration, dielectric fluid recovers its strength due to the recombination of ions and electrons [46] and flushes away molten and ejected materials from both electrode and workpiece.

Depending on the pulse frequency, thousands of sparks will be generated in a second, and each spark results in a bowl shaped crater on the workpiece surface. The superposition of individual craters results in the material removal from the workpiece and defines the morphology of the electrical discharge machined surfaces.

Based on the geometry requirements of the workpiece, the aforementioned mechanism is employed in different configurations, which are generally known as EDM-based fabrication techniques. These techniques are briefly introduced in the subsequent

sections and are used for micro-tool fabrications in this thesis.

2.3 EDM-based Fabrication Processes

There are several variations of EDM-based techniques depending on the geometry and configuration of the electrode and workpiece. The main EDM-based processes that found applications in micro-tool fabrication are discussed in this section.

2.3.1 Block-EDM Process

The simplest arrangement of workpiece (micro-tool) and sacrificial electrode (normally pure tungsten (99.95%)) for micro-tool fabrication can be found in what is so called as stationary block-EDM method. As it can be seen in Figure 2.3 (a), in this process in order to form a micro-tool, a combination of two or three different motions are used. The third motion, which is the rotational motion of the tool, is used for circular cross-sections. For flat surface generation, such as those of triangular or square end-mills, no rotational motion is required. In this process tool is fed towards the block while moving upward and downward (Z-direction). Since in this process, a larger area is exposed to the discharge process higher material erosion rates can be achieved.

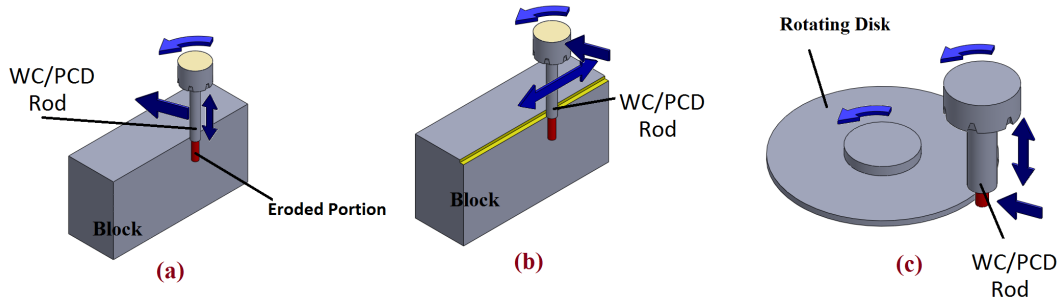

Figure 2.3: (a) Stationary block-EDM method, (b) Block EDG method, (c) Rotary disk EDM process.

The main disadvantage associated with this method is the wear of sacrificial electrode, which can be considered as the major systematic factor for dimensional inaccuracies. The wear also will result in a tapered micro-tool, which is undesirable in most applications. The wear rate can be reduced by moving the tool along block surface as can be seen in Figure 2.3 (b), which is called block electro-discharge grinding (Block-EDG). These methods are used by Ravi and Huang [48] in the fabrication of symmetrical electrodes and also by Rahman et al. [49] in the fabrication of PCD/WC micro end mills. In block-EDM method, the block can be modified based on the design requirements to increase fabrication flexibility in terms of creating angular and tapered surfaces as can be found in the work of Perveen et al. [36]. Since these methods suffer from obtaining an accurate dimensions due to the effect of electrode wear, they may be used as a rough machining of micro-tools to remove bulk of the material and to give an initial form to the tool. A subsequent high precision method, such as wire electro-discharge grinding (discussed in section 2.3.3) is required to fabricate high precision micro-tools.

2.3.2 Rotary Disk EDM Process

Another variation of EDM-based techniques for micro tool fabrication, is to use a rotary disk as sacrificial electrode as depicted in Figure 2.3 (c). The rotating disk acts like a grinding wheel which removes material as a result of successive electrical sparks. Although this method eliminates the wear problem of block-EDM techniques, however the rotating imbalances in the rotating disc may cause dimensional inaccuracies and variations in the gap width, which increases the possibility of short circuiting. Furthermore, when machining flat surfaces, where the tool is not rotating, the curvature of the disk will be imprinted into the machined micro-tools, resulting in a curved surface rather than a flat one.

2.3.3 Wire Electro-discharge Grinding (WEDG)

Figure 2.4 (a) schematically represents the WEDG process, which is known to be the most common technique to fabricate micro tools having various shapes. The principle of fabricating micro tools with this technique, proposed by Masuzawa et al. [50], is illustrated in Figure 2.4 (b).

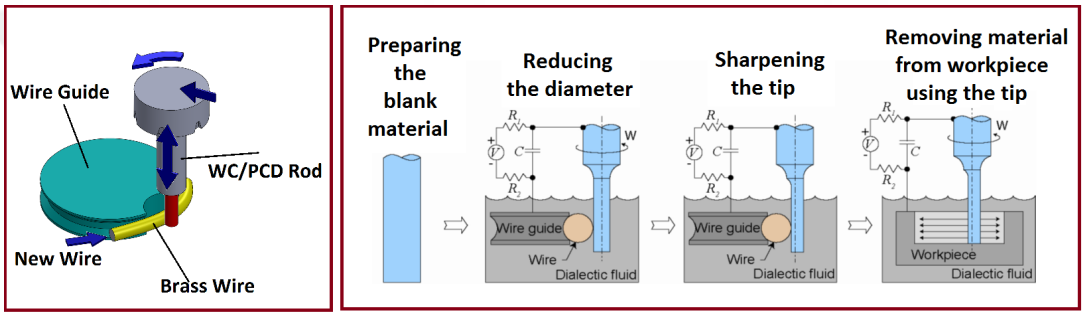

Figure 2.4: (a) Schematic representation of WEDG, (b) WEDG steps to fabricate micro tools [50].

In this process a guided traveling wire is used as a sacrificial electrode to erode tool material, where the tool is given positive polarity and the wire has negative polarity. Dielectric fluid (oil) is used to initiate and maintain sparks during the EDM process. In order to fabricate simple cylindrical micro-tools, as it has been shown in Figure 2.4 (b) the workpiece (micro-tool) is rotated and simultaneously moves upward and downward (in Z-direction) with a controlled gap between the tool and traveling wire. The fresh wire fed into the machining zone through a series of wire guides. In each complete upward and downward stroke, when the tool reaches to the upper dead point or bottom dead point, a depth of cut is given to the tool by moving towards the wire. This process will be repeated several times until the desired dimensions are achieved.

In WEDG, the fresh wire ensures the dimensional accuracy of the micro-tools, however the process has a low material removal rate. For complex cutting tools a specific tool path needs to be determined by the user depending on the final shape of the micro tools. In order to obtain axisymmetric tool shapes, the tool is rotated. It is also possible to obtain asymmetric shaped tools. Example of the application of WEDG in micro tool

fabrication can be found in the work of Egashira and Mizutani [51]. They used WEDG to fabricate D-shaped micro-tools of 20 μm diameter from cemented tungsten carbide. They reported an edge radius of 0.5 μm.

2.4 Some Applications of On-machine Fabrication of Micro-end Mills

On-machine micro-tool fabrication which incorporates a combination of block-EDM and WEDG in a single setup followed by a micromilling/grinding process on the desired workpiece, can be considered as an efficient and reliable method in the micro-fabrication industry. For applications requiring very tight dimensional and geometrical tolerances, on-machine micro-tool fabrication concept is becoming popular, since micro-tools are fabricated on the same spindles which are also used in machining operations. This enables manufacturers to achieve the required accuracy and to avoid tool wear and breakage by eliminating the errors due to tool runout and tool holding system. In this part of thesis, the potential application of on-machine micro-tool fabrication techniques for the manufacturing of micro end mills is discussed.

2.4.1 Experimental Setup for On-machine Fabrication of Micro-tools

The experiments were carried out in a hybrid micro-machine tool (MIKROTOOLS DT-110) available at Micro System Design and Manufacturing Center of Bilkent University. This machine can perform multiple machining processes such as micro turning, micromilling, micro-EDM, micro wire EDM and WEDG. The measurement of the processed parts can be performed using an on-machine measurement device (OMM). Figure 2.5 illustrates micro EDM setup used in this study.

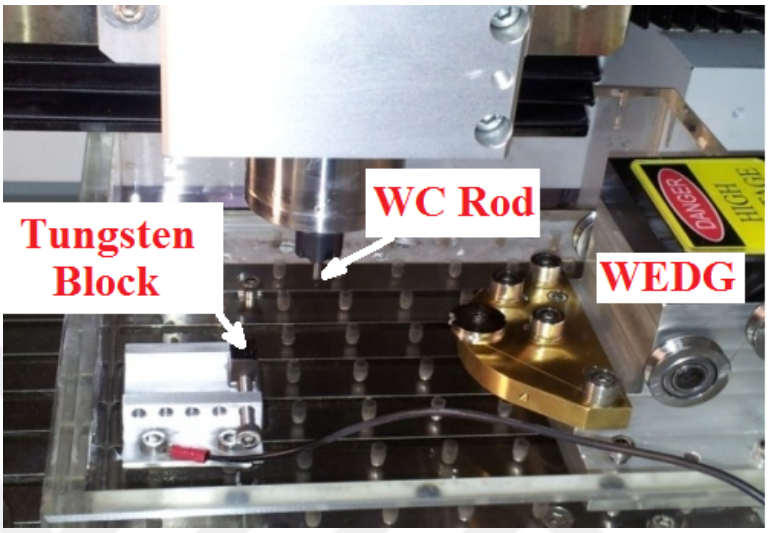

Figure 2.5: Experimental setup for on-machine fabrication of micro end mills.

Pure tungsten (99.95%) was used as a sacrificial electrode in block-EDM process and brass wire of 200 μm diameter has been used for WEDG. Tungsten carbide and polycrystalline diamond rods are mounted on a spindle (up to 3,000 rpm) with a positive polarity. Open voltage can be selected in the range of 80 to 130 V and capacitance can be set within the range of 10 pF to 400 nF. EDMfluid 108 MP-S with the specifications given in Table 2.1 is used as a dielectric fluid for all EDM processes described in this study. It has a medium viscosity and a flash point of 108 °C. In order to obtain complex geometries and desired clearance and rake angles, special indexing device has been designed, fabricated and integrated into hybrid machining center.

Table 2.1: Properties of the dielectric fluid (EDMfluid 108 MP-S)

Viscosity (at 20 °C)	**Flash Point (ASTM D 93)**	**Distillation Interval**	**Density**
3.0 (cSt)	≥ 108 (°C)	6(°C)	0.767(kg/l)

Micro-end mills can be produced in various forms and geometries depending on the intended applications. In this study, fabrication process of three common types of micro tools, i.e. cylindrical D-shaped, micro ball end mills, and lollipop end mills are investigated.

2.4.2 Fabrication of D-shaped Cylindrical End Mills

D-shaped cylindrical micro tools are among the simplest micro end mill geometries which show a good performance in micro machining operations [36]. To fabricate these micro tools, a PCD or WC rod is mounted on the spindle, and its diameter has been reduced to a value close to the desired dimension using block-EDG method. Then, the tool is further processes by WEDG process to achieve the desired diameter. In order to machine the flat part of the tool, which is to create a rake face on the tool, the spindle rotation is stopped and WEDG operations are done as described in section 2.3.3. Fabrication process is shown in Figure 2.6.

Figure 2.7 illustrates the fabricated D-shaped micro tool on WC and PCD, through a combination of block-EDM and WEDG process. It should be mentioned that, this tool has a zero clearance angle and effective rake angle of the tool can be changed by changing the position of the flat face with respect to tool center. This tool has a zero clearance angle, however a clearance angle can also be machined by adding one more WEDG step.

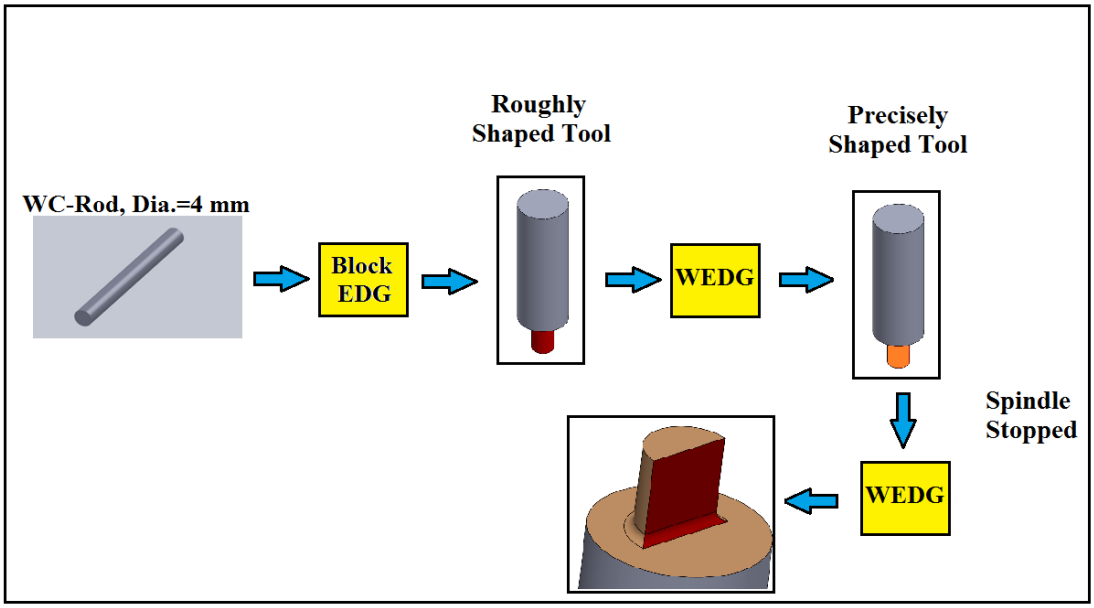

Figure 2.6: Fabrication of D-shaped flat end cylindrical micro end mill using a combination of block-EDG and WEDG.

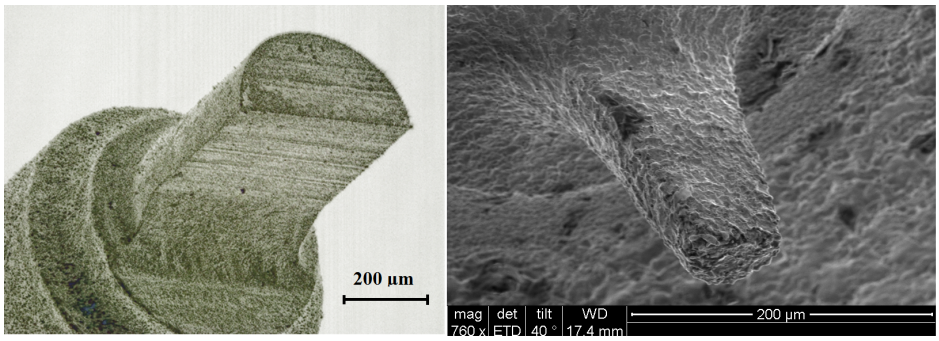

Figure 2.7: Fabricated D-shaped flat end cylindrical micro end mills on: (a) WC, (b) PCD.

2.4.3 Fabrication of Micro-ball End Mills by Block-EDG

Micro-ball end mills are an important tools for creating complex free-form surfaces. Two methods can be used for their fabrication through the use of experimental setup of Figure 2.5. The first method is based on block-EDG process as depicted in Figure 2.8.

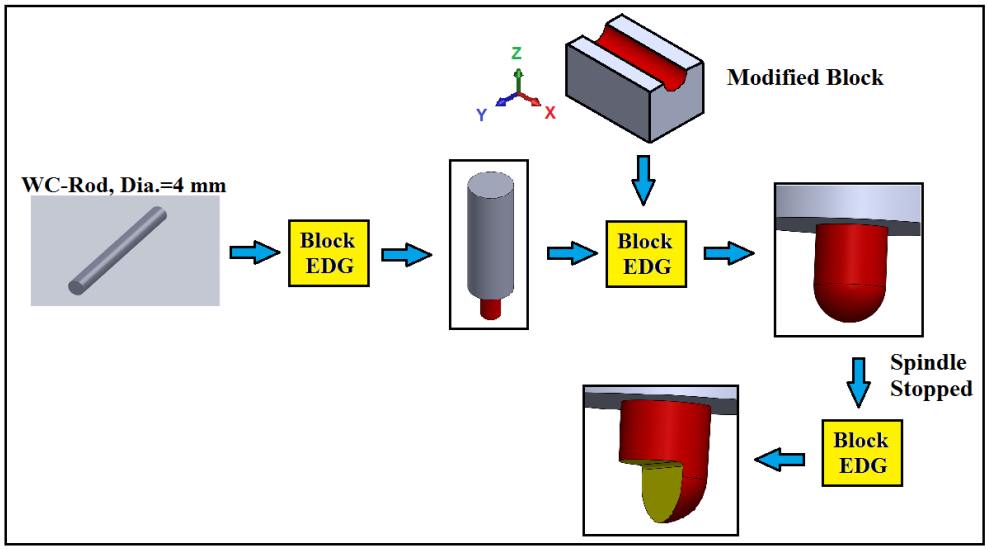

Figure 2.8: Micro-ball end mill fabrication by modified block-EDG process.

In this process, block-EDG is used to reduce the diameter of the WC/PCD rod to the dimension of interest. Then a modified sacrificial tungsten block is used depending on the desired ball end mill diameter. This modification can be done by milling a groove using a conventional ball end mill or by using wire electro discharge machining. To create rake face of the tool, the spindle should be stopped and another block-EDG operation should be performed.

2.4.4 Fabrication of Micro-ball End Mills by WEDG

Wire electro-discharge grinding can also be used to fabricate micro-ball end mills. This method can be used for applications where high precision micro-ball end mills are required. In this process the same steps mentioned in block-EDG methods are used. The only difference is the replacement of the sacrificial tungsten block with the wire. The challenging issue regarding the fabrication of micro-ball end mills using WEDG process is the motion of the tool with respect to the wire. In macro-scale processes the wire diameter is negligibly small compare to the wire trajectory, however in micro-tool fabrication, since the size of the wire and the tool are in the same order of magnitude, wire size cannot be neglected, because neglecting wire size effect may result in large differences between the desired and fabricated micro features. Therefore, regular circular interpolation commands generated by CNC controller units cannot be directly applied for micro-ball end mill fabrication using WEDG process.

In this study, in an attempt to compensate for the wire size effect in micro-ball end mill fabrication, following tool trajectory has been developed. It should be mentioned that, for successful use of this strategy, it is necessary to select a suitable zero point on the workpiece (denoted by 'O' in Figure 2.9).

To obtain tool trajectory, using notations given in Figure 2.9, we have:

$$X_{O'} = \left(\frac{D_T + D_W}{2}\right)(1 - cos\phi) \tag{2.1}$$

$$Z_{O'} = \left(\frac{D_T + D_W}{2}\right)\sin\phi \tag{2.2}$$

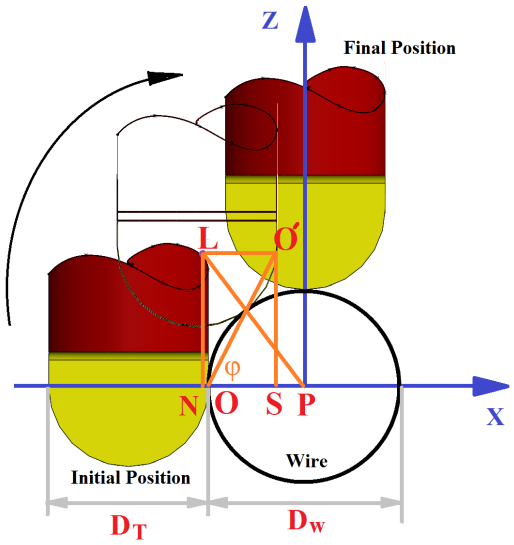

Figure 2.9: The designation used for wire diameter compensation.

For micro-ball end mill fabrication using WEDG, the angle should be in the range of $0 \leq \varphi \leq \frac{\pi}{2}$. Using the trajectory defined by equations 2.1 and 2.2, micro-ball end mills are successfully fabricated from PCD and WC as illustrated in Figure 2.10. The edge radius of the fabricated micro-ball end mills are measured using 3D laser scanning microscope (Keyence VK-X110) as depicted in Figure 2.11. An edge radius of 12 µm achieved using this method.

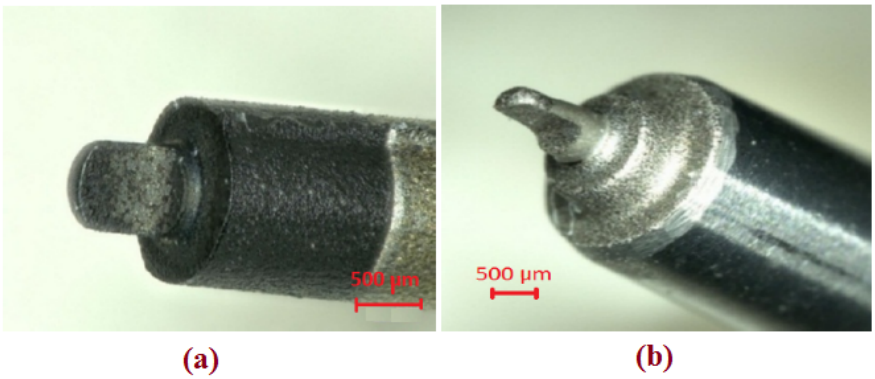

Figure 2.10: Micro ball end mills fabricated through WEDG process: (a) PCD tool (b) WC tool.

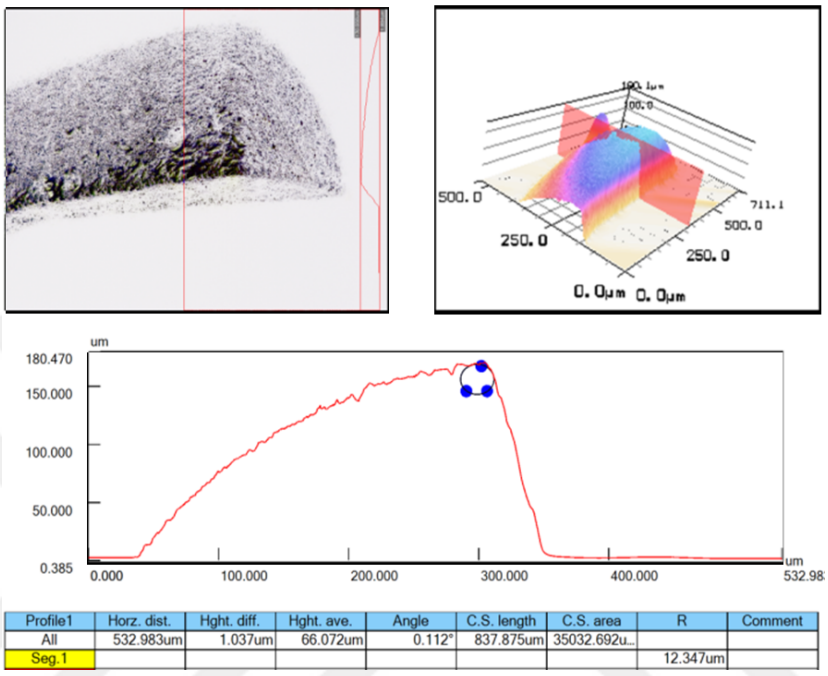

Profile1	Horz. dist.	Hght. diff.	Hght. ave.	Angle	C.S. length	C.S. area	R	Comment
All	532.983um	1.037um	66.072um	0.112°	837.875um	35032.692u...		
Seg.1							12.347um	

Figure 2.11: Measured cutting edge radius of micro-ball end mills.

2.4.5 Fabrication of Lollipop Micro-end Mills by Block-EDG

Lollipop end mills are effective cutters for milling complex geometries and cutting of curved surfaces and profiles with an undercut. In this study, a novel method has been introduced to fabricate micro-lollipop end mills using block-EDG technique. This method requires some modifications of the sacrificial pure tungsten block, which can be done through micromilling or WEDM operations. The sequence of fabrication process is shown in Figure 2.12

As it is shown in Figure 2.12, the diameter of the blank rod (D_b) is reduced to a diameter of the lollipop micro end mill ($2 \times R_L$), giving an appropriate depth of cut in the axial direction and simultaneous movement in longitudinal (X) and transverse (Y) directions. The movement in 'Y' direction should be controlled to achieve the desired diameter ($2 \times R_L$) taking into account sacrificial electrode wear and spark gap.

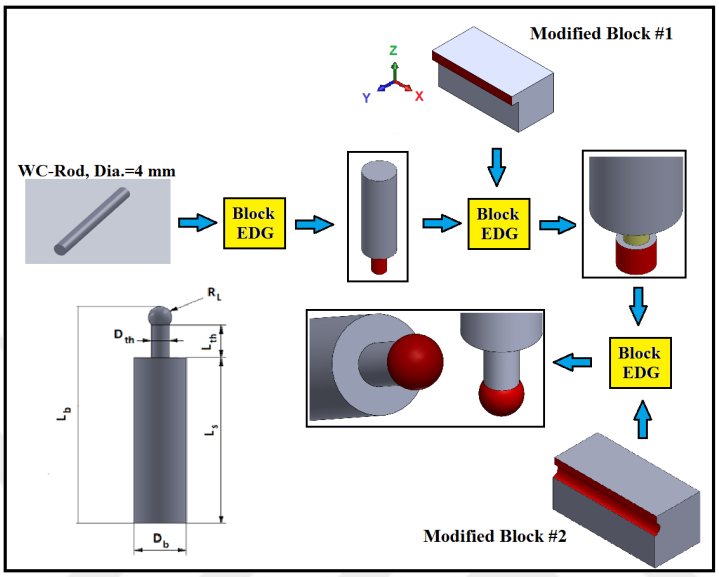

Figure 2.12: Fabrication of lollipop micro end mill by Block-EDG process.

After achieving the desired diameter, the next step is to use a modified sacrificial tungsten electrode to machine the throat of the end mill with a length of 'L_{th}' and diameter of 'D_{th}'. The width of the machined step determines 'L_{th}'. Again an appropriate controlled movement in 'Y' direction is necessary to obtain 'D_{th}'.

In the final step, modified sacrificial tungsten electrode which includes a hemispherical channel of radius of 'R_L' obtained by micromilling is used to give a final shape to the tool. It should be mentioned that the top portion of the block should also be modified based on 'D_{th}' of the tool. In the last step of the operation, the machined tool is brought into an appropriate position according to the desired dimensions of the tool and machined features of the block, and block-EDG is performed using appropriate machine movements. Figure 2.13 illustrates the fabricated lollipop micro end mill by this method. The fabricated lollipop micro end mill can be used in micro grinding operations, however, depending on the application requirements, a rake face similar to ball end mills can also be machined.

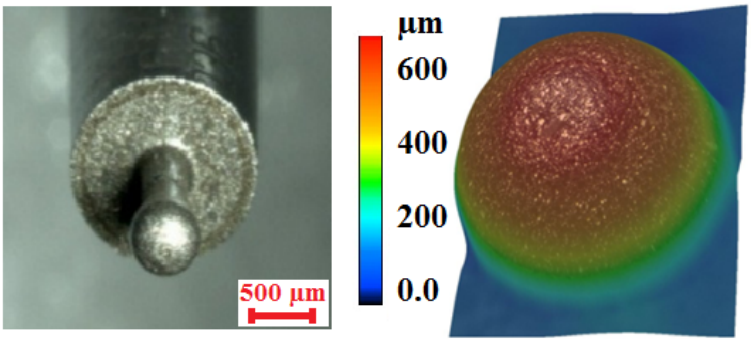

Figure 2.13: Lollipop end mill fabricated through block-EDG process.

2.5 Micro-tool Fabrication by Wire Electrical Discharge Machining (WEDM)

Wire electrical discharge machining (WEDM) is another variation of EDM-based methods, which has found wide acceptance in the industry, specially in high precision die making from difficult-to-machine materials. Owing to its non-contact nature, very small diameter cutting tools can be fabricated with this technique. As schematically depicted in Figure 2.14, WEDM uses a traveling wire as electrode to cut complex outlines and fine details in difficult-to-cut materials. In this process, wire derive system continuously feeds the fresh wire under a controlled tension to the working area, guided by a set of precise sapphire and diamond wire guides. New wire is always exposed to the workpiece, so electrode wear problem of block-EDM methods (discussed in section 2.3) will be completely eliminated.

In this thesis, WEDM is widely used in the fabrication of engineered cutting tools from cemented tungsten carbide and polycrystalline diamond. There is a limited technical and scientific knowledge about characteristics of micro-WEDM of ultra-fine grain tungsten carbide (WC-Co, grain size< 0.7 µm), a material used in this study for micro tool fabrication purposes. Number of studies on electrical discharge machining of WC-Co composites is limited in the literature, and most of the researches in this area are related to die-sinking EDM of WC [52, 53] and the literature is lack of studies

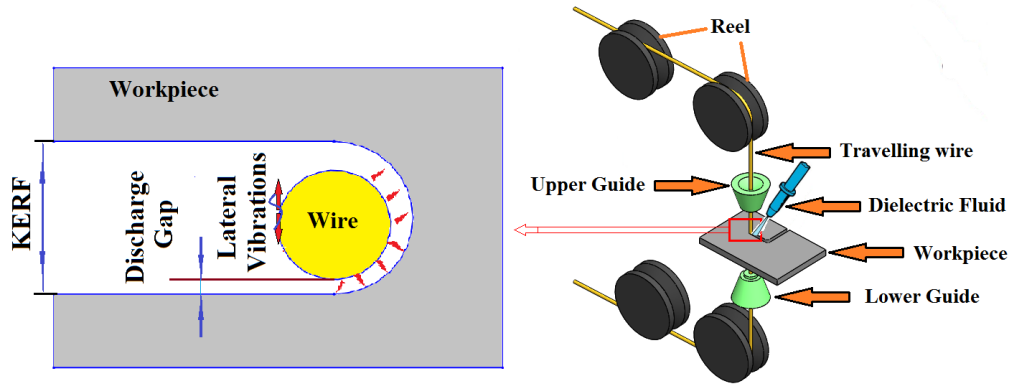

Figure 2.14: Schematic representation of WEDM process and KERF.

specifically devoted to the micromachining of ultra-fine grain tungsten carbide using micro-WEDM process.

Issues related to the traveling wire in WEDM process such as wire lag and vibrations makes WEDM process even more difficult to analyze compare to die sinking EDM. In some cases due to the stochastic nature of the process it is even difficult to observe a distinguishable single characteristic discharge crater on the WEDMed surface.

Dual composite of tungsten carbide and cobalt (WC-Co) has a non-homogeneous microstructure consisting of two phases of tungsten carbide (WC) and cobalt. This non-homogeneity in the microstructure has been addressed as the main difficulty in the EDM of WC-Co, due to different thermo-physical properties associated with each phase [54]. The thermo-physical properties for each phase is given in Table 2.2. The values given in Table 2.2 are taken from [55, 56] and [57].

Table 2.2: Thermo-physical properties of WC and Co

Phase	**Melting Point (°C)**	**Vaporization Point (°C)**	**Thermal Conductivity (W/m.K)**	**Molar Heat Capacity (J/mol.K)**
WC	2830	6000	110	39.8
Co	1495	2927	100	24.81

As it can be seen in Table 2.2, there is a big difference between thermo-physical properties of WC and Co. Therefore, during EDM process, cobalt matrix will be

melted faster than WC, due to a lower melting and vaporization point. This non-uniform erosion process may result in unstable machining as a result of WC particles dislodgement and accumulation in the gap. Therefore, machining dual composites of tungsten carbide and cobalt is a challenging task when compared to different grades of steels as common EDMed materials in the industry [54].

In a study of Pandey et al. [58], the effect of pulse parameters and carbide composition on material removal rate, electrode wear ratio, and crater shape and depth has been investigated experimentally. They indicated that cobalt content and its presence has a significant influence on the machining behavior of cemented carbides. Re-solidified layer, large electrode wear, and presence of thermal cracks are identified as problems of electrical discharge machining of cemented carbides.

Fine finish die-sinking micro-EDM of tungsten carbide using different electrode materials has been studied by Jahan et al. [59]. Their findings revealed that beside discharge energy, electrode material properties play a significant role in determining surface roughness of machined WC material. They showed that, silver tungsten (AgW) produces a better surface finish compare to the other electrode materials. In a study conducted by Lee and Li [60], the effect of EDM parameters on material removal rate, electrode wear ratio, and surface roughness of tungsten carbide has been investigated for different electrode materials and machining parameters such as polarity, open-circuit voltage, peak current, pulse duration, pulse interval and flushing pressure. They also investigate the effect of machining conditions on the surface integrity (microstructure, surface topography, micro-cracks, composition and hardness) of the tungsten carbide. A clear damaged layer distinguished by decreased amount of WC grains and presence of micro cracks has been observed [61]. The process of die-sinking EDM of cobalt-bonded tungsten carbide (94%WC6%Co), has been studied by Puertas et al. [62]. The results of their analysis revealed that intensity followed by pulse on-time are the most influential factors in the surface finish of tungsten carbide.

Based on literature survey, μ- WEDM of ultra-fine grain tungsten carbide has not been studied yet. Therefore, in this thesis, μ-WEDM of WC is studied in detail, in order to be successfully implemented for micro tool fabrication purposes of this research. Three important performance measures of WEDM process have been addressed to

have a full control on the process, i.e. surface quality, width of cut (KERF) and material removal rate (MRR). As it will be shown in the subsequent chapters of this thesis, surface roughness and dimensional accuracy of the fabricated micro end mills, directly affect their performance indices during micromachining operations. Therefore, in order to have a reliable micromachining studies, it is necessary to have cutting tools with consistent surface and dimensional qualities. The aim of the rest of this section is to provide a foundation for the fabrication of micro end mills from WC-Co in a controlled way, by understanding the effect of different WEDM input parameter settings on process outputs.

2.5.1 Materials

Material properties for this study are determined based on energy-dispersive X-ray spectroscopy (EDS) of the (WC-Co) material, which is depicted in Figure 2.15 . As it can be seen in Figure 2.15 the material contains about 11 wt% cobalt. The closest WC-Co material to the micro end mills of this study is 90WC-10Co with a grain size of (0.5-1 μm). The properties of this cutting tool material is given in Table 2.3. The values given in Table 2.3 are taken from references [63] and [64].

Table 2.3: Material properties of 90WC-10Co

Properties	**Value**	**Unit**
Grain size	0.5-1	μm
Density	14.6	g.cm $^{-3}$
Hardness	90.791.3	HRA
Young's modulus	620	GPa
Poisson's ratio	0.22	–
Transverse rupture strength	>3.7	GPa
Compression strength	5170	MPa

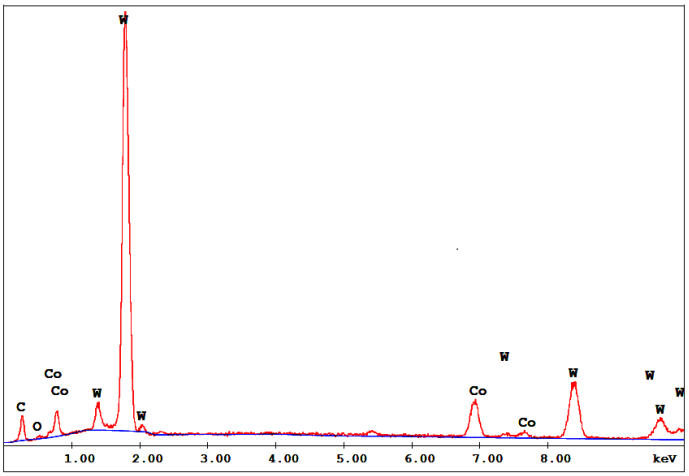

Element	Wt %	At %	K-Ratio	Z	A	F
CoK	11.45	28.74	0.1340	1.1899	0.9177	1.0716
W L	88.55	71.26	0.8503	0.9662	0.9938	1.0000
Total	100.00	100.00				

Element	Net Inte.	Bkgd Inte.	Inte. Error	P/B
CoK	159.61	28.17	1.57	5.67
W L	269.29	22.75	1.12	11.84

Figure 2.15: EDS analysis of the WC-Co material used for micro end mills.

2.5.2 Experimental Setup

In this study, a Sodick AP250L high precision WEDM machine was used to machine ultra-fine grain tungsten carbide rods of 4 mm diameter with the specifications given in Table 2.3. A brass coated piano wire of 100 µm in diameter is used. The brass coating in this wire produces high conductivity, and due to its high straightness is suitable for ultra-high precision machining purposes. EDMfluid 108 MP-S with the specifications given in Table 2.1 is used as a dielectric fluid. WEDM setup is shown in Figure 2.16 (a). In order to have equal upper and lower nozzle distances , a fixture was designed, fabricated and used for clamping of WC workpiece as depicted in Figure 2.16 (b). A lift position for the experiments is 8 mm, which is the distance between top surface of the lower nozzle and the lower surface of the workpiece. It should be mentioned that the nozzle position has a significant influence on machining accuracy, therefore it was kept constant during all WEDM experiments. The flushing of dielectric was also kept constant at 5 lit/min.

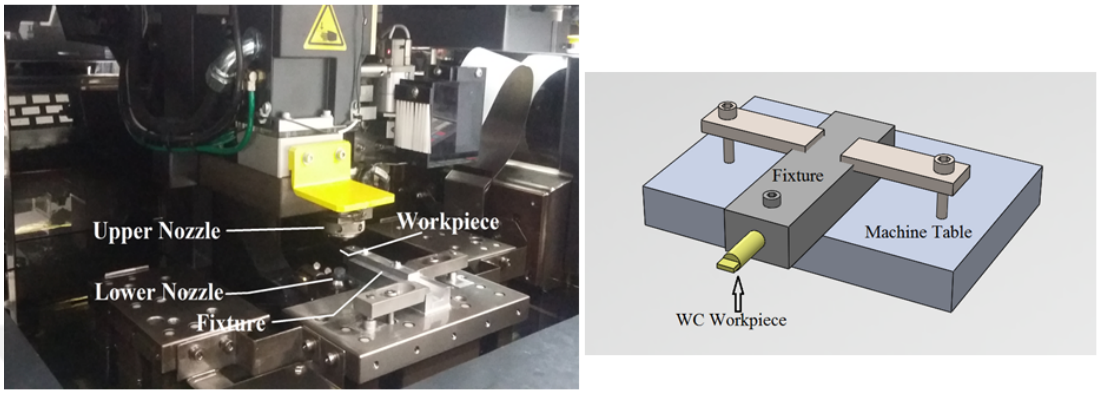

Figure 2.16: (a) WEDM experimental setup, (b) Schematic representation of workpiece fixing method.

2.5.3 Design of Experiments

A well defined experimental procedure is the main requirement in investigating the effect of process input parameters on the output characteristics of the process. In any WEDM process there exist various process parameters that affects performance measures of WEDM process, i.e. width of cut (KERF), surface quality and material removal rate (MRR) [65]. In most cases the objective is to have a better surface finish, smaller KERF and higher MRR.

WEDM parameters investigated in this study are briefly described below. More information can be found in Sodick AP250L machining condition manual. Nine WEDM parameters used in this study are: ON, OFF, IP, MAO, SV, V, C, WT and WS with descriptions given as:

- **ON:** Represents pulse ON time, which is the time duration that a voltage is applied to the gap between wire and workpiece. While the machine provides a wide range of pulse ON time settings, but increasing pulse ON time beyond a certain limit will result in short circuiting and wire breakage. Therefore, before conducting main experiments a series of pilot experiments are done to determine

the upper limit of the pulse ON time. For 100 μm wire, the upper limit for pulse ON is determined as 10 μs.

- **OFF:** Stands for pulse OFF time, which is the time duration that no voltage is applied to the gap. Similar to pulse ON time a wide range of values exists for OFF time. Small OFF time values will result in higher sparking frequencies. However, a very small pulse OFF time value increases the occurrence of short circuiting and wire breakage due to inefficient flushing. Similar to pulse ON time, a series of pilot experiments are conducted to determine the lower limit of pulse OFF time. The lower limit is determined to be 3 μs. For higher pulse OFF time values wire breakage was not observed, but the machining efficiency has been highly reduced beyond 20 μs.

- **IP:** Specifies the peak current, and its level has a significant influence on the discharge energy. The maximum peak current of the machine is 20 A, however, it has been observed that there is an upper limit of 11.3 A, where beyond this value under no machining condition wire breakage cannot be avoided. Therefore, the upper bound for IP is determined as 11.3 A.

- **MAO:** It is a combination of three different parameters for establishing a criteria for the stability of the EDM process. In normal mode machining used in this study, parameters 'A' and 'O' are kept constant, while the level of 'M' is changed to define a voltage level to establish a criteria for machining stability. It can be said that MAO mainly specifies a voltage level for the machine to decide whether the state of machining is stable or not.

- **SV:** Servo Voltage, which is the reference voltage for controlling advances and retracts of the wire.

- **V:** Is used to represent gap voltage, which is a parameter that defines the supply voltage to be placed on the gap.

- **C:** Defines the capacitance. Higher capacitance values will result in wire breakage because of higher discharge energies. The upper level for capacitance is determined as 2000 nF.

- **WT:** Controls wire tension.

- **WS:** It is used to control wire traveling speed.

For a complex system like WEDM, in which there are large number of factors to be studied, classical methods of design of experiment are inefficient because of proliferation in the number of experiments. Therefore, in this study a design of experiments based on Taguchi's orthogonal array L27 is used to study the effect of nine different WEDM process parameters described above on KERF, material removal rate and surface roughness. The use of L27 (nine factors at three different levels), makes it possible not only to have manageable experimental runs, but also to generate sufficient data to extract reliable conclusions from the results of experiments. Table 2.4 shows the experimental conditions used in this study.

2.5.4 Effect of WEDM Process Parameters on KERF

In micromachining operations, dimensional accuracy of the micro cutting tools is of significant importance, because it highly affects and dictates the dimensional accuracy of the final products. Therefore, it is important to fabricate very accurate micro cutting tools. In μ-WEDM process, KERF variation is a significant factor that determines the accuracy of the fabricated micro end mills. Wire deflection, discharge gap variation and lateral vibration of the wire are the main factors influencing KERF [66]. As it can be seen in Figure 2.14, the width of cut in WEDM is always larger than wire diameter and it can be defined as [66]:

$$KERF = D_w + 2D_g + 2A \tag{2.3}$$

where 'D_w' is the wire diameter, 'D_g' is the spark gap and 'A' is the amplitude of the lateral vibrations of the wire.

WEDM suppliers usually offer a database of recommended process parameters for wire cutting of commonly used materials under normal machining conditions. To the best of my knowledge, up to now, there exists no machining database exclusively developed for μ-WEDM process in terms of achievable dimensional accuracy and surface roughness. Suppliers recommended machining conditions cannot meet the requirements of machining miniaturized components. Using conventional WEDM database

Table 2.4: Taguchi's L27 experimental conditions.

Exp. #	ON (µs)	OFF (µs)	IP (A)	MAO (V)	SV (V)	V (V)	C (nF)	WT (g)	WS (m/min)
1	3.5	5	0.6	1	80	1	200	250	2.5
2	3.5	5	0.6	1	130	2.5	450	300	6
3	3.5	5	0.6	1	180	4	1500	350	8
4	3.5	10	6	4	80	1	200	300	6
5	3.5	10	6	4	130	2.5	450	350	8
6	3.5	10	6	4	180	4	1500	250	2.5
7	3.5	16	11	9	80	1	200	350	8
8	3.5	16	11	9	130	2.5	450	250	2.5
9	3.5	16	11	9	180	4	1500	300	6
10	5	5	6	9	80	2.5	1500	250	6
11	5	5	6	9	130	4	200	300	8
12	5	5	6	9	180	1	450	350	2.5
13	5	10	11	1	80	2.5	1500	300	8
14	5	10	11	1	130	4	200	350	2.5
15	5	10	11	1	180	1	450	250	6
16	5	16	0.6	4	80	2.5	1500	350	2.5
17	5	16	0.6	4	130	4	200	250	6
18	5	16	0.6	4	180	1	450	300	8
19	7.5	5	11	4	80	4	450	250	8
20	7.5	5	11	4	130	1	1500	300	2.5
21	7.5	5	11	4	180	2.5	200	350	6
22	7.5	10	0.6	9	80	4	450	300	2.5
23	7.5	10	11	9	130	1	1500	350	6
24	7.5	10	0.6	9	180	2.5	200	250	8
25	7.5	16	6	1	80	4	450	350	6
26	7.5	16	6	1	130	1	1500	250	8
27	7.5	16	6	1	180	2.5	200	300	2.5

for miniature part fabrication purposes will results in a very large dimensional errors. The use of such machining database in micro-scale will also put a limitation on the minimum achievable feature size in μ-WEDM process. These dimensional errors gain a great importance in micro tool fabrication, since these errors will be directly transferred into the machined workpiece. Therefore, development of predictive models to select machining parameters in a way that to reduce dimensional errors are of paramount importance in the field of μ-WEDM.

To illustrate inefficiency of the current available WEDM database usage for μ-WEDM applications, machining of several features having different sizes on ultra-fine grain tungsten carbide is considered. A geometry having different feature sizes has been designed as depicted in Figure 2.17. The thickness of the part is designed as 0.8 mm.

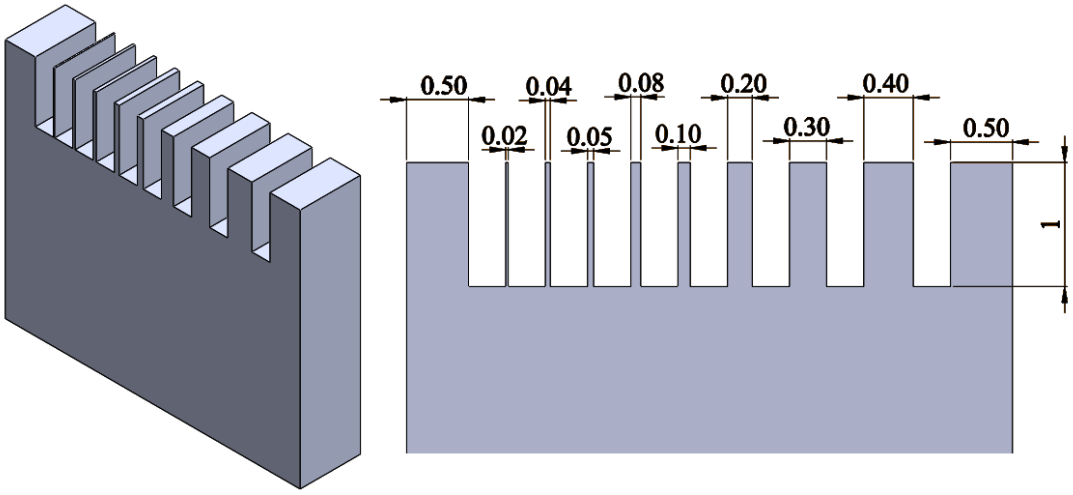

Figure 2.17: Part designed with different feature sizes.

The part illustrated in Figure 2.17 is machined using available manufacturer database. The machined part is shown in Figure 2.18. As it can be seen features less than 80 μm are broken because of inaccurate KERF settings. To further investigate the machined part by conventional database, the percent error for each feature is obtained by measuring dimensions of the machined features. The results for percent error are illustrates in Figure 2.19. In this Figure, since features less than 80 μm are

broken no percent error is reported. As it can be seen in the Figure 2.19, the percent error increases as the feature size decreases.

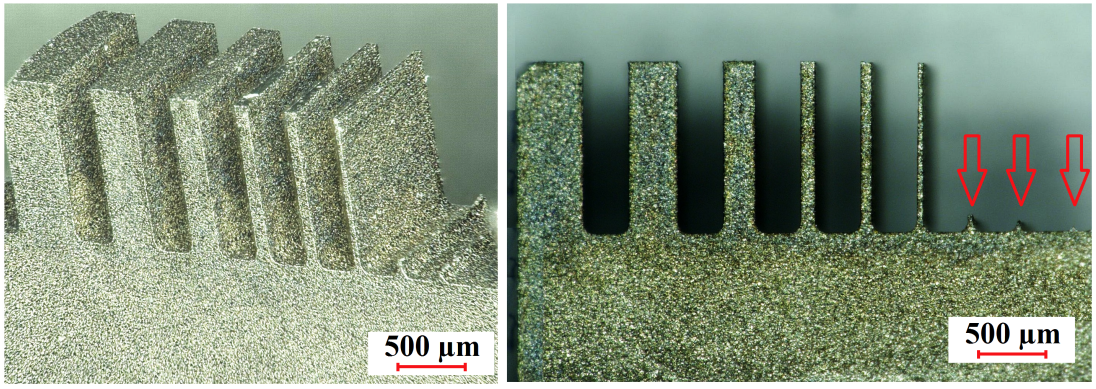

Figure 2.18: WEDMed part with different feature sizes.

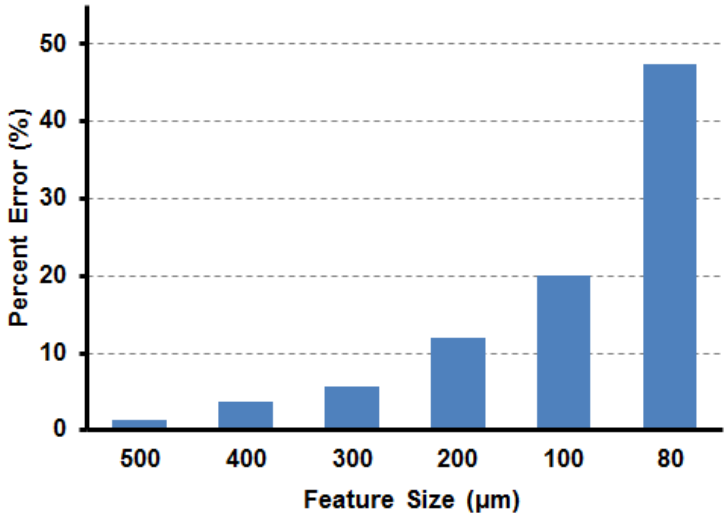

Figure 2.19: Percent error as a function of machined feature size.

Considering the results of Figures 2.18 and 2.19, it is essential to study the effect of machining process parameters on KERF during µ-WEDM process to have a control on the machined part dimensions, to reduce errors and to increase the possibility of fabricating smaller features. Therefore, the rest of this section is devoted to the analysis of the effect of WEDM process parameters on KERF.

The effect of workpiece thickness on the KERF is also considered. For this purpose, a sample with stepwise variable thickness has been fabricated as depicted in Figure 2.20. The part thickness starts from 100 µm and increases to 300 µm, 500 µm ends up with 1 mm. µ-WEDM experiments have been conducted on this sample at machining conditions mentioned in Table 1. The cutting width is measured using digital microscope (Keyence VHX1000) as it can be seen in Figure 2.21.

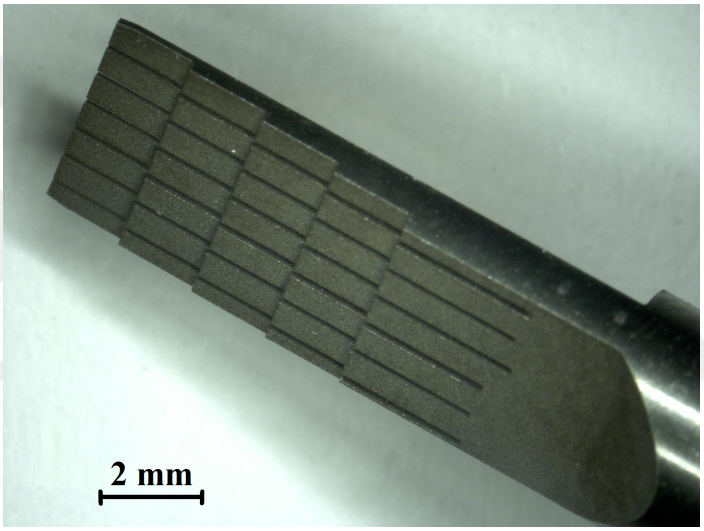

Figure 2.20: A WC part with stepwise variable thickness.

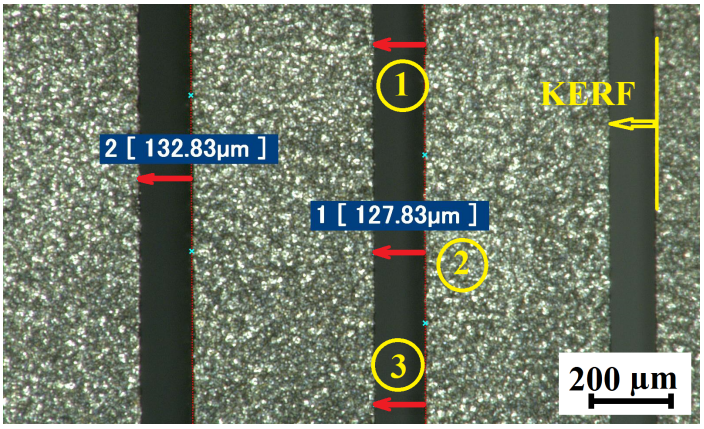

Figure 2.21: KERF measurement on WC part.

Using experimental setup of Figure 2.16 and conditions of Table 2.4, wire cutting experiments are performed. Each test has been repeated four times. For each experiment, KERF measurements are done at three different points as depicted in Figure 2.21. The average values of each measurement and its associated standard deviation are shown in Table 2.5 .

In order to establish statistically significant WEDM process parameters and determine percent contribution of each parameter, analysis of variance (ANOVA) is used. The percent contribution which is a function of sum of squares for each significant factor, reflects the portion of total observed variation attributed to each significant factor calculated as [67]:

$$P(\%) = \frac{SS'}{SS_T} \times 100 \tag{2.4}$$

where 'SS'' is the expected sum of squares due to the intended factor, and 'SS_T' is the total variation.

ANOVA is performed at 95% confidence level. The results for each thickness is summarized in Table 2.6. The significance of each factor can be determined based on F-value. According to Tosun et al.[68], higher F-values shows that a small variation of the process parameter can result in a significant influence on the output of the process. Taking into account the results of ANOVA for KERF given in Table 2.6, it can be seen that for all thicknesses, servo voltage (SV) is the most significant parameter which affects the KERF. The percentage contribution varies between 25% and 38% depending on the thickness.

For the second most significant factor, discrepancies can be observed at different thicknesses, which highlights the importance of studying WEDM process at different thicknesses and different length scales. The results of ANOVA analysis reveals that for micro-scale parts, where the thickness is in the order of 100 μm, MAO is the second most important parameter with a percent contribution of 14.4%. However, as the thickness increases, the effect of pulse OFF time becomes dominant. In this case, at a thickness of 300 μm, both MAO and OFF parameters gain the same significance with 12.5% contribution, and MAO becomes less significant moving towards a thickness of 1 mm. At thicknesses above 300 μm, capacitance becomes the third significant factor.

Table 2.5: Results of mean and standard deviation for KERF measurements at different thicknesses.

Exp. #	KERF T100 (µm)	KERF T300 (µm)	KERF T500 (µm)	KERF T700 (µm)	KERF T1000 (µm)	STD T100 (µm)	STD T300 (µm)	STD T500 (µm)	STD T700 (µm)	STD T1000 (µm)
1	117.3	118.8	119.1	120.6	121.6	1.0	0.6	1.2	0.9	1.1
2	129.4	129.8	130.1	131.6	132.0	1.2	0.4	0.9	1.1	0.5
3	124.7	131.5	133.8	137.8	138.3	0.7	0.8	0.7	0.5	0.8
4	118.9	120.1	122.0	122.0	126.1	2.2	1.2	0.7	0.9	1.4
5	125.1	126.0	126.4	126.6	127.6	1.2	1.0	1.3	0.6	1.1
6	127.3	133.7	137.0	138.2	141.1	3.1	1.8	1.8	1.7	1.7
7	125.1	121.5	119.0	118.1	116.8	1.2	0.8	2.0	1.4	1.9
8	121.6	124.3	126.0	126.4	126.5	0.9	1.8	1.2	1.3	1.6
9	126.3	133.6	134.7	136.6	136.3	1.5	2.0	1.5	0.9	1.8
10	129.0	136.8	138.4	141.6	141.9	3.1	2.8	1.7	2.0	1.5
11	131.3	133.4	135.7	138.2	139.6	2.7	1.5	1.7	2.5	1.4
12	127.7	129.4	130.1	132.4	132.1	2.5	2.2	2.8	2.2	2.7
13	117.4	118.6	117.2	118.6	122.0	2.5	2.2	1.8	2.8	2.9
14	127.0	126.1	126.0	124.7	123.7	1.0	0.8	1.3	0.6	0.5
15	129.3	134.1	136.1	136.2	135.2	1.5	1.1	1.1	1.2	1.4
16	122.7	123.9	123.4	124.3	124.9	3.0	0.4	0.8	1.2	1.4
17	125.9	123.7	122.3	122.2	122.8	1.5	2.4	0.5	1.6	0.5
18	120.2	125.1	128.1	130.7	131.2	2.8	2.8	2.7	1.9	2.1
19	118.2	122.6	123.4	131.6	135.2	1.0	2.5	3.0	2.7	1.9
20	129.9	135.1	136.8	134.6	135.0	2.9	1.1	0.7	1.3	1.5
21	125.7	128.2	129.7	131.1	131.0	2.1	1.1	1.2	0.8	1.5
22	126.6	129.9	127.9	125.2	124.0	1.5	2.3	3.0	2.9	2.8
23	127.7	130.2	130.8	129.7	131.6	1.4	1.2	2.9	2.8	2.3
24	129.4	131.5	131.9	131.7	130.8	1.6	1.7	1.5	1.1	0.8
25	112.6	115.2	117.1	118.9	122.0	0.9	0.8	1.6	1.6	2.5
26	130.0	130.5	131.9	133.3	133.7	2.9	2.8	2.4	2.1	2.4
27	119.8	125.0	128.1	128.6	131.1	2.8	1.4	1.4	1.7	2.8

Table 2.6: ANOVA for KERF at different thicknesses.

T=100 µm						T=300 µm					
Parameter	**Sum of Squares**	**Mean Square**	**F-value**	**P-value**	**P (%)**	**Parameter**	**Sum of Squares**	**Mean Square**	**F-value**	**P-value**	**P (%)**
ON	13.19	6.59	0.27	0.77	2.17	**ON**	8.58	4.29	0.19	0.83	1.02
OFF	53.24	26.62	1.08	0.38	8.74	**OFF**	104.6	52.3	2.31	0.16	12.47
IP	0.64	0.32	0.01	0.99	0.11	**IP**	2.65	1.32	0.06	0.94	0.32
MAO	87.74	43.87	1.78	0.23	14.41	**MAO**	104.42	52.21	2.31	0.16	12.45
SV	213.95	106.97	4.35	0.05	35.13	**SV**	262.69	131.35	5.81	0.03	31.32
V	2.84	1.42	0.06	0.94	0.47	**V**	2.03	1.01	0.04	0.96	0.24
C	33.06	16.53	0.67	0.54	5.43	**C**	131.01	65.5	2.9	0.11	15.62
WT	6.15	3.08	0.13	0.88	1.01	**WT**	35.14	17.57	0.78	0.49	4.19
WS	1.39	0.69	0.03	0.97	0.23	**WS**	6.7	3.35	0.15	0.87	0.80
Error	196.76	24.59				**Error**	180.94	22.62			
Total	608.95					**Total**	838.76				
T=500 µm						**T=700 µm**					
Parameter	**Sum of Squares**	**Mean Square**	**F-value**	**P-value**	**P (%)**	**Parameter**	**Sum of Squares**	**Mean Square**	**F-value**	**P-value**	**P (%)**
ON	6.57	3.28	0.14	0.87	0.63	**ON**	6.76	3.38	0.16	0.85	0.58
OFF	121.45	60.73	2.54	0.14	11.71	**OFF**	222.6	111.3	5.42	0.03	19.16
IP	25.59	12.8	0.54	0.61	2.47	**IP**	43.6	21.8	1.06	0.39	3.75
MAO	73.2	36.6	1.53	0.27	7.06	**MAO**	49.52	24.76	1.21	0.35	4.26
SV	395.36	197.68	8.27	0.01	38.12	**SV**	378.97	189.49	9.23	0.01	32.62
V	2.58	1.29	0.05	0.95	0.25	**V**	15.78	7.89	0.38	0.69	1.36
C	154.37	77.19	3.23	0.09	14.88	**C**	185.21	92.6	4.51	0.05	15.94
WT	56.43	28.22	1.18	0.36	5.44	**WT**	81.52	40.76	1.99	0.20	7.02
WS	10.37	5.18	0.22	0.81	1.00	**WS**	13.66	6.83	0.33	0.73	1.18
Error	191.18	23.9				**Error**	164.19	20.52			
Total	1037.1					**Total**	1161.81				
T=1000 µm											
Parameter	**Sum of Squares**	**Mean Square**	**F-value**	**P-value**	**P (%)**	**Parameter**	**Sum of Squares**	**Mean Square**	**F-value**	**P-value**	**P (%)**
ON	4.5	2.25	0.13	0.88	0.40	**V**	23.53	11.76	0.71	0.522	2.08
OFF	222.28	111.14	6.67	0.02	19.66	**C**	214.46	107.23	6.43	0.022	18.96
IP	95.48	47.74	2.86	0.12	8.44	**WT**	98.29	49.15	2.95	0.11	8.69
MAO	24.68	12.34	0.74	0.51	2.18	**WS**	22.15	11.07	0.66	0.541	1.96
SV	292.2	146.1	8.77	0.01	25.84	**Error**	133.32	16.66			
						Total	1130.88				

Since most of the fabricated micro tools in this study are in the order of 500 µm, for ease of analysis, the rest of investigations will be devoted to a workpieces with a thickness of 500 µm. A detailed analysis will be discussed in the subsequent section, after explaining the results of surface roughness and material removal rate.

2.5.5 Effect of WEDM Process Parameters on Surface Roughness

In all micro fabrication processes, control and measurement of surface features of miniaturized components is of significant importance, since components surface features may become large enough compare to the overall size of the part [69].

For micromilling tools fabricated by μ-WEDM process, surface quality plays a vital role either in terms of stiffness issues or its interaction with the workpiece. It is the surface topography of the micro tools, which determines the interaction properties between micro tools and workpiece including frictional, wear and contact properties. It also has a significant effect on the fatigue life of the micro tools. Therefore, it is important to characterize and control the surface texture of the fabricated micro end mills. Most of the studies in the literature characterize EDMed surfaces by studying 2D profile parameters. However, profile parameters cannot completely characterize a surface, because they use limited and local data points. Consequently, roughness values may show variations depending on the location and direction of measurements [69]. Moreover, surfaces having completely different textures may have a same Ra or Rz values when measured by a profilometer. Therefore, before beginning micro tool fabrication process, an extensive experimental study is performed to understand the evolution of a WEDMed surface under different process parameters. To achieve consistent and reliable measurements, specific methodology has been followed from measurement phase to the parameter extraction phase.

2.5.6 Measurement of Surface Roughness

As mentioned earlier, profile measurements suffer from true characterization of the processed surfaces. Therefore, surface roughness parameters based on 3D surface data are used to extract useful information from the surface of interest and also to make reliable comparisons. However, in order to come up with consistent results, a series of pre-processing steps are necessary. In this thesis, in order to have a consistent results and to make a reliable conclusions from surface roughness measurements, a unique pre-processing methodology is used. The methodology explained here, is used throughout this thesis to extract areal surface roughness parameters. Figure 2.22 illustrates the sequence of pre-processing performed on raw data to extract areal surface roughness parameters.

In this study, machined surfaces have been scanned by using a 3D laser scanning microscope (Keyence-VK-X110) to obtain a 3D topography of the machined surfaces.

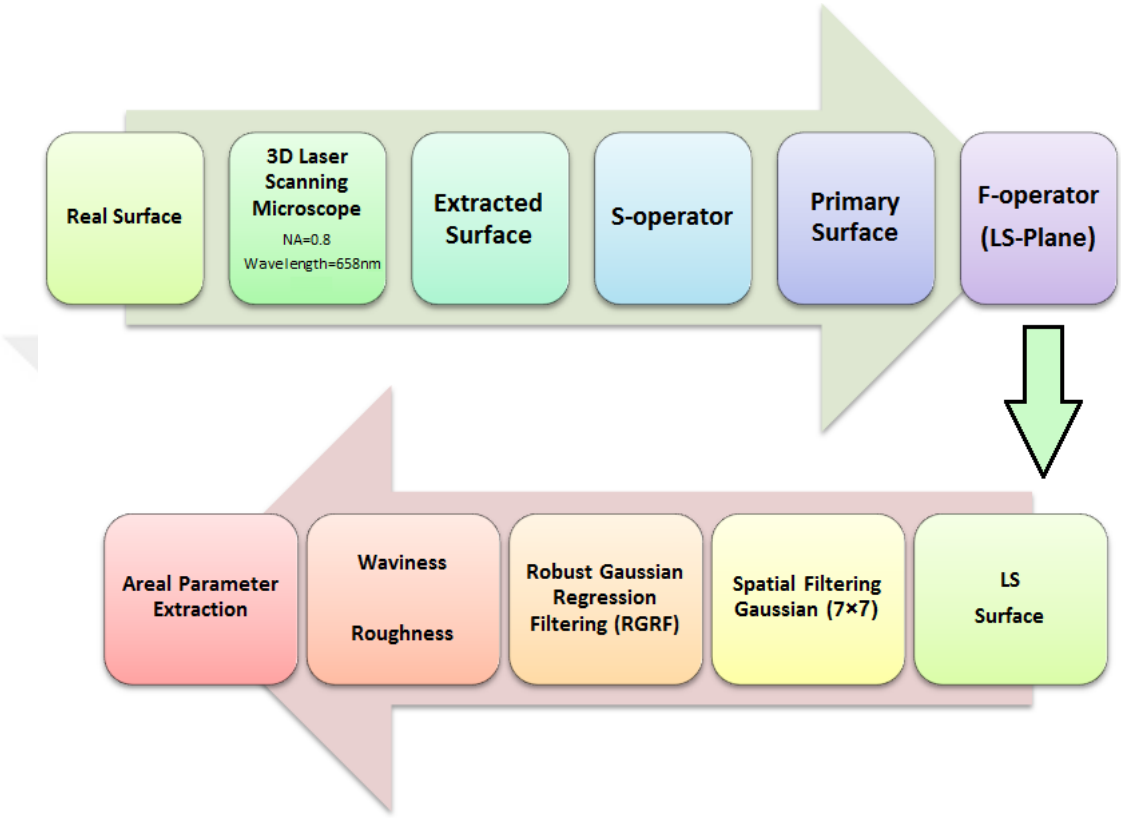

Figure 2.22: Sequence of processing operations to extract areal surface roughness paramaters.

Raw 3D topography measurements obtained by laser scanning microscope may have residual tilt (slope) due to a misalignment of the workpiece with respect to the datum of the device. Therefore, it is necessary to remove the general tilt of the measured surface. In accordance with ISO 25178, this general slope can be removed by applying an F-operator known as least square plane (LS-plane). Tilt correction is done by subtraction method where, LS-plane is subtracted form surface data, point by point.

Quite often topography measurements get corrupted by noise, which may be classified as internal noise of the instrument such as instability in the instrument electronics and environmental noise such as ground vibration, temperature fluctuations and external electromagnetic disturbances [70]. This unwanted noise can be removed by applying different filtering algorithms such as Fourier filtering, wavelet filtering and

matrix/spatial filtering. In this study noise filtering is done by matrix/spatial filtering using 7×7 Gaussian smoothing/denoising filter.

Considering the fact that any surface texture can be considered as a combination of waves with different wavelengths, it is necessary to separate these wavelengths to obtain form, waviness and roughness profiles. The process of decomposing a surface texture to the aforementioned components is known as filtering. Gaussian filtering has been widely used as a filtering technique to separate different spatial wavelengths of a surface texture, however it has some shortcomings such as distortion of the waviness profile near the edges. The filter also is not robust against outliers [71].

Robust Gaussian Regression Filters (RGRF) are introduced to overcome the problems of Gaussian filters. In this case, the waviness profile element at any location is obtained by minimizing a function E, which is the Gaussian weighted squared difference of the profile and a polynomial of either zero or second order. The coefficients of the polynomial are determined by minimizing E. Linear second order robust Gaussian regression filter can be described by the following minimization problem (Equation 2.5). The term "robust" means that the filter is capable of generating a mean line that is undisturbed by accidental or local features of a profile [72].

$$E = \int_0^l \int \rho \{z(\xi, \eta) - w(x, y)\} \; s(x - \xi, y - \eta) \, d\xi \, d\eta \quad \Rightarrow \quad Min \tag{2.5}$$

In equation 2.5, z(ξ,η) is the measured surface topography, s(x,y) is the weighting function and w(x,y) is the output reference surface topography. Figure 2.23 illustrates the application of RGRF to the WEDMed surface.

Arithmetic mean height 'Sa' is obtained for the WEDMed surfaces. 'Sa' can be defined as follows [72]:

$$Sa = \frac{1}{N_x N_y} \sum_{i=1}^{N_y} \sum_{j=1}^{N_x} \left| z(x_j, y_i) \right| \tag{2.6}$$

where 'Nx' and 'Ny' are number of data points in 'x' and 'y' direction, respectively. This parameter expresses the average of the absolute values of the height of asperities z(x,y) in the evaluation area. Using the procedure explained in section 2.5.6, 'Sa ' values are obtained for the experimental conditions of Table 2.4. It should be mentioned

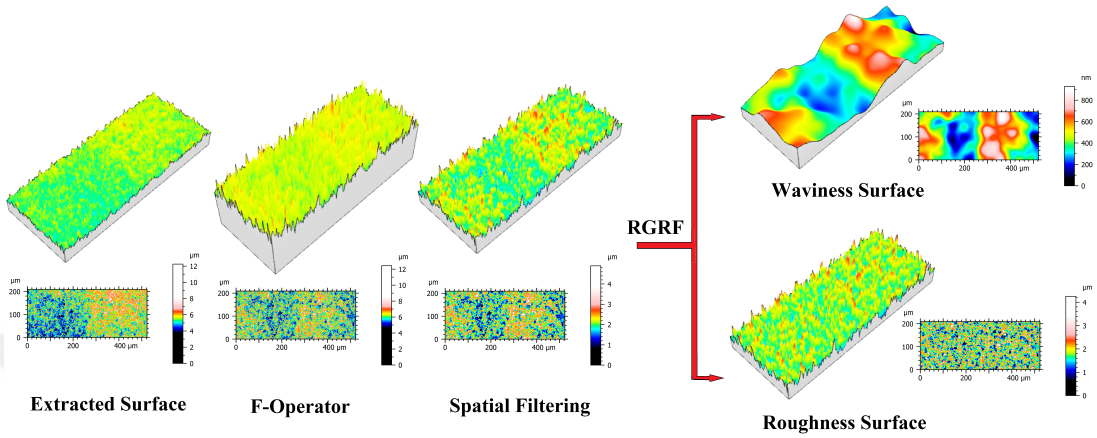

Figure 2.23: Pre-processing steps applied to a WEDMed surface to extract areal surface roughness parameters.

that, each experiment is repeated five times and for each sample the surface roughness is measured at three different points. The average 'Sa' values are shown in Table 2.7.

2.5.7 Material Removal Rate

In general WEDM process is categorized as a process with a low material removal rate. Therefore, any improvement in MRR without affecting surface quality and dimensional accuracy of the process, can have a significant influence on the process productivity. In order to obtain material removal rate for the experiments of Table 2.4, the average feed rate of the wire in each experiment is recorded, and material removal rate is calculated using following formula:

$$MRR\left(mm^3/\text{min}\right) = KERF\ (mm) \times Thickness\ (mm) \times Feed\,Rate\ (mm/\text{min}) \quad (2.7)$$

Table 2.7 illustrates the results of MRR calculations for a workpiece with a thickness of 500 µm.

Table 2.7: Experimental results for a constant thickness of 500 μm

Exp. #	KERF (μm)	Sa (μm)	MRR (mm^3/min)
1	119.102	0.421	0.112
2	130.093	0.597	0.154
3	133.783	0.671	0.067
4	122.009	0.49	0.11
5	126.387	0.613	0.142
6	137.034	0.664	0.055
7	118.997	0.444	0.092
8	125.959	0.627	0.088
9	134.652	0.723	0.018
10	138.394	0.741	0.048
11	135.675	0.899	0.047
12	130.116	0.617	0.049
13	117.188	0.674	0.188
14	125.994	0.476	0.107
15	136.116	0.566	0.036
16	123.386	0.68	0.157
17	122.276	0.463	0.081
18	128.063	0.567	0.015
19	123.44	0.567	0.093
20	136.824	0.636	0.137
21	129.66	0.506	0.051
22	127.935	0.542	0.176
23	130.805	0.666	0.168
24	131.941	0.481	0.036
25	117.057	0.724	0.158
26	131.929	0.679	0.104
27	128.052	0.679	0.019

2.5.8 Analysis of the Results

Table 2.7 illustrates the results of all three performance measures of WEDM process for a thickness of 500 μm. As mentioned earlier, the fabricated micro end mills have dimensions close to this value. In this part, in addition to ANOVA, signal to noise (S/N) ratio is also used to select the most significant WEDM process parameters. ANOVA analysis for KERF has been already given in Table 2.6. The results of ANOVA for MRR and Sa are given in Table 2.8 .

As it can be seen in Table 2.8, capacitance is the most significant factor in determining surface roughness of the WEDMed part with a percent contribution of 29.25 %. However, SV is the most significant process parameter which affects MRR, with a contribution of 56.06 %. IP which directly determines the energy of the sparks, is the second most significant factor in the surface roughness with a percent contribution of 21.9% and wire tension with a percent contribution of 8.92% is the second most significant factor for MRR.

Table 2.8: ANOVA results for 'Sa' and MRR

Sa						MRR					
Parameter	**Sum of Squares**	**Mean Square**	**F-value**	**P-value**	**P (%)**	**Parameter**	**Sum of Squares**	**Mean Square**	**F-value**	**P-value**	**P (%)**
ON	0.0104	0.0052	0.81	0.477	3.36	**ON**	0.0025	0.0012	2.08	0.19	3.43
OFF	0.0151	0.0076	1.18	0.356	4.87	**OFF**	0.0055	0.0028	4.62	0.05	7.62
IP	0.0680	0.0340	5.3	0.034	21.90	**IP**	0.0031	0.0016	2.63	0.13	4.34
MAO	0.0171	0.0086	1.33	0.317	5.51	**MAO**	0.0028	0.0014	2.32	0.16	3.83
SV	0.0078	0.0039	0.6	0.569	2.50	**SV**	0.0407	0.0204	33.98	0.00	56.09
V	0.0257	0.0129	2	0.197	8.28	**V**	0.0004	0.0002	0.32	0.73	0.53
C	0.0908	0.0454	7.08	0.017	29.25	**C**	0.0055	0.0027	4.59	0.05	7.58
WT	0.0207	0.0104	1.61	0.258	6.67	**WT**	0.0065	0.0032	5.4	0.03	8.92
WS	0.0035	0.0018	0.27	0.767	1.13	**WS**	0.0008	0.0004	0.64	0.55	1.06
Error	0.0513	0.0064				**Error**	0.0048	0.0006			
Total	0.3106					**Total**	0.0726				

Figure 2.24 illustrates the main effect plots for three performance measures. As it can be seen, surface roughness increases by increasing capacitance, because of the increased energy of the sparks and formation of larger and deeper craters on the surface. However, similar trend has not been observed for IP. It can be seen that material removal rate decreases when increasing SV, however KERF increases with increasing SV. Since, MRR is directly proportional with KERF, it can be concluded that as SV increases, machining feed rate decreases, which results in a decrease in MRR.

The impact of wire tension on KERF, is also worth to be emphasized. As it can be seen in Figure 2.24, as wire tension increases, KERF decreases. This decrease in the KERF can be mainly attributed to the amplitude of the wire vibration, as stiff wire has less vibration amplitude compare to a loose wire.

Signal-to-noise (S/N) is created by Taguchi to transform the repetition data to a value which is a measure of variation. Depending on the type of characteristics, several (S/N) ratios are available such as Larger is better (LB), Nominal is best (NB) and Smaller is better (SB) . Since for KERF and surface roughness, the goal is to have a

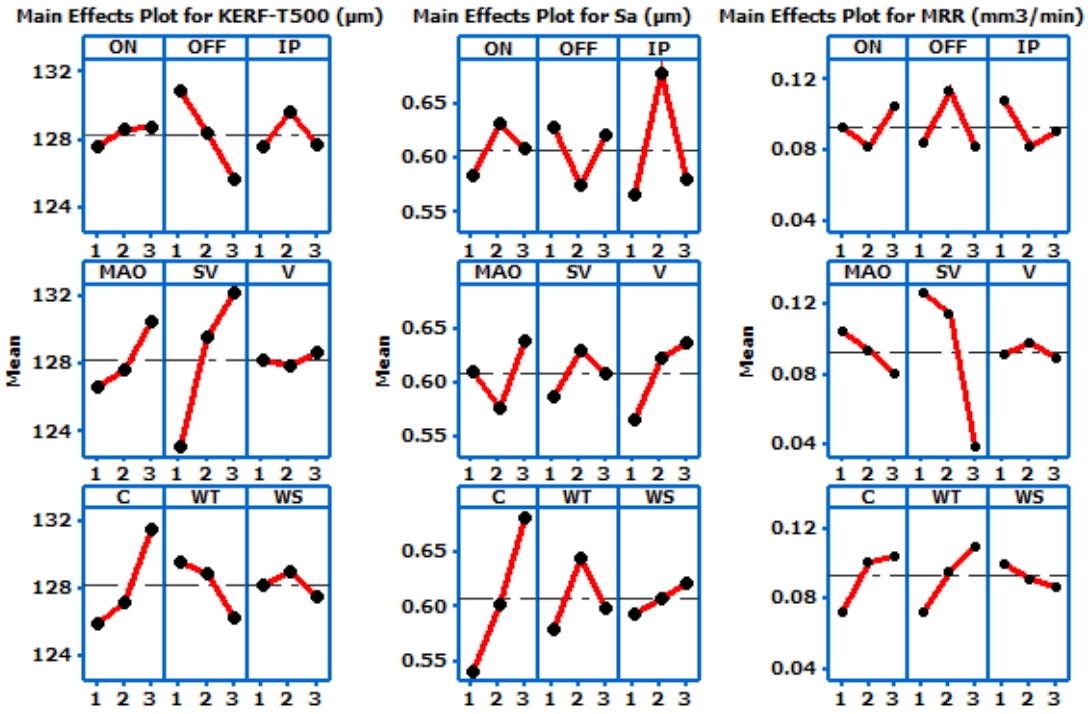

Figure 2.24: Main effect plot for the mean value of KERF, Sa and MRR.

smaller value, SB characteristics is selected. S/N ratio for SB characteristics is defined as [67]:

$$(S/N)_{SB} = -10\log\left(\sum_{i=1}^{n} y_i^2 \Big/ n\right) \tag{2.8}$$

For MRR, the objective is to increase MRR, because it directly affects machining time and hence the economics of the process. Therefore, for MRR, Larger is better characteristics is selected, which is defined as:

$$(S/N)_{LB} = -10\log\left(\sum_{i=1}^{n} \left(1/y_i^2\right) \Big/ n\right) \tag{2.9}$$

S/N ratios for three performance measures of WEDM, for all 27 experiments are shown in Table 2.9. The optimum level corresponds to a higher signal to noise ratio. The mean S/N ratio for each performance metrics for each level of process parameters are shown in Table 2.10, Table 2.11 and Table 2.12. Figure 2.25 provides a graphical representation of S/N ratios. It can be seen in Table 2.10 that SV, OFF, WT and MAO

Table 2.9: S/N ratio of KERF, 'Sa' and MRR for all experiments

Exp. #	KERF (dB)	Sa (dB)	MRR (dB)	Exp. #	KERF (dB)	Sa (dB)	MRR (dB)
1	-41.518	7.512	-19.019	**15**	-42.678	4.950	-28.857
2	-42.285	4.475	-16.277	**16**	-41.825	3.349	-16.064
3	-42.528	3.469	-23.493	**17**	-41.747	6.681	-21.797
4	-41.728	6.196	-19.187	**18**	-42.148	4.927	-36.268
5	-42.034	4.256	-16.943	**19**	-41.829	4.927	-20.670
6	-42.737	3.551	-25.222	**20**	-42.723	3.930	-17.277
7	-41.511	7.058	-20.759	**21**	-42.256	5.922	-25.923
8	-42.005	4.056	-21.156	**22**	-42.140	5.315	-15.094
9	-42.584	2.817	-35.137	**23**	-42.332	3.525	-15.489
10	-42.822	2.599	-26.296	**24**	-42.408	6.351	-28.965
11	-42.650	0.926	-26.469	**25**	-41.368	2.807	-16.025
12	-42.287	4.201	-26.233	**26**	-42.407	3.361	-19.641
13	-41.378	3.432	-14.540	**27**	-42.148	3.365	-34.330
14	-42.007	6.445	-19.405				

are the most significant parameters in causing KERF variation. Also it can be seen that, to have a minimum KERF, pulse ON time, IP, MAO, SV and capacitance should be selected at their minimum values with a medium gap voltage at level 2 and other parameters should be selected at their highest level of 3.

From Table 2.11, it can be seen that capacitance is the most dominant parameter affecting surface roughness variation in WEDM process, followed by IP, V and WT. It can be seen that in order to minimize surface roughness, OFF time and MAO should be set at level 2, while all other parameters should be selected at level 1.

The results of Table 2.12 indicates that SV is the most significant process parameters for MRR, followed by OFF, WT and MAO. Having IP, MAO, SV and WS at level 1, OFF and V at level 2, and other parameters at level 3, maximum material removal rate can be achieved.

Table 2.10: Selection of optimum levels for KERF based on S/N ratio

	Level 1	Level 2	Level 3	Rank	Optimum Level
ON	-42.1	-42.17	-42.18	8	1
OFF	-42.32	-42.16	-41.97	3	3
IP	-42.1	-42.24	-42.11	6	1
MAO	-42.04	-42.11	-42.3	4	1
SV	-41.79	-42.24	-42.42	1	1
V	-42.15	-42.13	-42.18	9	2
C	-42	-42.09	-42.37	2	1
WT	-42.24	-42.2	-42.02	5	3
WS	-42.15	-42.2	-42.1	7	3

Table 2.11: Selection of optimum levels for 'Sa' based on S/N ratio

	Level 1	Level 2	Level 3	Rank	Optimum Level
ON	4.821	4.168	4.389	7	1
OFF	4.218	4.891	4.269	6	2
IP	5.067	3.474	4.837	2	1
MAO	4.424	4.86	4.094	5	2
SV	4.799	4.184	4.395	8	1
V	5.073	4.201	4.104	3	1
C	5.606	4.435	3.337	1	1
WT	4.887	3.932	4.559	4	1
WS	4.636	4.441	4.301	9	1

Table 2.12: Selection of optimum levels for MRR based on S/N ratio

	Level 1	Level 2	Level 3	Rank	Optimum Level
ON	-21.91	-23.99	-21.49	6	3
OFF	-22.41	-20.41	-24.58	2	2
IP	-21.39	-23.37	-22.64	7	1
MAO	-21.29	-22.15	-23.96	4	1
SV	-18.63	-19.38	-29.38	1	1
V	-22.53	-22.28	-22.59	9	2
C	-23.98	-21.95	-21.46	5	3
WT	-23.51	-23.84	-20.04	3	3
WS	-21.53	-22.78	-23.08	8	1

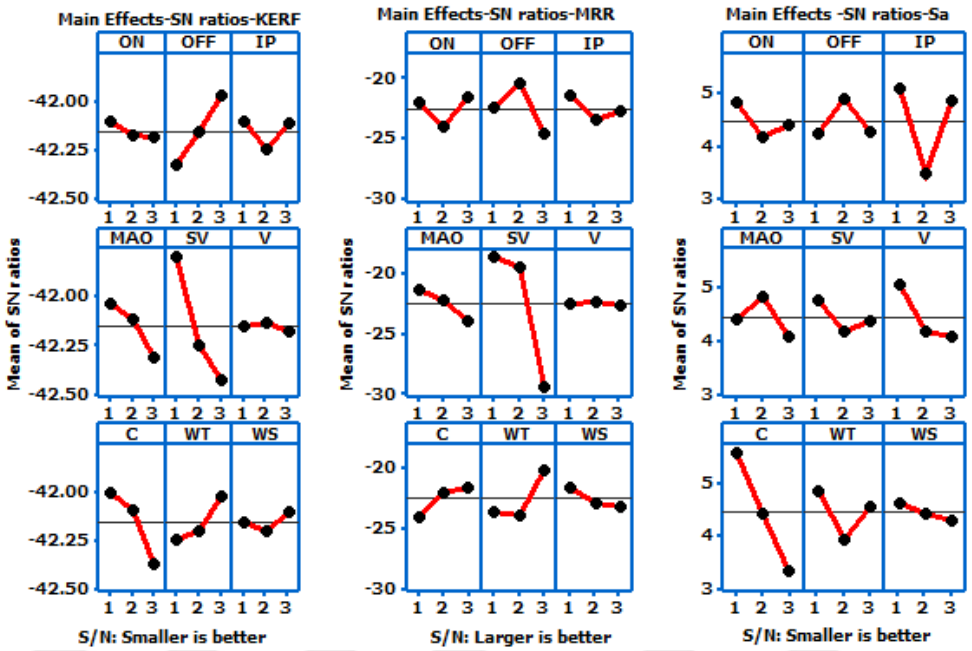

Figure 2.25: Main effect plot for the S/N ratio for KERF, Sa and MRR.

Conclusions

EDM-based techniques are successfully used to fabricate precise micro end mills of different geometries with a controlled surface roughness suitable for different micromachining applications. It has been shown in this chapter that, WEDM provides enough flexibility and precision to be used as a reliable method of micro tool fabrication in the rest of this thesis. The effect of different process inputs of WEDM process on three performance measures of the WEDM process (KERF, MRR and Surface roughness) has been studied in detail when machining ultra-fine grain tungsten carbide.The conclusions of this chapter are summarized as follows:

- A novel method for fabrication of micro-ball end mills and lollipop end mills are developed based on modified block-EDG method.
- A combination of block-EDM and WEDG was used to fabricate micro end mills of different geometries and dimensions from WC and PCD.

- Based on the results of the analysis in this chapter, it is found that servo voltage is the most significant process parameters affecting MRR, followed by pulse off time, wire tension and MAO.
- It has been found that capacitance is the most dominant parameter affecting surface roughness variation in WEDM process, followed by peak current, gap voltage and wire tension.
- S/N ratio results revealed that, servo voltage, pulse off time, wire tension and MAO are the most significant parameters in causing KERF variation.
- The findings of this chapter makes it possible to fabricate high precision micro cutting tools with a controlled surface characteristics using WEDM process.

Chapter 3

An Investigation of Micromilling using Conventional Micro End Mills

3.1 Introduction

Milling is one of the most commonly used conventional material removal processes, which normally uses a rotating multi-tooth cutting tools having relative motion with respect to the workpiece to remove material in the form of chips. It is known to be an intermittent cutting process [73].

Conventional milling operation has been well researched and studied during the last several decades. Its successful implementation in fabricating high precision complex 3D parts from variety of engineering materials was the main motivation for its adoption in the micro-manufacturing [74]. A gradual scaling down of conventional milling process and cutting tools together with the increased precision of the motion control systems, resulted in the creation of a process known as micromilling, which uses micro end mills having relatively small diameters, generally in sub-millimeter range [75]. Some of the advantages of micromilling are as follows:

- The ability of machining complex 3D micro-features including free-form surfaces [30].
- The ability of processing large variety of engineering materials other than silicon [30].
- The possibility of in-process part correction using on-machine measurement devices [4].
- Being cost effective for individual or small batch part production due to eliminating a need for very expensive clean room facilities [76].
- Having a small environmental footprint by eliminating a need for etching solutions and other chemical materials [31].
- The possibility of transferring the wealthy of knowledge gained in conventional milling to micromilling [32].
- and possible use of well-developed CAD/CAM technology.

Although micromilling is considered as the scaled down version of macro scale milling; however, the mechanics of machining at micro scale are quite different [77] and there exist many challenges which should be addressed, such as:

- In micromilling, the uncut chip thickness and the grain size of the work material are in the same order of magnitude.
- The feed per tooth variable set in the process maybe less than the cutting tool's edge radius.
- The runout of the tool/tool holder/spindle system may be larger than feed per tooth value.

These characteristics of micromilling process lead to process uncertainties and make modeling of process outputs a challenging task. An important difference is the influence of cutting edge radius, which cannot be neglected at micro scale. The edge

radius is comparable to the uncut chip thickness during machining, which leads to ploughing of the material onto the workpiece surface. It has been shown that there is a minimum uncut chip thickness value where continuous chip formation ceases and ploughing becomes the dominant cutting mechanism [4, 78]. In addition, when grain size is comparable to the uncut chip thickness, it has been shown that the influence of fracture in chip formation increases due to round cutting edge [79, 80]. The influence of microstructure has also been considered in micro scale machining studies, and shown to affect the process outputs significantly [81, 82].

In micromilling, since micro end mills have a relatively low bending stiffness, they experience a large deflections, which makes chip formation even more different than conventional milling [83].

Tool runout and tool deflections, which are usually neglected at the macro scale, also gain importance in micro scale machining. The influence of tool runout which results in varying chip loads on cutting edges of tools has been integrated into micromilling force models [84]. Tool deflection modeling in micromilling has received considerable attention recently, since it affects the quality of the machined micro components [32, 85, 86, 87].

Micro end mills with diameters less than a millimeter are usually used in micromilling and the majority of these tools are made from coated/uncoated tungsten carbide material. During operational conditions, micro tools rapidly wear out and they lose their sharpness, which influences the surface quality [88]. In addition, increased machining forces due to tool wear result in additional deflection of the tools. Tool wear measurement and tool breakage detection are challenging issues in micromilling in terms of achievable dimensional tolerances, surface quality and economy of the process. Furthermore, the principal wear mechanisms in micro scale cutting are not consensual and flank wear measurement is troublesome [89].

When difficult-to-cut materials are machined, the cutting edge radius of the micro tools immediately chips-off, which further complicates the process. Tool wear influences the surface roughness and increases milling forces which creates surface quality problems.

The aforementioned issues can be addressed as the main challenges in the adoption of micromilling for industrial applications. Therefore, it is necessary to overcome these challenges and to have an in-depth understanding of the physics of the process and influential factors before micromilling can be adopted as a popular method of fabrication in industry.

Another important issue in micromilling, is built-up edge formation, especially when machining titanium alloys, steel and aluminum alloys. Unstable BUE known to deteriorate the quality of the micro-machined features, degrade surface quality and shorten tool life. The presence of BUE has also reported to be the main factor causing inefficiency of the existing surface roughness prediction models to give good predictions when applied in micromilling [90]. It may also result in an irregular flow of material, and causes smeared and deposits on the machined surface [91]. Although, BUE formation known to have a significant influence on process outputs of conventional machining, however there is a very limited research about BUE in micromachining processes.

The limitations imposed on the micromilling during the scaling down process called size effect. Therefore, the available solid background and knowledge gained for macro-scale domain may not be directly transfered into the micro-scale. The following section briefly discusses the size effects in micromilling.

3.2 Size Effects in Micromilling

According to Vollertsen [92], a deviation from intensive or proportional extrapolated extensive values of process characteristics as a result of scaling of geometrical dimensions is defined as size effect. In machining, size effect can be related to two different aspects of the process. The first one is when the edge radius of the cutting tool and uncut chip thickness are in the same order of magnitude. The second one is due to the effect of material microstructure, where isotropic and homogeneous material assumptions are not valid anymore [30, 93], and polycrystalline material should be considered as heterogeneous and discrete [94].

A large edge radius to uncut chip thickness ratio in micromachining results in large effective negative rake angles during cutting. This large negative rake angle promotes ploughing, rubbing and burnishing [95, 96].

Specific cutting energy which is defined as the total energy required for removing a unit volume of material, is an important measure of machinability [97]. One important size effect in micromachining is a nonlinear increase in the specific cutting energy with decreasing uncut chip thicknesses, which becomes noticeable for uncut chip thickness values less than cutting edge radius [98]. This increase in the specific cutting energy can be attributed to different phenomena involved in the cutting process. At larger edge radius to chip thickness ratios, the cutting tool acts like a blunt tool, where according to Armarego et al. [99] in this case, the relative contribution of ploughing forces becomes significant, which in turn will result in the increased specific cutting energies. In a study of Lucca et al. [100], the increase in the specific cutting energy in micromachining is attributed to the energy dissipation of ploughing due to the edge radius and rubbing of the flank face of the tool due to the elastic recovery of the workpiece material.

Material strengthening effect due to the reduction in the density of movable dislocations has been reported by Becker et al. [101] as another factor influencing specific cutting energy. Filiz et al. [102] showed that material strengthening at small uncut chip thickness values occurs because at small scales the effect of strain hardening becomes more dominant than the effect of thermal softening of the material. The presence of short range inhomogeneities in commercial metals has been reported by Shaw [103] as another origin of size effect. Larsen and Oxley [104] used strain rate sensitivity of the flow stress to describe size effect in machining. Their experimental results on plain carbon steel revealed an inverse proportionality between maximum shear strain rate and undeformed chip thickness. They came into a conclusion that, as uncut chip thickness decreases, shear strain rate increases, and consequently flow stress of the material increases, which in turn results in a higher specific cutting energies.

In micromilling, since depth of cut is very small, the removal process takes place at a very small distance from the surface of the material, where mechanical, physical and structural characteristics differs significantly from bulk of the material. At these

small depth of cuts, different structural states can be distinguished such as contamination zone (a few nanometer), oxide layer, Beilby (work hardened) layer and modified crystalline bulk microstructure layer (several micrometer to several tens of micrometer) [105]. In addition, micro-scale topographic state of the surface may also influence the micro-cutting process. This will result in a noticeable differences in coefficient of friction, flow stress of the material being cut, and cutting and edge force coefficients.

3.3 Minimum Uncut Chip Thickness

Understanding minimum uncut chip thickness (MUCT) for a given tool/workpiece combination is an essential part of any micromachining study, since it specifies the lower bound of mechanical micromachining, where beyond this thickness material can be removed in a stable way under perfect performance of the machine tool [106]. In conventional machining processes the uncut chip thickness is much larger than cutting edge radius, therefore the effect of cutting edge radius is negligibility small in the cutting process. However, in micro-cutting processes the chip thickness is in a same order of magnitude as the cutting edge radius, which necessitates consideration of the concept of MUCT in micromachining operations. The concept of minimum uncut chip thickness can be used to distinguish between different cutting conditions in terms of chip formation [4, 107]. Figure 3.1 [107] illustrates three different scenarios.

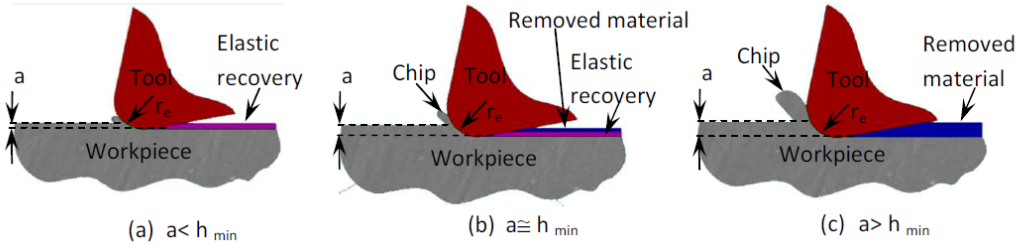

Figure 3.1: Different cutting scenarios based on uncut chip thickness [107].

When unreformed chip thickness is less than MUCT (Figure 3.1 (a)), there is no chip formation and due to the rubbing action of the cutting tool, workpiece material

will deform elastically underneath the cutting tool and elastic recovery takes place upon the passing of the cutting tool. Theoretically no chips will be formed in this case. When unreformed chip thickness becomes same as minimum chip thickness (Figure 3.1 (b)), chips will start to form in the presence of elastic recovery and ploughing. In this case the actual thickness of the material being removed is less than undeformed chip thickness. When uncut chip thickness becomes greater than minimum uncut chip thickness, (Figure 3.1(c)) shearing becomes the dominant material removal process and elastic recovery region becomes negligibly small. It has been emphasized by Weule et al.[108] that edge sharpness and material properties have a strong contribution to the minimum uncut chip thickness.

For orthogonal cutting process, a MUCT model has been developed by Son et al. [109] by dividing the workpiece into perfectly plastic and perfectly elastic regions. Using equilibrium of forces, they calculated the stagnation angle and assuming that at MUCT shear angle is equal to the stagnation angle they obtained the following equation for MUCT.

$$MUCT = r_e\left(1 - \cos\left(\frac{\pi}{4} - \frac{\beta}{2}\right)\right) \quad , \; r_e : \text{Edge radius} \; , \; \beta : \; \text{Friction angle} \tag{3.1}$$

Another analytical relation has been developed by Yuan et al. [96] to calculate MUCT as a function of cutting edge radius (r_e), horizontal and vertical components of the machining forces and coefficient of friction as follows:

$$MUCT = r_e\left(1 - \frac{F_y + \mu F_x}{\sqrt{F_x^2 + F_y^2\,(1+\mu^2)}}\right) \tag{3.2}$$

The same phenomena exist in micromilling, however the situation is more complicated than what is shown in Figure 3.1, because the chip thickness varies with tool rotational angle as depicted in Figure 3.2. As it can be seen in Figure 3.2, depending on the value of uncut chip thickness at different rotational angles, material removal can be ploughing dominant or shearing dominant. As a result of minimum uncut chip thickness effect, some materials which are not removed in the previous cutting edge pass, will be added to the current pass, resulting in chip thickness variation and fluctuations in the cutting forces.

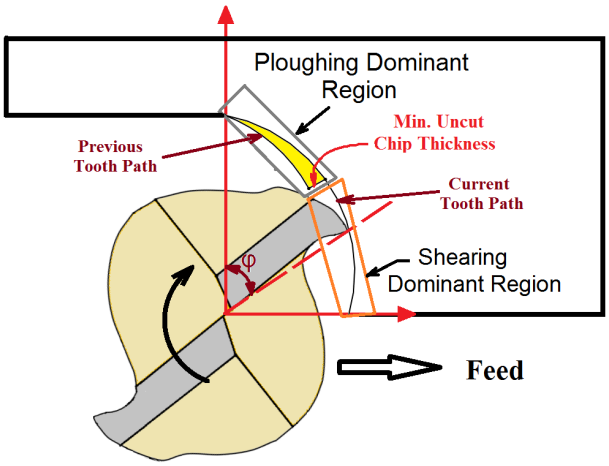

Figure 3.2: Minimum uncut chip thickness in micromilling.

The differences between micromilling and conventional milling, which are mentioned above, have a significant influence on the productivity of micromilling process. According to Vogler et al. [74] a major restriction in economic utilization of micromilling is the selection of proper combinations of micromilling process parameters, which can result in an increased productivity and longer tool life. To the best of my knowledge, there is a lack of understanding about the relationships between machining parameters and process outputs at micro-scale. Therefore, it is essential to investigate the influence of process input parameters such as cutting speed, depth of cut, feed per tooth and etc. on the outputs of micromilling.

The interaction between cutting tool and workpiece highly depends on the material behavior. Two different difficult-to-cut materials are investigated. Stavax ESR stainless steel, which has a widespread application in micro-mold industry and titanium alloy Ti6Al4V. While these two materials belong to a same group in terms of ductility, however they show completely different machinability characteristics. During micromachining of Stavax, tool wear is observed to be the factor limiting the productivity, while for micromachining of titanium alloy Ti6Al4V built-up edge is shown to affect the process outputs. Therefore, when dealing with Stavax, tool wear patterns (flank wear and edge rounding) of micro end mills and their relationship to machining

parameters have been investigated along with the influence of tool wear on tool deflections and tool breakage using both experimental techniques and finite element analysis, while for Ti6Al4V, BUE formation and its effect on the outputs of micromachining has been explored.

3.4 Experimental Investigations on Micromilling of Stavax Stainless Steel

Finding an appropriate combination of process parameters has been such a challenging problem that a great deal of research has been devoted to the topic. Biermann et al. [110] analyzed the machinability of hardened tool steel. Three different types of coated carbide tools were used in the experiments, where axial depth of cut, radial depth of cut and feed per tooth parameters were taken as process variables. They used machining forces, tool wear, surface quality and material removal rate as process outputs. The results showed that tool design is important and tool deflections and vibrations must be decreased to obtain good surface quality.

Filiz et al. [102] studied slot milling of pure copper using tungsten carbide cutting tools. They monitored cutting forces, surface roughness, tool wear and burr formation under various cutting speeds and feed rates to analyze the effects of micromilling parameters on the process outputs. They realized that MUCT causes irregular variations in the cutting forces at low feed rates. Lee et al. [111] conducted experiments on slot milling of Al-6061 in order to find the parameters that are effective on surface roughness. They analyzed chip load, cutting speed and depth of cut and found that chip load is the most dominant factor and interaction of cutting speed and chip load has a considerable effect on surface roughness. Tool runout is also shown to affect surface quality of machined parts.

Natarajan et al. [112] conducted an experimental study on micromilling of aluminum alloys. They considered spindle speed, feed rate and depth of cut as process parameters. The results revealed that low feed rate yields better surface finish and

spindle speed has no significant effect on surface roughness. Rahman et al. [113] studied tool life during micromilling of pure copper. They considered cutting speed, depth of cut, feed rate and tool helix angle as parameters. According to their results, decreasing of depth of cut may decrease tool life and tool life decreases as the cutting speed increases. Helix angle has an important role on tool life. Uhlmann et al. [114] studied micromachining of tungsten copper sintered composite materials. Their results revealed that increase in feed per tooth leads to cutting edge rounding which increases plastic deformation of the work material surface. Vázquez et al. [115] investigated surface finish, shape and dimensional features of micro slots machined on aluminum and copper. Process parameters in the experiments were spindle speed, depth of cut, feed per tooth and coolant application. It was concluded that quality of microchannels in aluminum is better than copper, average microchannel width in aluminum can be controlled in higher feed rates, coolant usage provides better surface quality and accurate microchannel dimensions.

Wang et al. [116] studied the influence of cutting parameters on surface roughness for brass. The parameters were spindle speed, feed rate, depth of cut and tool diameter. Based on the results, the increase of spindle speed and tool diameter increases surface roughness. Cutter stiffness is the most dominant factor in micromilling. The best surface quality is obtained when the vibrations are decreased by increasing tool stiffness. Weinert and Petzoldt [117] studied the machinability of NiTi shape memory alloy using solid TiAlN-coated carbide end mills. In their study, slot milling experiments were performed with 0.4 mm diameter tools under dry conditions and minimum quantity lubrication. The evaluation criteria were tool wear, machining quality and cutting forces. The results in which minimum quantity lubrication used provided better surface quality and longer tool life. Besides, it was shown that chip formation has an important effect on the extension of tool life and acquisition of better surface quality. Cutting with high feed rates and high width of cut provide better chip formation.

Thepsonthi and Özel [118] studied micromilling of Ti6Al4V, where spindle speed, feed per tooth and axial depth of cut were considered as process variables. The results revealed that axial depth of cut is the dominant factor for top burr formation and feed per tooth is the dominant factor for surface roughness. Thepsonti and Özel [119] also used a finite element based modeling of micromilling and calculated the optimized tool

path and milling conditions for micromachining of titanium alloy Ti6Al4V by considering surface roughness and burr formation. They concluded that tool path strongly affects tool wear. Li et al. [120] studied the influence of cutting parameters on tool wear. They concluded that feed per tooth has a greater effect on the tool wear than cutting speed and depth of cut. There is an optimal feed per tooth value that minimizes tool wear when the cutting speed and depth of cut values are fixed. Aramcharoen et al. [121] also investigated the tool wear of micro end mills while machining hardened tool steel. Slot milling experiments under dry machining conditions was performed. It was revealed that tool wear differs at each tooth, adhered material on the tool increases cutting forces and causes tool breakage. Tool wear rapidly increases while milling hardened steel.

Saedon et al. [122] considered micromilling of D2 steel and formulated a tool life equation by using response surface methodology. Their results showed that cutting speed is the most important factor, followed by feed and axial depth of cut. Cardoso and Davim [123] studied the effect of micromilling strategies and cutting parameters on surface roughness of Al 2011 aluminum alloy. Based on their findings, constant overlap spiral milling strategy resulted in best surface roughness. Liu et al. [124] found that low feed improves the surface quality in micromilling titanium alloy and emphasized the importance of tool runout on the process. Jun et al. [125] investigated the influence of feed rate on tool wear. They observed that each tooth experiences a different amount of wear during machining. They proposed a tool wear term defining the average increase in cutting edge radius.

The number of studies concerning the influence of tool wear on tool deflections and surface roughness in micromilling is limited in the literature. This research aims to advance the understanding of the interactions between process inputs and outputs with the use of experimental and modeling techniques. The evolution of tool wear in micro end mills under different machining conditions is investigated. The influences of tool wear on process outputs are studied using experimental and computational techniques. The selected work material is Stavax ESR (modified AISI 420) stainless steel, a common material used in the mold making industry due to its improved machinability.

Increasing material removal rate, satisfying dimensional and surface quality requirements are also important considerations in micromilling. Another aim of this study is to investigate the effect of micromilling process parameters while creating circular pockets. Circular pocket milling operation allows conducting uninterrupted micromilling experiments with longer tool path compared to slot milling operation and to investigate the influence of process input parameters such as cutting speed, depth of cut, feed per tooth, radial immersion percentage, and plunging method on process outputs.

3.4.1 Experimental Setup for Pocket Micromilling Experiments

A three axis micromachining center (Mikrotools (DT-110), Figure 3.3(a) and (b)) is used in pocket micromilling experiments. The machine has a range of X,Y and Z of 200×100×100 mm, respectively. The accuracy of the machine is ±1 μm, with a resolution of 100 nm. The micromilling machine is equipped with an electric high speed spindle (Fischer Precise SC 3062, 10,000-60,000 rpm, 1.3 kW max. power, 25 Ncm max. torque). Flat micro end mills (NS tools-MSE230, 2-flute, 30° helix angle) made of ultra- fine grain tungsten carbide (grain size<0.7 μm) are employed in micromilling experiments. Figure 3.3(c) shows the scanning electron microscope image of the micro end mill. Cutting tool edge radius is measured to be around 2-3 μm (Figure 3.3(d)). Micro machining forces are measured by Kistler mini dynamometer (9256C1, max 250 N, natural frequency ($f_n(x) \approx 4.0\ kHz$, $f_n(y) \approx 4.8\ kHz$, $f_n(z) \approx 4.6\ kHz$) with its charge amplifier (Type 5080A) and transferred to a PC through a data acquisition card (National Instruments PXI Series) with 10^5 samples/second. All experiments are performed under dry machining conditions.

Tool wear is investigated using Keyence VHX-1000 digital microscope (maximum images quality of 54 million pixels) and surface roughness is investigated using Keyence VK-X110 3D laser scanning microscope with a VK-X100 type controller. The device has a repeatability of 0.02 μm and maximum total magnification of 16000x.

The nominal tool diameter used in the experiments is 0.8 mm. The actual diameter of the end mills are smaller than the nominal diameter in order to compensate for possible runout in the tool holder-spindle system. However, there exist a size variation

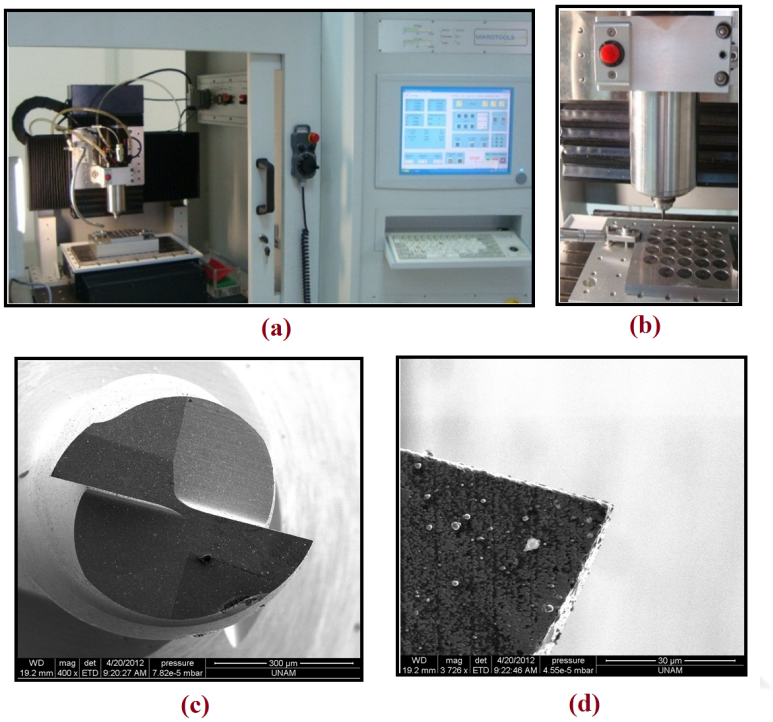

Figure 3.3: Experimental setup; (a) Micro machining center, (b) Mini dynamometer, (c) Micro end mill, (d) Cutting edge of the end mill.

due to the manufacturing process. Figure 3.4 illustrates the variability in the diameter of 30 up-sharp tools selected from same batch and are measured using Keyence VHX-1000 digital microscope at 600x magnification.

The mold materials are expected to have good corrosion and wear resistance with good machinability. The mold material considered in this thesis is Stavax ESR (modified AISI 420) stainless steel which is widely used in medical and optical industries. The work material used in machining experiments has hardness of 25 HRC. Table 3.1 shows the chemical composition of the material. The mechanical and thermal properties of Stavax are given in Table 3.2.

Similar to any other machining research the overall objective of this section is to study the interaction between the cutting tool and workpiece in order to optimize machining process parameters and to increase quality of the machined parts and maximize

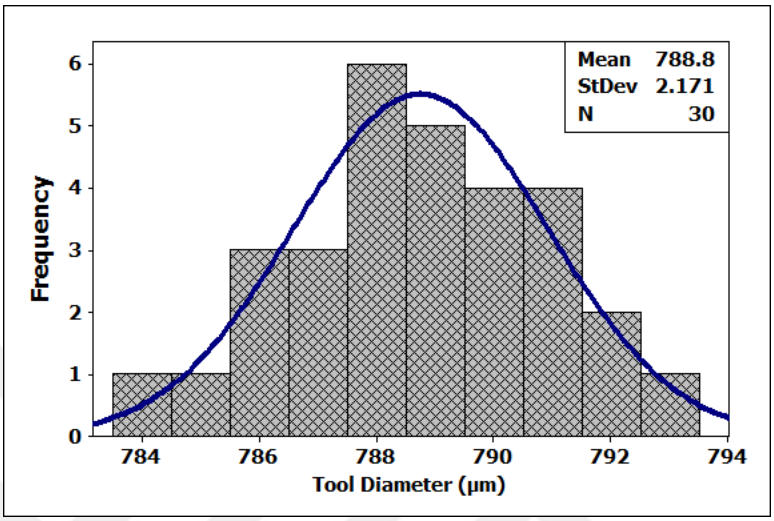

Figure 3.4: The measured diameter of 30 up-sharp micro end mills.

productivity [126]. This maximized productivity requires determining proper combinations of machining process parameters to have a longer tool life and better surface quality and dimensional accuracy.

Table 3.1: Chemical composition of Stavax ESR stainless steel

Typical Analysis %	**C**	**Si**	**Mn**	**Cr**	**V**
	0.38	0.9	0.5	13.6	0.3

Table 3.2: Mechanical properties of Stavax ESR stainless steel

Modulus of Elasticity (GPa)	**Thermal Conductivity (W/mC)**	**Specific Heat (J/KgC)**
200	16	460

3.4.2 Investigating the Influence of Process Parameters

In this section, plunging method, cutting speed, feed per tooth, axial depth of cut and radial immersion are investigated as process parameters. Tool wear, surface roughness and milling forces were considered to evaluate the influence of machining parameters.

Experimental investigations were performed during circular pocket micromilling operation which allows conducting uninterrupted micromilling experiments with longer tool path compared to slot micromilling operation. The diameter of the circular pocket is selected as 15 mm with a depth of 0.16 mm. Inside out spiral micromilling strategy was used and tool path is generated using Cimatron E11 computer aided manufacturing software. Figure 3.5 shows the spiral tool path produced by the software.

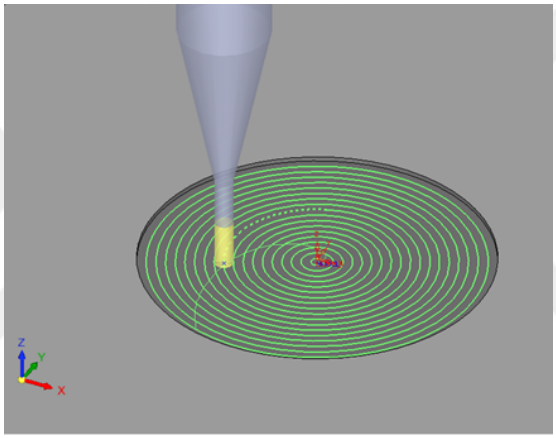

Figure 3.5: CAM simulation of circular pocket milling operation.

3.4.2.1 Plunging Method

Three different plunging methods have been investigated while micromilling of circular pockets as depicted in Figure 3.6. The first plunging method is drilling with ramping, the second method is trochoidal tool path during entry, and the last method is pre-drilled hole. Trochoidal tool path has been found favorable in the literature for macro-scale milling operations [127].

The micromilling operation is conducted under same process conditions with a spindle speed of 15000 RPM, feed rate of 120 mm/min and depth of of 0.16 mm. In drilling with ramping plunging method, plunging feed rate and ramping angle was set as 3 mm/min and 2.5 °, respectively. Trochoidal tool path was generated with pitch and radius settings of 0.48 mm and 0.24 mm, respectively. Pre-drilled hole diameter

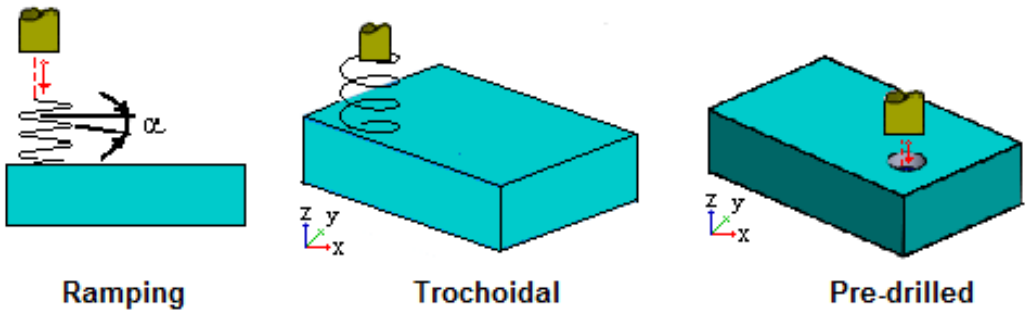

Figure 3.6: Different plunging strategies.

is 1 mm. A total number of 12 pockets were machined for each condition and tool wear was recorded after each pocket. The milling forces were also measured at the final pocket. Figure 3.7 shows the tool wear corresponding to each plunging method after 12 pockets. Figure 3.7 shows that cutting edges of the tool tips are chipped and rounded. A flank wear region due to abrasion can also be seen. Scanning electron microscope (SEM) image of the worn edge is shown in Figure 3.8.

In drilling with ramping and trochoidal path, tool wear region stretches to the tool center. Tool wear on the center of the tool is less for pre-drilled hole case. However, the edge chipping is similar in all cases. In order to observe the influence of plunging on the forces, milling forces were measured during machining of the final pocket. Milling forces in Fx, Fy, and Fz directions for pre-drilled hole method is shown in Figure 3.9. It must be noted that the variations in the direction of machining forces is due to circular tool path. Figure 3.10 shows that peak Fz forces in drilling with ramping, which are about 2.5 times higher than pre-drilled holes method.

Trochoidal path milling forces in Fz direction are also lower than drilling with ramping method. It must be noted that the process parameters of drilling with ramping and trochoidal milling are not studied in detail. Larger forces in 'Z' direction due to flank wear is expected to affect surface quality.

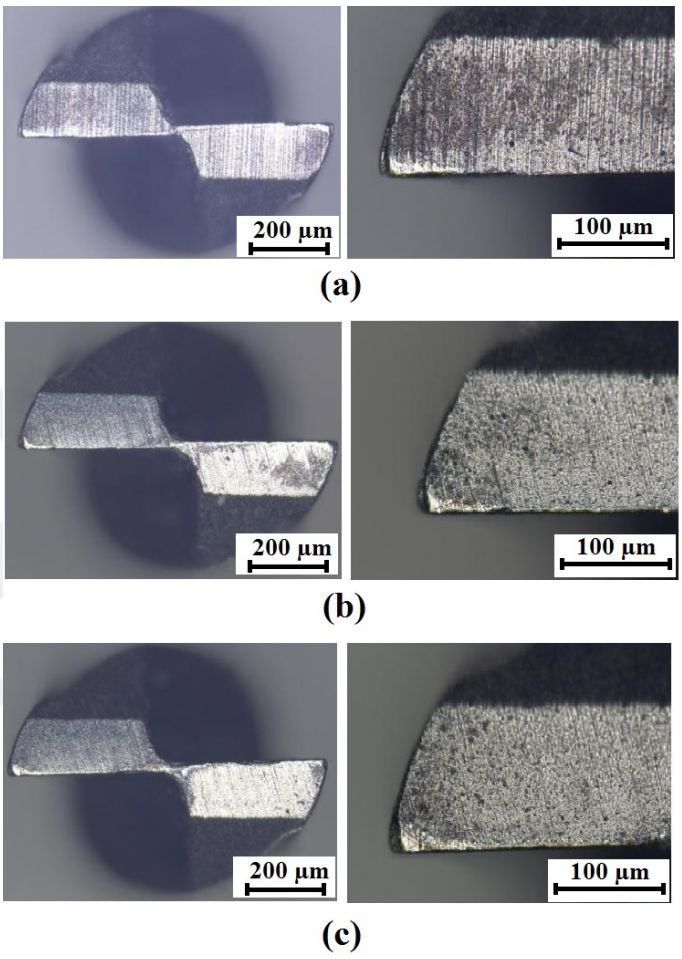

Figure 3.7: Effect of different plunging methods on tool wear: (a) pilot hole, (b) drilling with ramping, (c) trochoidal path.

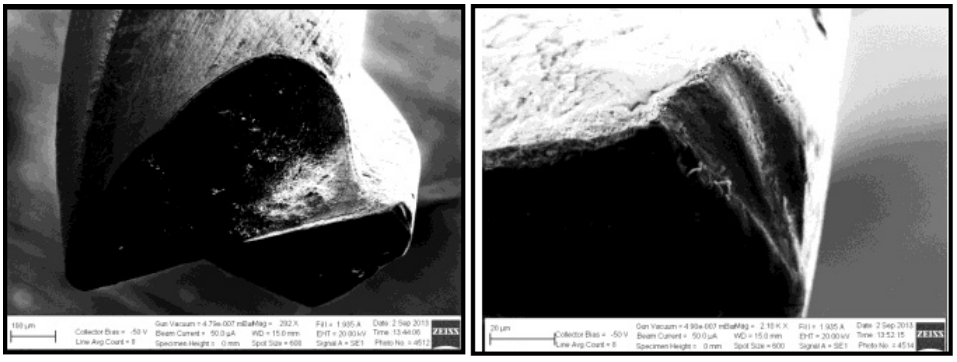

Figure 3.8: SEM images of the wear zone on the tool.

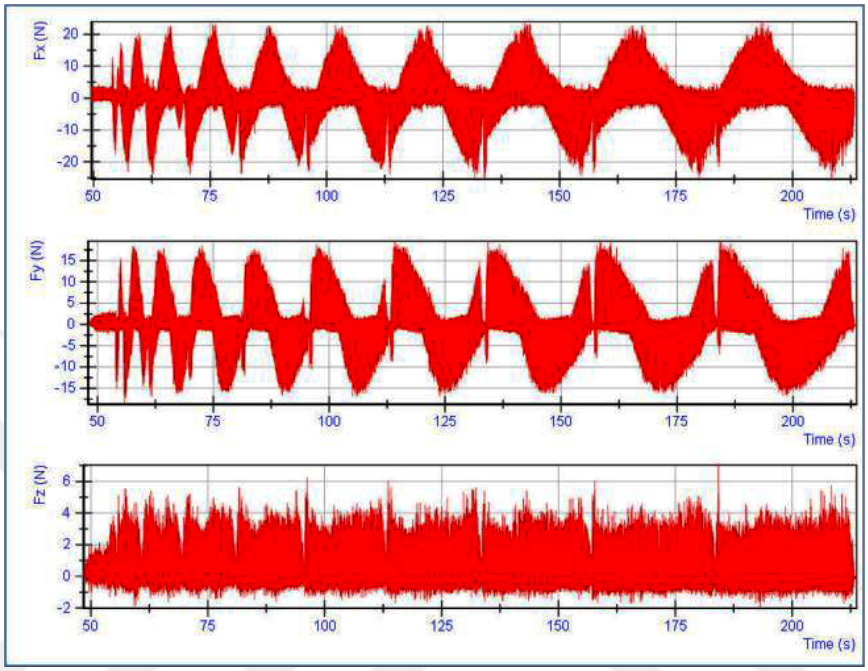

Figure 3.9: Milling forces for the case of pre-drilled hole.

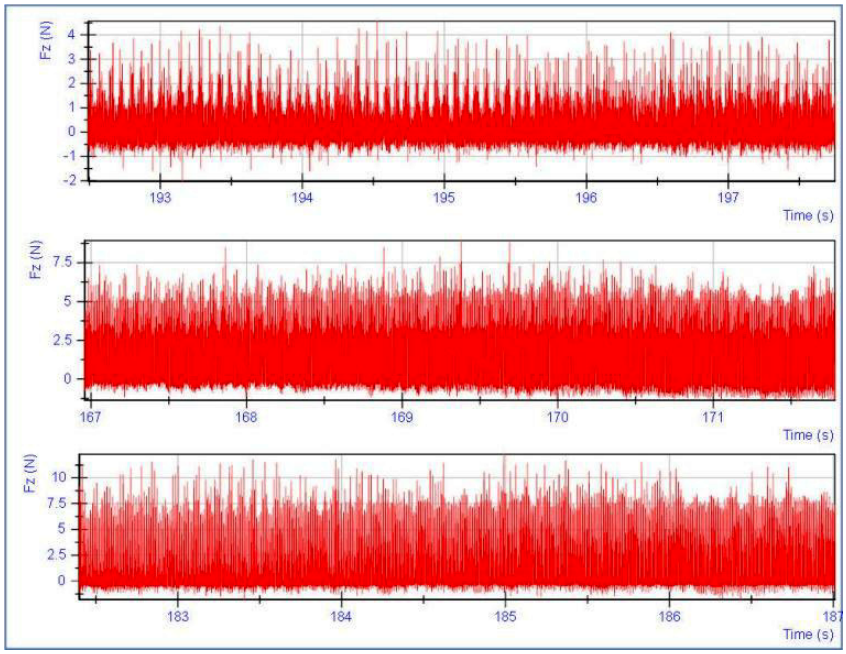

Figure 3.10: Comparison of milling forces in 'Z' direction: (top) pre-drilled hole, (middle) trochoidal, (bottom) drilling with ramping.

3.4.2.2 Relationship between Feed per Tooth, Radial Immersion and Tool Wear

The relationship between radial immersion and feed per tooth is important in terms of maintaining a balance between tool life and productivity during pocketing operations. In order to study this relationship, an experimental study was conducted. Cutting speed and axial depth of cut process parameters were fixed at 15000 RPM and 0.16 mm, respectively. Three levels for feed per tooth are selected as 2, 4 and 6 μm and three levels of radial immersion are selected as 20%, 60% and 80% of the tool diameter. For comparison purposes an extra experiment with a very low feed rate (0.5 μm/tooth) and high radial immersion (80%) is also considered (Exp. RI-10).

Six pockets were machined using pre-drilled hole plunging method. Tool diameters were measured as process outputs after machining of each pocket. Table 3.3 shows the list of experimental conditions. Figure 3.11 shows the cutting edges corresponding to the RI-1, RI-3, RI-4, and RI-7 experiments after machining 6 pockets with each tool.

Table 3.3: Experimental conditions for investigating the relationship between radial immersion and feed rate (N=15000 RPM, ap=0.16 mm).

Exp. #	**Feed (μm/tooth)**	**Radial Immersion (%D)**
RI-1	2	20
RI-2		60
RI-3		80
RI-4	4	20
RI-5		60
RI-6		80
RI-7	6	20
RI-8		60
RI-9		80
RI-10	0.5	80

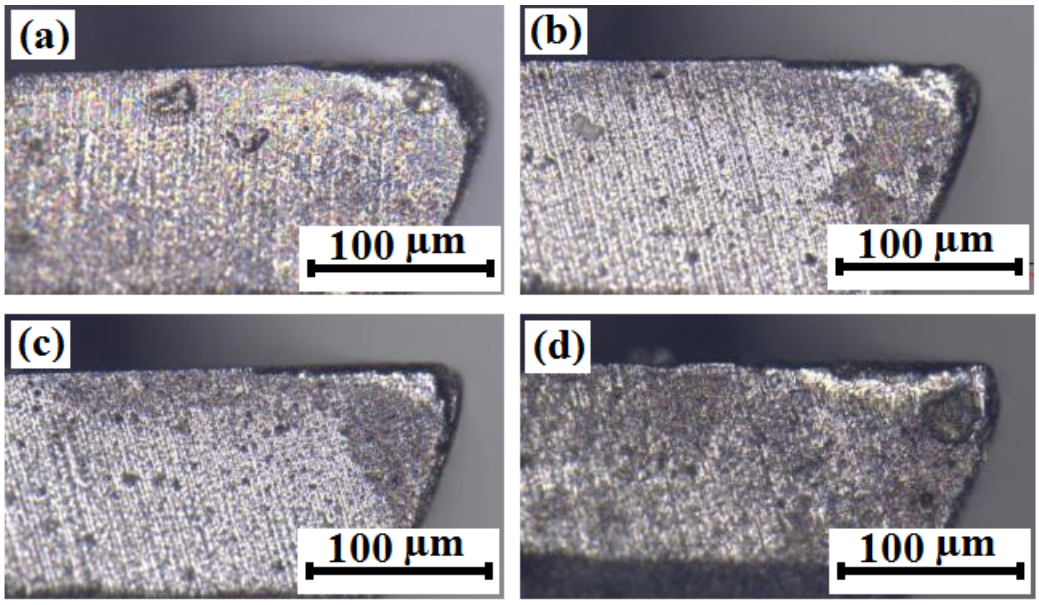

Figure 3.11: Comparison of cutting tool edge wear for: (a) Experiment RI-1, (b) Experiment RI-4, (c) Experiment RI-7, (d) Experiment RI-3.

Measuring of tool wear in micro end mills is challenging because of the small size of the tools. A reliable criterion about the condition of the cutting edge of the micro tools has not been set yet. Figure 3.12 shows the worn edges of the micro end mills obtained through a laser topography microscope (Keyence VK-X110) as a result of circular pocket milling under the conditions shown in Table 3.3. The images show a considerable amount of edge rounding and flank wear on the cutting edges. Built-up edge on the cutting edges was not observed.

To investigate tool wears, a similar approach as Jun et al. [125] has been used, where the effective diameter of the tool is measured. The edge rounding increases during machining and results in a decrease in effective tool diameter. As it has been shown already in Figure 3.4, diameters of the micro end mills are usually lower than their nominal diameter of 800 µm and they show a variability even when they are selected from a same batch. Therefore, in this study for all experimental conditions given in Table 3.3, the diameter of the micro tools at the beginning of the experiment was recorded, and average effective diameter of end mills has been measured at the end of each pocket milling operation.

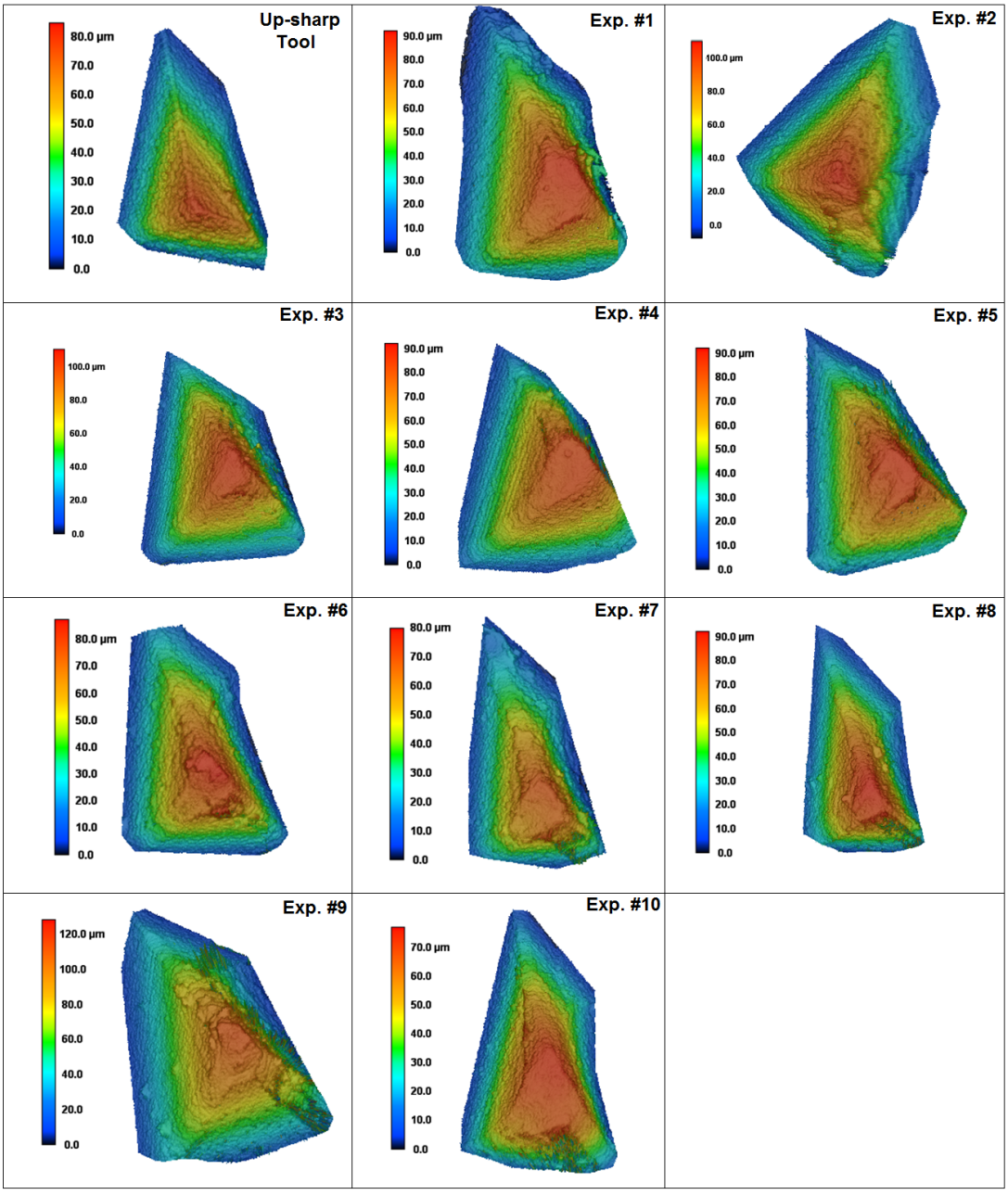

Figure 3.12: Laser topography images of worn cutting edges.

Figure 3.13 shows the comparison of up-sharp and worn tools. When the worn edges are investigated, a flank wear zone (VB) and edge rounding can be clearly seen. The diameter reduction due to edge rounding is shown in Figure 3.13 (b). The results of diameter reduction and flank wear length measurements for each experimental case are shown in Figure 3.14 (a) and (b) with respect to the number of pockets milled.

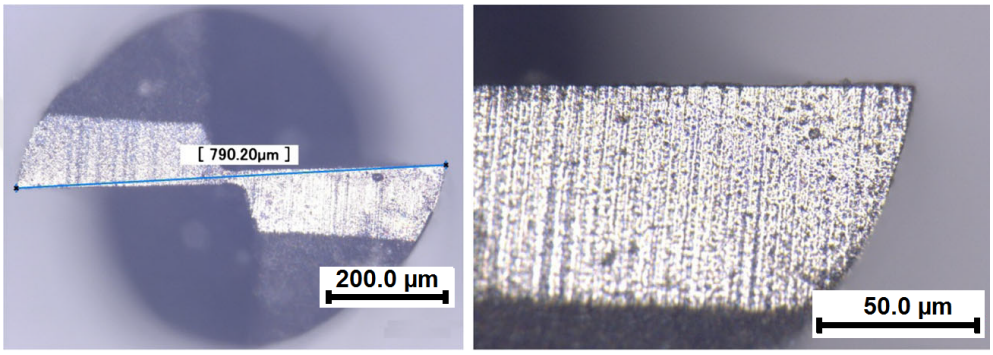

(a)

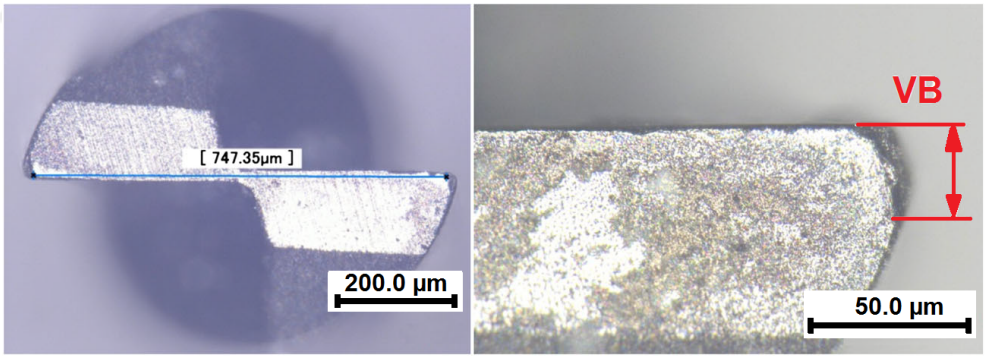

(b)

Figure 3.13: Optical images of tool profiles: (a) up-sharp tool and (b) worn tool.

In order to eliminate the influence of initial tool diameter on the diameter reduction values, the measurements are normalized relative to up-sharp tool diameter values for each tool. Equation 3.3 has been applied to obtain the ranked results as shown in Figure 3.15 (a). Figure 3.15 (b) shows the flank wear length measurements.

$$Relative\,Tool\,Dia.\,Reduction\% = \frac{D_{Up-sharp} - D_{Worn}}{D_{Up-sharp}} \times 100 \tag{3.3}$$

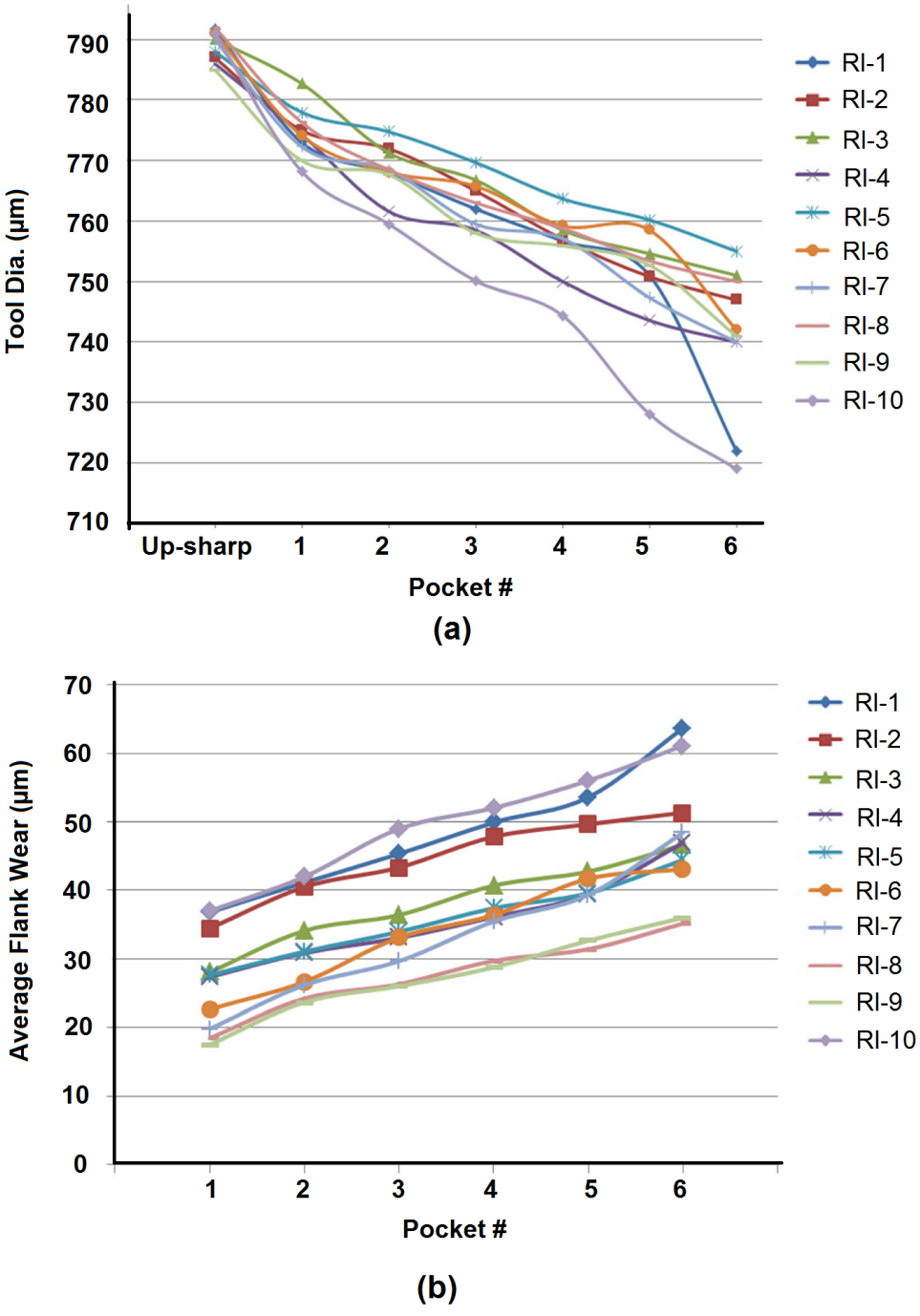

Figure 3.14: (a) Average effective diameters at the end of each pocket milling and (b) variation of average flank wear length as a function of pocket number.

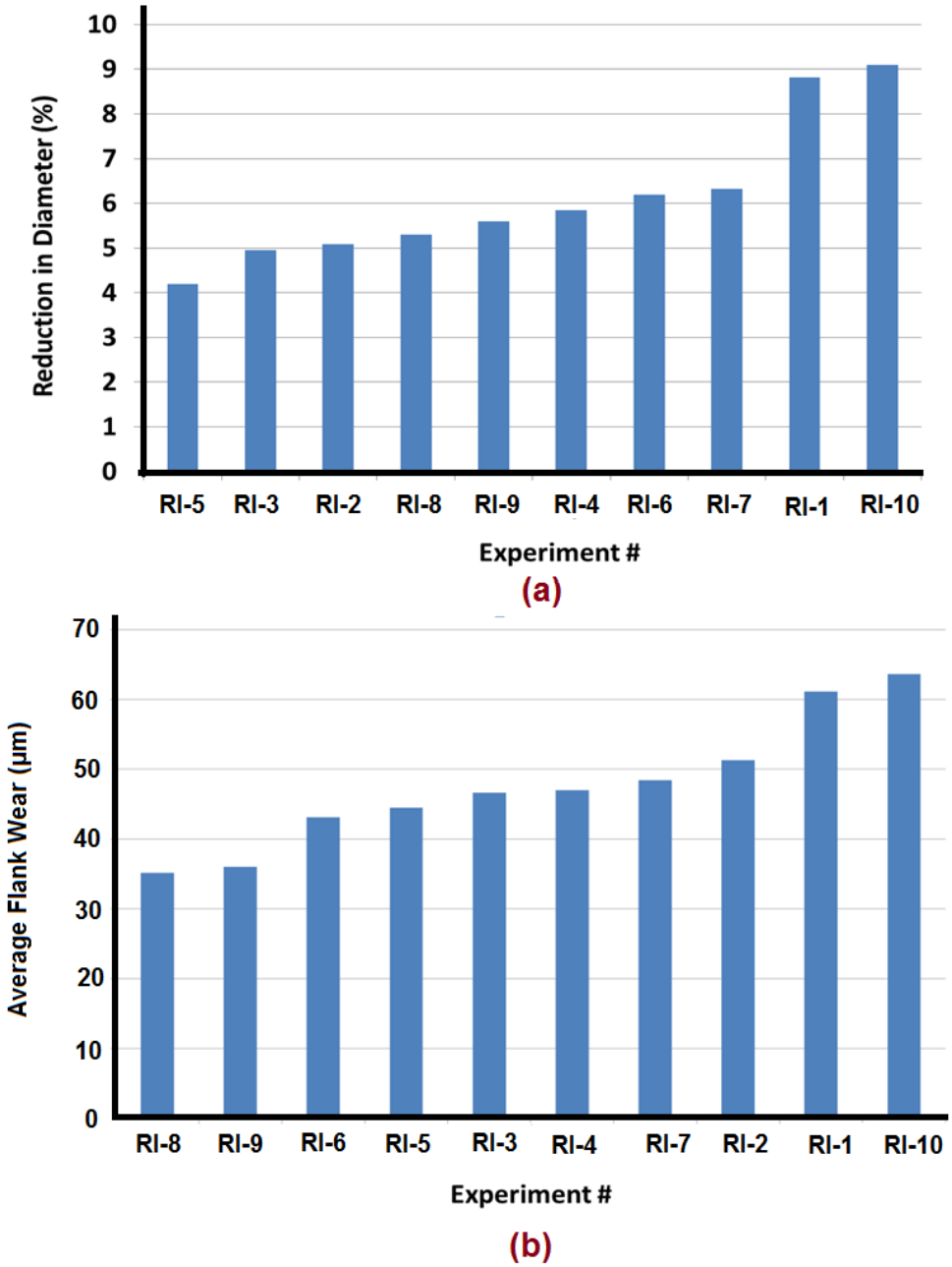

Figure 3.15: (a) Relative tool diameter reduction criterion and (b) comparison of flank wear length after machining tests.

Diameter reduction percentage and average flank wear length can be considered as two different measures of tool wear. According to the results given in Figure 3.15 (a), experimental condition RI-5, which is the medium level combination of feed and radial immersion, seems to be a favorable machining case in terms of relative diameter reduction criteria. Yet, it must be noted that the difference with other milling cases (experimental conditions RI-2 and RI-3) is quite small.

Figure 3.15 (b) compares flank wear lengths at the end of micromilling experiments. For flank wear values, however, experiments RI-8 and RI-9 yielded more favorable results compared to other cases.

The measurement of wear volume combines both flank wear and edge rounding effects on a single measurement indicating the total loss of material from the cutting tool edge. Wear volume is computed for each experimental case by considering the laser topography images of the cutting edges given in Figure 3.12. The ranking of measured wear volumes for each cutting edge is depicted in Figure 3.16.

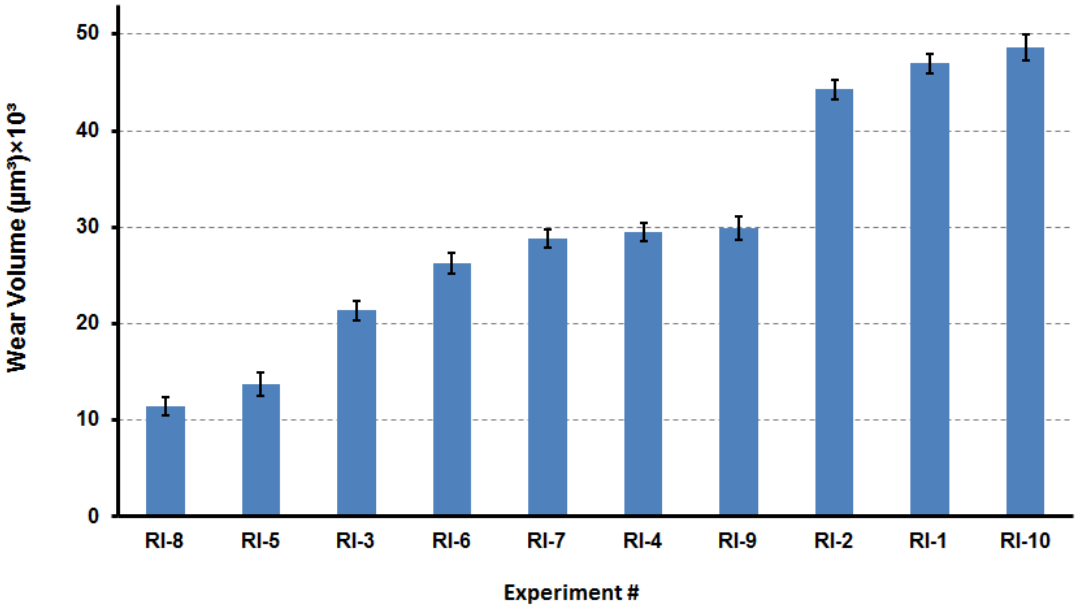

Figure 3.16: Wear volume comparison.

Based on the wear volume results, it can be understood that low radial immersion leads to higher wear volume. When low radial immersion is used, increasing feed rate improves the tool life. For high radial immersion (80 %), decreasing feed up to a certain level can also improve tool life, but for very small feed rates, tool life decreases drastically as is the case of experiment RI-10. Low feed milling cases yielded more flank wear and lower edge rounding on the tool.

3.4.2.3 Effect of Pocket Milling Parameters on Surface Roughness

Surface roughness is the most important process output yet the most difficult to analyze in micro scale. A contactless method of surface roughness measurement was used to analyze machined surfaces. Figure 3.17 shows the laser scanning microscope used in this study and a sample of micro-milled surface observed under the microscope.

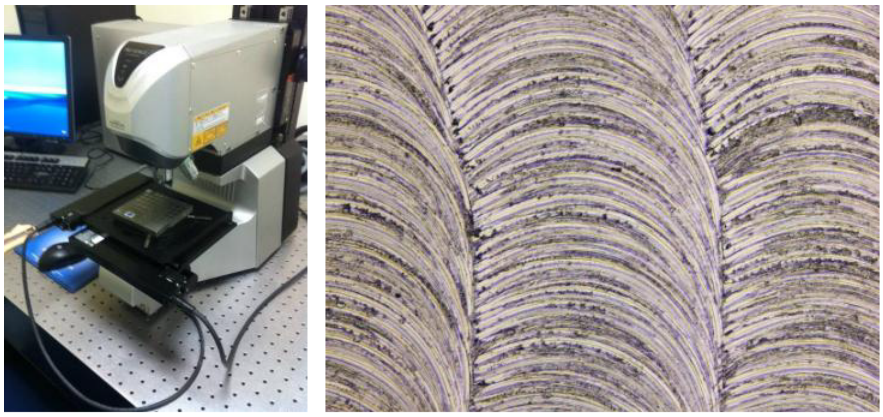

Figure 3.17: Surface roughness measurement setup and surface of the micro-milled circular pocket

The microscope allows measurement of line roughness (e.g. Ra) and areal topography surface roughness (e.g. Sa) (ISO 25178) [128]. The area of observation of the microscope at the highest objective lens magnification is 135 × 100 μm. Its vertical height display resolution is 5 nm. In order to measure the surface roughness, a 7 × 5 matrix (each cell 135-100 μm) was defined on the surface using the microscope's software. Figure 3.18 shows the stitched surface topography of the micro-milled surfaces

for first and last pockets. An example of 3D topography of the pocket surfaces at highest magnification is shown in Figure 3.19.

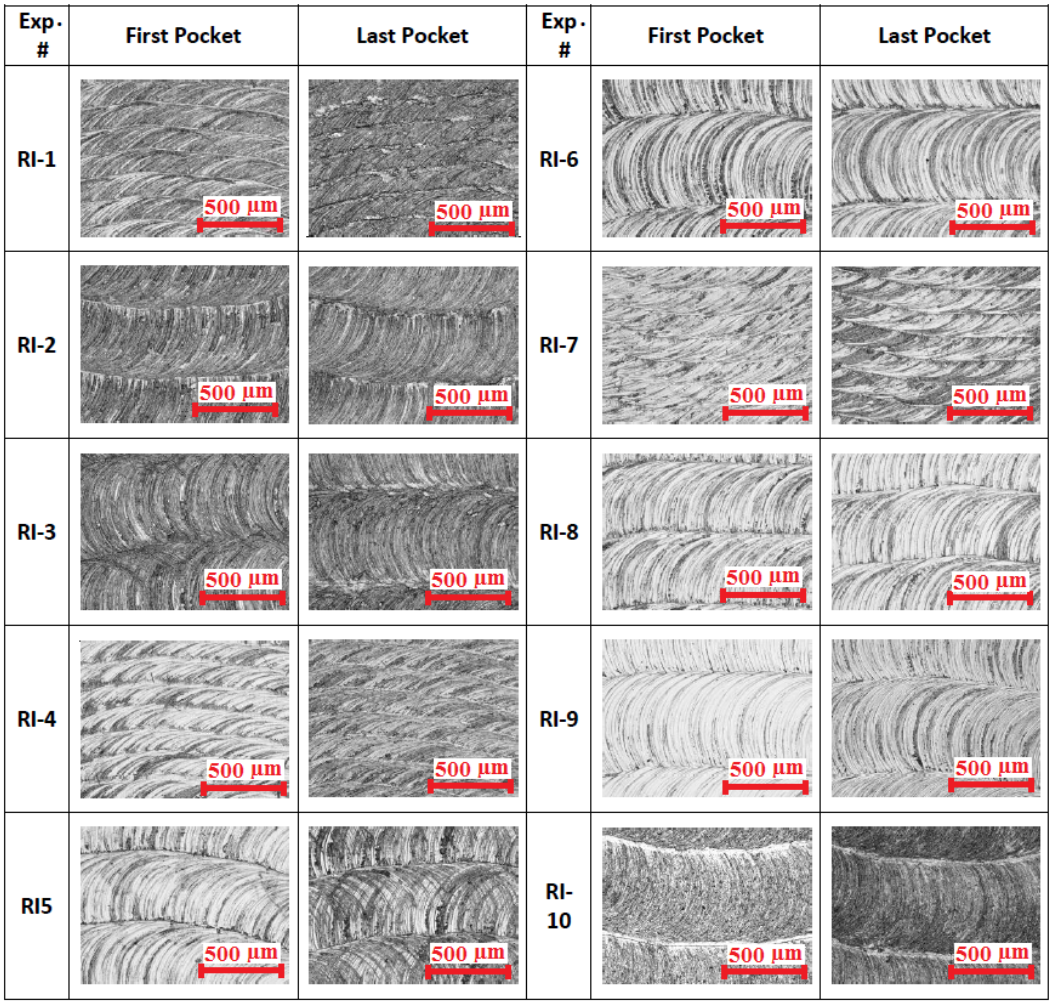

Figure 3.18: Machined surface of first and last pockets for different experiments

Figure 3.20 shows the areal surface roughness (Sa) measurements corresponding to experiments given in Table 3.3. The measurements are taken from the first machined pockets where the influence of tool wear is low. It is observed that low radial immersion experiments yield low surface roughness than high radial immersion tests. At high radial immersion, increasing feed yields better surface roughness. Based on our measurements, 20% radial immersion and 4 µm/tooth feed combination yielded the best areal surface roughness.

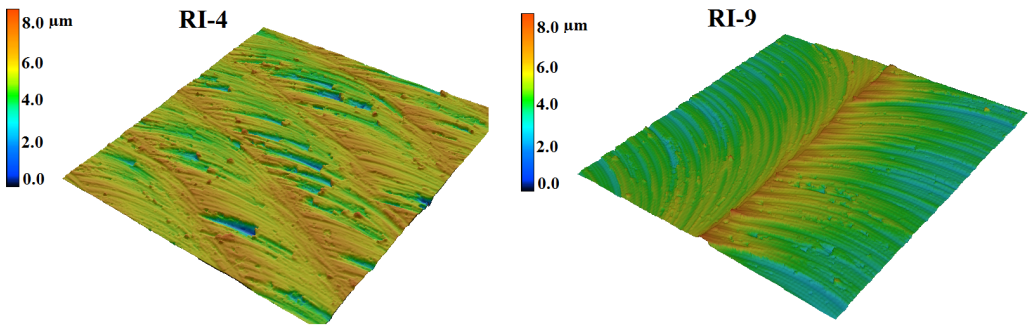

Figure 3.19: 3D surface topography of the micro-milled surface (100x magnification).

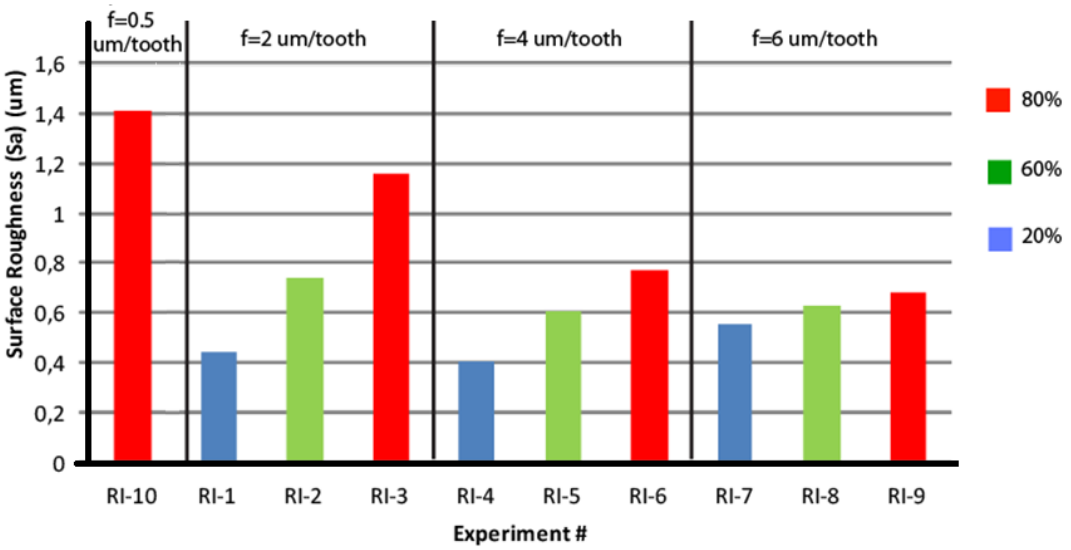

Figure 3.20: Surface roughness as a function of experimental conditions.

3.4.3 Influence of Tool Wear on Micromilling Forces and Surface Roughness

A new set of experiments has been conducted on worn tools, and the influence of tool wear on surface roughness and micromilling forces is investigated. Slot micromilling experiments were conducted at various feed rates, and forces and surface roughness of the machined microchannels were measured for each worn tool. Based on mechanistic modeling approach, cutting and edge force coefficients are calculated with the assumption that the influence of tool wear is reflected on the force coefficients.

3.4.3.1 Experimental Setup for Slot Micromilling Tests with Worn Micro Tools

In the new set of experiments, cutting speed and axial depth of cut are kept the same as previous tests. Four different feed per tooth values (4, 6, 8, and 10 μm/tooth) were considered as shown in Table 3.4. For each experiments cutting forces are recorded.

Table 3.4: Experimental conditions for slot micromilling tests with worn tools

Tool	Feed per Tooth	Depth of Cut
Worn tools used in experiments RI-1 to RI-10	4, 6, 8, and 10 μm/tooth	160 μm

A high-speed spindle NSK HES 510 was attached to the spindle of DMG HSC 55 milling machine. All experiments are performed under dry machining conditions. The tool runout is measured to be around 1 μm. Figure 3.21 shows the experimental setup.

3.4.3.2 Influence of Tool Wear on Surface Roughness

Surface roughness is an important process output of micromilling process, which highly affects the functional performance of the produced micro-parts. Micromilling parameters, tool offset, and machining vibrations are known to significantly affect the

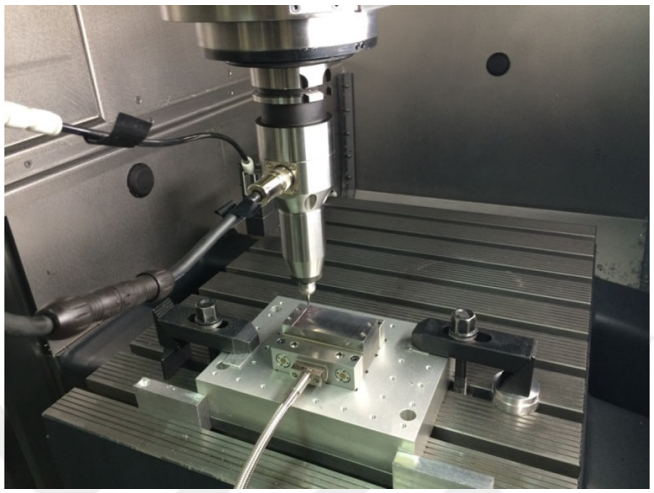

Figure 3.21: Experimental setup for slot micromilling tests.

surface topography [129, 130]. Laser scanning microscope is used for surface roughness measurements. A methodology described in chapter 2 for roughness measurements is used to extract surface roughness parameters of interest. Arithmetic mean height (Ra) and average distance between the highest peak and lowest valley (Rz) values are considered to characterize surface roughness parameters. A cut-off (λ_c) value of 80 μm was used to remove the influence of waviness from surface roughness measurements. Figure 3.22 illustrates the images obtained for different microchannels machined under the same machining conditions with worn micro tools (f=8 μm/tooth).

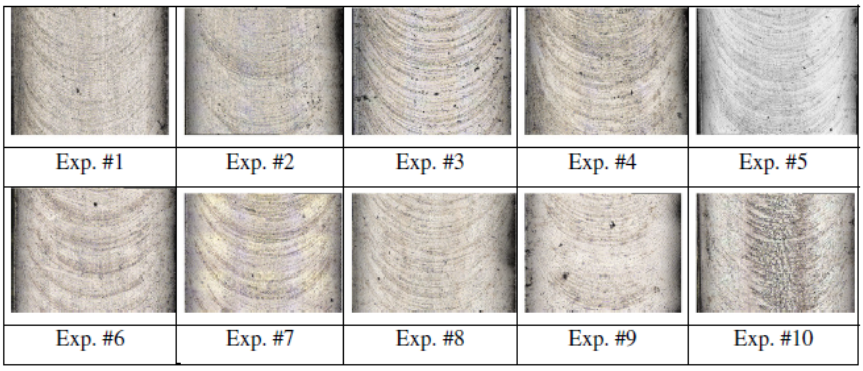

Figure 3.22: Surface roughness of the machined microchannels using worn micro end mills.

Figure 3.23 (a) and (b) shows the Ra and Rz values, respectively. The worn tools used at experiments RI-5 and RI-8 yielded lower Ra values. These results are in a good agreements with wear volume comparison. However, worn tool used at experiment RI-3 exhibited higher Ra value compared to tools used in experiments RI-5 and RI-8.

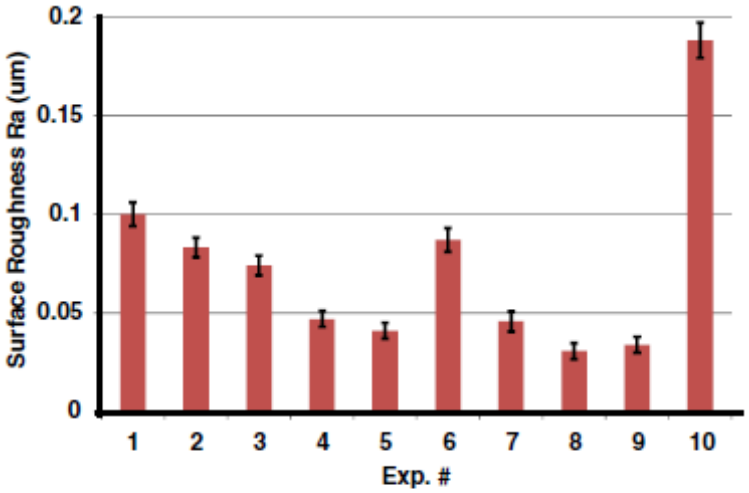

(a)

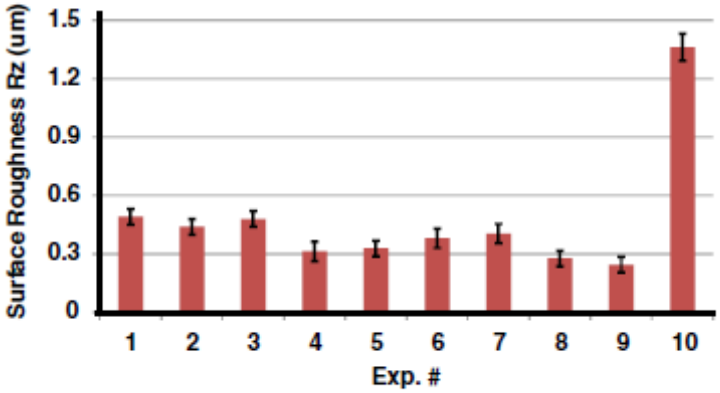

(b)

Figure 3.23: Surface roughness of the machined microchannels: (a) Ra value and (b) Rz value.

The worn tool used in experiment RI-10 presented the worst results in terms of surface roughness. The differences in surface roughness (Rz) between experiments RI-9, RI-10, and RI-6 are quite striking since both have the same radial immersion but different feed per tooth values. This result clearly shows the importance of selecting

compatible radial immersion and feed values during process planning stage. It must be noted that surface roughness is of particular concern during the finishing process, where up-sharp tools are usually utilized. However, selecting low feed and low radial immersion for better surface finish also leads to rapid tool wear, especially when machining difficult-to-cut materials.

It is worth mentioning that powder-like chips are observed while machining Stavax ESR stainless steel. These powder like chips get rubbed on the machined surface (Figure 3.24) and hence degrade the quality of the surface as also mentioned by Liao et al. [131] . The results of experiment RI-10 reveals this situation, where relatively poor surface finish with high Ra and Rz values was obtained (Figure 3.23).

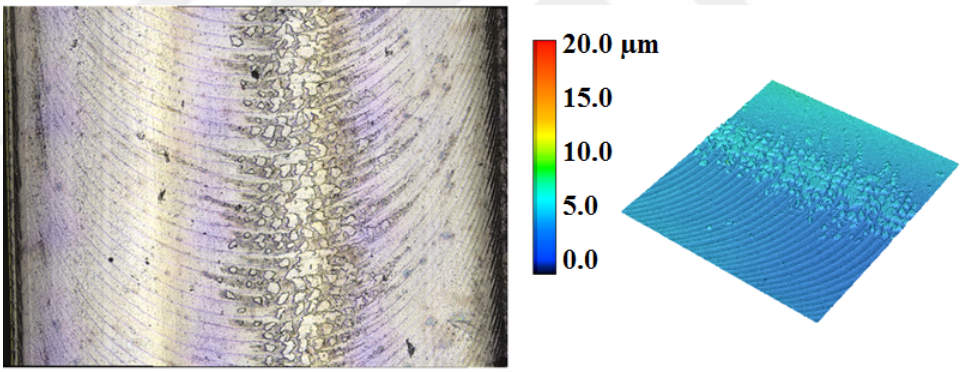

Figure 3.24: Powder-like chips get rubbed on the machined surface.

3.4.4 Effect of Tool Wear on Micromilling Forces

Figure 3.25 illustrates the cutting forces (Fx, Fy) obtained for each tool at a feed rate of 4 µm/tooth. Each slot milling experiment was repeated for all feed values and average forces in X (parallel to th direction of cut) and Y (perpendicular to the cutting direction) directions are calculated. Figure 3.26 illustrates the average of Fx and Fy forces as a function of feed per tooth values in slot milling experiments. Figures 3.25 and 3.26 also show the cutting forces obtained for up-sharp tool.

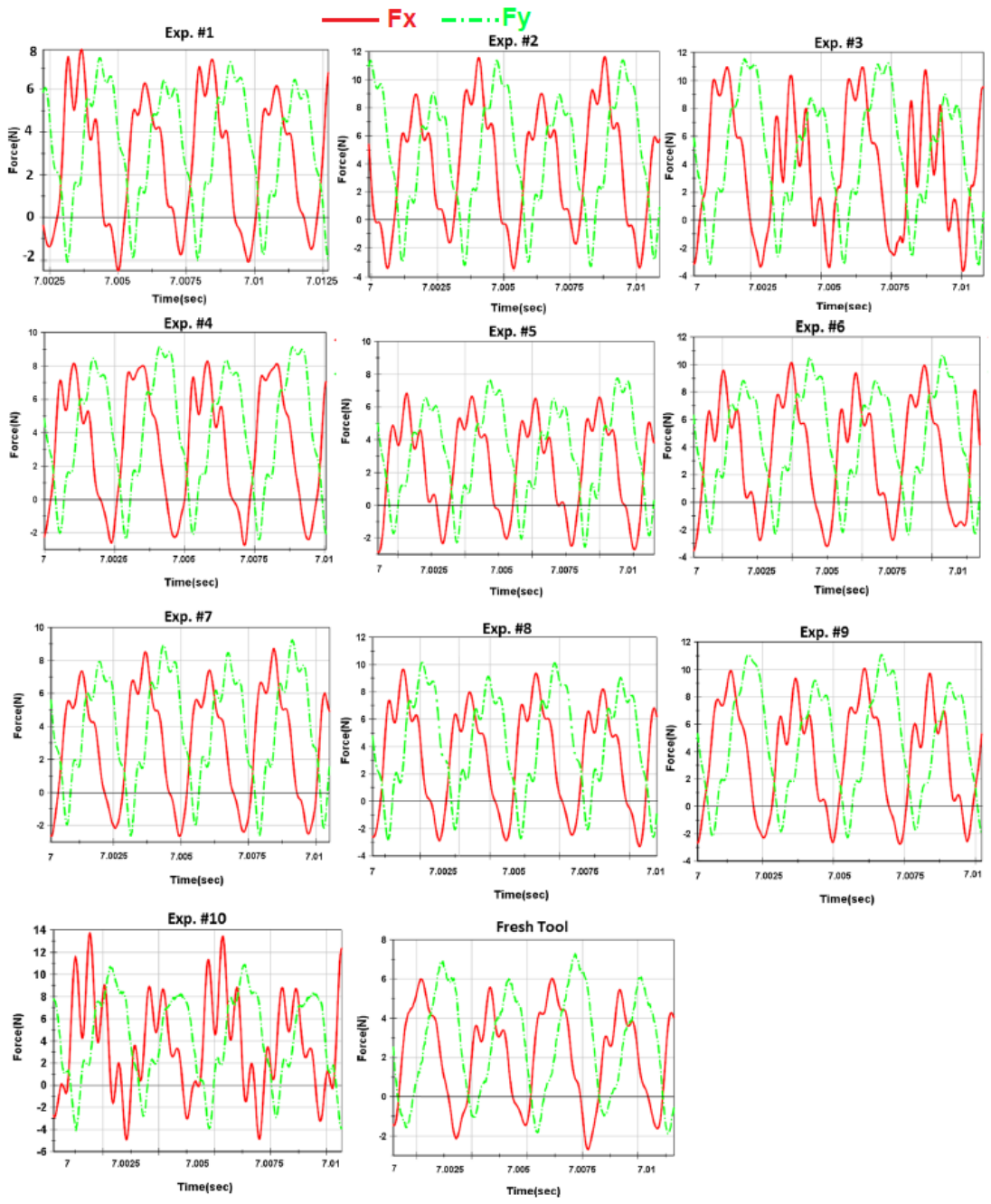

Figure 3.25: Force signals obtained during slot micromilling experiments.

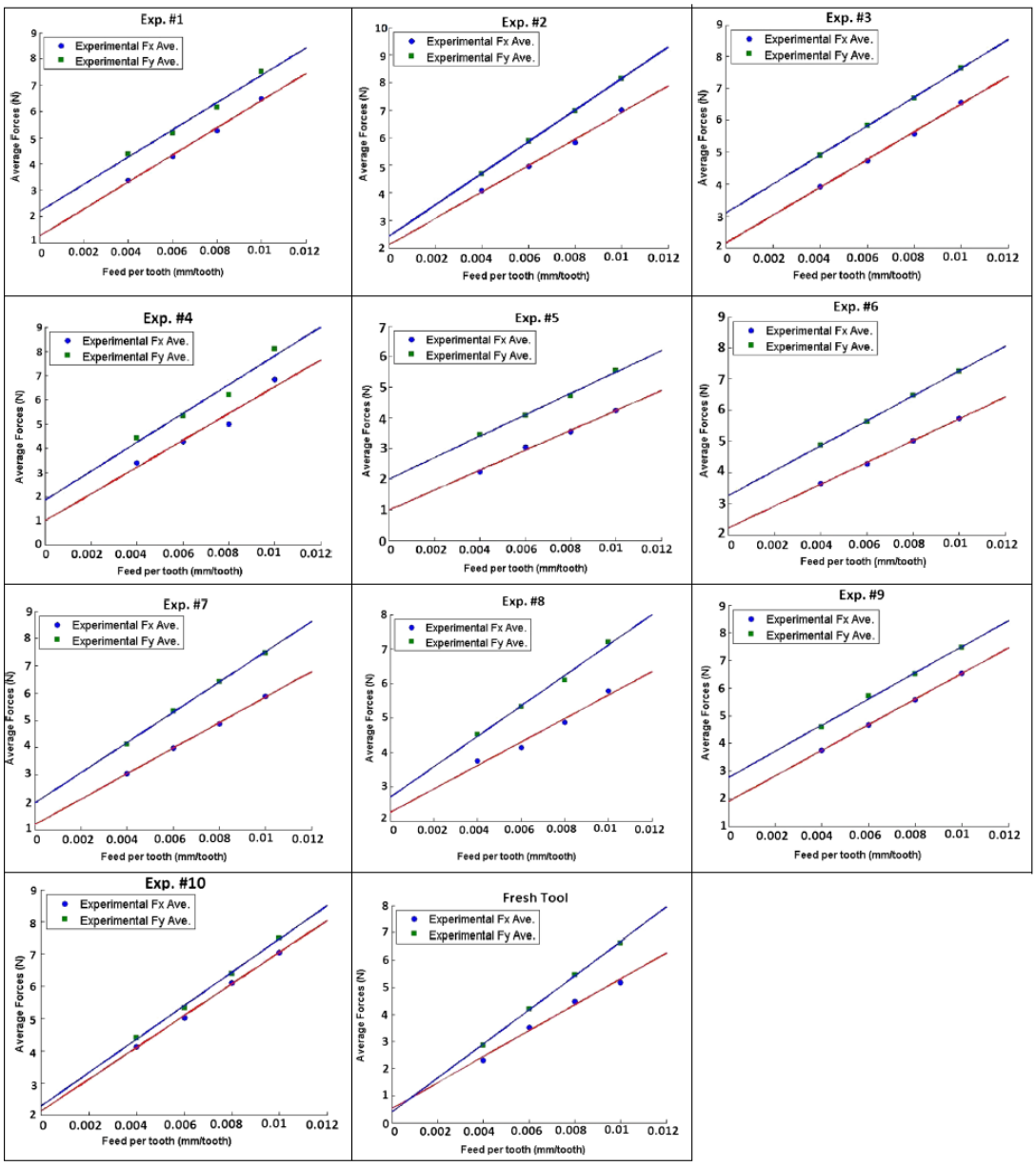

Figure 3.26: Average cutting forces in X and Y directions as a function of feed values

In milling force modeling, cutting forces in X and Y directions can be calculated by using equation 3.4, where a_p represents the depth of cut, ϕ stands for tool rotation angle. Tangential (Ft) and radial (Fr) forces acting on the tool are utilized to calculate the milling forces with respect to a fixed reference system. Milling forces are dependent on the number of teeth on the cutter (Z) and the radial immersion (a_e). Whether a given tooth is in contact with the material or not is controlled through the parameter g.

$$\begin{bmatrix} F_x(\phi) \\ F_y(\phi) \end{bmatrix} = a_p \sum_{j=0}^{Z-1} g_j \left(\begin{bmatrix} \cos\phi & \sin\phi \\ \sin\phi & -\cos\phi \end{bmatrix} \begin{bmatrix} F_t(\phi) \\ F_r(\phi) \end{bmatrix} \right) \tag{3.4}$$

Mechanistic modeling techniques have been used to relate the tangential and radial forces to uncut chip thickness (h) through cutting and edge force coefficients [132, 133].

$$\begin{aligned} F_t(\phi) &= K_{tc} h(\phi) + K_{te} \\ F_r(\phi) &= K_{rc} h(\phi) + K_{re} \end{aligned} \tag{3.5}$$

In Equation 3.5, Ktc, Kte, Krc, and Kre represent the unknown cutting and edge force coefficients, which must be calculated for a given combination of tool geometry and workpiece material.

Using Equations 3.4 and 3.5, unknown cutting and edge force coefficients can be calculated by utilizing slope and intercept values shown in Figure 3.26.

Figure 3.27 (a) shows the comparison of the calculated cutting force coefficients (Ktc and Krc), and Figure 3.27 (b) shows the comparison of edge force coefficients (Kte and Kre) for each worn tool. As expected, the up-sharp micro end mill yielded the lowest edge force coefficients and high cutting force coefficients. For worn tools, edge force coefficients in the tangential direction are larger than in the radial direction, which would imply that edge rounding is more severe than flank wear.

Figure 3.28 shows the cross-sectional area of the micro end mill (used in experiment RI-2) obtained after slicing with micro wire electrical discharge machining. There is

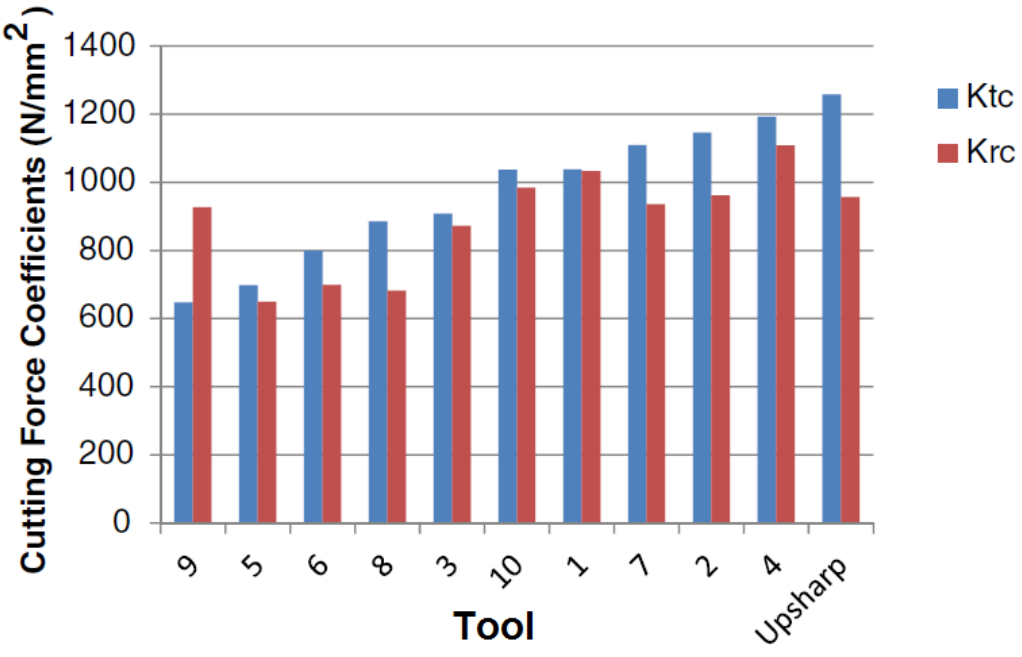

(a)

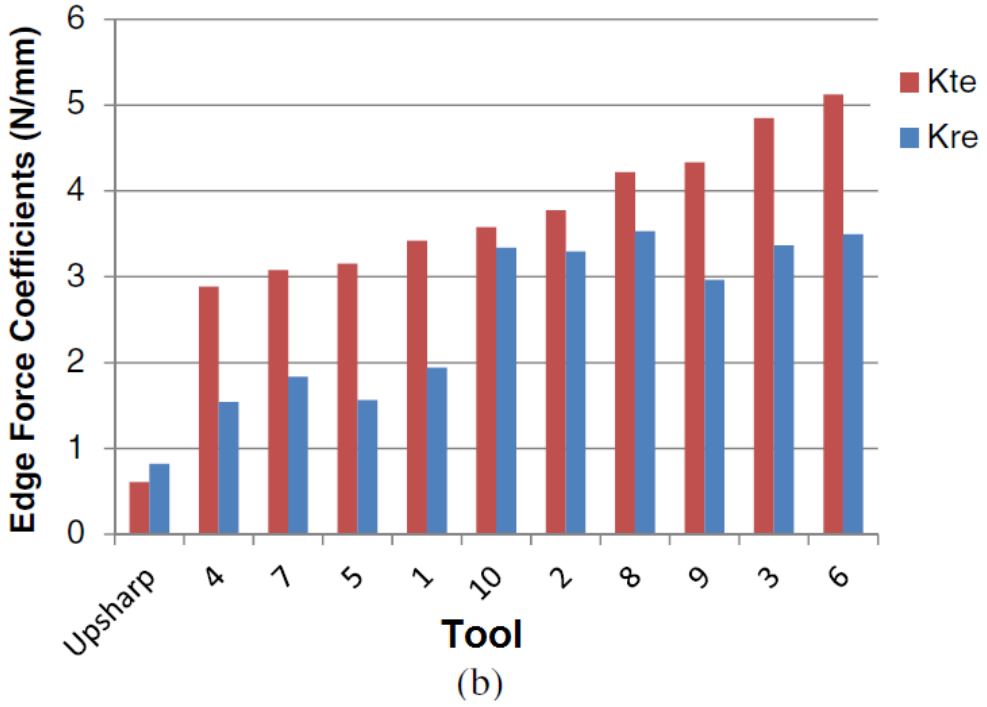

(b)

Figure 3.27: Comparison of: (a) cutting force coefficients and (b) edge force coefficients.

a considerable increase in the cutting edge radius from the initial ~2-3 μm to ~20 μm on one edge and to ~12.6 μm on the other edge.

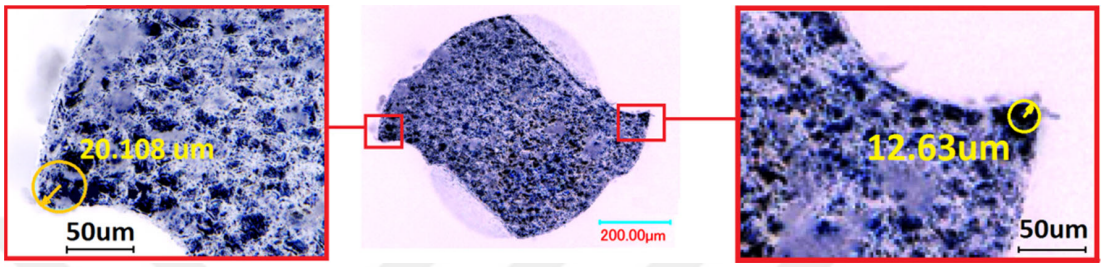

Figure 3.28: Cross-sectional area of micro end mill and edge radius (Experiment #2).

Interestingly, the worn tool used in experiment RI-5 which exhibited low wear volume and produced the lowest Ra and Rz values also has the lowest Kre value along with worn tools used in experiments RI-4 and RI-7. However, Ktc and Kte values of the worn tool used in experiment RI-5 are also lower. This result implies that a large edge rounding has occurred and increasing feed per tooth does not increase the average forces significantly, probably due to the feed values less than the edge radius of the tool. As for the worn tool used in experiment RI-4, edge force coefficients are low and cutting force coefficients are large, similar to up-sharp tool, whereas its wear volume measurements were high. It implies that edge sharpening due to flank wear yields larger cutting force variation with increasing feed values, although the wear volume is larger. Figure 3.29 shows the sections of the cutting edges that explain the situation observed here.

The analysis of cutting forces and surface roughness in conjunction with wear measurements reveals that the tool used under the conditions of experiment RI-5 (f=4 μm/tooth and radial immersion of 60 %) experiences lower cutting forces and produces better surface quality. This result agrees well with the diameter reduction-based analysis of tool wear as shown in Figure 3.15 (a).

In general, tool wear during micromilling of circular pockets is observed to evolve as edge radius and flank wear increase, as illustrated in Figure 3.30. Two different wear types can be identified. In type I wear, a large edge rounding has been observed with a small flank wear. In type II wear, a larger flank wear ($VB_2 > VB_1$) has been observed

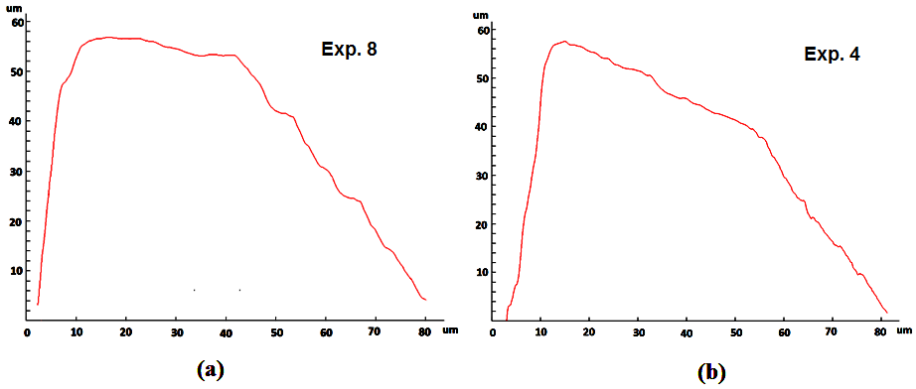

Figure 3.29: Two different cases of edge wear identified from experiments: (a) worn tool used in experiment #8 and (b) worn tool used in experiment #4.

with a smaller edge rounding ($r_{f2} < r_{f1}$). In both wear types the final edge radius (r_f) is larger than initial edge radius (r_i). Therefore, our findings reveals that edge rounding and flank wear development follow a certain pattern depending on the selection of feed and radial immersion parameters.

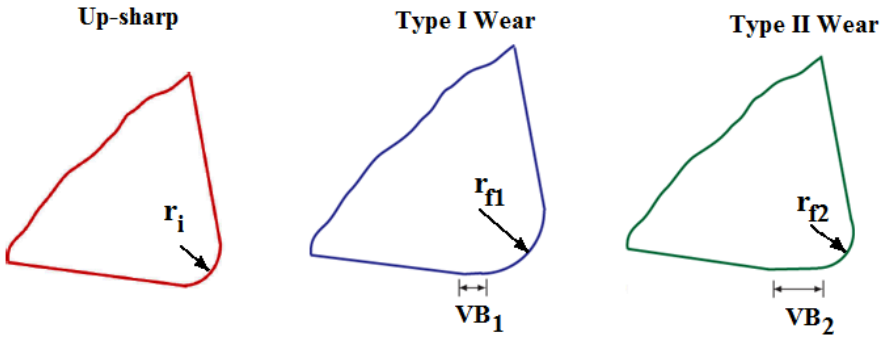

Figure 3.30: Two different wear mechanism identified from experiments (initial edge radius (r_i) is smaller than final edge radius (r_f)).

Tool wear evolution is important, since it affects the directions of radial and tangential forces acting on the cutting edge. In order to continue machining effectively with worn tools, one possible strategy would be to increase feed per tooth as cutting edge radius increases. However, this increase is limited by the tool deflection and tool breakage, which is investigated in subsequent sections.

3.4.5 Effect of Tool Wear on Machined Microchannel Accuracy

In order to investigate the effect of tool wear on the accuracy of the machined microchannels, profile of the microchannels has been studied in detail. For this purpose μ-WEDM process has been used for slicing of the workpiece perpendicular to the axis of produced microchannels as depicted schematically in Figure 3.31. After slicing, the corner radius of the microchannels are measured using VKX-1000 digital microscope as illustrated in Figure 3.32. The results of corner radii measurements under experimental conditions of Table 3.4 are shown in Figure 3.33.

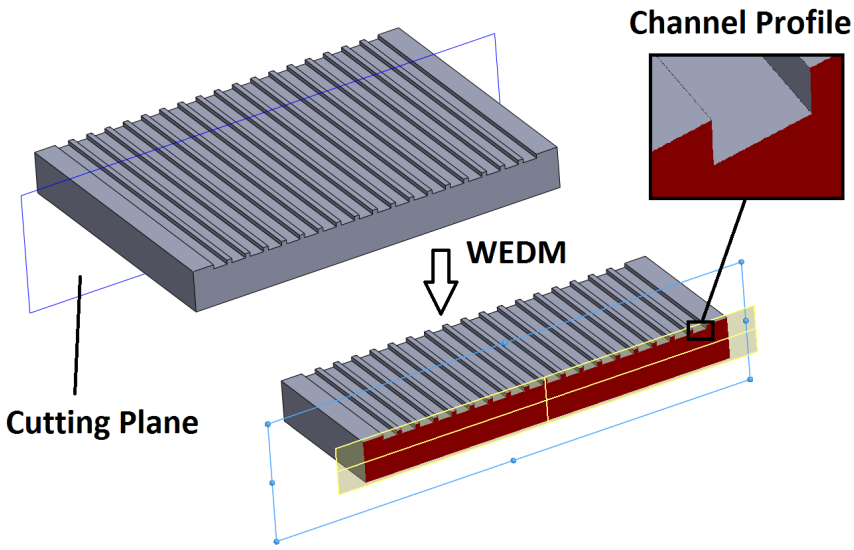

Figure 3.31: Schematic representation of slicing using μ-WEDM.

It can be seen from Figure 3.33 that the rounded edge of the micro end mills are directly imprinted into the microchannel profile. Tool used in RI-4 experiment, which is experienced type II wear, resulted in smaller corner radius. As expected, the tool of experiment RI-10, which experienced type I wear, resulted in the larges corner radius. These findings reveals that, in order to have accurate micro-parts, a tool condition monitoring system should be used to provide information regarding tool condition.

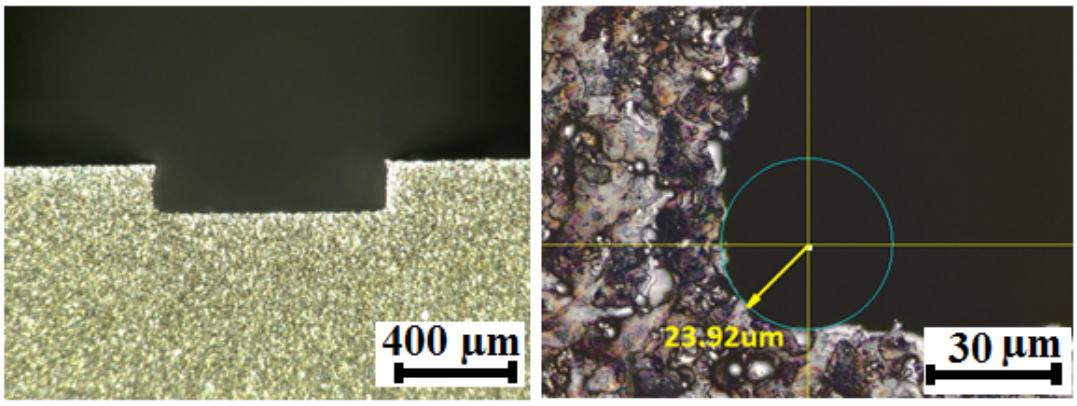

Figure 3.32: Corner radius of the machined microchannels using worn micro end mills.

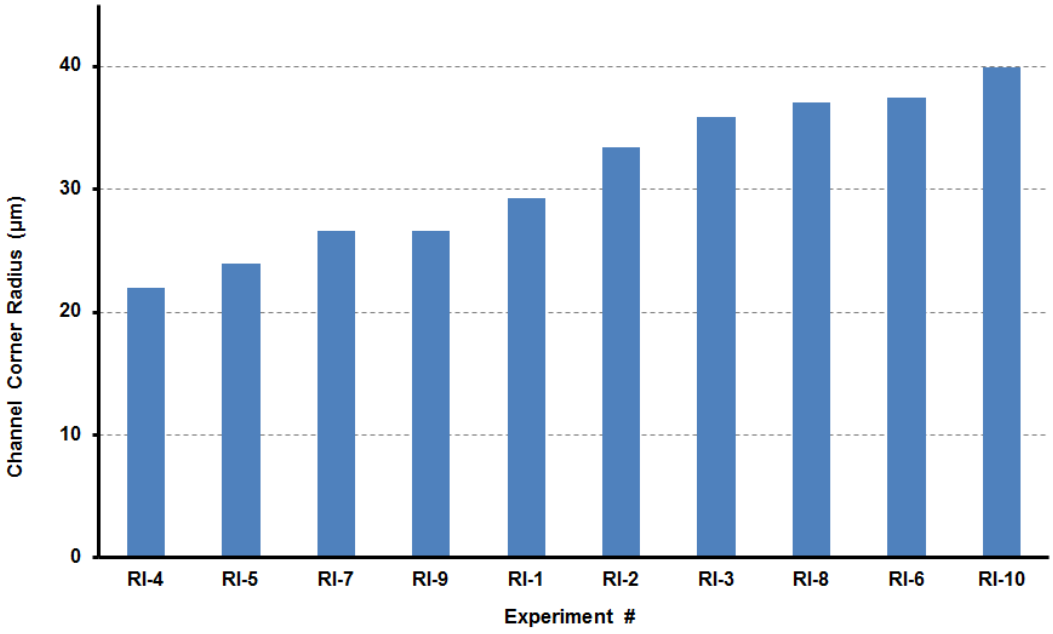

Figure 3.33: Measured corner radius for different micro end mills.

3.4.6 Tool Deflection Modeling by Finite Element Analysis

As tool wear progresses, micromilling forces increase, and as a result of increasing machining forces, micro end mills considerably deflect and finally reach to the point of fracture. The limits of tool fracture are important especially for process planning, tool condition monitoring, and tool design purposes. According to Uriarte et al. [32] tool deflections due to machining forces are the main source of error which should be dealt with to improved machine part accuracy in micromilling operations. Using an experimental approach, Uriarte et al. [32] obtained the stiffness chain of the micromilling machine by considering the stiffness levels of the machine tool, spindle, tool holder and the tool itself. Based on their assessment, for micromilling, the compliance of the tool accounts for up to 80-90 % of the total compliance of the system. Therefore, unlike conventional milling, micro tools are the main source of compliance in the micromilling stiffness chain [134].

By modeling micro end mill as a cantilever beam, which is stiffly clamped to the machine spindle, Kim et al. [135] obtained tool deflections in radial direction. They obtained one-dimensional displacement of the end mill by modeling it as a Hookean spring. The spring constant assumed to be same as stiffness of the micro end mill in radial direction. They calculated actual chip thickness by subtracting deflections from ideal chip thickness. In a similar way Feng and Menq [136] modeled ball end mills as solid cantilever beam and established a deflection-dependent chip load. Kline et al. [137] also used simple cantilever beam model to predict tool deflections. They integrated deflection model to the cutting force model to predict surface error profile during conventional end milling. A two step cantilever beam model (considering shank and flute part) is used by Kim et al. [138] to obtain static deflection of ball end mills. By integrating deflection model, cutting force model and error estimation model they predicted form errors in 3D ball end milling process. Dow et al. [139] proposed an open-loop technique for deflection compensation in micromilling. They used beam theory to calculate the stiffness of micro end mills. They mentioned about complexity of 3D CAD modeling because of lack of access to the required data. They also showed that using deflection compensation, the accuracy of the machined parts can be improved.

In this section, the influence micromilling forces of worn micro end mills on tool deflections are studied by using finite element modeling. An experimental setup has been prepared to measure the tool deflection under the action of static forces as depicted in Figure 3.34.

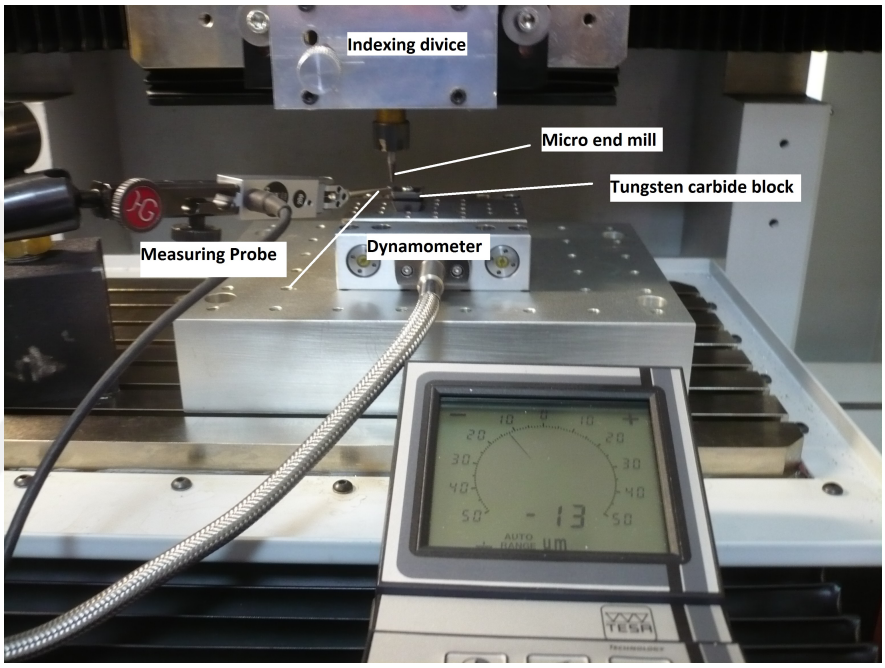

Figure 3.34: Experimental setup used for tool deflection measurements.

The cutting tool is mounted on a self-developed indexing device attached to the Z axis of the machining center (Mikrotool DT-110) with the same overhang used in micromilling experiments. The use of an indexing device makes it possible to lock the tool to avoid its rotation and to apply the force at different angles. To measure the tool deflection, a TESA GT31 lever probe with a repeatability of 0.1 µm is used. The probe is attached to a Tesatronic TT10 display unit. The static force is applied by pushing the tool against a rigid tungsten carbide block mounted on Kistler mini dynamometer. The tool is programmed to move 0.5 µm towards the tungsten carbide block at a low feed rate of 0.5 mm/min. Figure 3.35 illustrates the time history of the applied forces on the tip of the micro end mill.

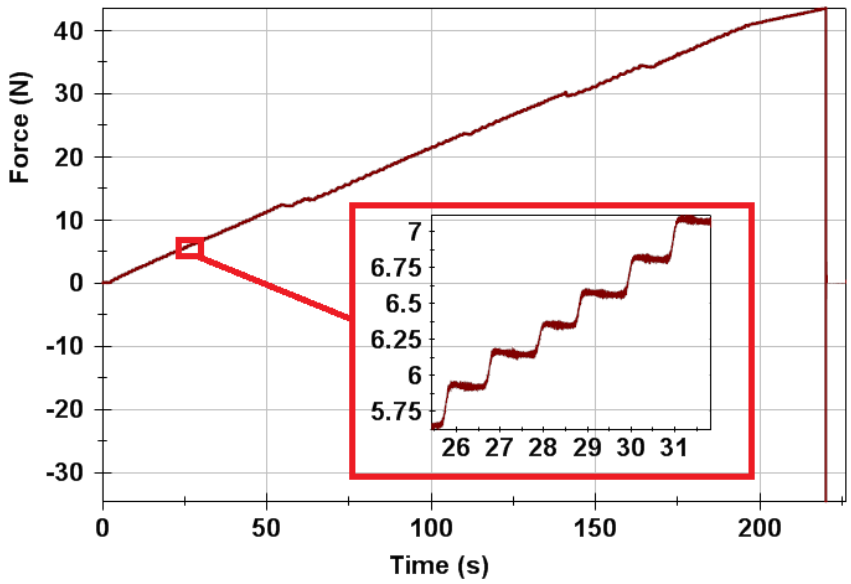

Figure 3.35: Force applied to the cutting tool during deflection test.

In order to have an accurate geometrical model of the micro end mills, three-dimensional topography of the tools are obtained using 3D laser scanning microscope. Information regarding cross-sectional properties of the tools are obtained by slicing the cutting tools by using electro discharge machining. These information are used to construct a detailed solid model, which is very close to the real micro end mill. A 3D CAD design software (SolidWorks) is used to build a solid model of the micro end mill. The Solid model is imported into COMSOL Multiphysics finite element software to analyze the deflection of the micro end mill under the action of cutting forces. Figure 3.36 illustrates the finite element model used in this study.

Material properties for finite element analysis are determined based on EDS data, which are already given in Section 2.3. In the loading of the model, a fixed constraint has been applied to a portion of the shank, which is used for clamping, to provide the same overhang used in experiments. A user-controlled mesh with tetrahedral elements was applied. The recorded force history is imported into COMSOL Multiphysics, and cutting tool deflections are simulated and then compared to the experimental measurements as depicted in Figure 3.37. It should be mentioned that the nominal measuring

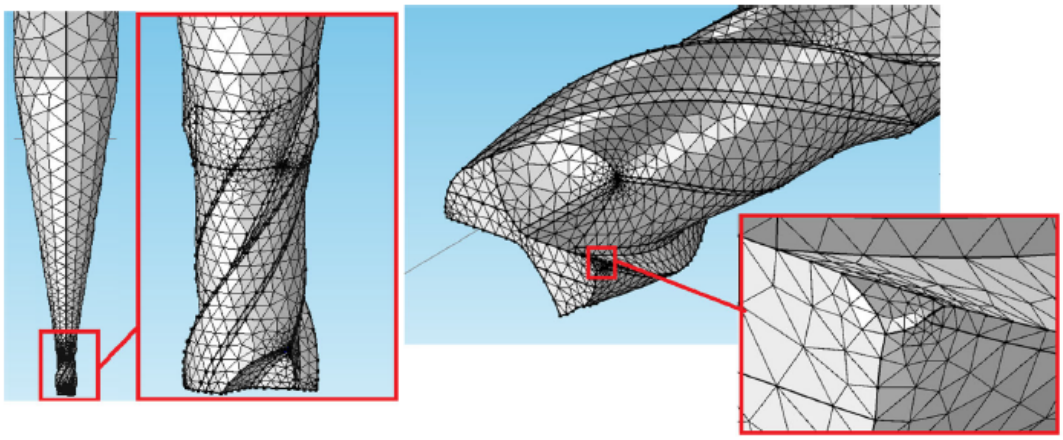

Figure 3.36: Meshed model of the micro end mill.

force of the probe is 0.1 N, so it is quite negligible compared to the measured forces.

3.4.7 Finite Element Simulation-based Analysis of Tool Deflection

Once the finite element model is validated, it is possible to simulate the influence of worn tool forces on the tool deflection. The radial and tangential components of the machining forces identified in the previous section are used in simulations. In order to consider the influence of tool wear, the 3D wear zone images obtained in Figure 3.12 are transferred to the finite element models as shown in Figure 3.36. Machining forces are distributed over the worn area. A static analysis has been performed using Solid Mechanics Module of COMSOL Multiphysics software, and one revolution of the cutting process is simulated and corresponding deflection of the end mills are obtained. Figure 3.38 illustrates the maximum deflection of the micro end mill used in experiment RI-5 corresponding to 126°. A deflection value around 20 μm was calculated.

Tool tip deflection as a function of tool rotation angle for different experiments is depicted in Figure 3.39 for up-sharp and for the tool in experiments RI-3, IR-5 and RI-10. Simulated tool tip deflection in polar coordinates at various angles with 5° increments are also represented in Figure 3.39. The results of finite element analysis

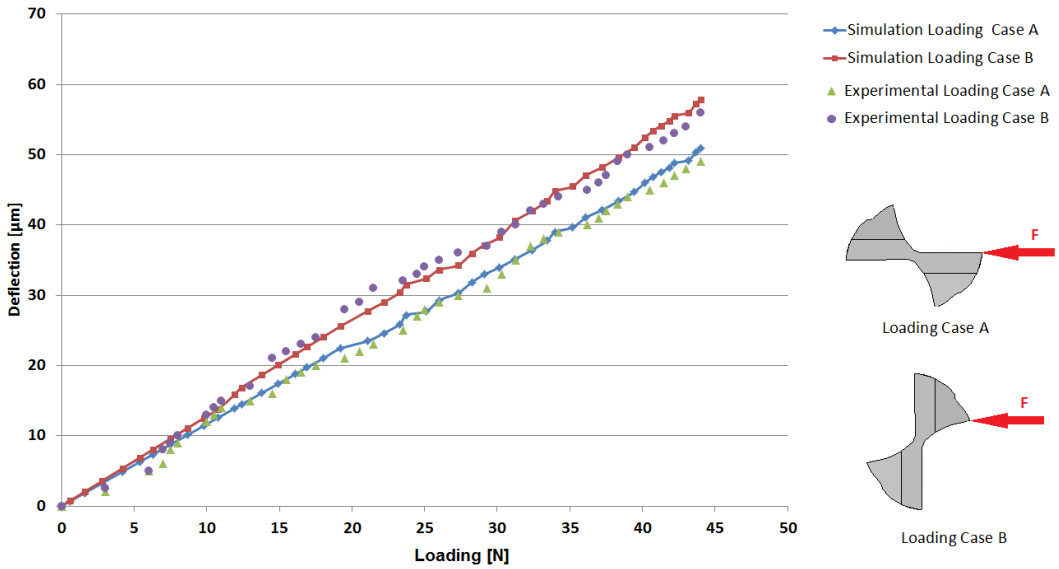

Figure 3.37: Comparison between measured and simulated tool deflections.

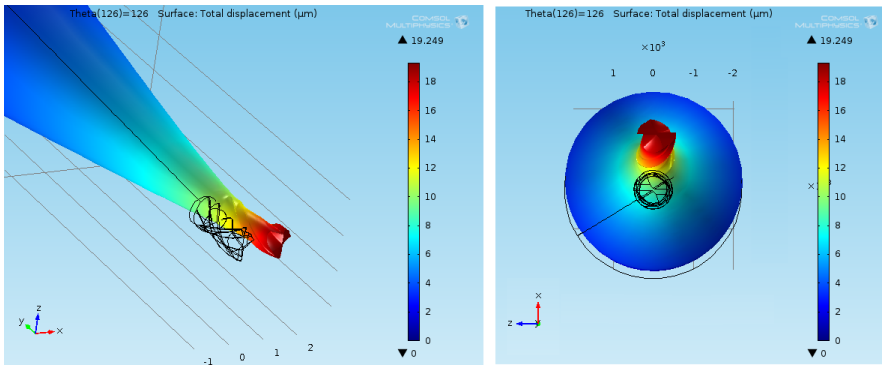

Figure 3.38: Maximum deflection of the tool tip for end mill of experiment #5 at $\theta = 126°$.

show that tools with a higher amount of wear experience a larger amount of deflections, as expected. Based on the results given in Figure 3.39, maximum tool deflections are ranging between 14 and 28 μm. The magnitude of deflections is in the same order of magnitude when compared with studies from the literature [85, 86, 87].

In this study, the developed finite element model is used to predict tool failure using transverse rupture strength (TRS) as failure criterion. The worn tool of experimental test case RI-10 was considered, and additional micromilling tests were performed with this tool until the tool fractures. The milling forces at the point of tool breakage were recorded. Figure 3.40 (a) shows the 3D topography of the machined slot at the point of tool breakage. Figure 3.40 (b) depicts the force measurement at the instant of tool breakage.

Investigation of the tool trace left on the workpiece at the end of the produced microchannel reveals that tool failure occurs at maximum tool deflection. The resultant force acting on the tool also agrees with the static tool deflection test results. The location of tool breakage agrees with the results shown in Figure 3.38. Excessive burr formation around the microchannel also shows the influence of rounded cutting edges.

At this point, it is possible to investigate the condition of the micro cutting tools. The recorded forces are imported into the COMSOL software and the stresses on the tool body are calculated. Fang [64] reported traverse rupture strength of ultra-fine grain tungsten carbide as $TRS > 3.7$ GPa. Figure 3.41(a) shows the results of finite element analysis for tool of experiment RI-10 where the calculated maximum point of stress on the tool shank is shown. Figure 3.41(b) shows the tip of the broken tool and its length. It can be seen that the finite element model predicts the tool failure point with a high accuracy. The deflection calculated in Figure 3.41(c) also matches well with the deflection experiments.

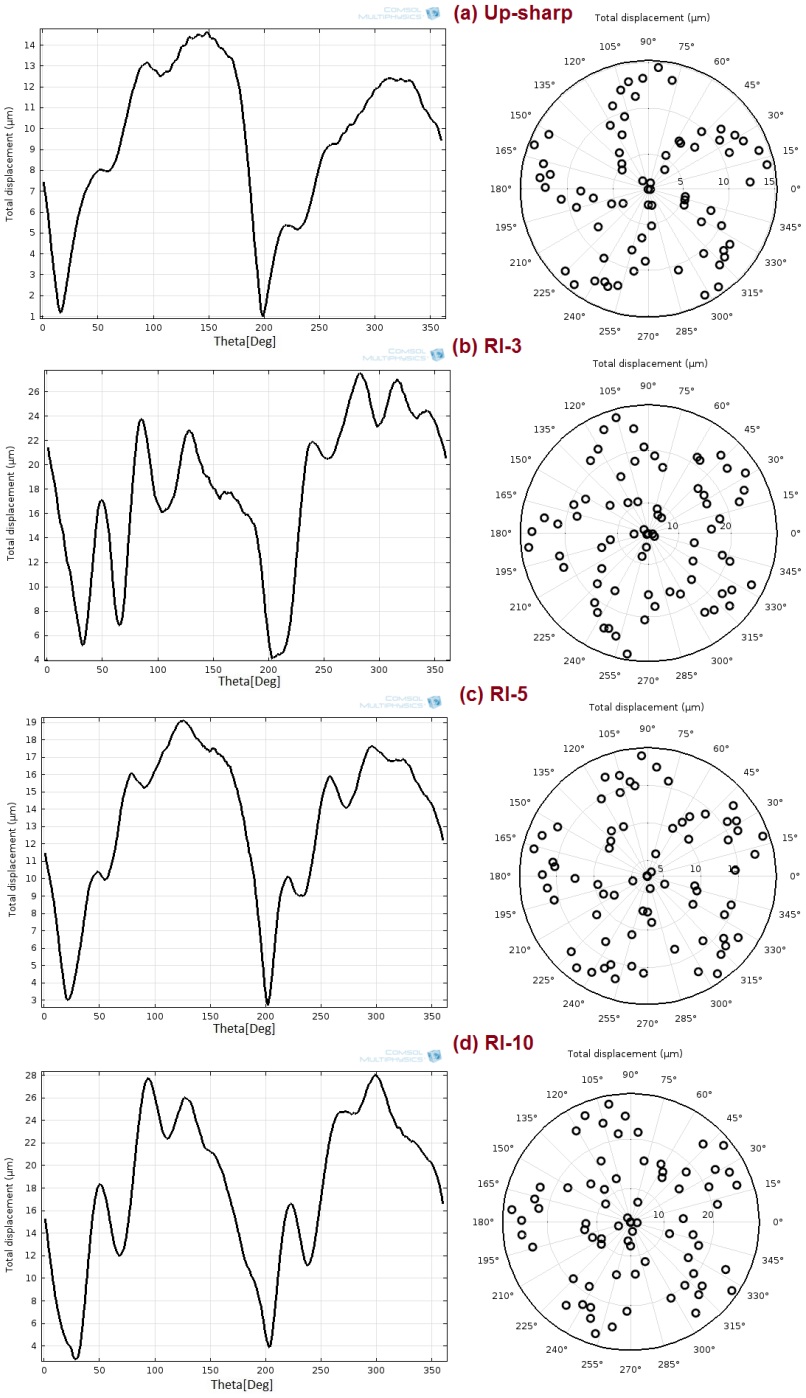

Figure 3.39: Total displacements for: (a) up-sharp and (b) tool used in RI-3, (c) tool used in RI-5 and (d) tool used in RI-10 when machining with feed at 8 µm/tooth.

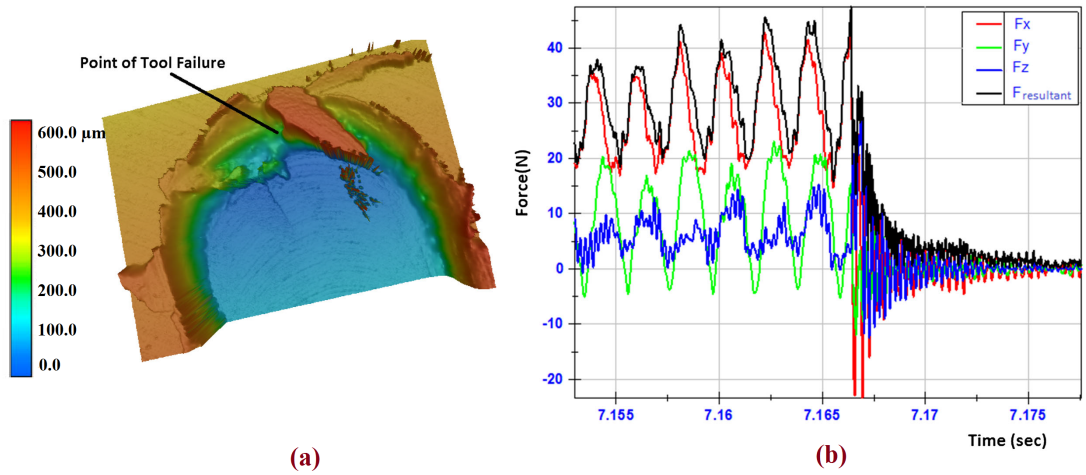

Figure 3.40: (a) Trace left by the tool at the point of failure as measured on workpiece and (b) force measurements at the instant of tool breakage.

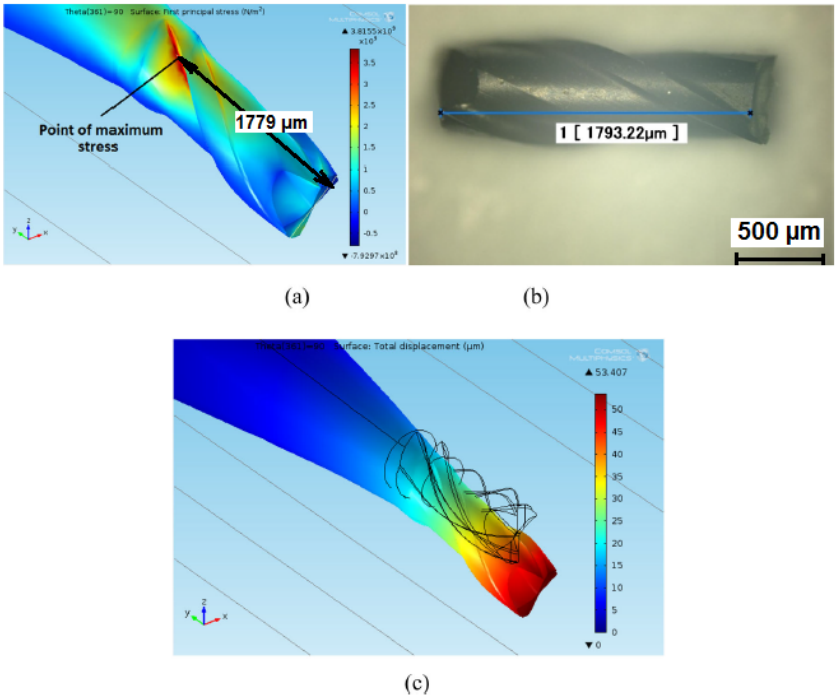

Figure 3.41: Total displacements for: (a) up-sharp and (b) tool used in RI-3, (c) tool used in RI-5 and (d) tool used in RI-10 when machining with a feed rate of 8 µm/tooth.

3.4.8 Analytical Modeling of Conventional Micro End Mill Deflections

In previous section, finite element modeling is successfully used to predict micro end mills deflection and stresses. Although, this method provides very useful information about the performance of the cutting tools under the action of different forces, however their integration into the existing cutting force models to improve force predictions of micromilling is not an easy task.

In order to improve the accuracy of cutting force predictions in micromilling operations, the effect of tool deflections should be included in the calculation of instantaneous uncut chip thickness. To achieve this goal an analytical model of tool deflections is necessary. Therefore, an analytical model of the conventional micro end mills are developed.

A precise solid model of the micro end mills has been developed and successfully implemented in finite element simulations of tool deflections and stresses. Using this solid model, it is possible to extract cross-sectional properties of the helical part of micro end mills. This can be done by slicing the cutting tool at different locations and calculate cross-sectional properties. Having obtained moment of inertia of the cross-sections in radial and tangential directions, the average value of moment of inertia in each direction can be calculated as:

$$(I_{rc})_{ave} = \frac{\sum_{i=1}^{N} (I_{rc})_i}{N} \qquad \text{and} \qquad (I_{tc})_{ave} = \frac{\sum_{i=1}^{N} (I_{tc})_i}{N} \tag{3.6}$$

where subscripts 't' and 'r' represent tangential and radial directions, respectively. Based on average moment of inertia, the equivalent diameter in each direction can be calculated as:

$$\left(D_{eq}\right)_{rc} = \sqrt[4]{\frac{64(I_{rc})_{ave}}{\pi}} \tag{3.7}$$

$$\left(D_{eq}\right)_{tc} = \sqrt[4]{\frac{64(I_{tc})_{ave}}{\pi}} \tag{3.8}$$

Castigliano's second theorem is used to calculate the end deflection of the micro end mills. Using this theory the deflection of a micro end mill (δ) can be related to the

elastic strain energy stored in the micro end mill (U) under the action of machining forces (F) by using following equation:

$$\delta = \frac{\partial U}{\partial F} \tag{3.9}$$

It should be mentioned that for end mills, the axial stiffness is much larger than radial stiffness. Therefore, the bulk deflection of the end mills are mainly due to the radial component of the machining forces and deflection due to axial forces can be neglected [139, 138].

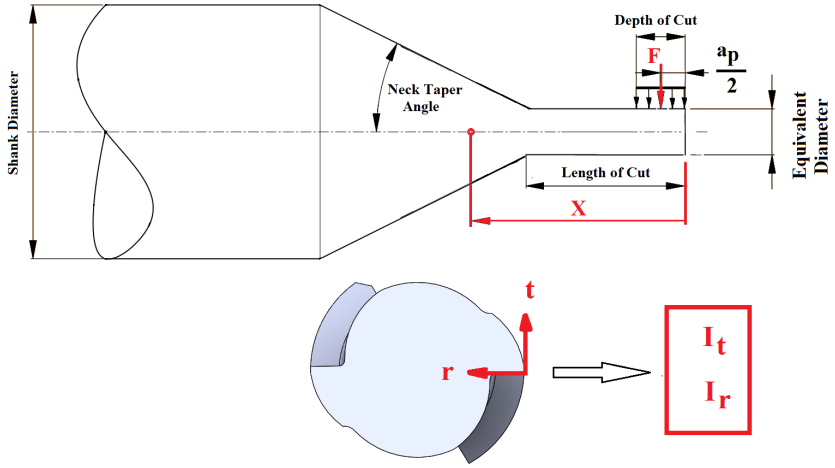

Figure 3.42: Schematic representation of the equivalent micro end mill

Considering Figure 3.42, the energy stored in the micro end mill as a result of different components of the machining forces (F_r: radial force and F_t: tangential force) can be expressed as:

$$U_t = \int_0^{L_c} \frac{M_{tc}^2}{2EI_{tc}} dx + \int_{L_c}^{L_T} \frac{M_{tT}^2}{2EI_{tT}} dx + \int_{L_T}^{L_s} \frac{M_{ts}^2}{2EI_{ts}} dx \tag{3.10}$$

$$U_r = \int_0^{L_c} \frac{M_{rc}^2}{2EI_{rc}} dx + \int_{L_c}^{L_T} \frac{M_{rT}^2}{2EI_{rT}} dx + \int_{L_T}^{L_s} \frac{M_{rs}^2}{2EI_{rs}} dx \tag{3.11}$$

Where subscript 'c' stands for cutting portion, 'T' stands for tapered part and 's' stands for the shank part. For instance, 'I_{rT}' is the moment of inertia of the tapered part in the radial direction.

Assuming a uniform distribution of forces over engagement depth (depth of cut (a_p)), the distributed uniform force can be replaced by a concentrated force acting in a position of 'a_p/2' from tool tip as depicted in Figure 3.42. Therefore at any point in a distance 'x' from tool tip, the moment can be written as:

$$M(x) = F\left(x - \frac{a_p}{2}\right) \tag{3.12}$$

In the absence of any other external force acting on the micro end mill, the moment at different portions are the same function of 'x' which is calculated as:

$$M_{tc} = M_{tT} = M_{ts} = F_t\left(x - \frac{a_p}{2}\right) \tag{3.13}$$

similarly

$$M_{rc} = M_{rT} = M_{rs} = F_r\left(x - \frac{a_p}{2}\right) \tag{3.14}$$

Therefore, equations 3.10 and 3.11 can be simplified as:

$$U_t = \frac{F_t^2}{2E}\left(\int_0^{L_c} \frac{\left(x - \frac{a_p}{2}\right)^2}{I_{tc}}dx + \int_{L_c}^{L_T} \frac{\left(x - \frac{a_p}{2}\right)^2}{I_{tT}}dx + \int_{L_T}^{L_s} \frac{\left(x - \frac{a_p}{2}\right)^2}{I_{ts}}dx\right) \tag{3.15}$$

$$U_r = \frac{F_r^2}{2E}\left(\int_0^{L_c} \frac{\left(x - \frac{a_p}{2}\right)^2}{I_{rc}}dx + \int_{L_c}^{L_T} \frac{\left(x - \frac{a_p}{2}\right)^2}{I_{rT}}dx + \int_{L_T}^{L_s} \frac{\left(x - \frac{a_p}{2}\right)^2}{I_{rs}}dx\right) \tag{3.16}$$

In order to calculate strain energies, it is necessary to determine the moment of inertia of each portion. Except for the cutting part of the micro end mill, the tapered and shank parts are axisymmetric; therefore they have same radial and tangential cross-sectional properties. The moment of inertia for the cutting part has already been calculated. For the tapered part the change of moment of inertia along 'x' should be calculated. The diameter as a function of 'x' can be written in terms of neck taper angle of the tool (γ) as follows:

$$D(x) = D_{eq} + 2x\tan(\gamma) \tag{3.17}$$

where

$$D_{eq} = \frac{\left(D_{eq}\right)_{rc} + \left(D_{eq}\right)_{tc}}{2} \tag{3.18}$$

Therefore, the moment of inertia for tapered part as a function of 'x' can be written as:

$$I_T(x) = \frac{\pi\left(D_{eq} + 2x\tan(\gamma)\right)^4}{64} \tag{3.19}$$

The moment of inertia for the shank portion can be written as:

$$I_s = \frac{\pi(D_s)^4}{64} \tag{3.20}$$

Having determined moment of inertia of each portion; the elastic strain energy can be calculated as:

$$U_t = \frac{32F_t^2}{\pi E}\left(\int_0^{L_c} \frac{\left(x-\frac{a_p}{2}\right)^2}{\left(D_{eq}\right)_{tc}^4}dx + \int_{L_c}^{L_T} \frac{\left(x-\frac{a_p}{2}\right)^2}{\left(D_{eq}+2x\tan(\gamma)\right)^4}dx + \int_{L_T}^{L_s} \frac{\left(x-\frac{a_p}{2}\right)^2}{D_s^4}dx\right) \tag{3.21}$$

$$U_r = \frac{32F_r^2}{\pi E}\left(\int_0^{L_c} \frac{\left(x-\frac{a_p}{2}\right)^2}{\left(D_{eq}\right)_{rc}^4}dx + \int_{L_c}^{L_T} \frac{\left(x-\frac{a_p}{2}\right)^2}{\left(D_{eq}+2x\tan(\gamma)\right)^4}dx + \int_{L_T}^{L_s} \frac{\left(x-\frac{a_p}{2}\right)^2}{D_s^4}dx\right) \tag{3.22}$$

After integration and applying equation 3.9 we have:

$$\delta_t = \frac{64F_t}{\pi E}\left[Q_1 + Q_2 - Q_3\right] \tag{3.23}$$

where

$$Q_1 = \left(\frac{3(\frac{a_p}{2})^2 L_c - 3(\frac{a_p}{2})L_c^2 + L_c^3}{3\left(D_{eq}\right)_{tc}^4}\right)$$

$$Q_2 = \left(\frac{3(\frac{a_p}{2})^2 (L_s - L_T) - 3(\frac{a_p}{2})\left(L_s^2 - L_T^2\right) + \left(L_s^3 - L_T^3\right)}{3D_s^4}\right)$$

$$Q_3 = \frac{A - B\left(6\tan(\gamma)(L_T - L_c) + D_{eq}\right) + H\left(L_T^2 - L_c^2\right) + 6\tan(\gamma) D_{eq}(L_T - L_c) + D_{eq}^2}{16\tan^3(\gamma)\left(2\tan(\gamma) + D_{eq}\right)^3}$$

$$A = a_p^2\tan^2(\gamma) \quad , \quad B = a_p\tan(\gamma) \quad \text{and} \quad H = 12\tan^2(\gamma)$$

δ_r can be determined in a similar way by replacing F_t with F_r and $\left(D_{eq}\right)_{tc}$ with $\left(D_{eq}\right)_{rc}$. Having determined δ_t and δ_r, total deflection can be determined as:

$$\delta_{total} = \sqrt{\delta_t^2 + \delta_r^2} \tag{3.24}$$

In order to test the developed analytical model, a comparison has been made between finite element simulations of COMSOL Multiphysics and developed analytical

model for different radial and tangential forces. Figure 3.43 illustrates the comparison results. As it can be seen in Figure 3.43, the developed analytical model is capable of modeling cutting tool deflections with a results very close to the finite element simulations.

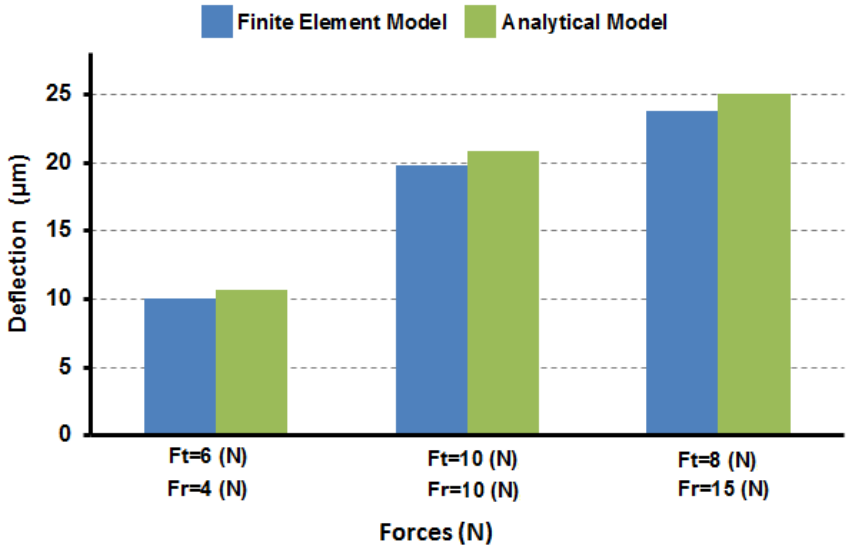

Figure 3.43: Comparison between finite element and analytical tool deflection models.

3.4.9 Tool Life

Tool life is an important in terms of process parameters selection, as it directly affects the economics of the process. Table 3.5 represents the experimental conditions (Taguchi-L9) used to investigate tool life of the micro end mill. Four parameters; cutting speed (N), feed per tooth (f), axial depth of cut (ap), and radial immersion (ae) are considered as process variables each with three levels. In addition, machining time per pocket and number of pockets machined with each tool are also given in Table 3.5.

After machining each pocket, micro end mills are investigated using digital microscope and the flank wear length and decrease in tool diameter values was measured. A flank wear limit of 30 µm and tool diameter reduction limit of 10% is used. Figure

Table 3.5: Experimental set for investigating tool life

Exp. #	N (RPM)	ft (µm)	a_p (µm)	ae (%D)	Time per Pocket (sec)	# of Pockets
S1	15000	2	80	40	228	9
S2		4	160	60	79	12
S3		6	320	80	41	15
S4	25000	2	160	80	74	5
S5		4	320	40	68	7
S6		6	80	60	31	14
S7	35000	2	320	60	68	7
S8		4	80	80	26	12
S9		6	160	40	32	10

3.44 shows the variation of tool life with respect to experimental cases shown in Table 3.5.

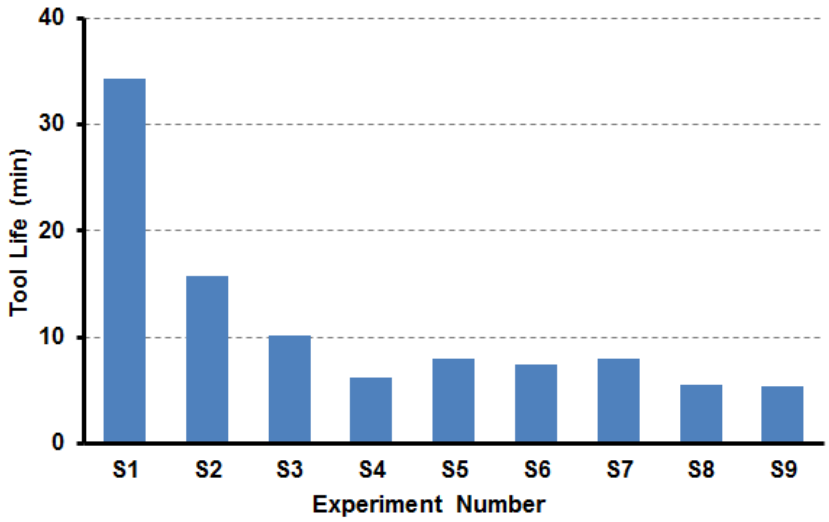

Figure 3.44: Tool life variation with experiments.

Due to limited recourses, only a single replicate of the experimental design given in Table 3.5 was conducted. Based on the results given in Figure 3.44, the influence of cutting speed on the tool life can be clearly seen. In a recent study [122], it is shown that cutting speed is the main factor influencing the tool life followed by feed per tooth and depth of cut. Additional experimental study is required to reveal the

relative importance of feed per tooth, axial depth of cut and radial immersion on the tool life.

3.5 Micromilling Experiments on Ti6Al4V

Application of light weight and energy saving materials plays a significant role in different industries including automotive and aerospace industry. With the emergences of micro-mechanical machining processes and discovering its suitability and capabilities of processing materials other than silicon for the fabrication of miniaturized components for micro-electro-mechanical systems (MEMS), micromachining of titanium alloys is gained an importance because of their excellent chemical and mechanical properties such as high strength to wait ratio (high specific strength), high corrosion resistance and etc. [140].

Understanding the process of micromachining of titanium alloys can be helpful in making this alloy a candidate structural material for the fabrication of micro-components. Since among different titanium alloys, Ti6Al4V is the most commonly used titanium alloy in the market, it has been selected for the micromachining experiments in this study. It belongs to the ($\alpha + \beta$) titanium alloys which contains both α stabilizers (Al, O, N, C and Ga) and β stabilizers (Mo, V, Cr, Mn, Ni, Fe and etc.).

There are several challenges associated with the machining of titanium. It is considered as a difficult-to-cut material because of several inherent properties. It has the tendency to weld to the cutting tool due to its high chemical affinity [140]. The low thermal conductivity of the titanium will result in increased tool/workpiece interface temperature due to low heat dissipation, which has an adverse effect on tool life. Additionally, the ability of maintaining its strength at elevated temperatures and its low Young's modulus further reduces its machinability [141]. High chemical affinity of titanium can be attributed to its two unpaired 'd' electrons, which are responsible for the increased surface energy of the titanium, which in turn facilitates the adhesion of the titanium to the cutting tool surface [142]. Taking into account the aforementioned difficulties associated with the machining of titanium, the aim of this section is to further

characterize its machinability in micro-scale using conventional micro end mills. Machining forces, surface quality of the machined part and tool condition after machining were analyzed to have an insight into the nature of micro-scale machining of titanium.

3.5.1 Experimental Setup for Micromilling Experiments on Ti6Al4V

A same experimental setup used in slot micromilling of Stavax (Figure 3.21) is used for micromilling tests on Ti6Al4V. Similar to any rotating mechanical system, there is a rotational imbalance in the cutting tool-spindle system which is reflected in the tool tip. In order to have an insight into the quality of the high speed spindle in terms of tool runout, a measuring setup is prepared as illustrated in Figure 3.45. After the spindle is mounted on the DMG vertical milling center, a precisely ground 4 mm diameter tungsten carbide rod is mounted on the spindle with a collet type tool holder. Tool runout is measured using Mahr Federal Electronic lever type gauge (EHE 2056) with a sapphire ball tip of 1.6 mm, connected to a Mahr Millimar C 1208 display with linearity of 0.1% over full range of ±0.250 mm with a resolution of 0.1 μm.

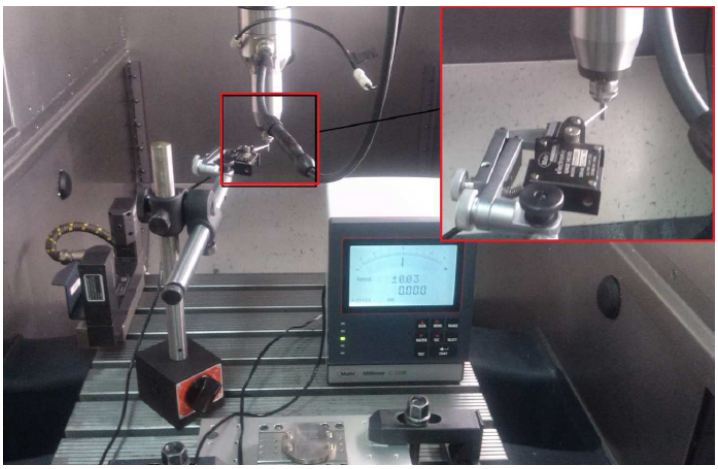

Figure 3.45: Experimental setup for runout measurements.

For this purpose, the probe of the indicator is brought into contact to tungsten carbide rod, and this point is accepted as the reference zero point for measurement at a

certain length from the starting point of clamping. The rod is rotated manually by 30° angular increments, which are already marked on the tool. At each increment the deviation from the reference value is recorded. The maximum deviation with respect to the reference point is specified as tool runout. This process was repeated at various axial levels (Z axis) of the rod and the measurements were performed. Figure 3.46 illustrates the measured values at a distances of 5 mm and 15 mm from clamping point. As it can be seen in Figure 3.46 the measured deviations from the reference were less than 1 μm over a length of 15 mm.

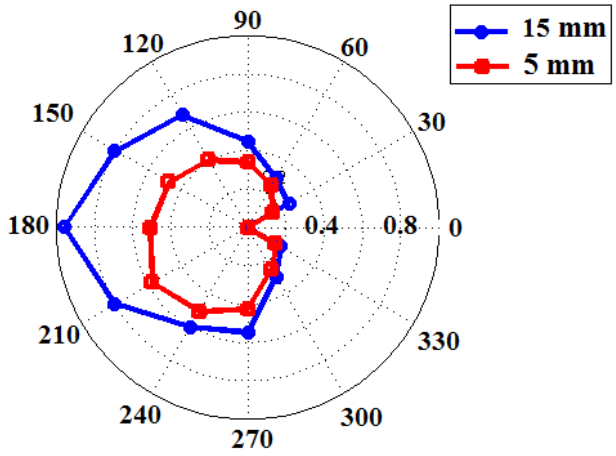

Figure 3.46: Measured spindle runout.

3.5.2 Experimental Micromilling Tests on Ti6Al4V

Slot micromilling tests with 0.4 mm diameter end mill (NS Tools-MSE230-double flute, 0.4 mm length of cut, 30° helix angle, 9° neck taper angle) on titanium alloy Ti6Al4V were conducted. Figure 3.47(a) shows the scanning electron microscope image of the cutting edge of 0.4 mm diameter micro end mill. The measured cutting edge radius by laser scanning microscope is shown in Figure 3.47 (b). The micro end mill has a radius around 2 μm. In order to eliminate the effect of tool wear on the experiments, up-sharp tool is used in each cutting experiment.

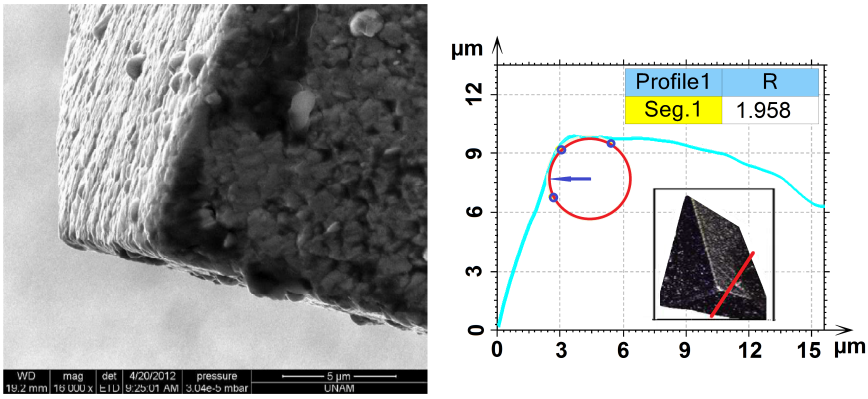

(a) (b)

Figure 3.47: (a) Scanning electron microscope image of the tool, (b) Edge radius measurement using laser scanning microscope.

Table 3.6: Experimental conditions for micromilling of Ti6Al4V

Experimental Set	Depth of Cut (µm)	Feed per Tooth (µ/tooth)
1	40	0.4, 0.8, 1.2, 2, 3 and 4
2	80	1.5, 2, 3, 4, 6 and 10

Two different experimental sets are considered, where depth of cut was considered as the variable at two different levels as shown in Table 3.6. The cutting speed was set constant and feed per tooth values were varied from less than the edge radius up to 3-5 times the edge radius. Cutting speed is selected as 32.6 m/min (26000 RPM). It is an acceptable cutting speed for titanium alloy machining, which is also selected considering tooth passing frequency and bandwidth of the dynamometer which has a natural frequency around 1800 Hz. Axial depth of cut is selected as 20% (80 µm) and 10% (40 µm) of the nominal tool diameter.

3.5.3 Investigation of the Micromilling Forces

Unfiltered Micromilling forces for a depth of cut of 40 µm at different feed per tooth values are shown in Figure 3.48. One important use of experimental cutting force data

is to develop predictive mechanistic forces models. These models are based on conducting machining experiments at various levels of chip load and calculating specific machining energies. The slope of the cutting force and the intercept can be calculated and named as cutting and edge coefficients. This representation is generally viable for cutting conditions where large uncut chip thicknesses are machined. However, for micromachining operations, where the edge radius of the cutting tool and the uncut chip thickness are in the same order of magnitude; the relationship between cutting force and uncut chip thickness start deviating from the linear trend depending on the cutting conditions, work material, and tool edge radius. As a result, the uncertainty increases as the uncut chip thickness decreases.

Figure 3.49 explains the relationship between forces and scale of machining. In micromachining region, where small uncut chip thickness values exist, ploughing is known to be the dominant cutting mechanism. Therefore a nonlinear relationship is expected to be seen in a region where ploughing is the dominant material removal mechanism.

In the first set of experiments low feed rates are selected to further investigate the nature of cutting forces for chip loads smaller than cutting edge radius. The experimental average cutting forces in X, Y and Z direction are shown in Figure 3.50. It can be seen that, below cutting edge radius which is measured to be around 2 μm, the average cutting forces show completely nonlinear behavior. As feed per tooth value increases the relation between average cutting forces and uncut thickness becomes almost linear. Although in the first set of experiments, a low depth of cut value of 40 μm is used, however there exist large forces in Z direction. This can mainly be attributed to the elastic recovery of Ti6Al4V together with material accumulation and clogging due to improper cutting conditions.

In addition to average cutting forces, the peak-to-valley forces are also calculated. The variation of peak-to-valley forces as a function of feed rate are shown in Figure 3.51.

Peak to valley forces not only affected by the mechanism of material removal, but also they are influenced by tool runout. It can be seen in this Figure 3.51 that at low

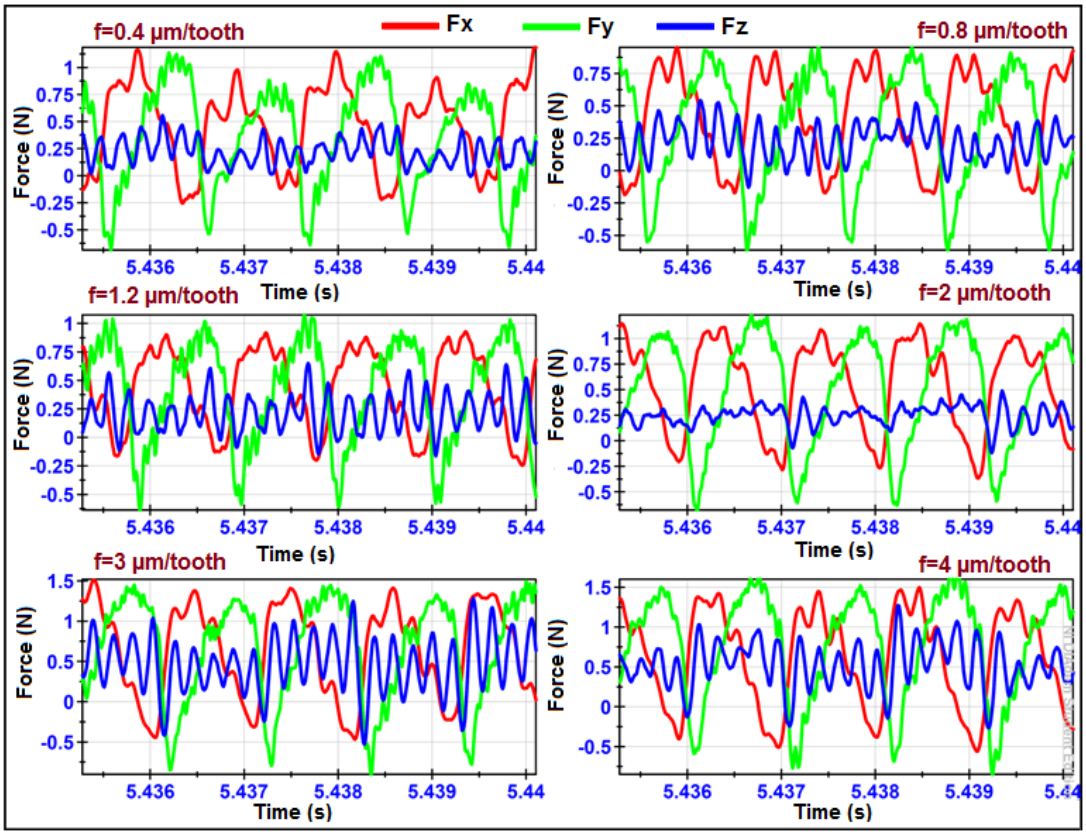

Figure 3.48: Measured micromilling forces for the micromilling case with 0.4 mm diameter at 40 µm depth of cut.

feed per tooth values peak-to-valley forces are highly influenced by runout and they show a nonlinear behavior. As feed per tooth increases the forces start to show a linear trend. Another important consideration is the differences between peak forces corresponding to each teeth especially at low feed per tooth values where the runout issue is more pronounced. Figure 3.52 shows the statistical distribution of peak forces in X and Y directions during milling operation.

It can be seen in Figure 3.52 that at low feed values (0.4 and 0.8 µm/tooth), two distinct peak forces were observed. As feed value increases, the double peak combines into a single peak since the magnitude of runout compared to feed per tooth becomes lower.

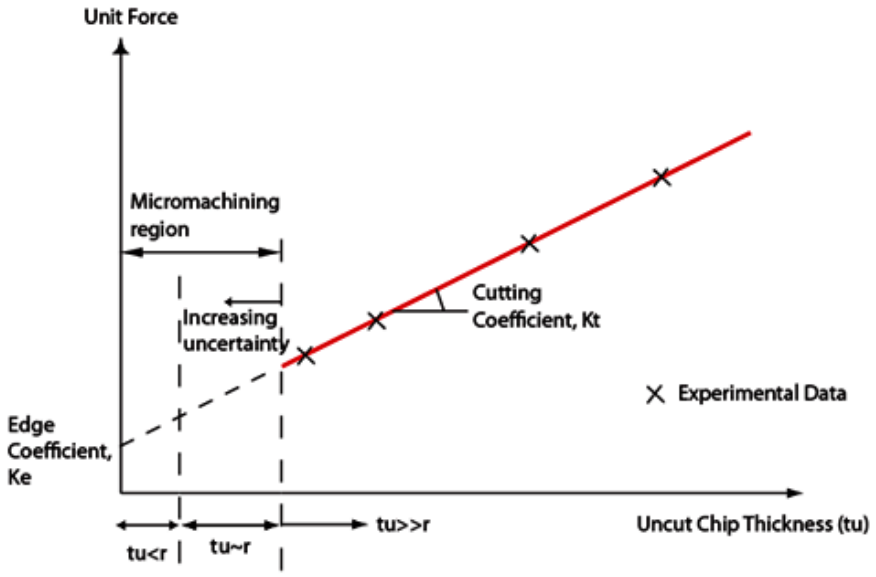

Figure 3.49: The relationship between uncut chip thickness and cutting forces.

A similar analyses are also performed for the second set of experiments where the depth of cut increased to 20% of the tool diameter. In these experiments feed values are also increased to cover a wider range of feed values compare to the first set of experiments. Figure 3.53 shows the measured micromilling forces for the second experimental set, where unfiltered force measurements in X, Y, and Z directions are shown.

Figure 3.54 shows the statistical distribution of peak forces in X and Y directions during milling operation. It can be seen that, at low feed values, two distinct peaks exist. As feed value increases, the double peak combines into a single peak since the magnitude of runout compared to feed per tooth becomes lower. The situation is very similar to the results observed for the first set of experiments, which are done at a low axial depth of cut value of 40 μm.

Figure 3.55 shows the variation of peak-to-valley forces as a function of feed rate. It can be seen that, peak to valley forces increase as feed per tooth value increases. The magnitude of forces in X and Y directions are close. While a linear trend between 3-10

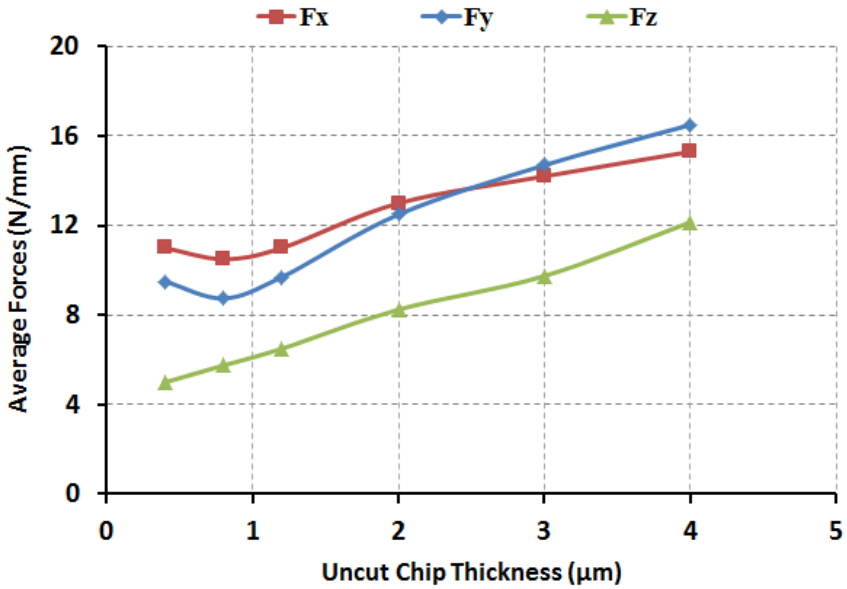

Figure 3.50: Average forces for different uncut chip thicknesses.

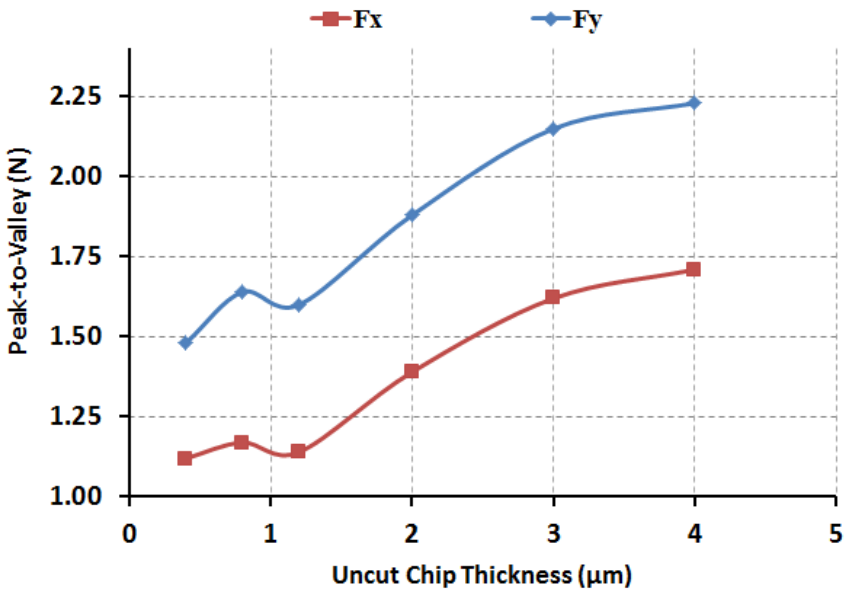

Figure 3.51: The relationship between uncut chip thickness and peak-to-valley of first set of micromilling experiments.

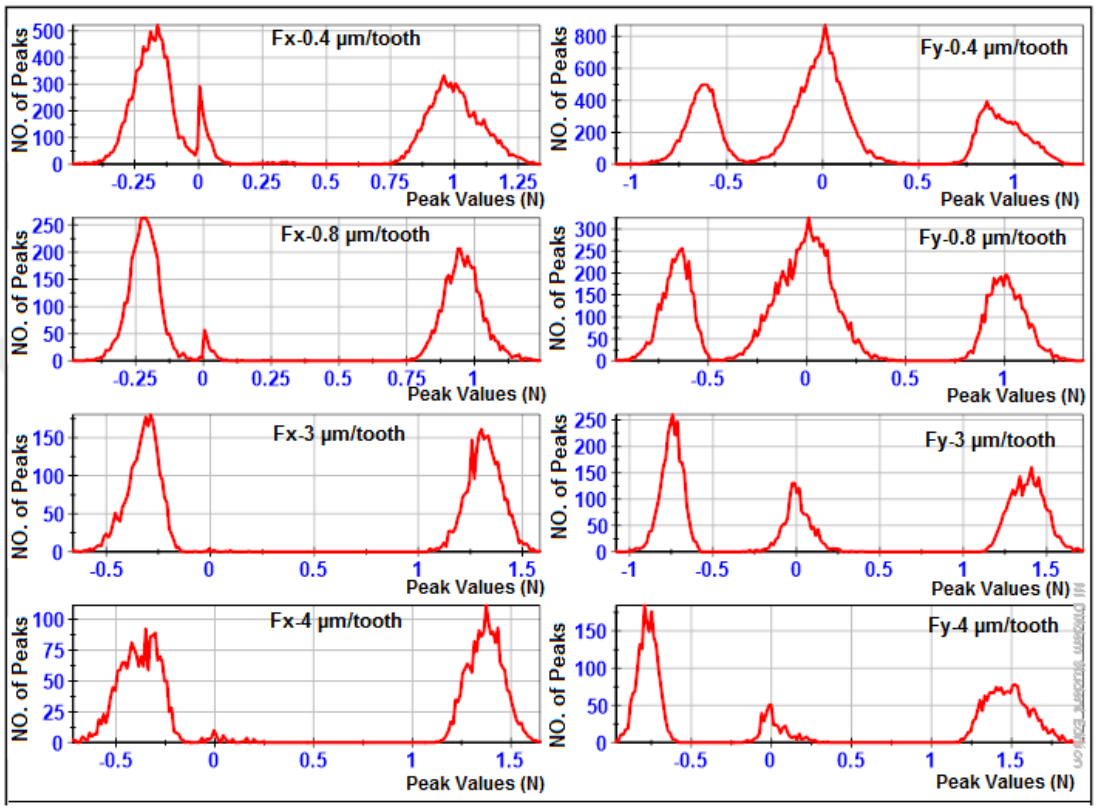

Figure 3.52: Statistical distribution of peak forces at a depth of cut of 40 µm.

µm exist, a deviation from the linear trend at low feed per tooth values can be seen. Another important consideration is the differences between peak forces corresponding to each tooth especially at low feed per tooth values where the runout issue is more significant. Figure 3.56 shows the variation of peak force ratios as a function of feed which decreases steadily as feed per tooth value increases.

3.5.4 Investigation of Micro End Mills after Micromilling Tests

Figure 3.57 shows the image of the micro end mill after second set of experiments. It can clearly be seen that the edges of the same tool do not have same conditions. One edge is covered with built-up edge, and the other one experienced edge rounding and flank wear. This uneven tool wear, is due to tool runout, which changes the chip

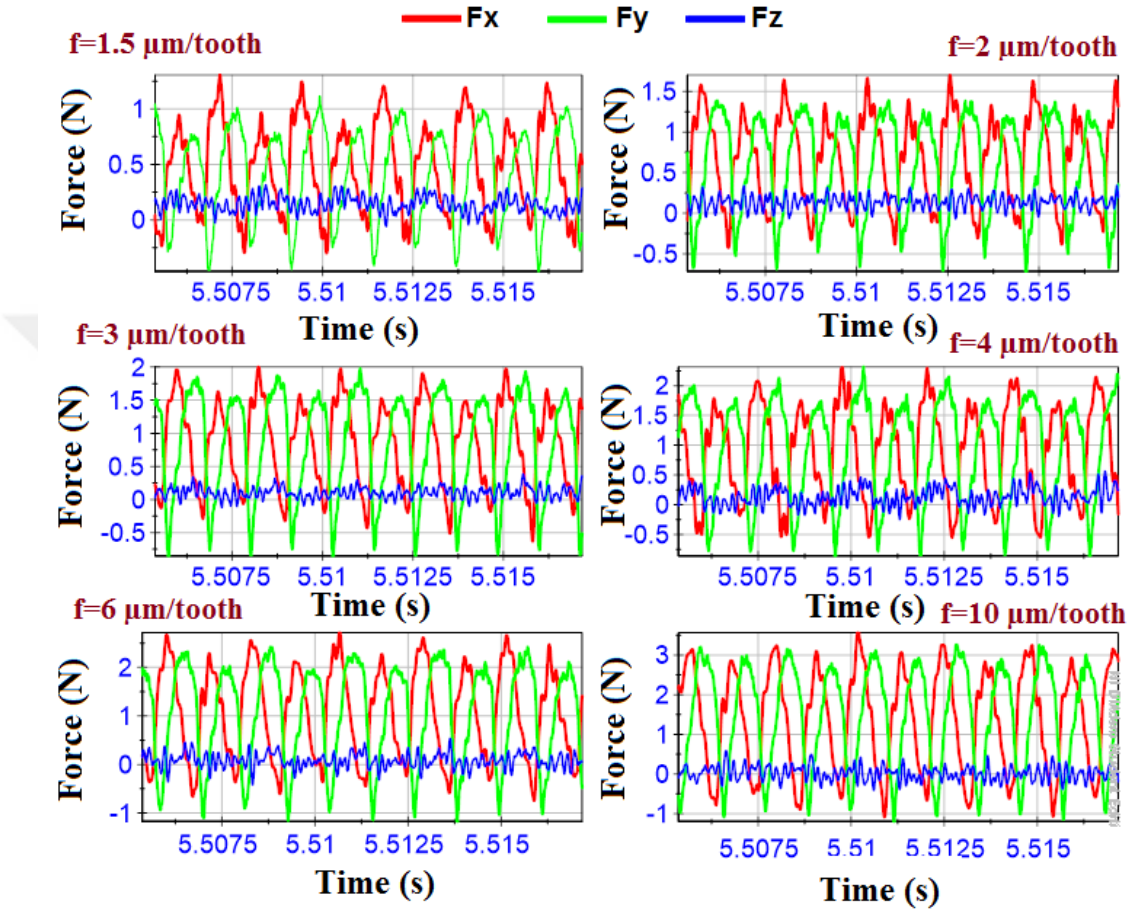

Figure 3.53: Measured micromilling forces for the micromilling case with 0.4 mm diameter at 80 µm depth of cut.

load experienced by each cutting edge. The uneven wear of cutting edges, further decreases tool life during micromachining. An important phenomenon which should be emphasized is BUE formation. It can be seen that the edge with BUE experienced little wear compare to the edge without BUE.

Since both cutting edges belong to a same cutter, the only difference in their operating conditions is the chip load variation due to tool runout and the edge condition after break-in period. These observations reveals that, it is necessary to further explore how micro end mill interacts with workpiece at micro-scale, and under which machining and tool condition there is a possibility of stable BUE formation. Also the possibility

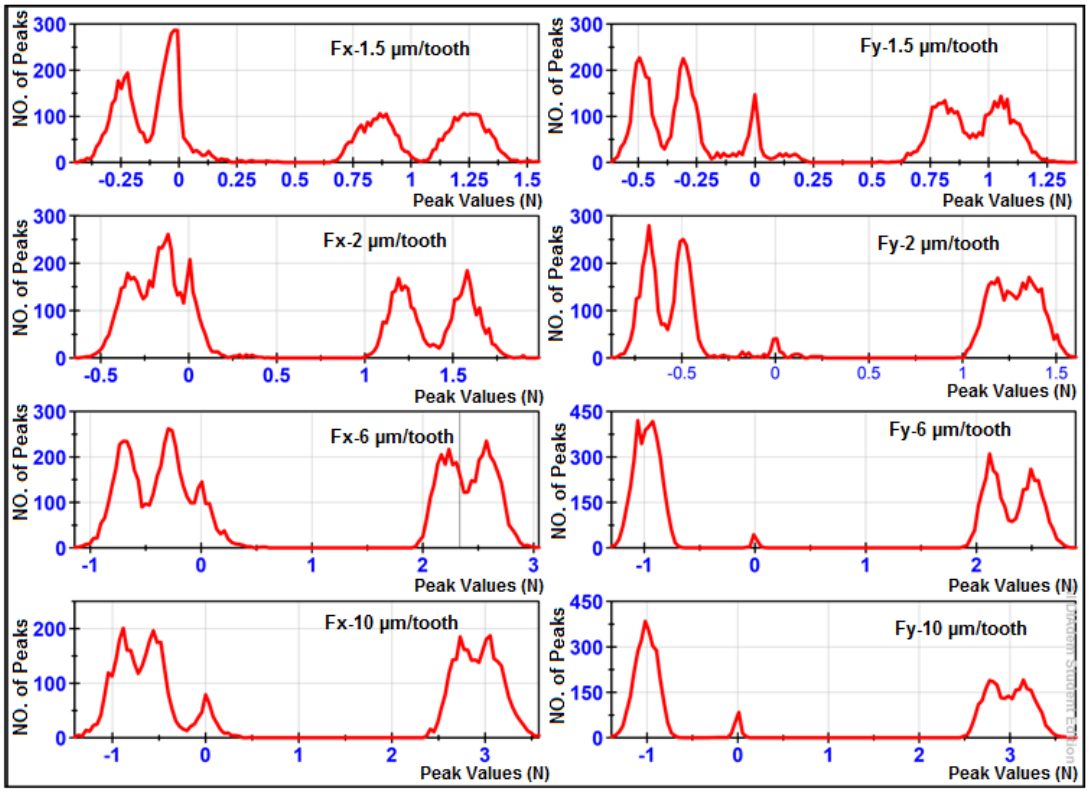

Figure 3.54: Statistical distribution of peak forces for the second set of experiments.

of protective effect of BUE during micromilling of Ti6Al4V needs to be further explored. It should be mentioned that, BUE has also been observed when using micro end mills with different diameters. Figure 3.58 illustrates the BUE formed when using three different micro end mills with diameters of 0.2, 0.4 and 0.6 mm. BUE has formed on all micro end mills independent from their sizes.

Conclusion

The process of micromilling of two difficult-to-cut ductile materials (Stavax ESR stainless steel and titanium alloy Ti6Al4V) which are widely used in micro part fabrication are studied to understand the mechanism of cutting in micro-scale, effect of micromilling process parameters on the outputs of the process and to understand the

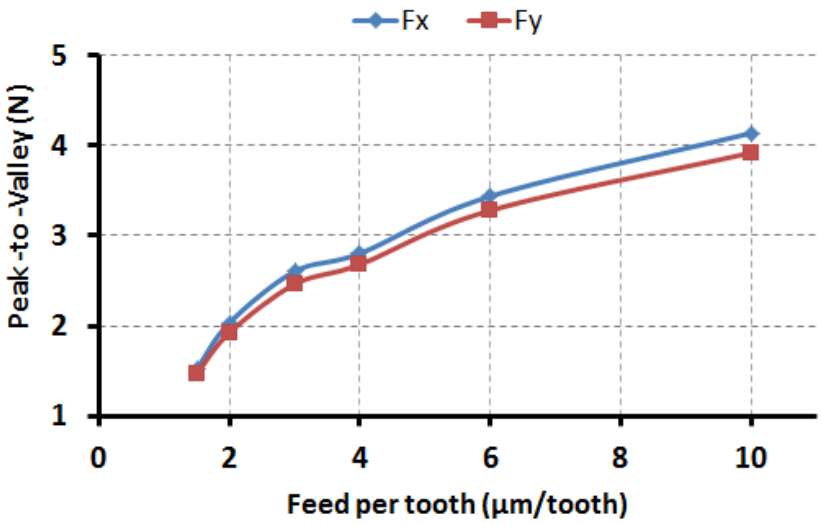

Figure 3.55: Peak-to-valley forces for the micromilling case with 0.4 mm diameter at 80 µm depth of cut.

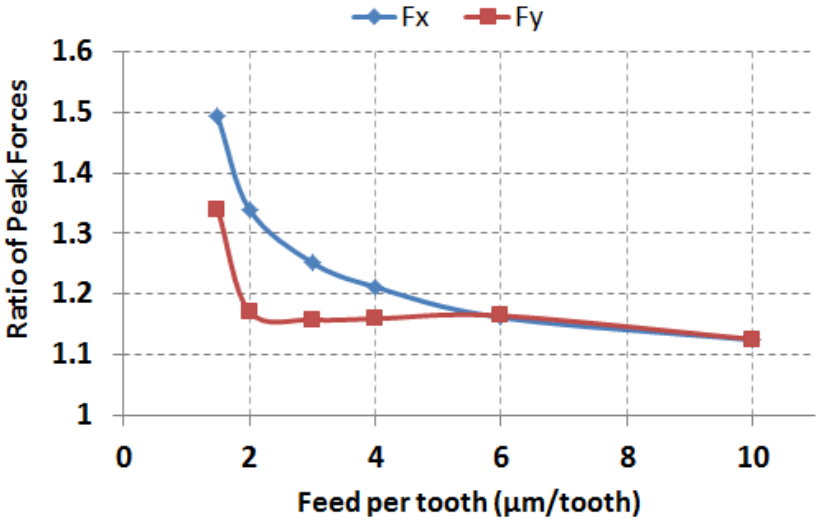

Figure 3.56: Ratio of peak forces as a function of feed rate.

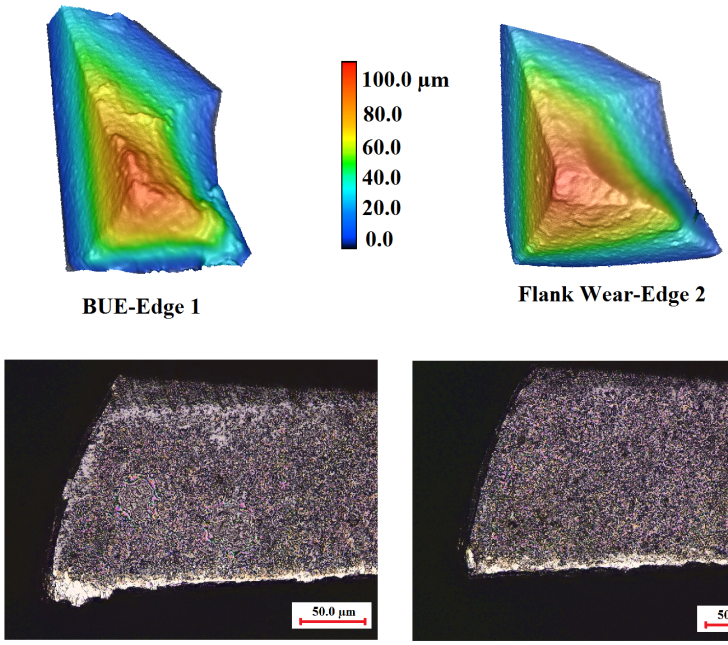

Figure 3.57: Edge condition after micromilling.

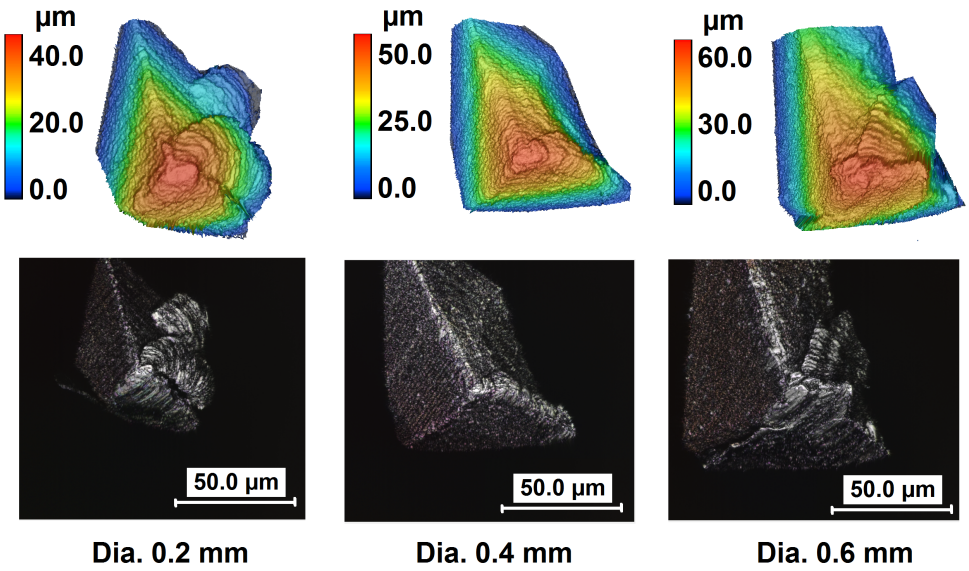

Figure 3.58: Edge condition after micromilling of Ti6Al4V using tools of different diameters.

challenges of micromilling of difficult-to-cut materials.

The study of Stavax ESR stainless steel are mainly focused on the influence of tool wear on micromilling forces, surface roughness, and tool deflections. The influence of micromilling conditions on the tool wear and the influence of tool wear on micromilling forces have been investigated using experimental, analytical and computational techniques. The tool wear and micromilling forces are used in the finite element simulation of the micro end mill as inputs to analyze the tool deflections and breakage. The developed model is shown to produce results matching the experimental observations. The main findings are summarized as follows:

- The influence of process parameters is investigated and suitable process parameters for circular pocketing operation of Stavax stainless steel are identified.
- Experimental results show the influence of plunging method on tool wear, which in turn affects micromilling forces and surface quality. The positive impact of using pre-drilled hole is also demonstrated.
- The relationship between radial immersion and feed per tooth is shown to affect tool wear and surface quality of the machined parts. Areal surface roughness measurements revealed that low radial immersion values yields lower surface roughnesses compare to the high radial immersions.
- Radial immersion and feed per tooth values must be selected in conjunction during the process planning stage of pocket micromilling. In our experiments, 60 % radial immersion yielded better tool performance compared to lower and higher radial immersion values.
- During circular pocket micromilling operation, tool wear is observed to evolve as edge rounding and flank wear increase. Relative tool diameter reduction, which is directly related to edge rounding of the tools, is considered as a measure of tool wear, which is relatively easy to monitor during the micromilling process.
- A proper selection of feed per tooth and radial immersion leads to a balanced edge rounding and flank wear development. In this wear case, feed per tooth may be increased in order to be able to conduct machining effectively as tool

wear progresses. However, it has been shown that the increase in feed rate is limited by the allowable tool deflections and stresses.

- Finite element models has been successfully used for the prediction of machining induced tool deflection and stresses.
- An analytical model is developed to calculate the deflection of conventional micro end mills.

Micromilling experiments on Ti6Al4V revealed that:

- Tool runout results in an uneven tool wear and largely affects the cutting forces in micromilling process, specially at low feed per tooth values.
- Statistical distribution of peak forces are used to identify the effect of tool runout on micromilling forces. At low feed values, two distinct peak forces were observed, as feed value increased, the double peak combined into a single peak since the magnitude of tool runout becomes lower compared to feed per tooth value.
- A nonlinear relationship between cutting forces and uncut chip thickness has been observed at uncut chip thickness values smaller than cutting edge radius, which indicates a ploughing dominant cutting process.
- Built-up edge formation has been observed when machining titanium alloy Ti6Al4V, using cutting tools of different diameters and different cutting conditions, which affects the process mechanics of micromilling through changing of the way cutting tool interacts with the workpiece material.

In summary, tool runout is identified as a problematic issue in micromilling processes, which highly affects machining forces and tool life. To diminish the effect of tool runout, higher feed rates can be used, however the allowable tool deflections and stresses should be taken into account to avoid tool failure and out of tolerance micro-machined components. BUE formation is observed to be the characteristics of micromilling of titanium alloy Ti6Al4V, which requires to be studied in detail to

understand its formation mechanism and its effect on tool life, surface quality and dimensional accuracy of the machined parts.

Chapter 4

An Investigation of BUE Formation in Micro-cutting of Ti6Al4V

4.1 Introduction

Mechanical micromachining is defined as the machining of precision parts made out of a wide range of engineering materials with complex surfaces [30]. One important material which shows a high potential for micro-part fabrication is Ti6Al4V. It is among the most commonly used materials for biomedical and aerospace industry, which accounts for about 50-60% of the total titanium alloy production [143, 144].

In 1955, Siekmann[145] mentioned that machining of titanium alloys would always be a problem independent of chip removal process. Even with the very many sophisticated developments in the cutting tool industry, this fact still remains true, and titanium alloys remain as difficult-to-machine materials [146, 147].

An important phenomenon which has been observed in micromilling experiments on Ti6Al4V was built-up edge formation. BUE has been studied in conventional machining processes, however to the best of my knowledge, there is very limited information regarding BUE formation in micro-scale cutting. In conventional machining BUE

is known to be a commonly observed phenomenon which appears during continuous chip formation. It is known to affect surface roughness and tool wear. However, the effect of BUE on the process outputs of micro-scale cutting requires special attention, and its effects in micro-scale cutting needs to be carefully explored. A solid understanding of the mechanics of cutting at micro-scale with the presence of BUE seems to be a crucial step in building predictive models and controlling the quality of micro parts made of Ti6Al4V.

A BUE consists of material layers which are deposited onto the tool surface, changing the tool geometry and, hence, the mechanics of the process. A stable and thin BUE is known to protect the cutting edge [148]. Small uncut chip thicknesses machined with tools having a comparable edge radius creates suitable conditions for BUE formation in micro-scale machining. Gaining a better understanding of the influence of BUE on process outputs have resulted in an increased interest in machining research.

Due to the micro cutting tool fabrication process and tool material grain size limitations, the edge radius cannot be easily decreased without sacrificing the strength of the tool, which in turn affects the chip formation process and the surface quality of the machined workpiece. Weule et al. [108] showed the importance of edge roundness when tungsten carbide micro end mills are used to machine ferrous materials. Woon et al. [149] studied the interaction between uncut chip thickness and edge radius using experimental and finite element based techniques when micromachining AISI 1045. They showed that the edge radius acts like a negative rake angle and found that a constant stagnation point on the tool exists for a large range of uncut chip thickness values. However, in an earlier study, Waldorf et al. [150], studied ploughing models during orthogonal cutting and found that a stable built-up edge model described experimental observations better than a stagnation point model.

Fang and Dewhurst [151] used slip line field analysis to predict the size of the built-up edge during machining. Karpat and Özel [152] also presented a slip line field based approach for machining with round edged tools, including built-up edge. Karpat [80] considered the influence of cutting edge radius including built-up edge during micro-scale machining and studied the effect of fracture on machining outputs. Childs [153]

developed a finite element model to predict built-up edge formation during machining of steel by integrating a damage model. Some preliminary results on simulating built-up edge during micro-scale machining were also presented in [153]. A detailed investigation of how built-up edge influences micro-scale machining is the aim of this section.

In micro-scale machining, the cutting tool edge radius and the amount of material being cut are in the same order of magnitude. There is a value of uncut chip thickness after which continuous chip formation ceases. This critical value is defined as minimum chip thickness, which is known to be a function of the tool material, cutting edge radius, and workpiece material [106]. Lucca et al. [100] and Lucca et al. [95] indicated the importance of sliding and ploughing at tool/workpiece interface due to edge radius of the tool during ultra precision machining conditions. Kim et al. [135] analyzed the periodicity of forces during micromilling and identified the transition between non-cutting and cutting regimes near the minimum chip thickness value. They concluded that the periodicity of cutting forces is affected by the minimum chip thickness, feed per tooth, and cutting position angle. They observed a local maximum in the thrust forces that takes place around minimum chip thickness value. Jun et al. [154] investigated the dynamics of micro end milling and observed peaks in the thrust force around minimum chip thickness during micromachining of ferrite and pearlite. They concluded that the minimum chip thickness effect causes instability at low feed rates. The same phenomenon was observed by Liu et al. [3] and named as feed rate instability.

Son et al. [109] studied minimum uncut chip thickness and its relation to the edge radius during diamond turning of various materials. They developed a relationship between minimum uncut chip thickness, friction angle, and edge radius. Malekian et al. [155] used a minimum energy based method to model minimum uncut chip thickness while machining aluminum alloy. They found the stagnation point to be approximately 23 % of the edge radius, and it is not a constant point but a region on the tool. Cuba Ramos et al. [156] emphasized the importance of built-up edge formation during transition from ploughing to cutting during micro-scale machining of AISI 1045 and developed a new model for the estimation of minimum chip thickness. In this research, minimum uncut chip thickness phenomenon in the presence of BUE

is investigated by focusing on the interaction between BUE and surface roughness.

Due to its high reactivity with cutting tool materials and its low thermal conductivity, titanium alloys are considered difficult-to-cut, so rapid tool wear is an important issue that affects the quality of the machined products. BUE formation during machining of titanium under macro-scale machining conditions has been well studied in the literature. The issues related to BUE and tool wear have been summarized in Ezugwu and Wang [140], Armendia et al. [157] and Pramanik and Littlefair [158]. Thepsonthi and Özel [159] studied micromilling of titanium alloy Ti6Al4V and observed BUE when cutting edge is worn. The wear mechanisms of titanium alloys were shown to be quite different from steels and nickel alloys in Hartung and Kramer [160]. It was shown that tool wear was greatly reduced when adhesion occurs between tool and chip. The adhesion layer prevents sliding at the interface and improves tool life under certain conditions. In a recent study, Kümmel et al. [161] showed that tool wear performance may be improved when cutting tools with intentional built-up edge are employed in machining. Kümmel et al. [162] used laser surface texturing to create different dimple structures and channels on the rake face of the tool. The dimple textures are shown to increase BUE adhesion on the tool. In order to produce a surface containing a morphology composed of dimple like features, electrical discharge machining (EDM) technique is used to prepare the cutting edges. Using EDM process creates micro-scale craters on the surface of the tool, which may also promote BUE adhesion during machining.

In this section, the influence of built-up edge on process forces, surface quality and minimum uncut chip thickness during micromachining of titanium alloy has been investigated in detail. Cutting edges with small edge radii were specifically fabricated and uncut chip thickness values were set to be less than the edge radius to create micro-scale machining conditions. Cutting edges and machined surfaces were investigated after the tests to reveal the influence of built-up edge on process outputs.

4.2 Experimental Procedure

4.2.1 Fabrication of Cutting Edge Micro-geometry

The cutting edge micro-geometry is obtained through μ-WEDM technique. The WEDM technique is advantageous in terms of controlling the micro-geometry of the edge. The feasibility of edge preparation using EDM technique was shown by Yussefian et al. [163]. In this section, the edge geometries of the uncoated carbide tools (DCMW 11 T3 04H13A) with 0° rake angle are modified by using a high precision wire EDM machine (Sodick AP250L). The U and V axes of the wire EDM machine are utilized to obtain necessary clearance (relief) angles on the cutting edges as shown in Figure 4.1. An EDM brass wire of 100 μm was used. The wire EDM machine uses oil as dielectric fluid in order to obtain superior surface quality. Cutting edges with two different clearance angles (7° and 14°) were prepared and the edge radius of each insert was measured. Figure 4.2 shows the profile of a cutting edge before and after edge preparation by WEDM.

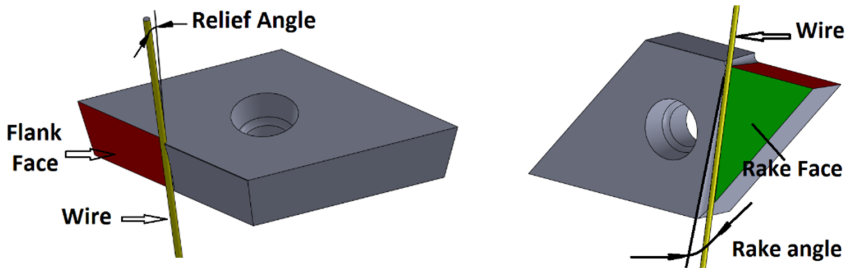

Figure 4.1: Schematic of wire-EDM processing to obtain required rake and clearance angles.

A 3D laser scanning microscope (Keyence VK-X110) was used to measure the edge radius and clearance angle of the inserts. The edge radius after WEDM is measured as 1.95 μm, where the initial edge radius of the insert was 25 μm. A detailed discussion on the influence of edge radius on machining and the uncertainties related to its measurements were described in Denkena and Biermann [164]. Scanning electron microscope image of the tool surface after WEDM is shown in Figure 4.3(a). The

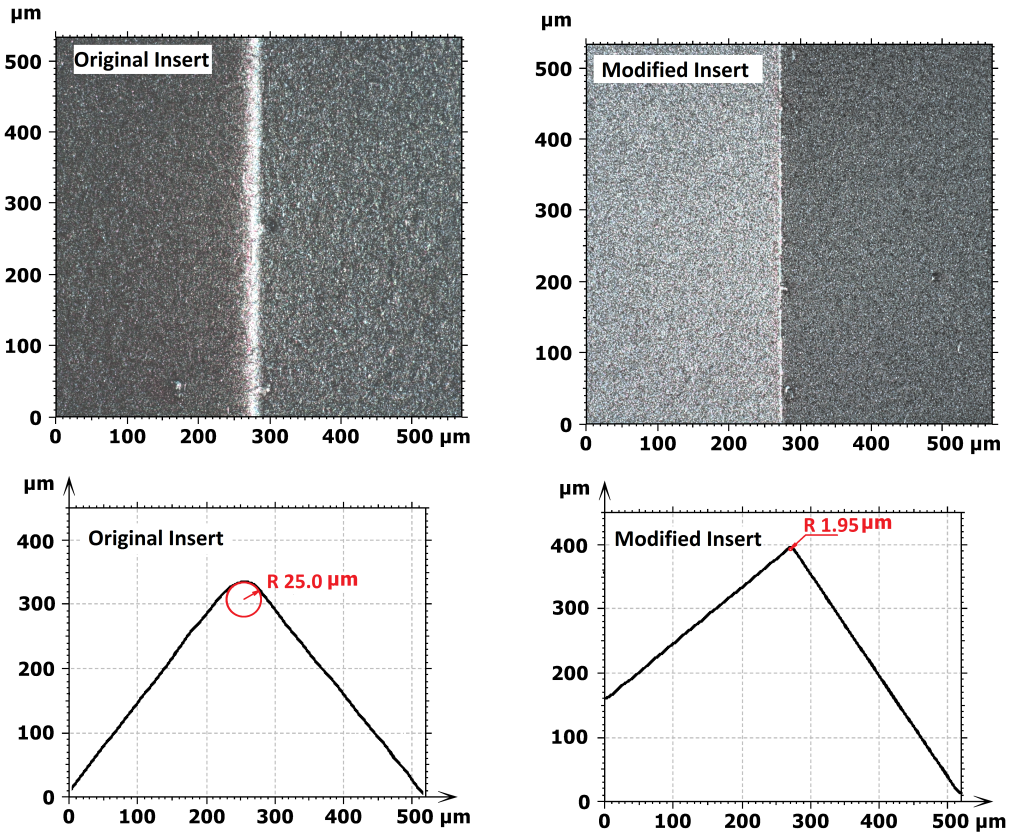

Figure 4.2: Edge radius measurement of the insert, before and after edge preparation.

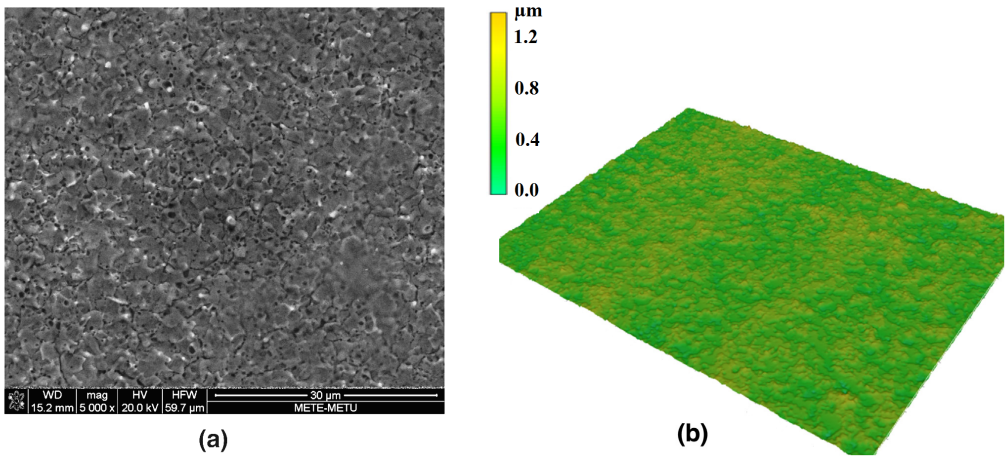

Figure 4.3: Investigation of the tool surface after wire EDM: (a) SEM image, (b) Surface topography of the rake face

surface roughness (Ra) of the insert was measured as 0.11 μm using a laser scanning microscope after WEDM process which is shown in Figure 4.3(b).

4.2.2 Experimental Setup for Orthogonal Micro-cutting Tests

A three-axis hybrid micromachining center (Mikrotools DT110), capable of performing micro turning processes, was used to conduct micro orthogonal cutting experiments. The machine is equipped with a spindle with maximum rotational speed of 3000 rpm. Titanium alloy shafts with 10 mm outer diameter and 0.25−0.35 mm wall thickness were prepared. Only one end of the shaft was machined to be hollow. The depth of hollow side was kept at 3−4 mm. Inserts with engineered edges were placed on a SDACR 1212 K 11S tool holder, which was then attached to the Kistler mini dynamometer (9256C) as shown in Figure 4.4. Micro machining forces were measured and transferred to a PC through a data acquisition card (National Instruments PXI series).

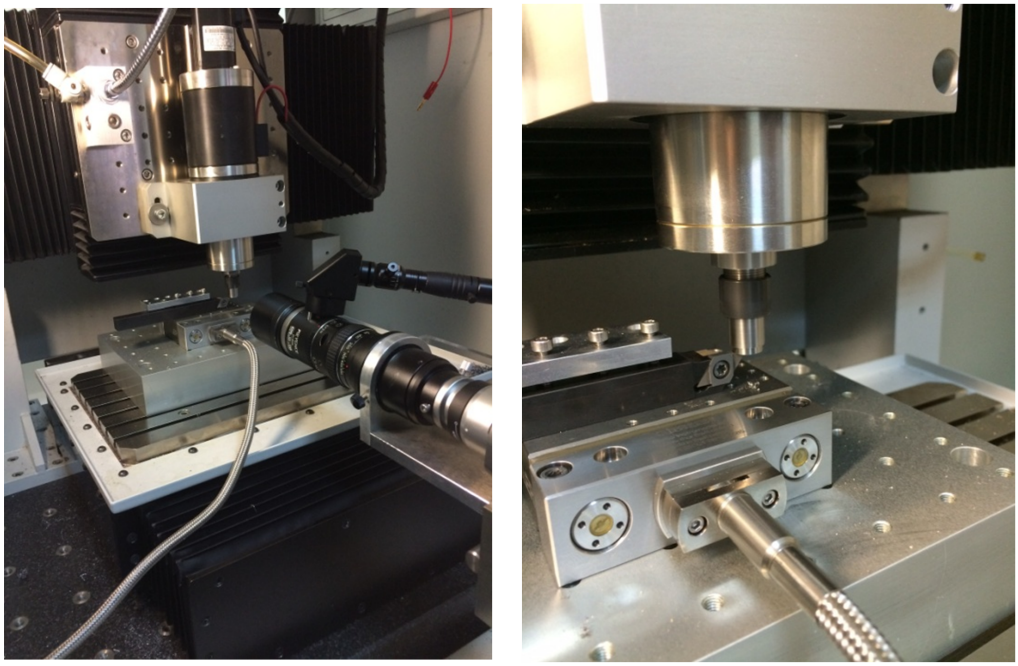

Figure 4.4: The experimental setup used for micro orthogonal cutting tests.

The titanium alloy Ti6Al4V (α+ β) work material with lamellar microstructure (grains of average 25 μm length and 5 μm thickness), which is shown to be suitable for micromachining applications in Attanasio et al. [165], was used in the experiments as depicted in Figure 4.5 (a). It had a hardness of 328 HV. The workpiece was fed towards the cutting tool with necessary feed rate to obtain the required uncut chip thickness during orthogonal tests. The machining time and distance were checked using a high speed microscope to make sure that the desired feed rate was achieved during tests. Figure 4.5 (b) shows a typical continuous chip produced during micromachining experiments.

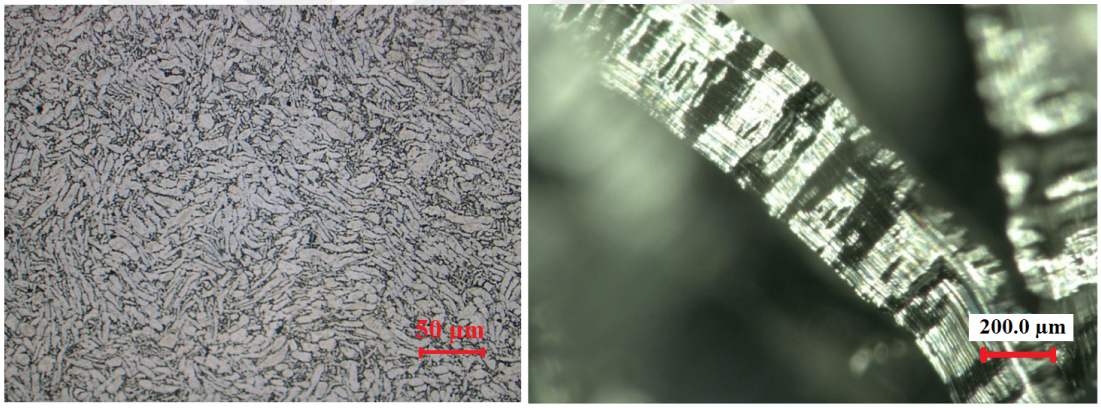

Figure 4.5: (a) Microstructure of Ti6Al4V (b) A typical chip produced during micro turning experiments.

A different cutting edge was used in each test. Cutting tools have clearance angles of 7° and 14°. The reason for using a low clearance angle is to change machining conditions in the cutting zone and observe its influence on the process outputs such as built-up edge formation and surface roughness. A range of cutting speed values was considered, set at 30, 47, 62, and 78 m/min based on practical machining conditions of titanium alloy Ti6Al4V within the limits of the spindle. Uncut chip thickness values were considered as 0.2, 0.4, 0.6, 0.8 and 1 μm, which are all smaller than the edge radius. Experimental conditions are summarized in Table 4.1. The experiments were conducted over 12 s for each cutting condition during force measurement studies.

Table 4.1: Experimental conditions of orthogonal micro-turning tests.

Initial Cutting Edge Radius	Clearance Angle	Uncut Chip Thickness	Cutting Speed
1.95 μm	7°-14°	(0.2-0.4-0.6-0.8-1) μm	(30-47-62-78) m/min

4.2.3 Investigation of BUE after Micromachining Experiments

Experiments were performed at each condition and the cutting edges of the inserts are investigated after each experiment. Figure 4.6 shows the SEM image of the rake face of the cutting edge where the built-up edge formation can be clearly seen. A relatively large BUE length (around 20-100 μm), compared to the uncut chip thickness is observed. Based on these images, the thickness of the BUE is larger at the tip of the tool and gradually decreases on the tool rake face.

Hartung and Kramer [160] observed built-up layer (BUL) and built-up edge (BUE) formation while macro scale machining of titanium alloy Ti6Al4V with different cutting tool materials. They observed that tool wear is considerably reduced at certain conditions as a layer prevents relative sliding at the tool chip interface and limits the diffusion rate of the tool constituents. At high speeds, this protective layer is removed and tool wear increases quickly. The thickness of this layer is determined by the balance between the rate of diffusion of the tool material through it, and the rate of dissolution of the reaction layer in the work material. They observed the absence of cobalt and a layer of TiC was formed on the tool surface which was replenished by the carbon atoms removed from the WC grains below. Similar observations were also made by Ikuta et al. [166], Armendia et al. [157], Gerez et al. [167] and Arrazola et al. [168] under conventional machining cases where elevated temperatures (700-800 °C) exist at the tool chip interface. At micro-scale machining the temperature rise at the tool/chip interface is expected to be lower compared to macro scale machining conditions.

In order to investigate the chemical composition of the tool and BUE, an EDS analysis was performed and the results are shown in Figure 4.7. A scanning electron microscope image of the BUE region can be seen in Figure 4.7(a). Titanium, aluminum, and vanadium elements in the built-up edge region can be clearly identified as shown in

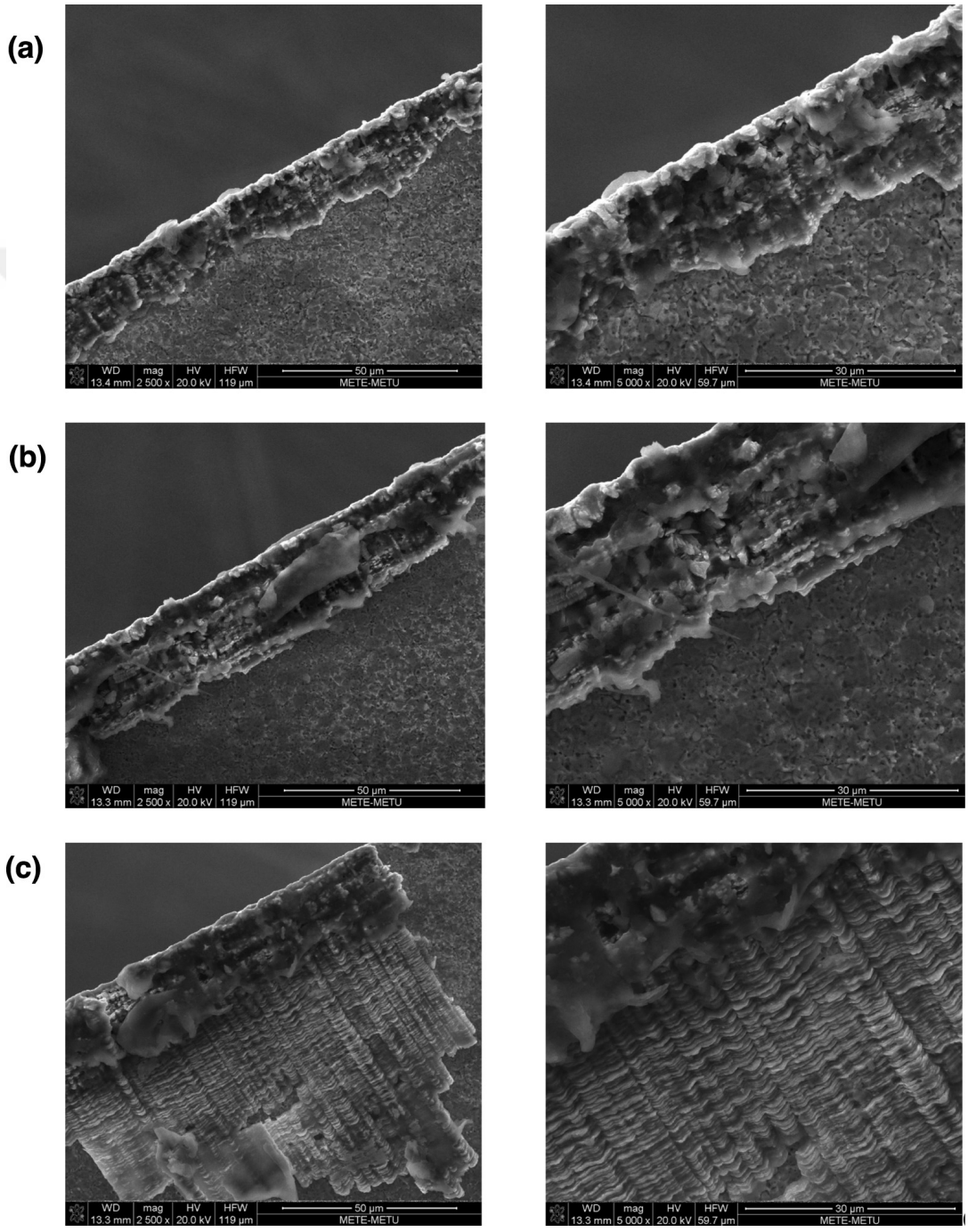

Figure 4.6: SEM images of the cutting edges after machining tests: (a) 0.2 µm, (b) 0.4 µm, (c) 0.6 µm

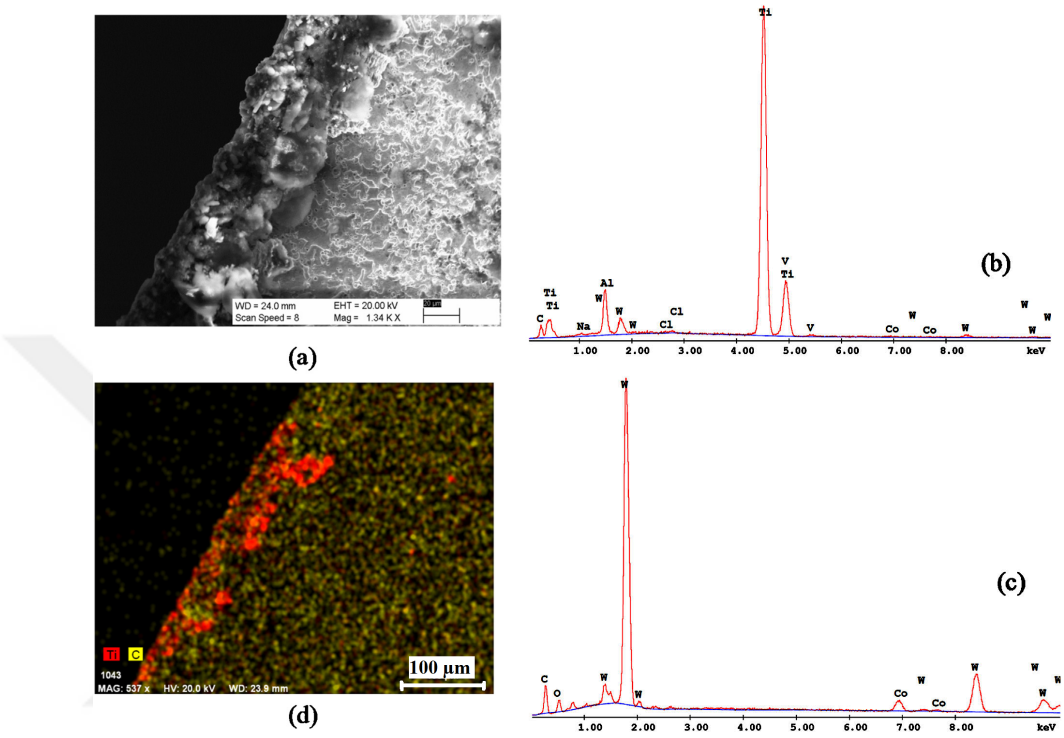

Figure 4.7: (a) Scanning electron microscope image of the BUE region and corresponding EDS map, (b) EDS spectrum analysis of the built-up edge zone on the rake face, (c) EDS spectrum analysis of the tool surface, (d) Color map of the Ti and C elements on the BUE.

Figure 4.7(b) and its detailed chemical composition is given Table 4.2. The EDS analysis of the tool surface before machining is also shown in Figure 4.7(c) and its chemical composition is also given in Table 4.2. A color map of Ti and C elements on the BUE and tool surfaces are shown in Figure 4.7(d). The EDS analysis was performed for all uncut chip thickness values and similar results are observed.

In order to investigate the influence of BUE on the tool/chip interface, the section of the tool under the BUE is also investigated after cleaning it using an ultrasonic process. EDS analysis was repeated on the region where BUE existed. Figure 4.8 shows the EDS spectrum of the tool surface where Co (% 4.65) and W (% 93.95) was detected. The amount of Co is slightly lower compared to the original tool surface (see Table 4.2). This is in accordance with the observations of Hartung and Kramer [160], although the difference is quite low.

Table 4.2: EDS analysis of surface on the tool

Insert surface before machining	Analysis of BUE	Insert surface after cleaning
Co %5.19 W %94.81	Al %5.66 Ti %82.82 V %3.46 Co %0.59 W %7.48	Co %4.65 W %93.95

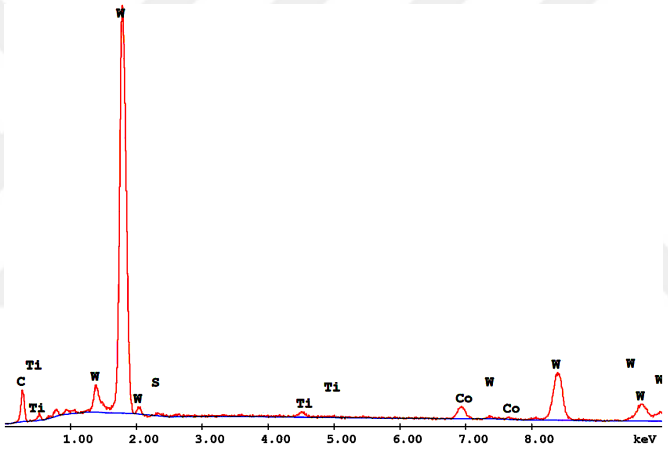

Figure 4.8: EDS analysis of the surface underneath BUE.

Figure 4.9 shows the edge profiles obtained through a laser scanning microscope, where shapes of built-up edge for each cutting case can be seen. Figure 4.10 shows the optical microscope images taken from the flank face of the cutting edges.

Figure 4.11 shows edge profiles of cutting edges where the shape of the built-up edge around the tool tip can be seen. Based on these images, as uncut chip thickness increases, the average tip length of BUE increases (from around 10 µm to 19 µm in Figure 4.10). The length of BUE on the rake face is longer at lower uncut chip thickness. No significant difference in terms of BUE size was observed due to different clearance angles.

Figure 4.12(a) shows the edge profile of the tool after 12 s of continuous machining after cleaning of the BUE. No sign of crater and flank wear was observed, confirming

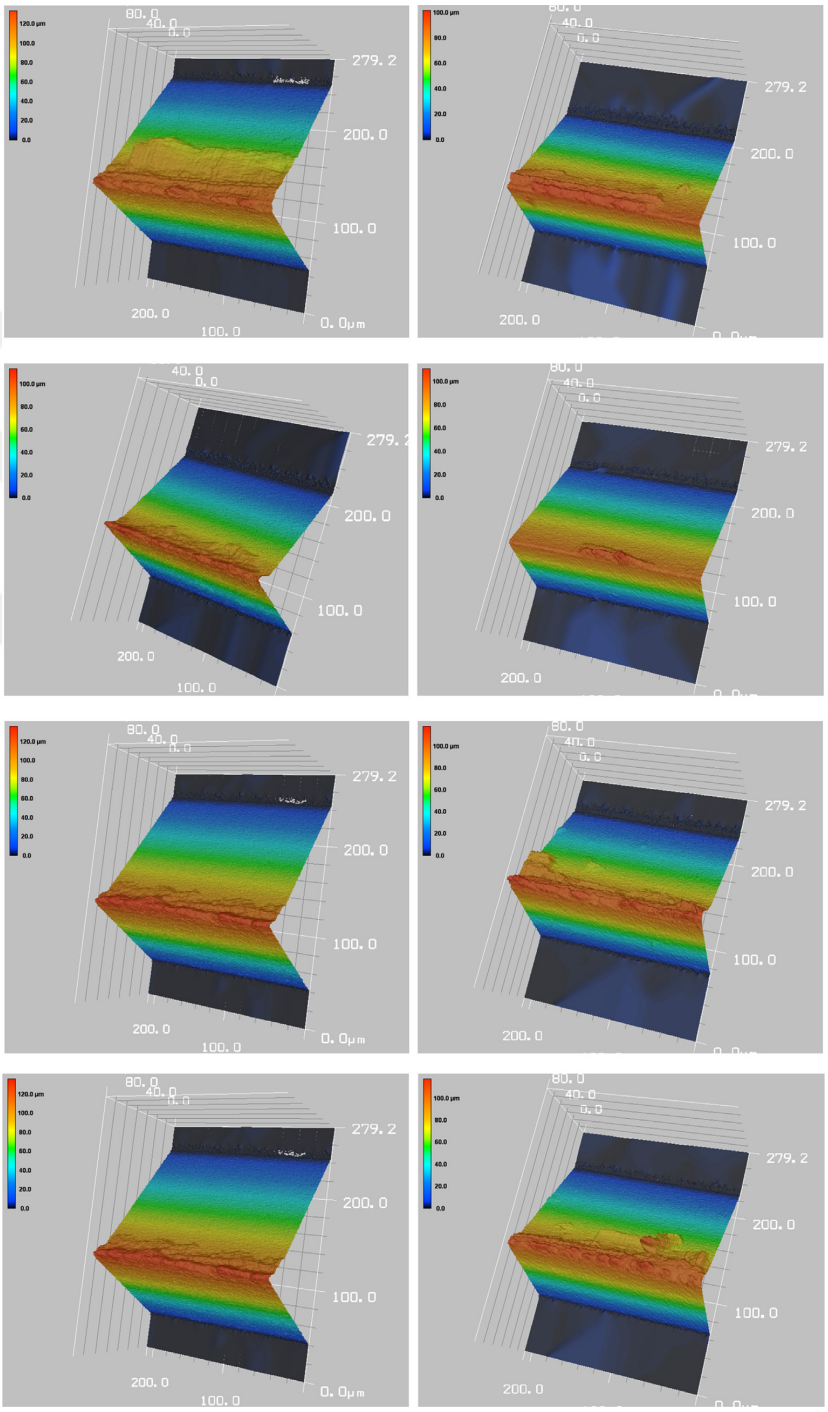

Figure 4.9: 3D edge profile measurements. Left column 7°, right column 14° clearance angle. Uncut chip thickness from top to bottom 0.4, 0.6, 0.8, and 1 µm. Cutting speed is 62 m/min.

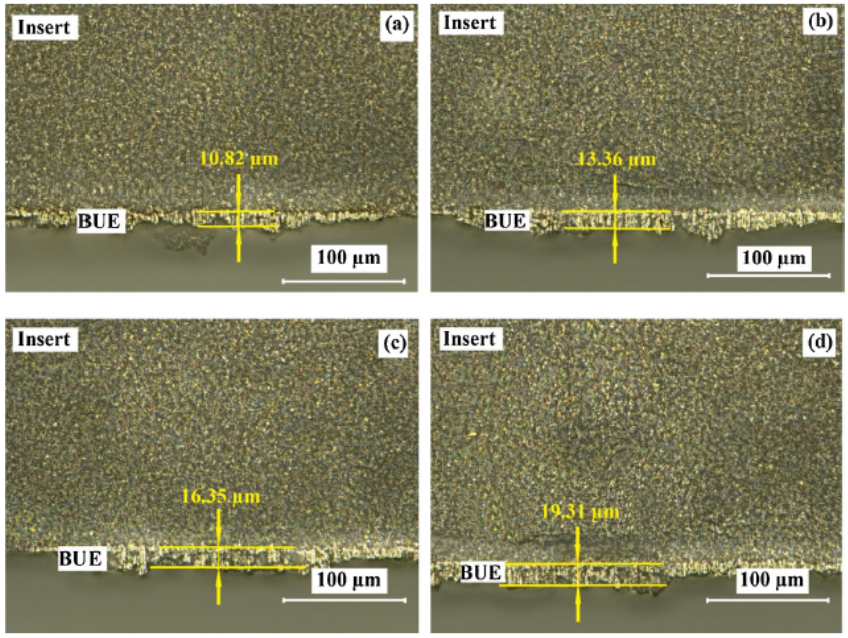

Figure 4.10: Increasing BUE tip length with increasing uncut chip thickness: (a) 0.4, (b) 0.6, (c) 0.8, and (d) 1 µm.

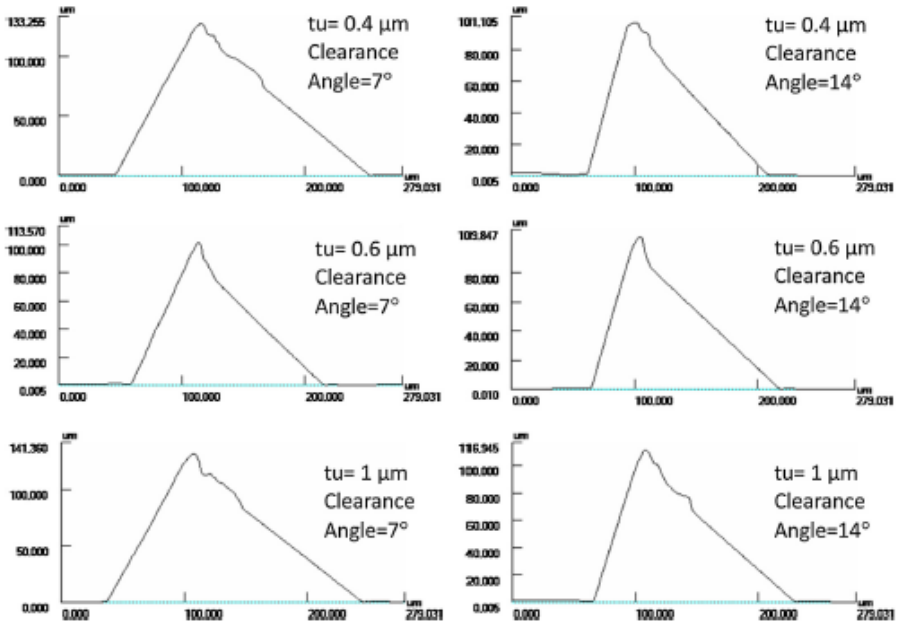

Figure 4.11: 2D edge profile measurements at cutting speed of 62 m/min.

the protective effect of BUE. However, the edge profile measurement revealed that edge radius increased to 3-4 μm at the end of the machining test. Edge rounding is a known form of tool wear during micro-scale machining. The machining process was further lengthened to 2 and 9 minutes of continuous machining. The edge radius was also measured to be around 3-4 μm and again no sign of flank/crater wear was observed on the tool. Figure 4.12(b) shows the tip length of BUE after 9 minutes of machining from flank side of the tool. The increase in edge radius may have happened during break-in period of the tool, and it further promotes the accumulation of material in front of the tool. The influence of BUE on machining forces and surface quality are investigated in the next section.

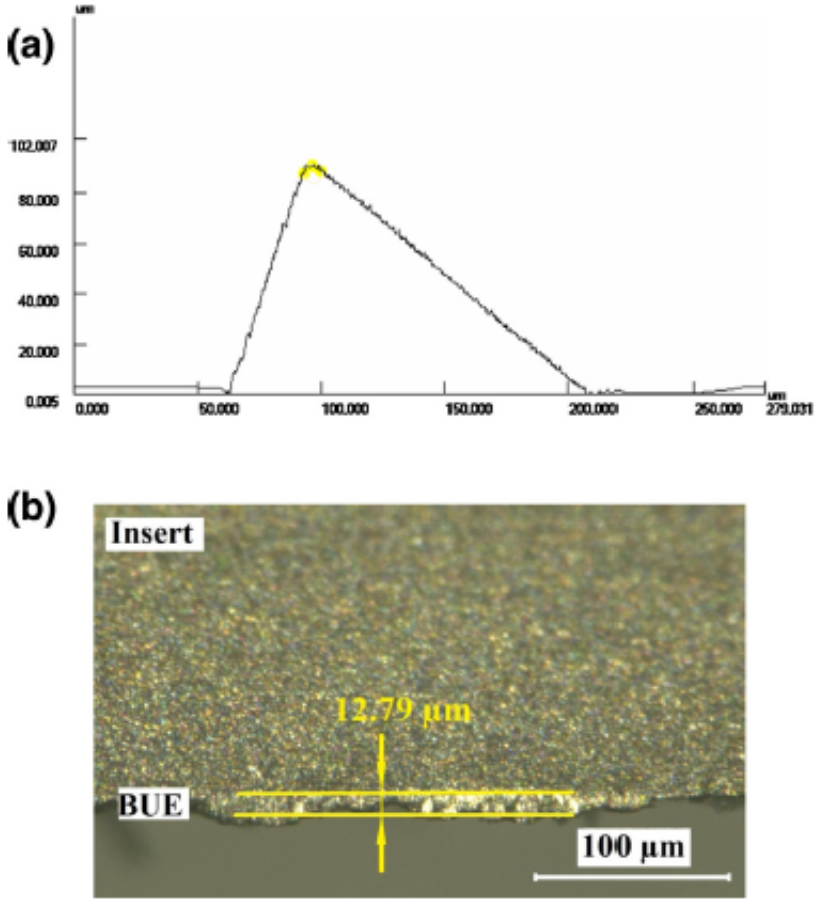

Figure 4.12: (a) 2D edge profile corresponding to 14° clearance angle at 0.4 μm uncut chip thickness after 2 min of continuous machining, (b) Tip length of BUE after 9 minutes of continuous machining (62 m/min cutting speed).

4.2.4 Force Measurements during Micro-scale Machining of Ti6Al4V

Measuring forces during micromachining tests allows the investigation of the process forces in the presence of BUE formation. Figure 4.13 shows the force measurements obtained for 7° and 14° clearance angle tools for different uncut chip thickness values at 62 m/min corresponding to 12 s of cutting. These measurements correspond to the cutting edge images shown in Figure 4.9. Each orthogonal cutting experiment was repeated at least three times with up-sharp tools, and consistent results were obtained. The measured forces were filtered with a low pass filter and average machining forces and force variations around average forces were calculated.

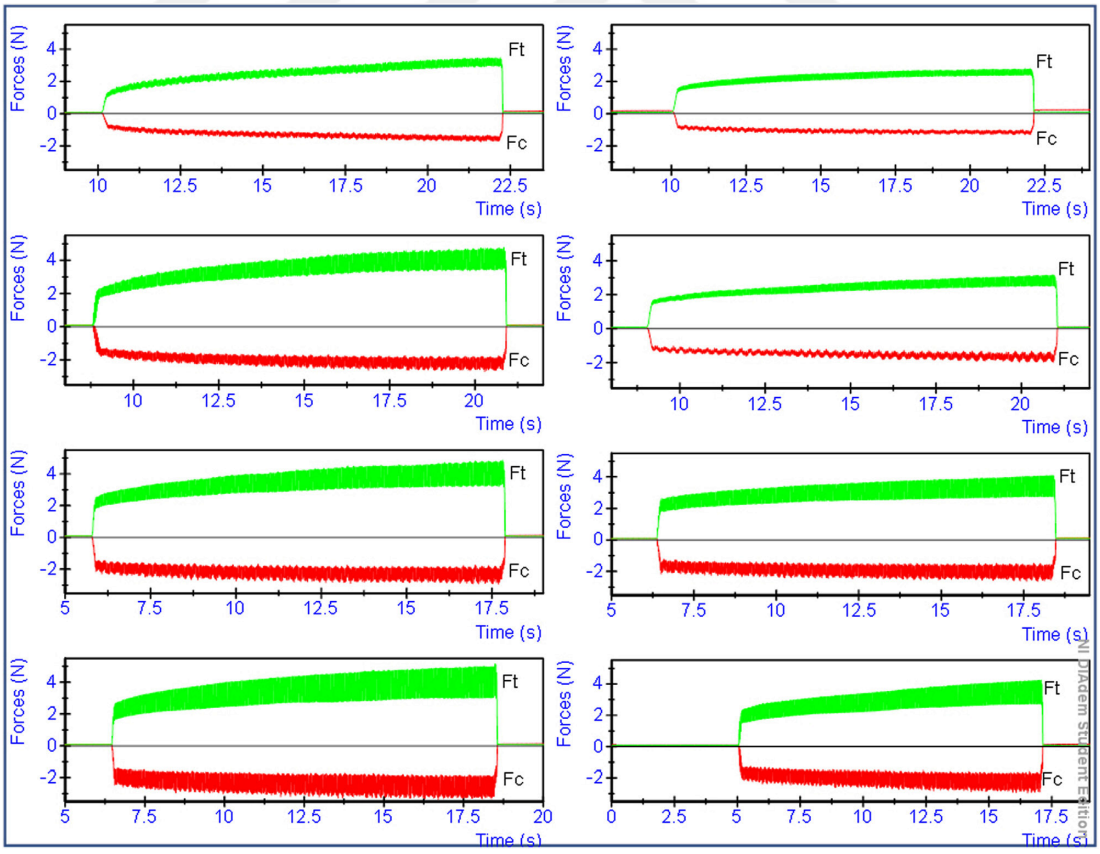

Figure 4.13: Force vs. time measurements. Left column 7°, right column 14° clearance angle. Uncut chip thickness from top to bottom 0.4, 0.6, 0.8, and 1 μm.

Machining forces were observed to increase at the initial stages of machining, indicating changing contact conditions at the tool tip and BUE formation on the rake face. Increasing average force may be related to edge rounding and increasing force variations may be related to BUE formation. The thrust force (Ft) seems to be affected by the BUE more than the cutting force (Fc). Force measurements follow a steady trend indicating the formation of a stable BUE.

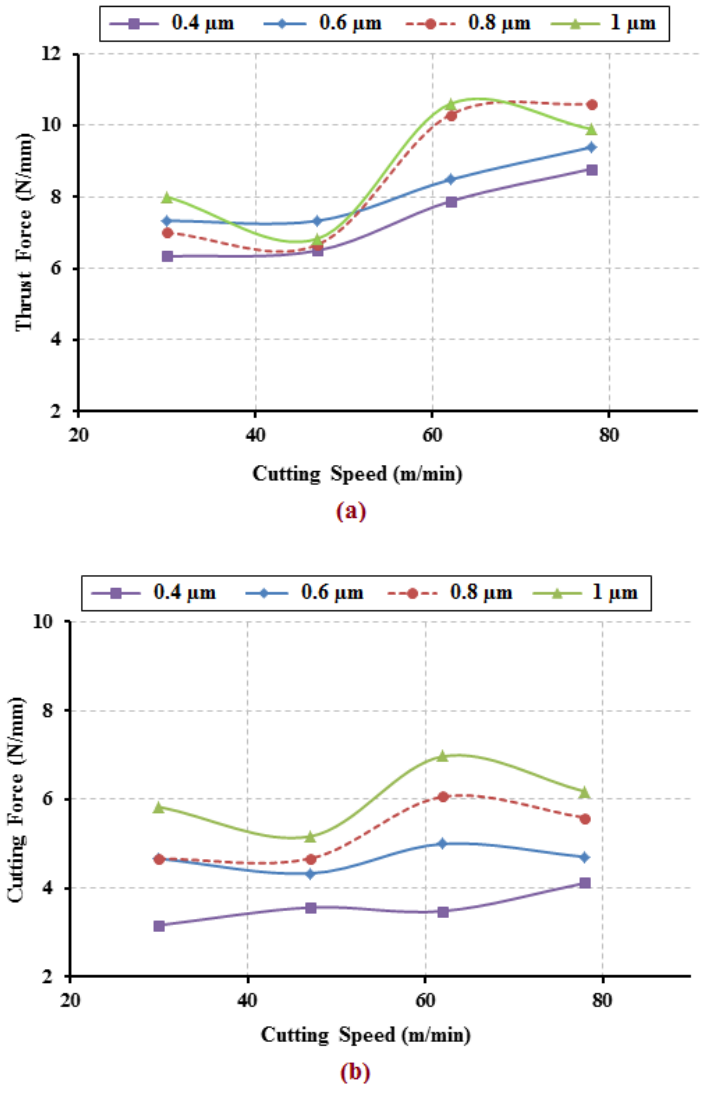

Figure 4.14: Mean values of: (a) thrust and (b) cutting forces as a function of cutting speed.

Figure 4.14 shows the influence of cutting speed on thrust and cutting forces for different uncut chip thickness values. Thrust forces increase with increasing cutting speed for 0.4–0.6 μm uncut chip thickness. There is a significant jump in thrust forces at 62 m/min for uncut chip thicknesses of 0.8–1 μm. These results indicate the influence of increasing built-up edge tip length with increasing uncut chip thickness and cutting speed. As cutting speed is increased to 78 m/min, thrust forces plateau, which may be due to sharp tip of BUE. Cutting forces mostly peaked around 62 m/min and tend to decrease at 78 m/min.

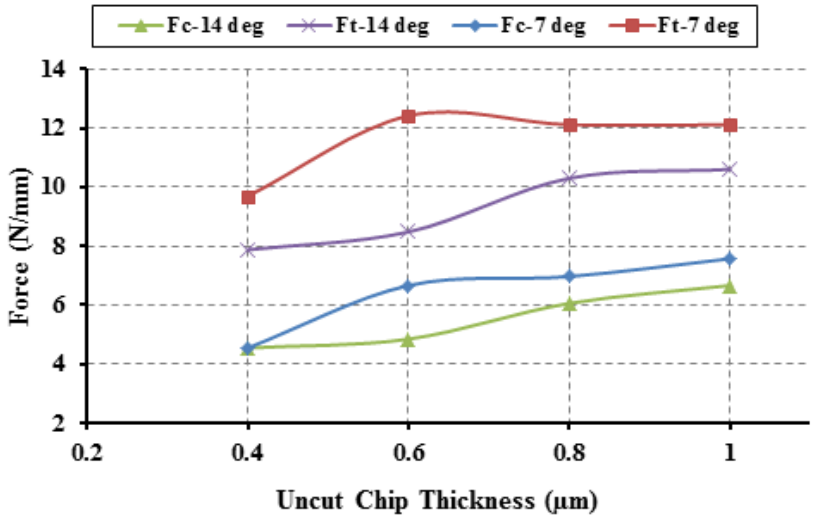

Figure 4.15: Mean values of cutting and thrust forces at 62 m/min cutting speed for cutting edges

Figure 4.15 shows the average cutting and thrust forces as a function of uncut chip thickness for cutting edges with 7° and 14° clearance angles. Although no clear difference in BUE shapes was observed between 7° and 14° clearance angles, force measurements increase as clearance angle decreases as expected. Cutting force measurements increase with increasing uncut chip thickness. Thrust force measurements for 7° clearance angle exhibit a peak at 0.6 μm and then plateau between 0.8 and 1 μm. Thrust force measurement for 14° clearance angle tool exhibited a similar trend, however it plateaus between 0.8 and 1 μm uncut chip thickness. The presence of a built-up edge is known to be important since a large contact area with the workpiece and the tool exists as a result of BUE. Therefore, larger thrust forces are obtained in

the measurements.

4.2.5 Effect of BUE on Surface Roughness

In micro-scale machining, the influence of machining conditions on the surface roughness is quite important as shown in Cuba Ramos et al. [156]. This section investigates the influence of BUE on surface quality. As mentioned earlier, the uncut chip thickness where the thrust force reaches its peak value is identified as minimum chip thickness which defines the transition from a shearing-dominated to a ploughing-dominated machining region. In previous studies, the influence of the surface roughness being cut is usually neglected.

In this research, after each test, the machined surfaces are investigated by using a laser scanning microscope (Keyence VK-X110) for contactless surface roughness measurements where arithmetic mean height (Ra) and average distance between the highest peak and lowest valley (Rz) values are considered to study the effect of built-up edge on surface roughness.

In measurements, image stitching capability of the laser microscope is used to investigate a large area for detailed surface characterization. Noise filtering and planar tilt correction is applied to a region of interest of (750 μm × 200 μm) before extracting Ra and Rz values. A cut-off (λ_c) value of 80 μm was used to remove the influence of waviness from surface roughness measurements. Figure 4.16 shows surface topologies after machining at 62 m/min at 0.4 and 1 μm uncut chip thicknesses. The ridges on the machined surface due to nonuniform BUE tip formation can be clearly seen.

Figure 4.17 shows the surface roughness measurements as a function of speed for various uncut chip thickness values. It is interesting to see that surface roughness (Rz) values improve around 62 m/min cutting speed, corresponding with high cutting and thrust force values (Figure 4.14). After 62 m/min cutting speed, the surface quality deteriorates significantly mainly due to scratching effect of BUE. The results indicate that there exists a complex relationship between uncut chip thickness, cutting speed, BUE formation, and surface roughness. Relatively better surface quality values were

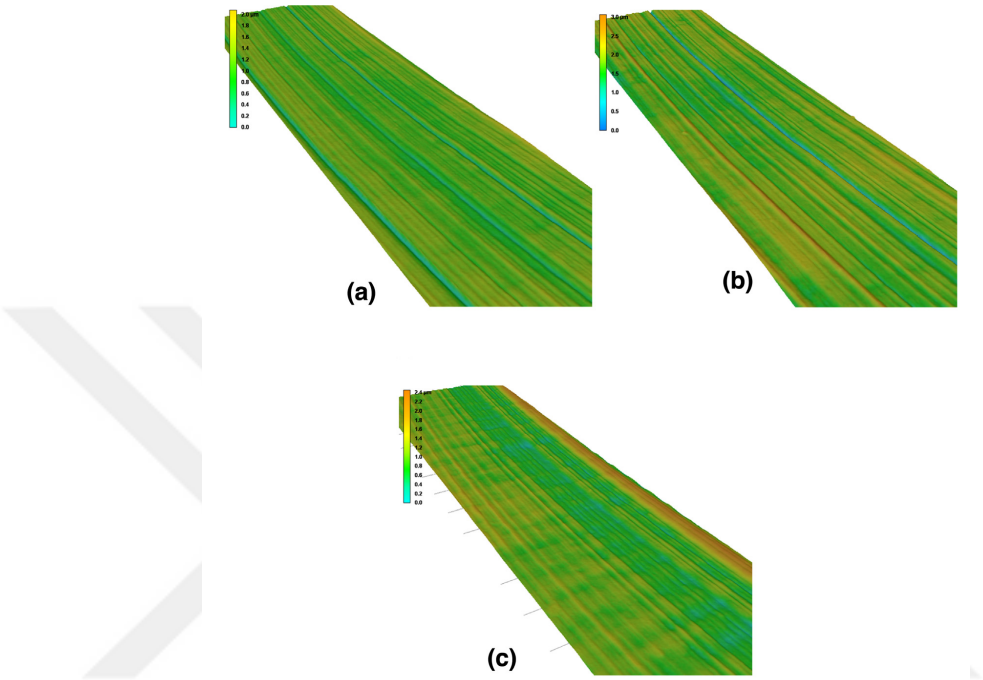

Figure 4.16: Laser topography images of the surfaces machined at 62 m/min cutting speed at: (a) 0.4 μm uncut chip thickness, (b) 1 μm uncut chip thickness, (c) 0.8 μm uncut chip thickness at 78 m/min (with 300x height magnification).

obtained at lower uncut chip thickness values.

In Figure 4.17, at 0.2 μm uncut chip thickness, average surface roughness (Rz) value of 0.13 μm was measured. As for 0.4 μm uncut chip thickness, average surface roughness (Rz) value of 0.16 μm was measured. It must be noted that the Rz and uncut chip thickness values are quite close to each other. In order to observe the chip formation during micro-scale machining, a high speed microscope (Keyence VW 9000 series) is used. Due to limitations of the high speed microscope, the recording was only made from the backside of the chip. Based on the video recordings, under 0.4 μm uncut chip thickness value, the chip formation transitioned from continuous to discontinuous. From high speed camera recordings continuous (0.8 μm uncut chip thickness) and intermittent (0.2 μm uncut chip thickness) machining cycles can be clearly distinguished. It must be noted that in the experimental setup used in this study, the workpiece is continuously fed towards the cutting edge. Therefore, intermittent chip

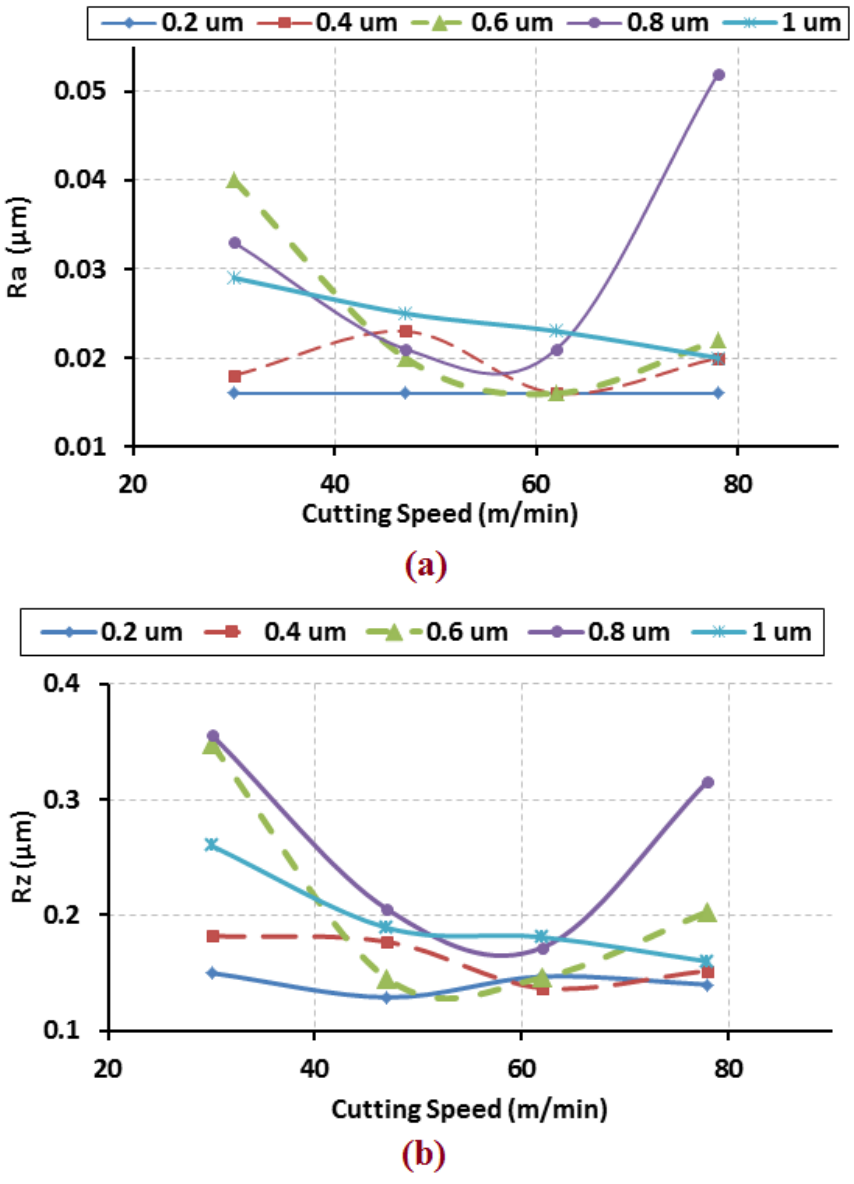

Figure 4.17: Surface roughness analysis as a function of cutting speed: (a) Ra, (b) Rz.

formation is expected when uncut chip thickness is less than minimum chip thickness. Based on these findings, the transition from continuous to intermittent chip formation happens around 0.4 μm. Assuming that the edge radius is 4 μm, the minimum uncut chip thickness in the presence of BUE is around 10% of the edge radius. This ratio is smaller than those reported for stagnation point assumption in the literature.

The findings in this section provide useful information regarding the effect of BUE on machining forces and surface finish. In the subsequent section attempt has been made to apply the findings of this section to develop reliable finite element models to predict micro-scale cutting process outputs in the pretense of BUE.

4.3 Finite Element Simulation Model of Micro Scale Machining with the Presence of Built-up Edge

Developing predictive techniques to improve the quality of micro parts has emerged as an important research area. Several approaches can be used to predict outputs of micro-cutting operations including analytical modeling, numerical methods, molecular dynamics simulation and experimental approach. Since experimental studies are expensive, time consuming and are only valid for the conditions and range of machining parameters used in the experiments, numerical methods are used as an alternative method to predict machining process outputs.

Among various numerical methods, finite element method is the most widely accepted numerical method for the simulation of metal cutting processes [169]. However, the effectiveness of finite element methods highly depends on the accuracy of the input data and how actual cutting conditions are reflected in the model, including workpiece material behavior, interaction between cutting tool and workpiece, boundary conditions and etc. [170].

It has been shown through an extensive experimental study in the previous section that, an important observation in micro-scale machining of Ti6Al4V is the formation of built-up edge on the cutting tool, which can mainly be defined as the accumulation

of damaged work material layers on the tool surface, affecting the outputs of micro-scale cutting including cutting forces, surface quality, minimum uncut chip thickness and etc.

In the literature, the influence of stable BUE has been considered in analytical models of machining such as Waldorf et al. [150], Fang and Dewhurst [151], Karpat and Özel [152], and Karpat [80]. The number of studies that simulate BUE in finite element based models is limited. Recently, Childs [153] developed a damage model and integrated it into a finite element simulation software to predict BUE during macro scale machining of steel, and micromachining was considered as a special case. The formation of BUE is a time-dependent phenomenon, therefore it is a challenge to capture it in finite element models. In addition, BUE also affects the friction conditions at the tool/chip and tool/workpiece interfaces, where the cutting tool material is no longer directly in contact with the chip and the machined surface.

This section considers finite element simulation of micro-scale orthogonal machining with the presence of BUE. Its approach modifies cutting edge geometry based on experimental BUE observations. The focus is on friction models and their influence on the process outputs. The objective is to use the findings of previous section to develop predictive finite element models of orthogonal cutting of Ti6Al4V with BUE. This orthogonal models are quite important because they can be used to predict outputs of oblique cutting processes through a set of coordinate transformations.

4.4 Analysis of Stable Built-up Edge Formation at Micro Scale Machining

In previous section of this chapter a 3D laser scanning microscope (VK-X110) has been used extensively to investigate the geometry of the tools with stable built-up edge. In this section, 3D topography measurements obtained in the experimental phase of this research, are further analyzed to extract more geometric parameters related to BUE formation as a function of machining process parameters. Figure 4.18 illustrates

a sample BUE measurement obtained at a cutting speed of 47 m/min at an uncut chip thickness of 0.8 µm. It can clearly be seen that BUE formation significantly alters the edge radius, rake and clearance angles of the cutting tool.

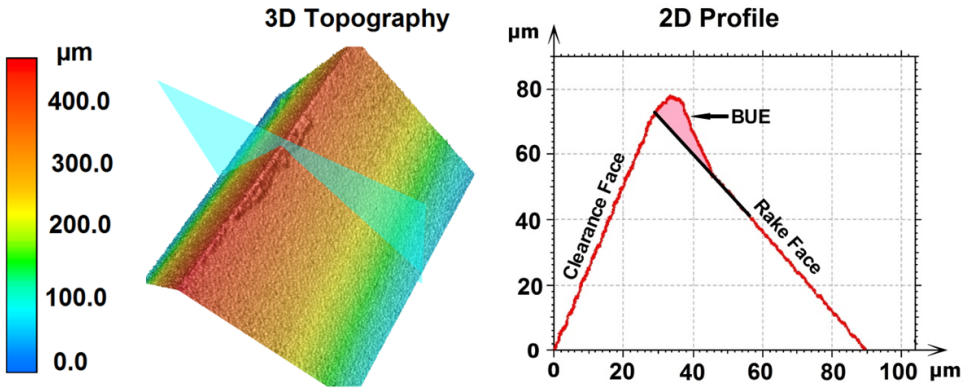

Figure 4.18: Built-up edge formation at 0.8 µm uncut chip thickness.

In order to analyze BUE formation as a function of process parameters, some features are defined as shown in Figure 4.19. As a result of BUE, the effective tool rake angle which is usually negative during micro-scale machining becomes positive and the clearance angle decreases. As a result of low clearance angle and BUE length on the flank face, there is considerable contact between the workpiece and the cutting edge.

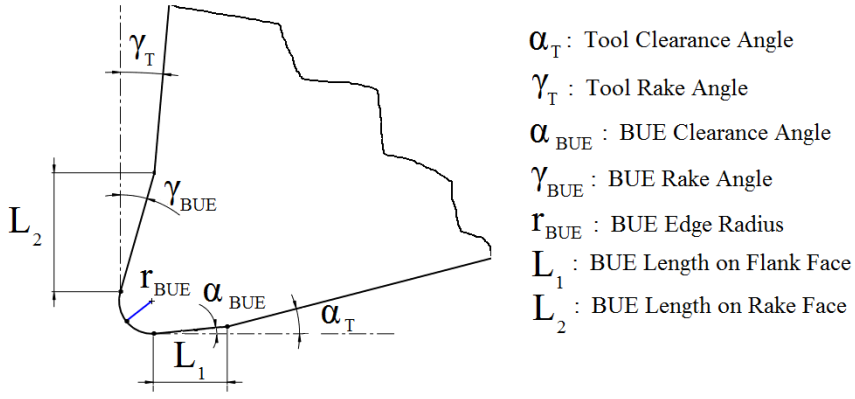

Figure 4.19: Cutting tool parameters in the presence of stable BUE.

The BUE parameters obtained for each experiment are shown in Table 4.3. Based on the results given in Table 4.3, as uncut chip thickness (t_u) increases, the length of BUE (L_1 and L_2) increases. Decreasing cutting speed leads to a smaller BUE formation and the edge radius of the BUE becomes smaller.

Table 4.3: BUE parameters obtained under different machining conditions.

Cutting Speed (m/min)	t_u **(µm)**	α_{BUE} **(deg.)**	γ_{BUE} **(deg.)**	r_{BUE} **(µm)**	L_1 **(µm)**	L_2 **(µm)**
47	0.4	1	12	2.5	8	10
	0.6	1	15	2.5	10	16
	0.8	2	16	2	13	18
	1	2	15	2	14	22
62	0.4	2	22	3	11	18
	0.6	3	18	3	13	20
	0.8	3	18	4	16	26
	1	3	20	4	19	35

4.4.1 Finite Element Simulation Model of Micro Scale Machining with the Presence of Built-up Edge

Finite element simulations are indispensable tools for machining research as they allow investigation of the relationship between machining conditions and process outputs. However, finite element simulation models of machining are not capable of simulating BUE formation during machining. Therefore, in this study, the cutting edge geometry is modified based on experimental observations of BUE formation. For each simulation condition, the cutting edge geometry is modified based on the values given in Table 4.3. The modified geometry of the cutting with the presence of stable BUE is shown in Figure 4.20.

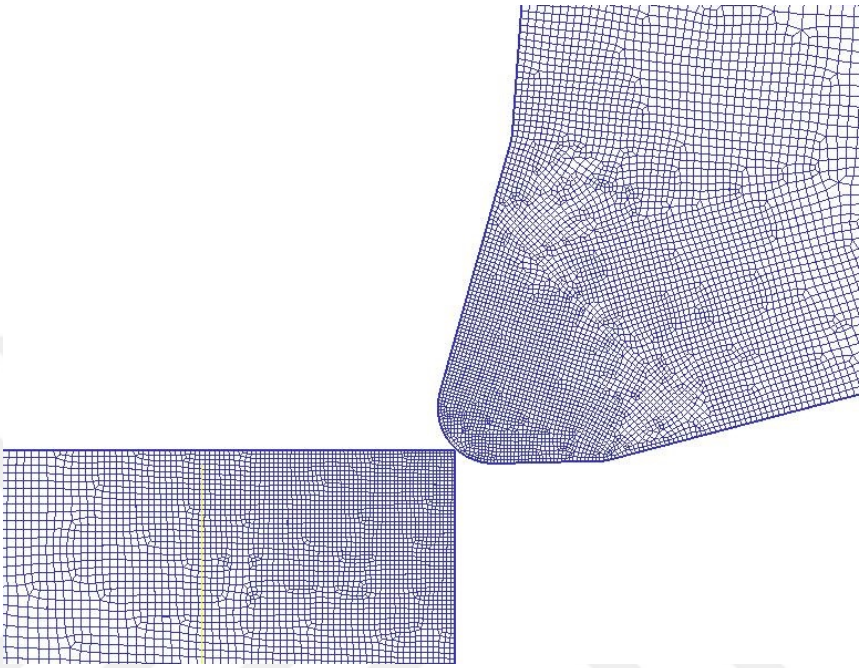

Figure 4.20: Modified geometry of the cutting edge including BUE used in finite element simulations.

It is a well known fact that there is a very complex contact conditions at the tool/chip and tool/workpiece interface, and 50%-70% of the total machining energy will be dissipated at these two interfaces[171]. Therefore, Defining the friction condition at the tool/chip and the tool/workpiece interfaces is important, since it affects heat generation at the interfaces. Many different friction models have been proposed [172, 173, 174] and it is an ongoing research area [175]. Two basic friction models are considered in this study. The first one relates the frictional stress (τ_f) at the tool/workpiece interface to normal stress (σ_n) via Coulomb friction as:

$$\tau_f = \mu\sigma_n \tag{4.1}$$

The second one considers the relationship between friction (τ) at the tool/workpiece interface and the shear flow stress (k) of the work material through shear friction factor (m) as:

$$\tau = mk \tag{4.2}$$

In the studies of finite element simulation of micromachining, a combination of these friction models are usually used. Thepsonti and Özel [176] considered sticking contact conditions (m=0.9) around the edge radius and Coulomb friction on the rake face (μ=0.7 for tungsten carbide and μ=0.4 for CBN cutting tool material) while micromachining titanium alloy Ti6Al4V. Jin and Altintas [177] used sticking and sliding contact conditions during finite element modeling of micromilling where the Coulomb friction was taken as 0.15 for brass workpiece material. Afazov et al. [178] also assumed sticking and sliding conditions with a coefficient of friction of 0.4 for micromilling modeling of AISI 4340 steel. Thepsonti and Özel [159] used finite element simulation to model micromilling of titanium alloy Ti6Al4V. They considered sticking and sliding contact condition with Coulomb friction of 0.2.

Considering that BUE acts like a cutting edge, the contact conditions between BUE and the work material would be different. Budinski [179] investigated the tribological properties of titanium alloys and reported coefficient of friction between Ti6Al4V pair as 0.31. Zhang and Tanaka [180] used molecular dynamics approach to study wear and friction for low uncut chip thickness values. They concluded that Coulomb friction rule is valid during micro cutting regime and lower coefficient of friction values were calculated as a function of indentation depth during adhering stage. Venkatachalam and Liang [181] also studied the variation of coefficient of friction during micro-scale machining and stated that for low values of indentation, the coefficient of friction depends on the adhesion effect.

The material constitutive model employed in finite element simulation, together with friction definition, significantly affects the process output predictions. Many research papers have been published on this issue, mostly considering macro scale machining of titanium alloys [182, 183]. In recent studies, material constitutive models have been improved to consider microstructural changes at high temperature machining conditions [184, 185].

In this study, a material model developed by Karpat [186] is adopted to simulate micro-scale machining of titanium alloy Ti6Al4V. This material model was validated in a previous study for its ability to predict macro scale machining forces under various machining conditions. This material model considers strain softening as a function of

temperature and it was developed such that the influence of strain softening decreases as temperatures decrease. The model also considers the relationship between strain rate and strain. The material model is shown in Equation 4.3 and the material model parameters are given in Table 4.4.

$$\sigma(\varepsilon, \dot{\varepsilon}, T) = \left(a\varepsilon^{n^*} + b\right)\left(cT^{*2} + dT^* + e\right) h\left(\varepsilon, \dot{\varepsilon}\right) \tag{4.3}$$

where

$$h\left(\varepsilon, \dot{\varepsilon}\right) = \left(1 - \left[1 - \left(\frac{\ln\left(\dot{\varepsilon}_0\right)}{\ln\left(\dot{\varepsilon}\right)}\right)^q\right]\left[\frac{1}{l \times \tanh\left(\varepsilon + p\right)}\right]\right) \text{ and } T^* = \frac{T}{T_r} \tag{4.4}$$

Table 4.4: The coefficients of the material model

a (MPa)	**n***	**b (MPa)**	**c**	**d**
590	0.27	740	7.1903e-5	-0.0209
Q	**l**	**p**	$\dot{\varepsilon}_0$**(1/s)**	**E**
0.035	1.1	0.08	800	1.6356

A flow softening function, which initiates after a critical strain and temperature, was also integrated into Equation 4.3 as shown in Equation 4.5. The proposed function would control the softening behavior which occurs after a critical strain value. For strain values less than that critical strain, Equation 4.3 is valid.

$$\sigma_{soft}\left(\varepsilon, \dot{\varepsilon}, T\right) = \sigma - \left(\sigma - \sigma_s\right)\left(\tanh\left(k\varepsilon^*\right)^r\right) \tag{4.5}$$

Mechanical and thermo-physical properties of titanium alloy Ti6Al4V are defined as a function of temperature (T): The Youngs modulus $E(T) = -57.7 \times T + 111672$ (MPa), thermal expansion $\alpha(T) = 3 \times 10^{-9}T + 7 \times 10^{-6}$ (1/°C), thermal conductivity $\lambda(T) = 0.015T + 7.7$(W/m.K), heat capacity $Cp(T) = 2.7e^{0.0002T}$(N/mm^2/°C) [26]. The heat transfer coefficient at the tool/chip interface is taken as a constant 5,000 (W/mm^2/°C). In this study micro-scale cutting simulations are done using DEFORM 2D software which has a utilization percentage of 47 % in machining simulations [170]. In DEFORM, modeling of machining is based on implicit integration method and Lagrangian formulation. The adaptive meshing techniques used in the software makes it possible to model large deformations by reducing mesh distortions [187]. The workpiece is represented with 10,000 quadrilateral elements and is modeled as elastic-plastic, whereas the cutting edge is modeled as rigid. The material constitutive model was kept constant and only friction model coefficients are varied.

4.4.2 The Influence of Friction Models on FE Simulations

4.4.2.1 Finite Element Simulations with Coulomb Friction Model

The influence of the coefficient of friction on the finite element simulation outputs is first investigated under Coulomb friction assumption between the BUE and the work material. Four different friction conditions are considered: Coulomb friction of 0.1, 0.2, 0.3, and 0.4 based on the findings of Budinski [179] and Zhang and Tanaka [180]. Figure 4.21 shows the chip formation for 1 μm uncut chip thickness under four different friction conditions.

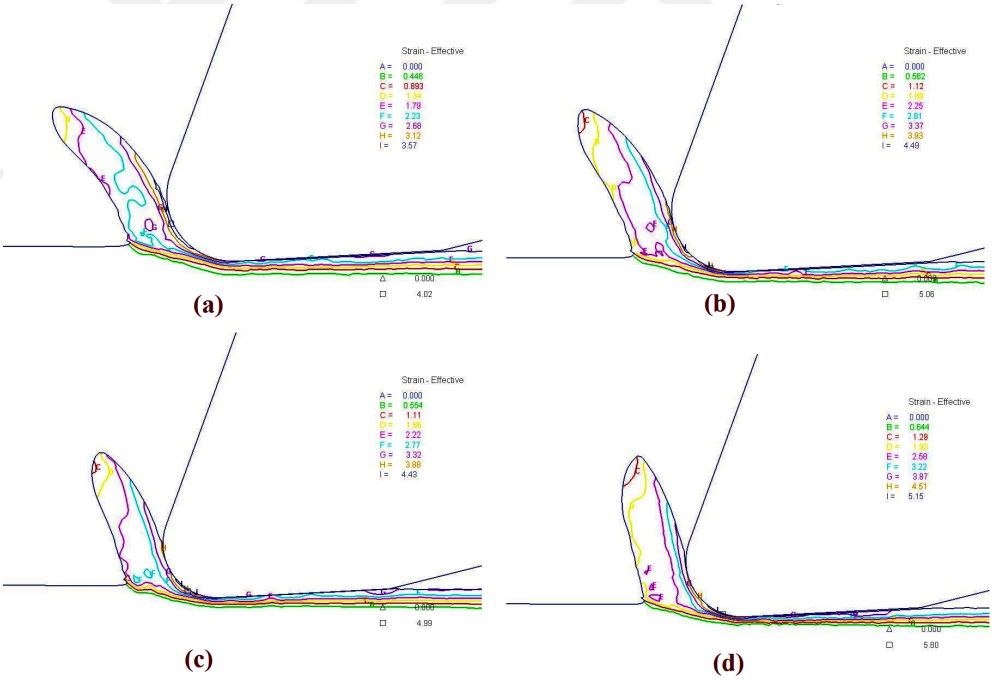

Figure 4.21: Influence of coefficient of friction on the chip formation at uncut chip thickness of 1 μm, cutting speed of 62 m/min and a Coulomb friction of: (a) 0.1, (b) 0.2, (c) 0.3, (d) 0.4.

It can be seen in Figure 4.21 that, as coefficient of friction increases, calculated strain on the machined surface also increases. The coefficient of friction affects the thickness and shape of the chip. Increasing coefficient of friction decreases chip curvature. Considering the fact that the cutting edge is actually the BUE, one may expect to

observe contact between the chip and the BUE along the rake face. With Coulomb friction model, however, finite element simulation did not yield such chip shapes. Since micromachining requires small uncut chip thickness values, it is a challenge to measure the cut chip thicknesses. Therefore, no reliable measurement of cut chip thickness was possible in the experiments.

Figure 4.22 shows the variation of cutting and thrust forces with time for different coefficient of friction values. The cutting (Fc) and thrust (Ft) forces reach a steady state value after micro-chip is formed. The thrust forces are simulated to be larger than cutting forces, which agrees with the experiments. Figure 4.23 shows the influence of coefficient of friction on simulated cutting and thrust forces in comparison to experimental forces.

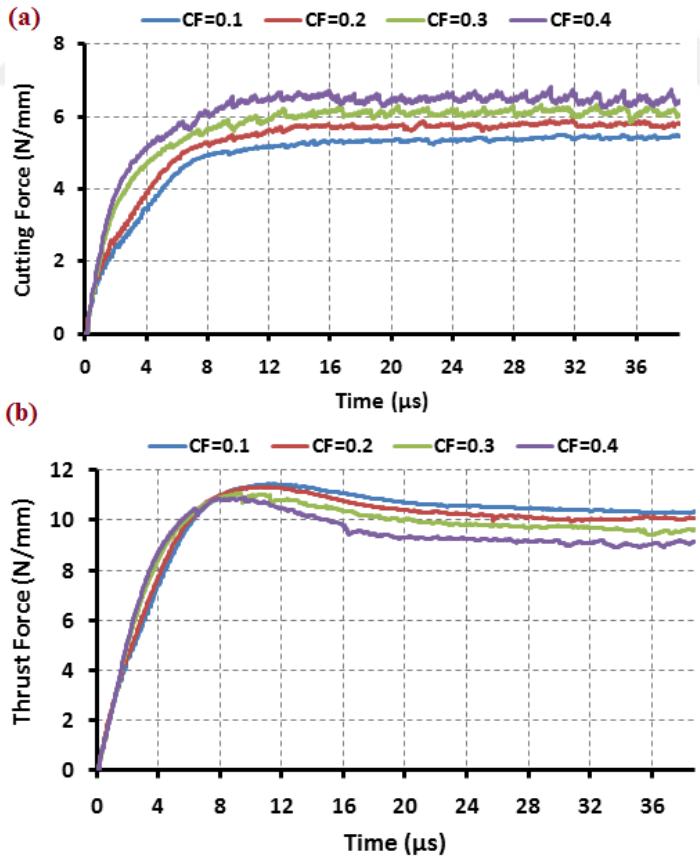

Figure 4.22: Force predictions versus time obtained from finite element simulation model for uncut chip thickness of 1 µm at 62 m/min.

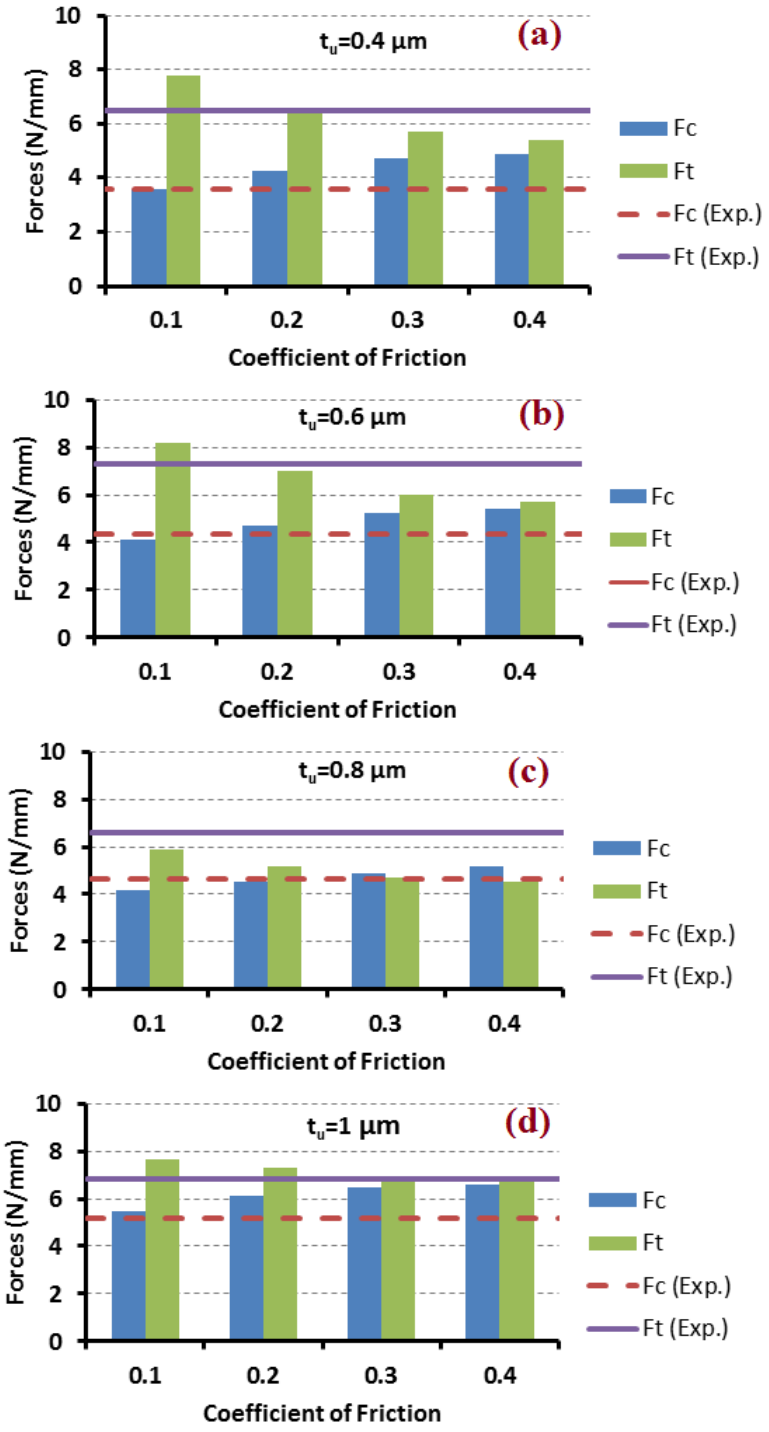

Figure 4.23: Force predictions as a function of coefficient of friction for uncut chip thickness of (a) 0.4, (b) 0.6, (c) 0.8, and (d) 1 µm at 47 m/min.

It can be seen in Figure 4.23 that, increasing coefficient of friction increases cutting force and decreases thrust force. Based on the simulation results, coefficient of friction of 0.2 yielded better predictions for uncut chip thickness values of 0.4 and 0.6 μm, whereas coefficient of friction of 0.1 yielded better predictions for uncut chip thickness values of 0.8 and 1 μm. In the simulations for the cutting speed of 62 m/min, a coefficient of friction of 0.3 resulted in best predictions. Figure 4.24 summarizes the force predictions at 47 and 62 m/min cutting speed under Coulomb friction model assumption. Force predictions at 47 m/min matches experimental results better compared to 62 m/min considering the upper and lower experimental limits.

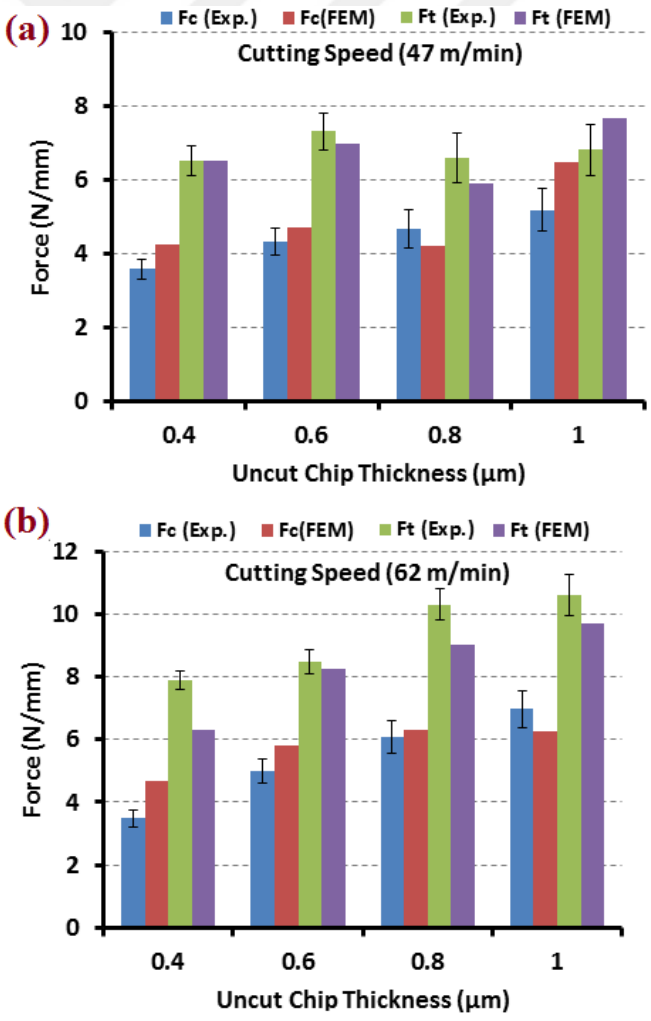

Figure 4.24: Force predictions for different uncut chip thickness values for: (a) Cutting speed of 47 m/min, (b) Cutting speed of 62 m/min.

4.4.2.2 Finite Element Simulations with Shear Friction Condition

In finite element simulation studies, a high friction factor (m) creates sticking conditions at the tool/chip interface and corresponding low speed region in front of the cutting edge is assumed to behave like a BUE [160, 161, 162, 150]. Figure 4.25 shows the comparison of the measured and predicted forces for various uncut chip thickness values with friction factor of 0.95. As uncut chip thickness decreases, the agreement between measurements and predictions worsens, especially for cutting force. At small uncut chip thickness values (0.4 and 0.6 μm), Coulomb friction with equivalent edge yielded better predictions compared to high friction factor with original edge. The cutting force prediction of the finite element model seems to be insensitive to variation of uncut chip thickness in high friction factor assumption.

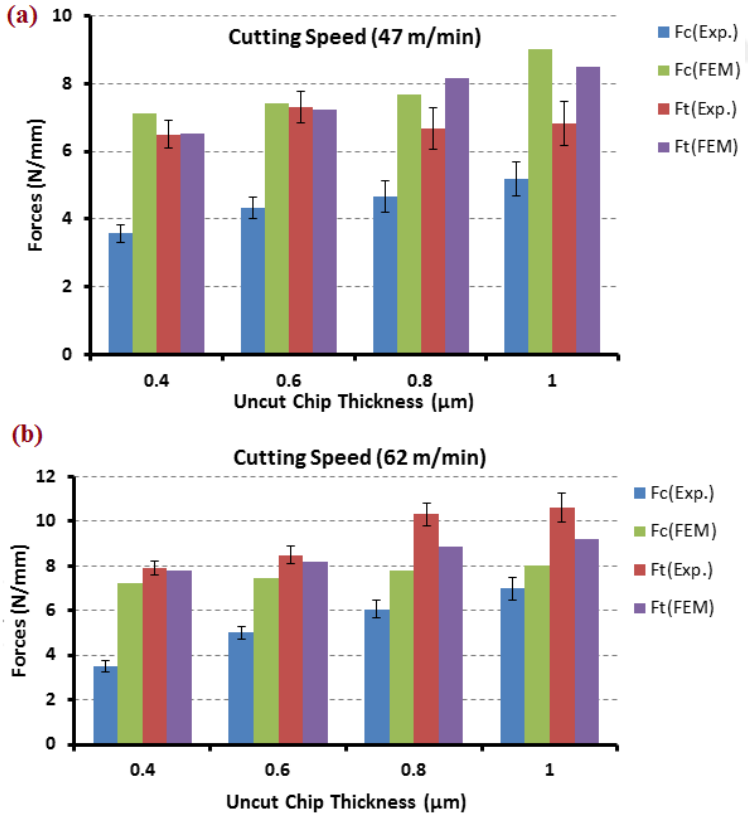

Figure 4.25: Comparison of force measurement and predictions for friction factor of 0.95 at cutting speed of: (a) 47 m/min, (b) 62 m/min.

4.4.2.3 Finite Element Simulation with Hybrid Friction Conditions

In this section, a hybrid friction model is applied and finite element simulations were conducted. In hybrid friction model, a friction window approach has been used in which sticking conditions are assumed on the rake face and sliding friction conditions are assumed on the flank face of the cutting tool. Figure 4.26 shows the hybrid friction model used in this study. Different combinations of Coulomb friction (μ) and shear friction (m) values are considered. Shear friction is varied between 0.7 and 0.95, while Coulomb friction is varied between 0.1 and 0.3. Table 4.5 shows the combinations used in the simulations where a total of nine cases are considered.

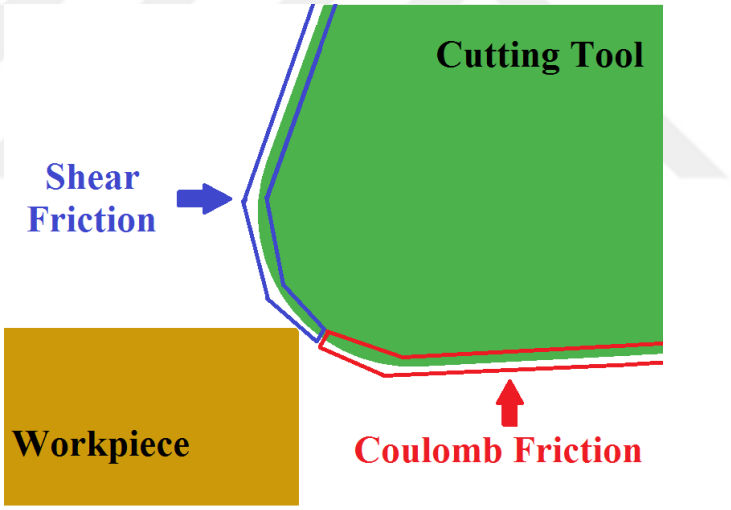

Figure 4.26: Hybrid friction model used in the finite element simulation with the presence of BUE.

Table 4.5: Friction definitions in the hybrid model.

Model	**1**	**2**	**3**	**4**	**5**
Friction definitions	μ=0.1 m=0.7	μ=0.1 m=0.8	μ=0.1 m=0.95	μ=0.2 m=0.7	μ=0.2 m=0.8
Model	**6**	**7**	**8**	**9**	
Friction definitions	μ=0.2 m=0.95	μ=0.3 m=0.7	μ=0.3 m=0.8	μ=0.3 m=0.95	

Figure 4.27 illustrates the influence of hybrid friction on the chip formation at uncut chip thickness of 1 μm and cutting speed of 62 m/min. Compared to Figure 4.21, chip shape formation is changed and the chip flows on the rake face formed by the BUE. As a result of using an elastic-plastic finite element model, the contact at the BUE-work surface interface also matches the experimental observations.

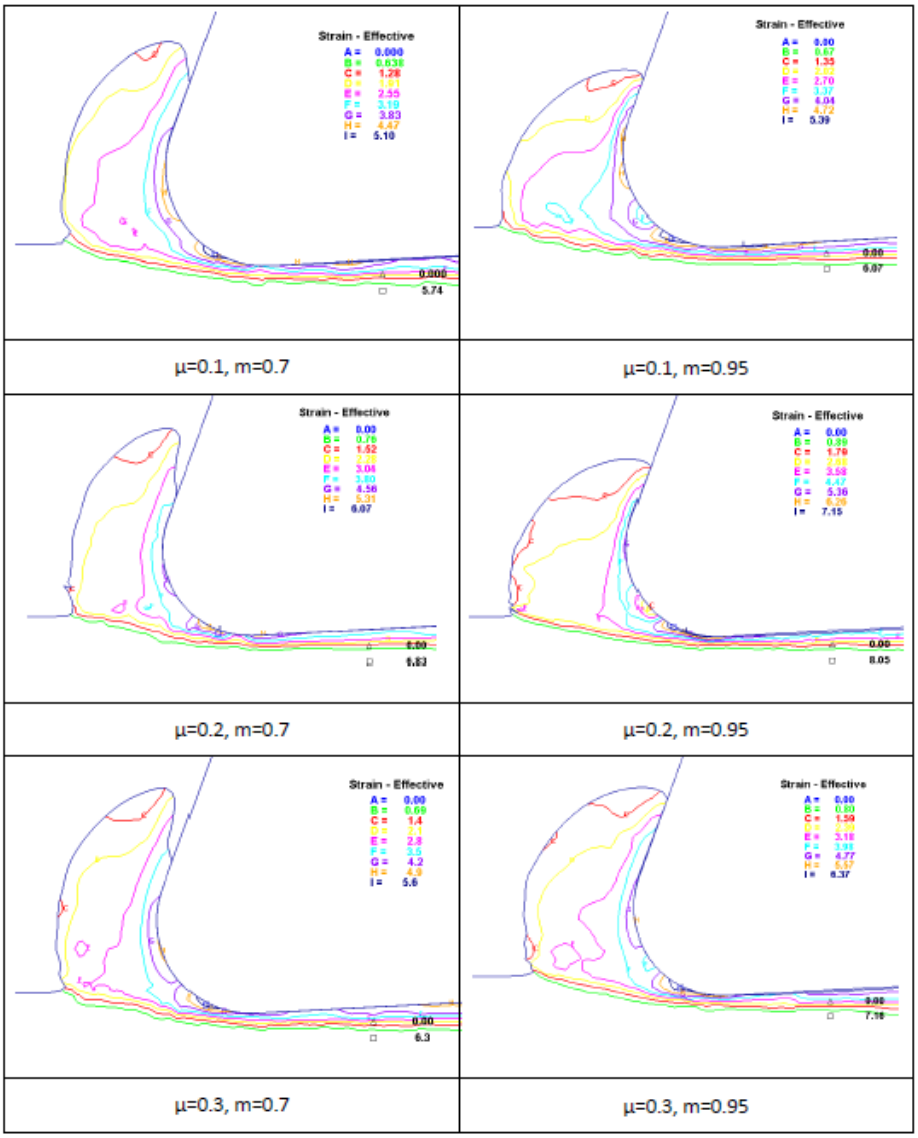

Figure 4.27: Finite element simulations of chips for hybrid friction model.

Figure 4.28 illustrates the finite element force predictions at different combinations of Coulomb friction and shear factor for uncut chip thickness of 1 μm at a cutting speed of 62 m/min. A Coulomb friction of 0.2, and a shear factor of 0.8 resulted in the closest predictions compared to experimental results. For all other uncut chip thickness values, Coulomb friction of 0.2, and shear factor of 0.8 also yielded the best results.

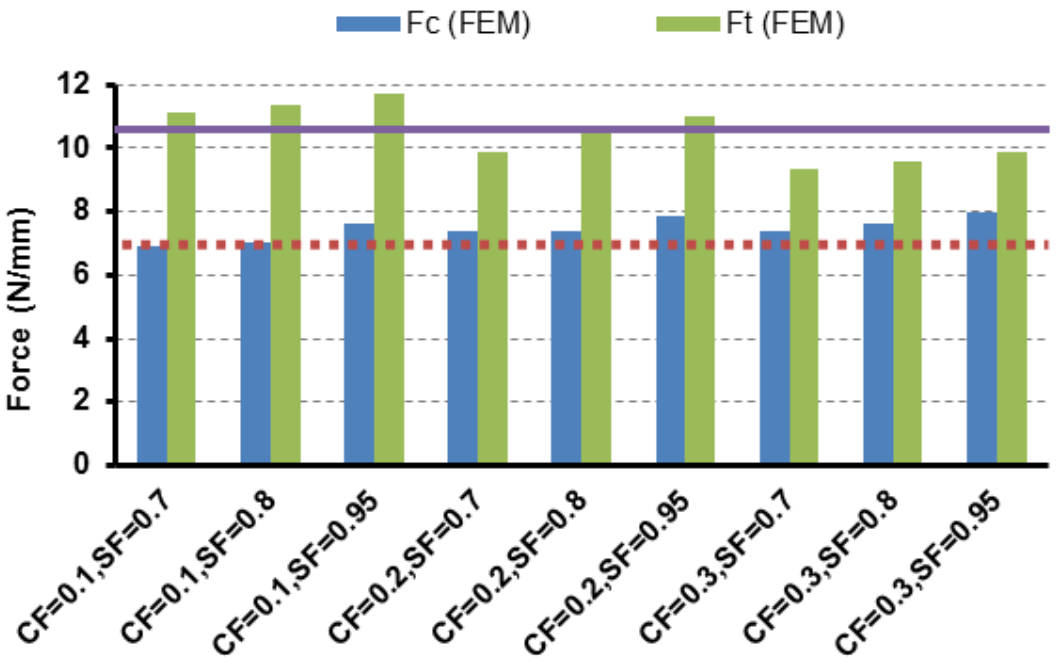

Figure 4.28: Finite element predictions at different μ and m values for an uncut chip thickness of 1 μm at cutting speed of 62 m/min.

Figure 4.29 illustrates finite element predictions and experimental machining forces at two different cutting speeds using the hybrid friction model. Based on these results, a good fit is obtained between experimental measurements and finite element model predictions for uncut chip thicknesses of 0.6, 0.8 and 1 μm. As for uncut chip thickness of 0.4 μm, while the thrust force measurements are acceptable, the cutting force predictions and measurements did not match well. It must be noted that, uncut chip thickness of 0.4 μm was found to be the minimum uncut chip thickness as obtained in the experimental phase of this research. It is highly likely that the mechanics of cutting and contact conditions is changed significantly below this value.

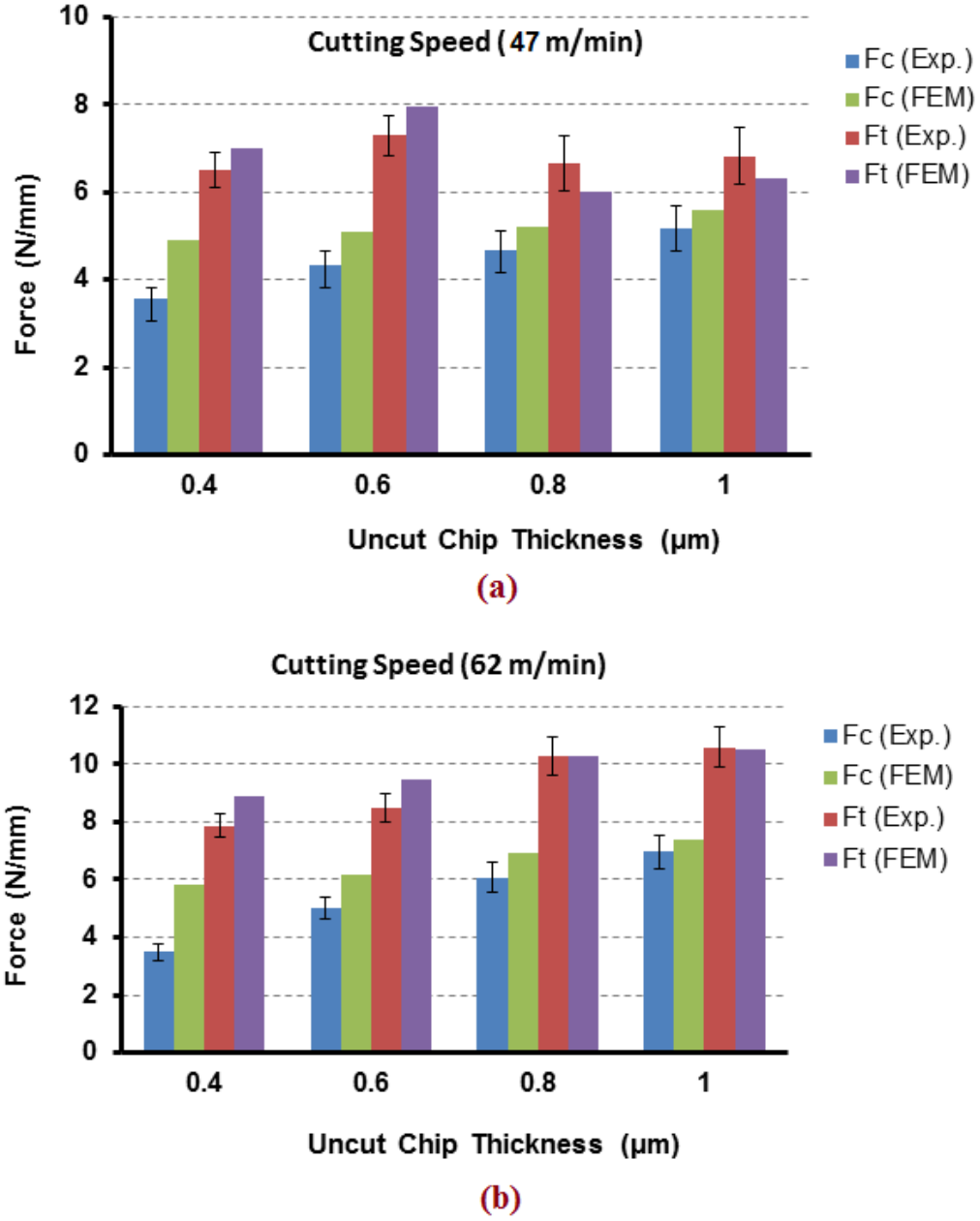

Figure 4.29: Comparison of force measurement and predictions for hybrid friction conditions (Coulomb friction of 0.2 and shear factor of 0.8) at cutting speed of: (a) 47 m/min, (b) 62 m/min.

Conclusion

In this chapter attempt has been made to study BUE formation at micro-scale cutting process by using engineered cutting tools. Based on the findings in the experimental phase of the research, finite element simulation has been performed to predict the outputs of micro-scale cutting operations. In the experimental phase, the influence of built-up edge on tool wear, forces, and surface roughness under micro-scale machining conditions is investigated. The uncut chip thickness, cutting speed, and clearance angle are considered as process variables. The results of experimental phase can be summarized as follows:

- During break-in period, the cutting edge radius increases which promotes BUE formation.
- It is observed that machining process inputs (uncut chip thickness, cutting speed, and clearance angle) affect the size of the built-up edge, which in turn affect the process outputs.
- A stable BUE formation exists under micro-scale machining conditions of the titanium alloy Ti6Al4V, which protects the cutting edge from flank and crater wear. EDS analysis of the insert surface indicated a small change in the chemical analysis of the surface. But it is not as significant as those in macro scale machining processes.
- It is observed that the influence of built-up edge on the surface roughness varies depending on the cutting speed and uncut chip thickness. A cutting speed of 62 m/min resulted in larger forces and better surface roughness values.
- Our findings also indicate a close relationship between the minimum uncut chip thickness and the mean roughness depth (Rz) of the machined surface. The minimum uncut chip thickness is found to be around 10 % of the edge radius in the presence of built-up edge.

A finite element simulation model has been developed for micro-scale machining of titanium alloy. Built-up edge formation has been included in the simulation by modifying the cutting edge geometry based on experimental observations. The influence of friction conditions on finite element simulations has been investigated based on basic friction models. The results of finite element modeling phase are as follows:

- Proposed finite element model is successful in predicting machining forces and chip shapes.
- A hybrid friction model where the rake face is modeled with shear friction factor of 0.8 and flank face is modeled with Coulomb friction of 0.2 yielded the best results.
- Finite element simulation predictions at uncut chip thickness of 0.4 μm significantly deviate from measurements in terms of cutting force. It must be noted that uncut chip thickness of 0.4 μm was the limit of transition from continuous to discontinuous chip formation. At this value, the surface roughness (Sz) and uncut chip thickness become almost equal, therefore machining is conducted through surface asperities. Finite element simulation predictions improve as uncut chip thickness increases and chip formation becomes continuous.
- The results reveal the importance of predicting the size and shape of built-up edge during micromachining. A significant accumulation of BUE drastically affects the process.
- A material constitutive model, which was validated in a previous study at macro-scale conditions, is also shown to work at micro-scale machining conditions under the identified friction conditions in this study.

Chapter 5

A Micro End Mill Design Methodology for Ti6Al4V Micromachining

5.1 Introduction

The importance of micromilling as a versatile micro-fabrication technique has been discussed in detail in chapter 3. It has been mentioned already that micro end mills directly influence the productivity and accuracy of the micromilling process. Issues related to micro end mills such as tool deflection, tool wear, tool breakage and vibrations need special attentions in order to have a successful micromilling operations.

In micromilling operations, the feed per tooth and depth of cut values are small. The spindle speed is usually high in order to obtain an acceptable cutting speed. The feed per tooth values are in the same order of magnitude as cutting edge radius. In some cases, spindle runout may be larger than commanded feed per tooth values, which results in only single tooth to function during micromilling process. It must be noted that each spindle has a characteristic runout, and this characteristic runout differs between spindles. Compensation of runout induced errors using standard end mills seems to be impossible, because these cutting tools are designed and fabricated in standard size and geometries for general use in micromilling processes and user has no control on

tool dimensions.

In conventional micro end mills, a helical tool geometry is usually used. If the tool diameter is less than 500 μm, the depth of cut is usually set around 50 μm which is only a short section of the tool tip. Considering small feed per tooth values, the cut chip thickness is small, therefore evacuating the chip from the cutting zone is not an important issue as macro-scale cutting.

The accuracy of the micromilling process depends on factors including tool runout, tool wear, tool deflection and etc. It is a challenge to obtain desired dimensional accuracy without excessive experimentations. Depending on the workpiece material, especially if ductile materials are being machined such as aluminum and titanium alloys, built-up edge (BUE) also affects the process as discussed in previous chapters. Since, stable BUE acts as a cutting edge, its dimensions has a significant influence on the machined parts in terms of part tolerances and machined surface integrity. The protective effect of BUE when using engineered cutting tools has been explored in orthogonal cutting processes, which is attributed to the morphology of the WEDMed surface. This observation requires to be extended and tested in micromilling operations, as tool life is a crucial factor in this process.

Based on the issues mentioned above, this chapter investigates the feasibility of the micromachining of Ti6Al4V using tailored micro end mills. In order to minimize the effect of tool runout, single edge cutting tools are fabricated. The dimensions of the tool together with its micro cutting geometry is designed so that required part accuracy is obtained at the end of machining process. Process mechanics of tailored micro end mills are also investigated in this section. Experiments have been conducted at different cutting speed and depth of cut combinations to investigate the effect of process parameters on BUE formation. The effect of BUE on micromilling outputs such as micromilling forces, surface roughness, tool life and burr formation has been studied in detail using tailored micro end mills. A design methodology is proposed to design tailored micro end mills with minimized tool deflections.

5.2 Design of Micro End Mills

In this part a novel single edge cutting tool geometry has been designed. Taking into account the side effects of tool runout in micromilling, single edge cutting tools can be used in some applications, especially when studying micro scale cutting processes. Also, when compared to the multi-flute micro end mills, single edge cutting tool provides a lower tooth passing frequency, which can be helpful in having a stable machining process. Furthermore, knowing the fact that most of the micromilling applications do not require deep micro features, and in most cases very low depth of cut values are used (because of low stiffness of the cutting tools), and considering requirements for reducing depth of cut with reduction in tool diameter to avoid tool breakage, the helical geometry is not always a requirement and cutting tools having straight edges can be a good alternative.

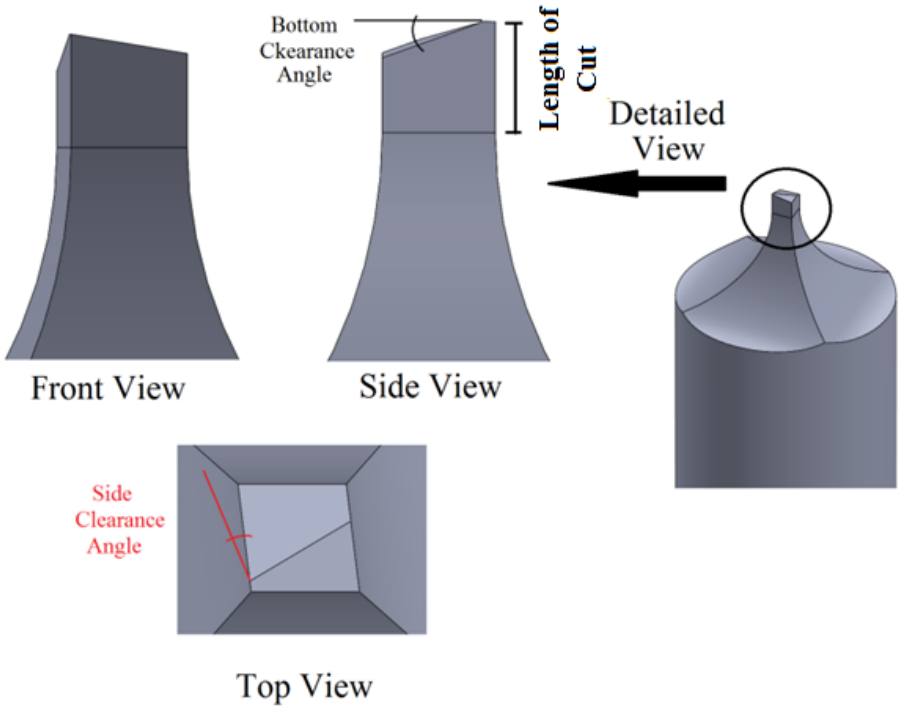

Figure 5.1: Geometry of the designed single edge cutting tool.

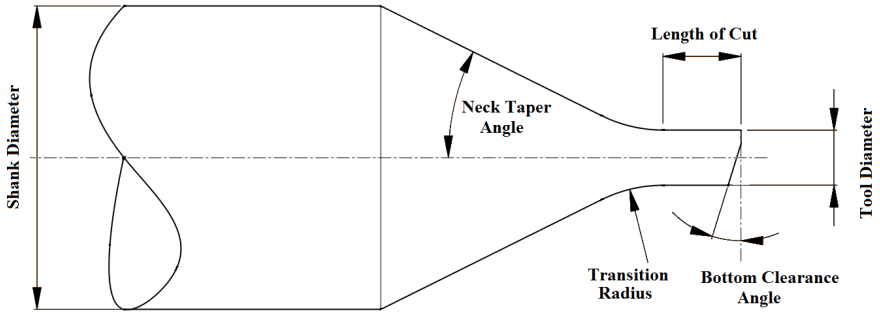

Figure 5.2: Design parameters of the tool.

The simple geometry of this cutting tools not only contribute to their ease of fabrication, but also makes it possible to further analyze and understand the process of chip formation and cutting mechanism during micromilling operations, by eliminating complexities arising from helical geometry. In addition, the elimination of helical flutes can further strengthen the micro end mill, which in turn will result in lower deflections, as a result tool can be used at higher feed and depth of cut values, which increases material removal rate and process productivity. The solid model of the proposed cutting tool geometry is depicted in Figure 5.1. Detailed tool design parameters can be seen in Figure 5.2. Length of cut, bottom and side clearance angles, neck taper angle and transition radius can be named as important micro end mill design parameters.

5.3 Fabrication of Micro End Mills

μ-WEDM process is used to fabricate micro end mills using Sodick AP250L high precision WEDM machine with oil as dielectric fluid. Ultra-fine grain tungsten carbide rods (grain size < 0.7 μm) of 4 mm diameter are used for micro end mills fabrication. Tungsten carbide rods are mounted on the indexer of the WEDM machine (as shown in Figure 5.3) with a runout less than ±1 μm.

The tools are fabricated in two steps. Firstly, an open contour machining is done

having included bottom clearance angle, then the tool is rotated based on the designed side clearance angle, and another open contour machining is performed. Depending on the required surface finish, multi-pass WEDM has been performed with different rough, semi-finish and finish WEDM passes. It should be mentioned that all machining operations are done based on the user developed machining database created based on the extensive study made in chapter 2. The user developed database made it possible to have a full control on the surface roughness, dimensional accuracy and edge radius of the machined micro end mills. Figure 5.4 schematically illustrates the process of micro end mill fabrication.

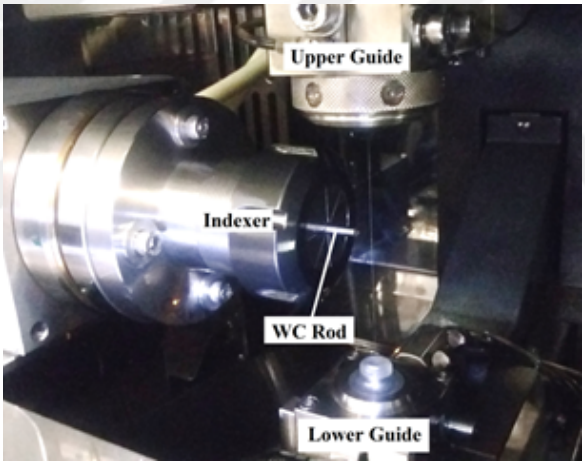

Figure 5.3: WEDM setup used for micro end mills fabrication.

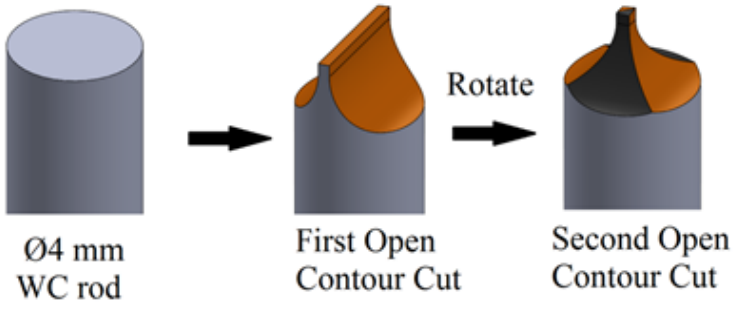

Figure 5.4: Schematic representation of micro end mill fabrication process.

In order to analyze the effect of surface roughness obtained during WEDM process on the machining performance of the micro end mills, tools with a low surface roughness and high surface roughness values are fabricated having two different clearance angles of 7° and 14°. The specifications of each tool are shown in Table 5.1. Figure 5.5 illustrates an example of the fabricated tailored single edge micro cutting tools.

Table 5.1: Specifications of the fabricated tailored single-edge micro end mills

Tool #	**Clearance Angle**	**Surface Roughness Sa (µm)**	**Edge Radius (µm)**
1	7 °	0.15 ± 0.02	2-3
2		0.6 ± 0.05	4-5
3	14 °	0.15 ± 0.02	1.5-2.5
4		0.6 ± 0.05	4-5

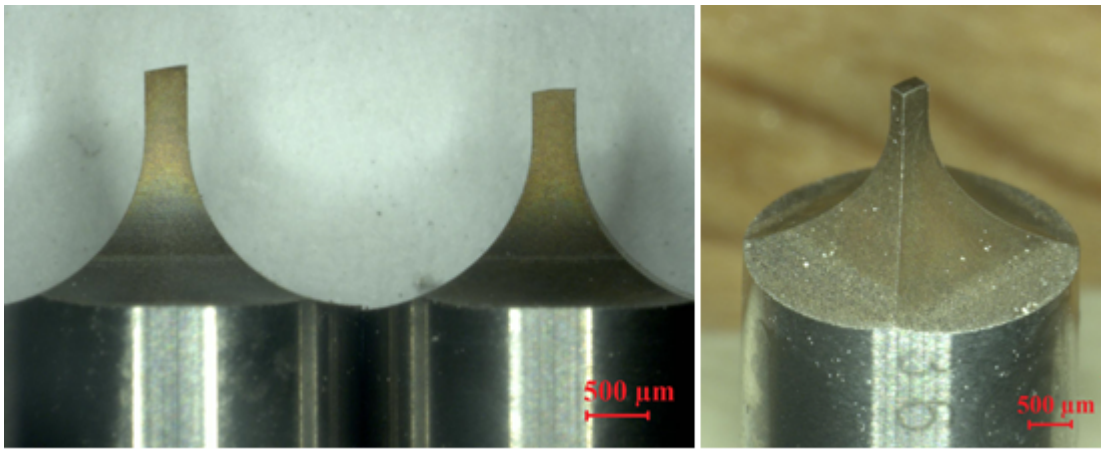

Figure 5.5: Fabricated single edge WC micro end mills.

As discussed in chapter 2, EDM surface is obtained as a result of craters induced by a series of successive random sparks on the workpiece. The size and depth of each individual spark together with the overlap between different craters determine the final morphology of the EDMed surface. Using high spark energies will result in large and deep craters, and consequently a rough EDMed surface will be achieved. In finish

WEDM process, in contrast to the rough WEDM, sparks with lower energies will result in small craters and as a result a better surface roughness can be obtained. Therefore, combinations of WEDM parameters determine the morphology of the EDMed surface. Figure 5.6 (a) illustrates the SEM image of the WEDM surface. EDS analysis of the WEDM surface is shown in Figure 5.6 (b). The composition of the WEDMed surface is same as bulk tungsten carbide material and no significant change in the composition has been observed.

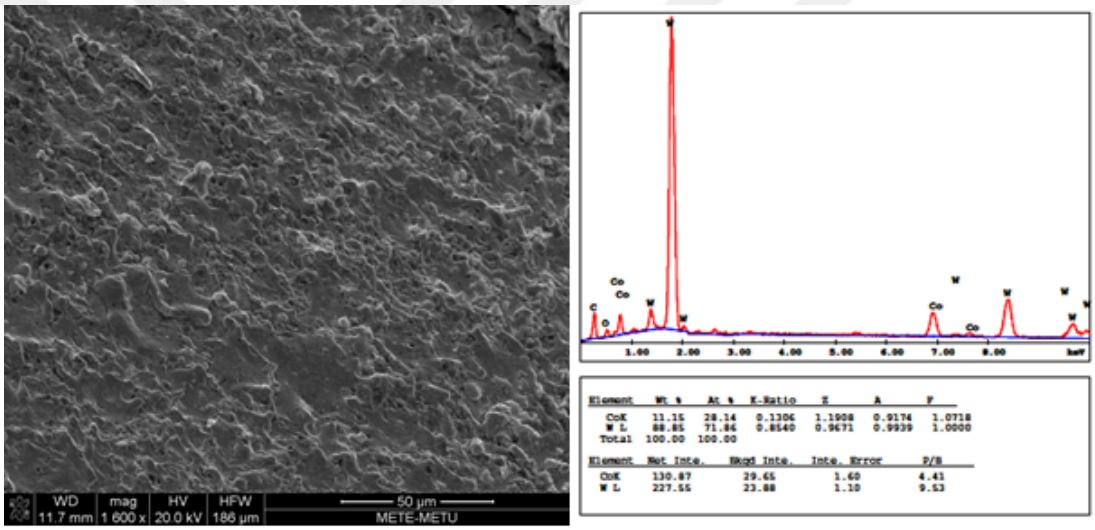

Figure 5.6: (a) SEM image of a WEDMed surface, (b) EDS analysis of WEDMed surface.

The surface roughness is believed to have a significant influence on the performance of micro end mills and micromachining process outputs. In order to analyze its effects, tools with rough and finished WEDMed surfaces are fabricated and used for micromilling of Ti6Al4V. Figure 5.7 illustrates 3D topography and top view of two micro end mills fabricated under different WEDM conditions. It should be mentioned that, in addition to surface roughness, the edge radius is also affected by the EDM process parameters. Rough EDM conditions will result in larger edge radii compare to the finish EDM conditions. As it can be seen in Figure 5.7, the difference in surface roughness and edge quality of micro end mills fabricated under different EDM conditions is completely clear.

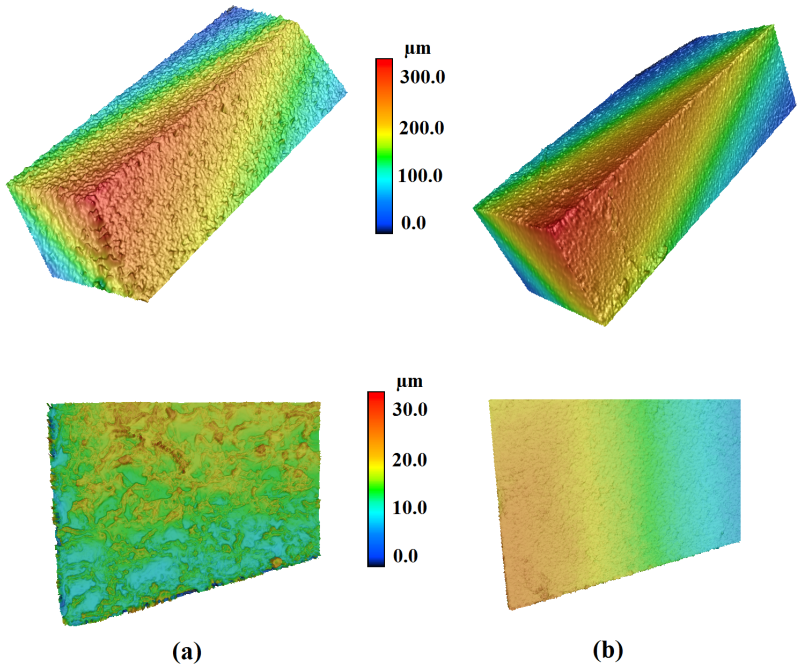

Figure 5.7: 3D topography and top view of the cutting tools: (a) rough WEDMed tool, (b) finish WEDMed tool.

5.4 Preliminary Micromilling Experiments with Tailored Micro End Mills

In order to analyze the effect of tool conditions (surface quality, clearance angle and edge radius) on the performance of micro end mills, a series of full immersion micromilling experiments (slot micromilling) are conducted on Ti6Al4V using DMG HSC 55 milling machine equipped with a high speed spindle NSK HES 510. A same experimental setup explained in chapter 3 is used for micromilling experiments. The experiments are done at different feed per tooth values of (0.6, 0.8, 1, 2, and 4) µm/tooth, while spindle speed and depth of cut are kept constant at 28000 RPM and 30 µm, respectively. No coolant was used during experiments.

In order to analyze the performance of each tool under long term cutting operations, three circular pockets with 15 mm diameter has been machined at three different

feed rates of 20 mm/min, 84 mm/min and 112 mm/min between each group of slot micromilling experiments, as schematically illustrated in Figure 5.8. The radial immersion was 60% of the cutting tool diameter in all pocket micromilling operations. Total machining time for three pockets was approximately 15 minutes.

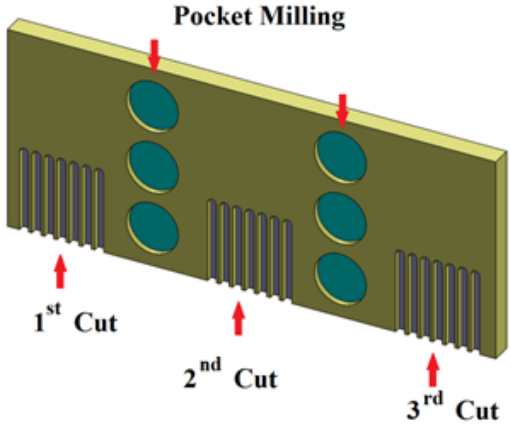

Figure 5.8: Schematic representation of micromilling experiments.

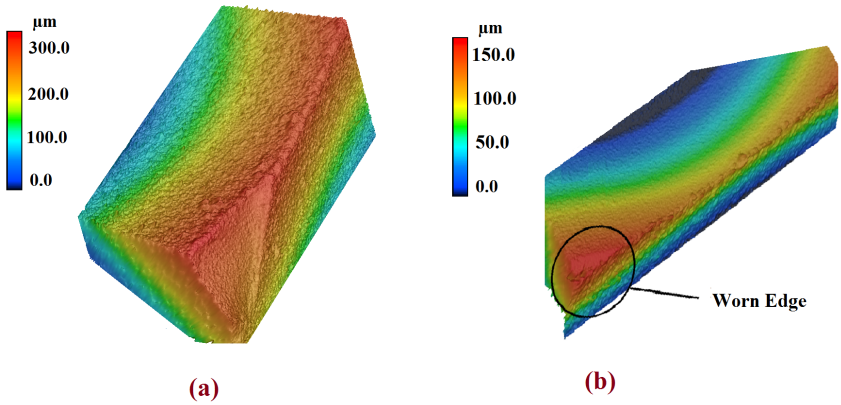

Figure 5.9: (a) Chipped cutting edge (Rough WEDMed-CA=14°), (b) Worn tool (Finish WEDMed-CA=14°).

For each set of experiments, micromilling forces are measured. For comparison purposes, the experiments are also conducted by using a conventional micro end mill. Root mean square (RMS) of the resultant cutting force (F_{res}) is calculated and used for

comparison purposes.

For a tool with a clearance angle of 14° fabricated under rough WEDM conditions, chipping has been observed at the early stage of the experiments as depicted in Figure 5.9 (a). Edge chipping may be attributed to the weakening effect of both large clearance angle and rough WEDM conditions, because large clearance angle weakens the wedge of the cutting tool and high spark energies of rough WEDM conditions results in a larger heat affected zone, resolidified layer and may result in the creation of micro-cracks. Due to the failure of the rough WEDMed micro end mill with 14° clearance angle, no cutting force data are reported.

After micromilling experiments edge conditions has been monitored using scanning electron microscope (SEM) and 3D laser scanning microscope. The edge condition for a finish WEDMed tool with 14° clearance angle is shown in Figure 5.9 (b). As it can be seen there exist a flank wear and edge rounding in the cutting edge. The edge radius of the micro end mill has been increased from initial radius of 2 μm to 6 μm. For other cutting tools a built-up edge has been observed. Figure 5.10 illustrates a BUE formed on a finish WEDMed tool with 7° clearance angle. The results of cutting force analysis for each cutting tool are shown in Figure 5.11.

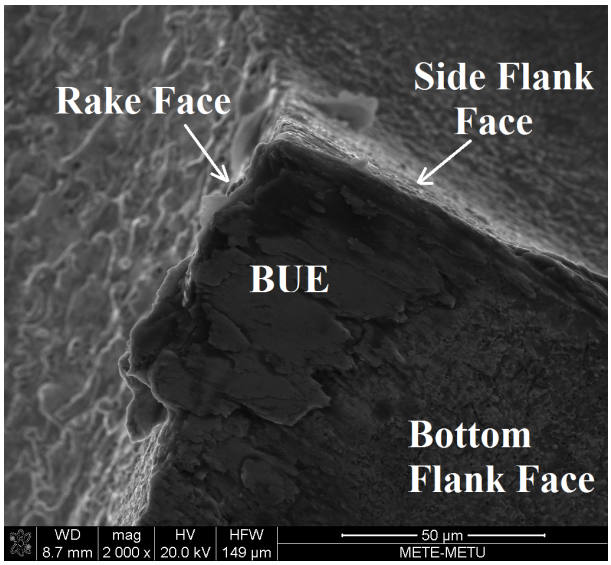

Figure 5.10: SEM image of the BUE formed in a finish WEDMed-CA=7°.

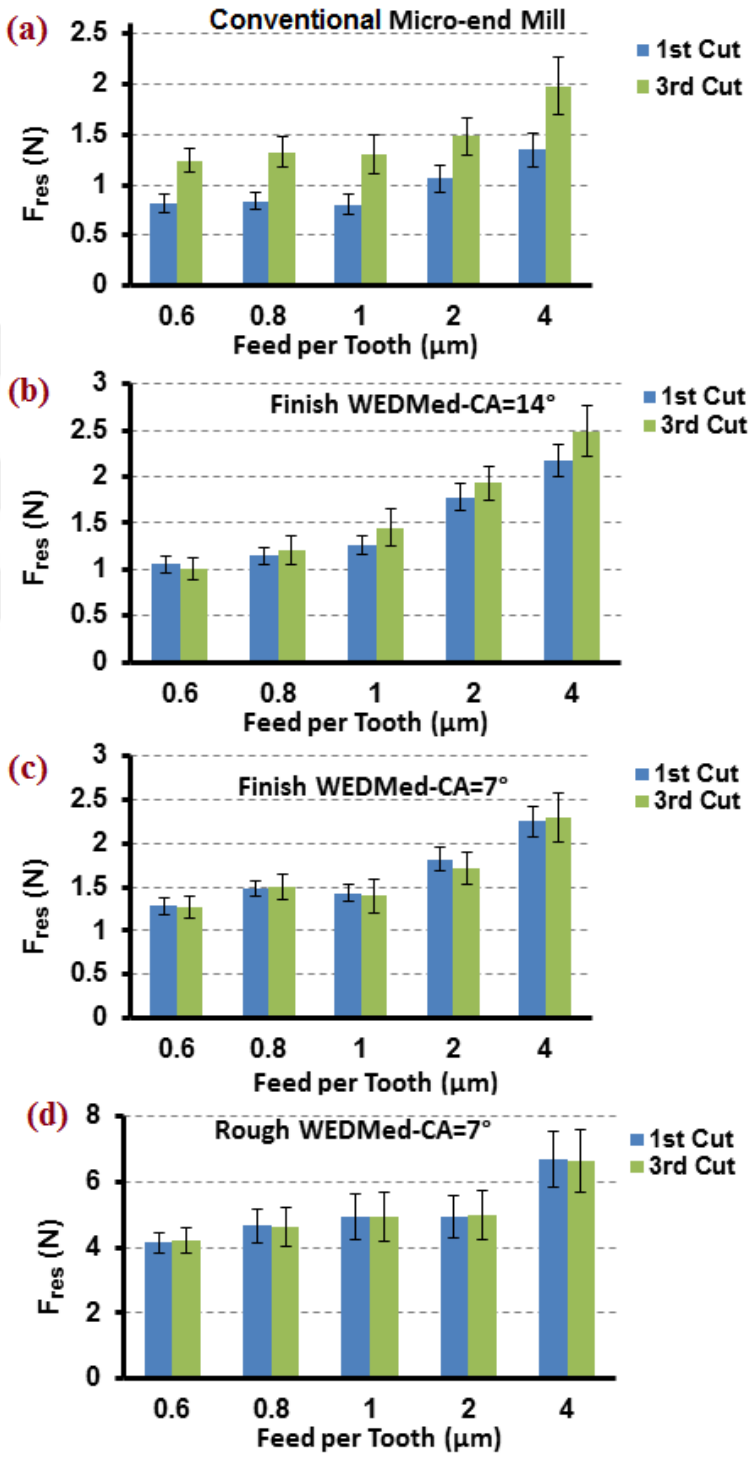

Figure 5.11: RMS of the resultant force: (a) Conventional micro end mill, (b) Finish WEDMed-CA=14°, (c) Finish WEDMed-CA=7°, (d) Rough WEDMed-CA=7°.

Investigation of root mean square of the resultant cutting force for conventional micro end mill reveals that there is a significant increase in the RMS of the resultant force between first and third group of slot micromilling experiments (Figure 5.11 (a)). This can mainly attributed to the wear of the conventional micro end mill, which is in the form of edge rounding as depicted in Figure 5.12.

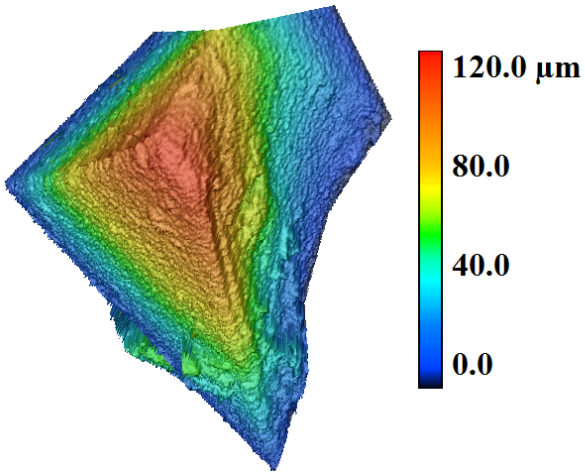

Figure 5.12: Edge rounding observed in conventional micro end mill.

A same trend similar to conventional micro end mill, has also been observed for the case of finish WEDMed cutting tool with a clearance angle of 14° as depicted in Figure 5.11 (b), however the differences are smaller compare to the conventional micro end mill. The edge rounding is the reason of increased cutting forces at third group of slots compare to the first group for these cutting tools. Both tools with large clearance angles (independent of their surface quality) experience tool life issues in the form of edge chipping or edge rounding, which shows the significance of edge strength and adverse effect of edge weakening when using large clearance angles.

As it can be seen in Figure 5.11, the RMS of the resultant forces for tools having 7° clearance angle, do not show an increasing trend similar to those observed in conventional micro end mill and finish EDMed tool with a clearance angle of 14°. The major difference between rough and finish WEDMed tools of 7° clearance angle is in the magnitude of the cutting forces. It can be seen in Figure 5.11 that, rough WEDMed tool has larger RMS forces. These large cutting forces can be attributed to the larger

cutting edge radius, which results in increased ploughing forces. Investigation of the cutting edges after micromilling experiments shows a built-up edge (BUE) formed on the rake face of these cutting tools as depicted in Figure 5.10.

Based on the results obtained from preliminary micromilling experiments, this section aims to further investigate the BUE formation in micromilling of Ti6Al4V, with the aim of understanding the effect of BUE on micromilling process outputs such as micromilling forces, surface quality, dimensional accuracy and burr formation. Also, this section investigates the protective effect of BUE in micromilling of Ti6Al4V using tailored micro end mills by performing long term cutting experiments.

5.5 Micromilling Experiments for BUE Investigations

In order to investigate BUE formation and its effects on process outputs of micromilling, the same setup of preliminary micromilling experiments are used. Two single edge micro end mills with 0.4 mm diameter and two different length of cuts of 200 μm and 400 μm are fabricated under same finish WEDM parameters with dimensional tolerances of ±2 μm. The objective of selecting two different length of cuts is to have an insight into the effect of tool deflections on the process outputs, knowing the fact that under same cutting tool geometry parameters, deflection of micro end mill increases with increasing length of cut. Slot micromilling experiments are done under the conditions of Table 5.2, while feed rate is kept constant at 4 μm/tooth. For each experiments the average BUE height, cutting forces, surface roughness, and burr parameters are measured.

The average BUE length is measured by laser scanning microscope as shown in Figure 5.13. The results of average BUE height measurements for two different cutting tools are shown in Figure 5.14. As it can be seen in Figure 5.14 for both cutting tools, BUE height increases when changing depth of cut from 30 μm to 40 μm and it decreases by changing depth of cut from 40 μm to 50 μm. It can also be seen that for all micromilling conditions BUE height for lower cutting speed of 28000 RPM is larger than higher cutting speed of 36400 RPM.

Table 5.2: Experimental conditions used for BUE studies

Exp. #	Spindle Speed (RPM)	Depth of Cut (µm)
1	28000	30
2		40
3		50
4	36400	30
5		40
6		50

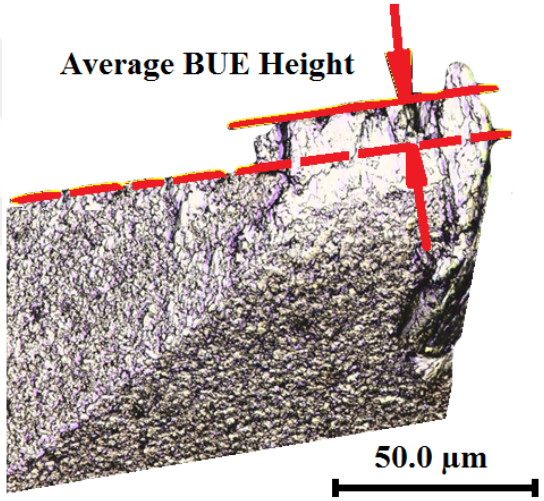

Figure 5.13: Measurement of average BUE height by 3D laser scanning microscope.

To further understand the correlation between cutting forces and BUE formation, RMS of the resultant forces are obtained for the experiments of Table 5.2. In order to remove the effect of depth of cut variations, RMS of the resultant forces are normalized with respect to depth of cut obtained by profile measurements using 3D laser scanning microscope. Figure 5.15 illustrates the results of normalized RMS of resultant forces.

As it can be seen in Figure 5.15, except for one case (Lc-400 µm at 36400 RPM) there is a correlation between BUE height and machining forces, where larger BUE size resulted in a larger resultant forces.

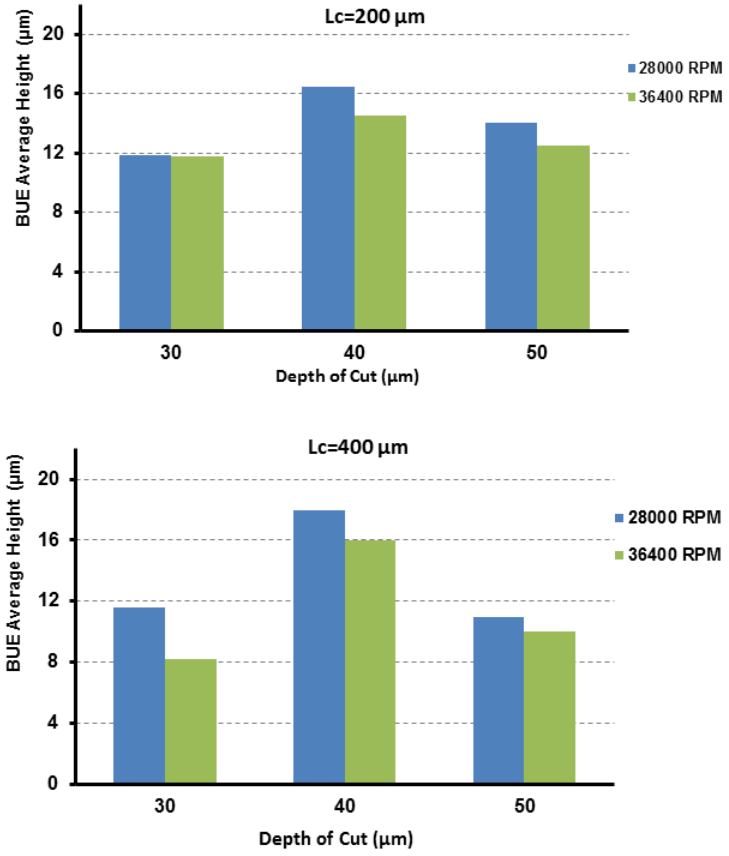

Figure 5.14: Average BUE height for tools having different length of cuts.

In order to have an insight into the effect of BUE on the surface quality of the machined micro-slots, 3D laser topography of the machined microchannels are obtained. For each slot, arithmetic mean height (Sa) is obtained. Figure 5.16 illustrates an example of the surfaces obtained by the conditions of experiments 4, 5 and 6 of Table 5.2, using a cutting tool with a length of cut of 200 µm. It should be mentioned that a height magnification of 300% is used. The results of surface roughness measurements are shown in Figure 5.17.

Analysis of the surface roughness of the experiments revealed that for all experiments better surface roughness has been achieved at the highest BUE height. This can be mainly because of the burnishing effect of the BUE on the surface. Also it can be seen that a cutting tool with a larger length of cut gives larger Sa values compare to

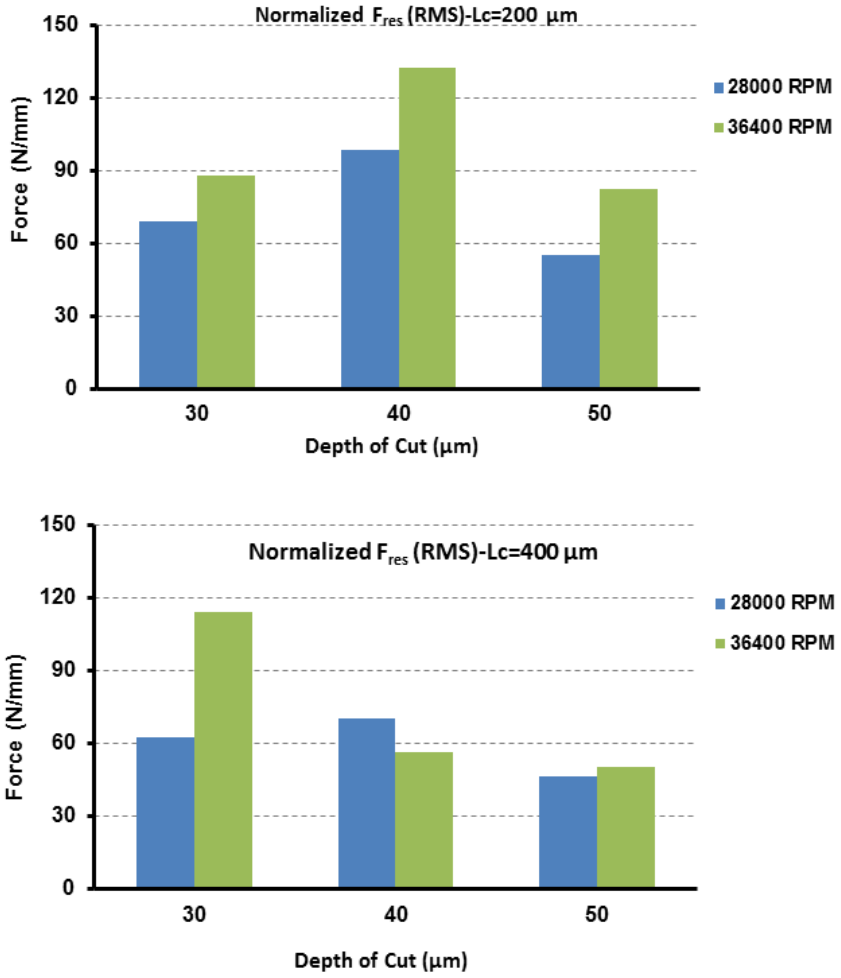

Figure 5.15: Normalized resultant forces for tools having different length of cuts.

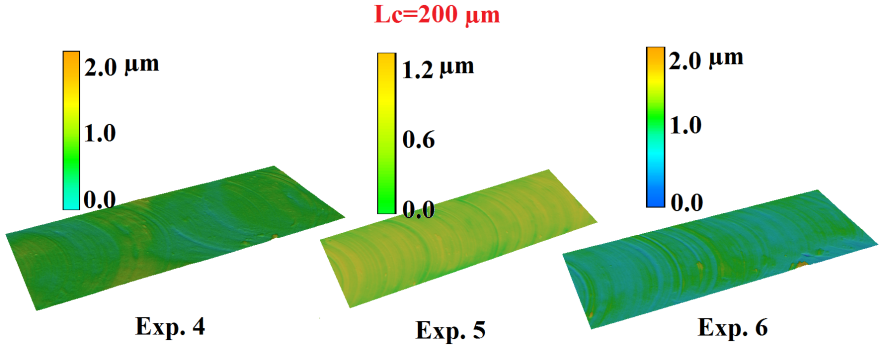

Figure 5.16: Surface roughness of the machined microchannels.

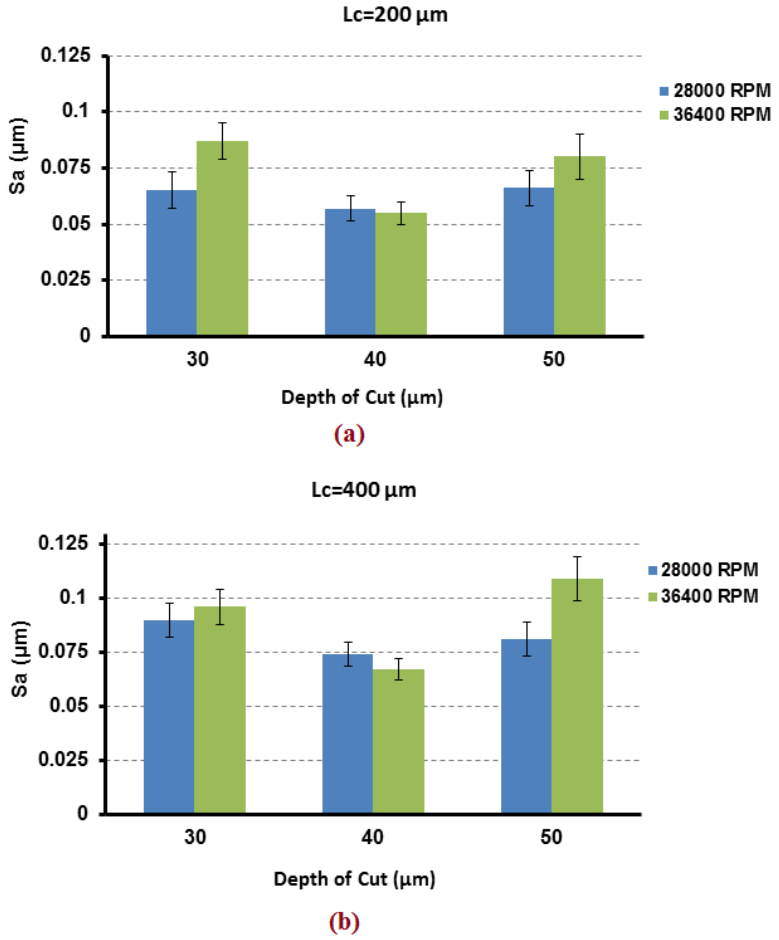

Figure 5.17: Arithmetic mean roughness values for the machining conditions of Table 5.2.

a tool with shorter length of cut. This can be interpreted as the adverse effect of tool deflections on the machined surface quality, which will be discussed in detail in the subsequent sections of this thesis.

Having determined the effect of BUE on surface roughness, it is important to discover the effect of BUE formation on tool life during micromilling operations. In chapter 4, the protective effect of BUE in orthogonal machining of Ti6Al4V has been explored. The aim of next section is to investigate the possibility of observing same phenomena when using tailored micro end mills.

5.6 Effect of BUE on Tool life

In order to analyze the effect of built-up edge formation on tool life of the tailored micro end mills, long term micromilling experiments has been done on Ti6Al4V. For this purpose 80 microchannels with a length of 50 mm has been machined at a spindle speed of 28000 RPM, feed rate of 112 mm/min and a depth of cut of 50 μm.

The machining process has been interrupted after machining each 20 microchannels, and tool condition is monitored using 3D laser scanning microscope. In all cases a BUE has been observed. No significant difference has been observed between BUE of different microchannels. Figure 5.18 illustrates the SEM image of the BUE formed at the 80th microchannel.

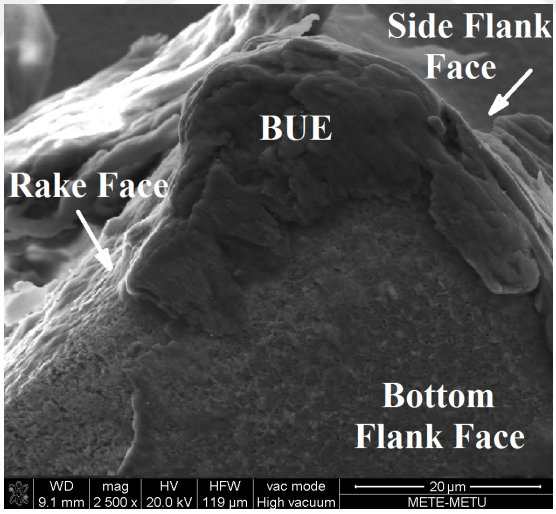

Figure 5.18: SEM image of BUE after machining 80 microchannels.

After machining 80 microchannels, in order to gain an understanding about the possibility of chemical reaction between tool and material during the process of micromilling, BUE has been removed from the cutting tool by a very fine mechanical cleaning process and EDS analysis is performed in a location exactly underneath the BUE, to check for a change in the chemical composition of the micro end mill. The EDS analysis underneath the BUE is shown in Figure 5.19 (a). Also EDS analysis of the bulk tool material has been obtained for comparison purposes which is shown in

Figure 5.19 (b).

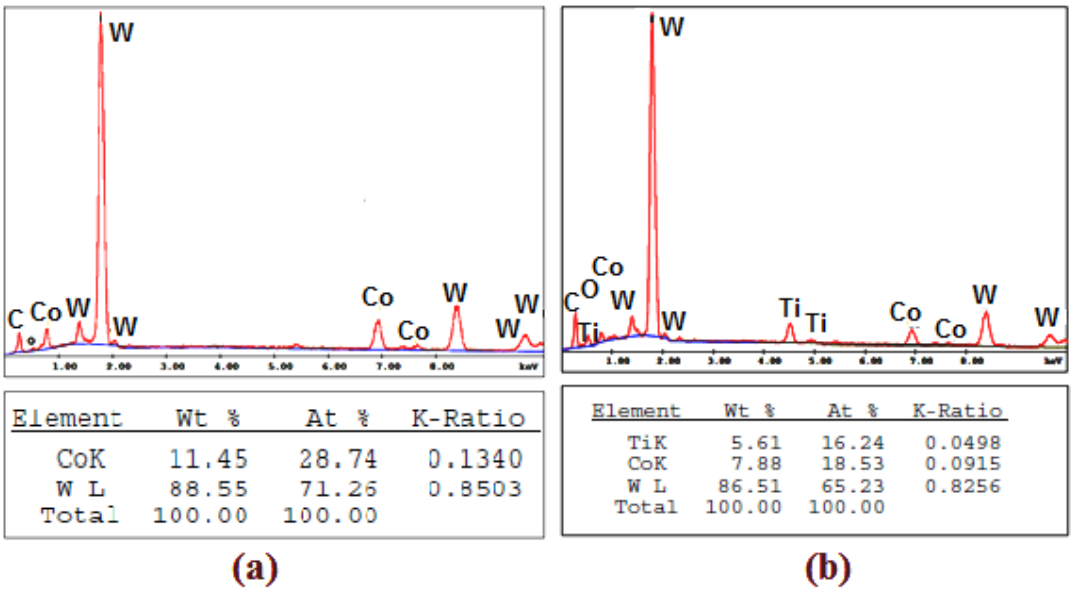

Figure 5.19: EDS analysis of (a) bulk tool material, (b) Underneath of the BUE.

As it can be seen in the EDS analysis, the cobalt content of the tool material underneath BUE has been decreased from 11.6 wt% to about 8 wt%, when compared to the cobalt content of the bulk material, which is mainly due to the high chemical affinity of the titanium alloy.

For each microchannel cutting forces are also recorded. Figure 5.20 (a-d) illustrates the measured cutting forces for the first, second, 40th and 80th microchannel, respectively. As it can be seen in Figure 5.20, at the first microchannel the cutting forces, especially forces in Y direction are smaller than other microchannels. This can be mainly attributed to the very sharp edge of the tool at the beginning of the machining. However, when the first microchannel is machined and the initial phase of wear occurred, the edge radius increases. As a result of increased machining forces due to edge rounding, high pressures necessary for the BUE formation will develop. It can be seen in Figure 5.20 that the forces in the second microchannel has been increased with respect to the first microchannel. After BUE formation process stabilizes, the cutting forces almost remain the same when 40th and 80th microchannels are compared. This can be interpreted as the protective effect of the BUE under stable conditions, which

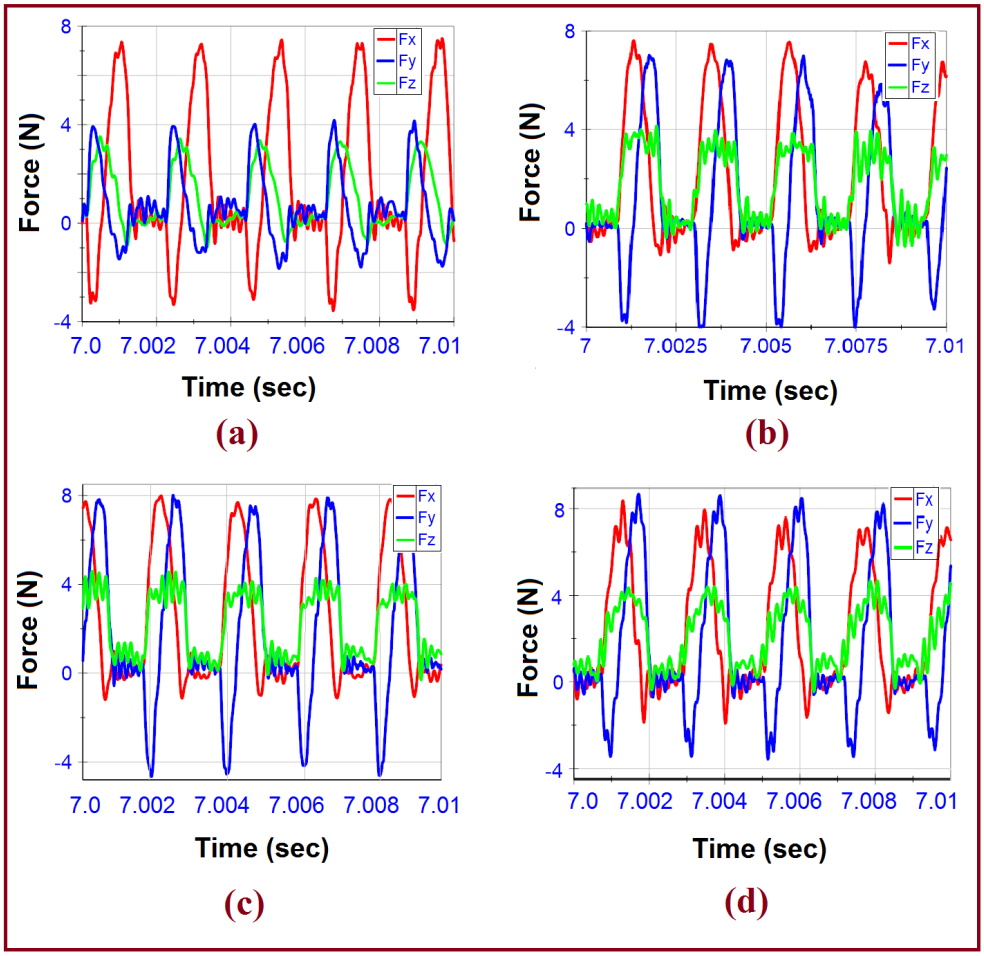

Figure 5.20: Measured cutting forces for: (a) First microchannel, (b) Second microchannel, (c) 40th microchannel, (d) 80th microchannel.

has also been observed in orthogonal cutting experiments.

5.7 Relationship between BUE and Burr Formation

Since in micromilling operations the feature size is small, the removal of burrs becomes much more difficult compare to the conventional milling processes [188]. When burr removal is done by mechanical deburring methods, there is a risk of distortion because of low stiffness of the machined micro-features. Therefore, minimizing burr formation

gains significant importance in micro mechanical machining processes.

This study deals with the effect of machining parameters and BUE on the burr formation when machining Ti6Al4V using tailored micro end mills made from WC. For this purpose the burrs which are formed as a results of experimental conditions of Table 5.2 has been analyzed using SEM and 3D laser scanning microscope. SEM is used to measure burr width and laser microscope is used to measure burr height. Figure 5.21 illustrates SEM images of the burrs formed when micromilling with a tool of Lc=200 μm under experimental conditions of Table 5.2. The measured burr height and width for each cutting tool are shown in Figure 5.22.

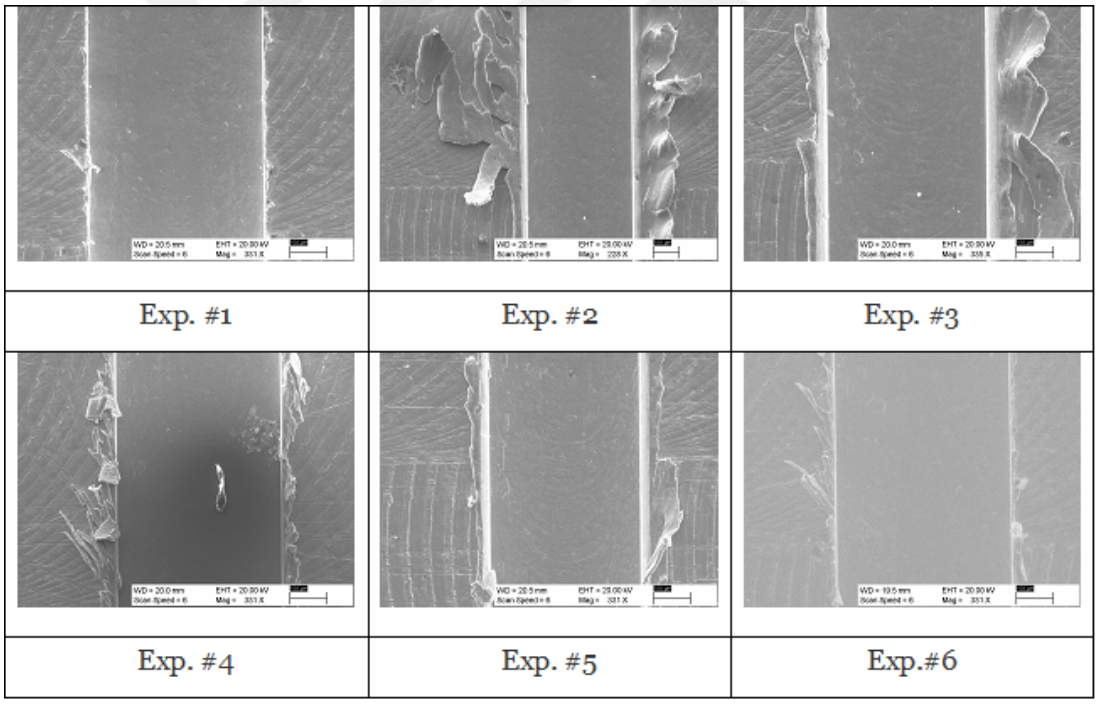

Figure 5.21: SEM image of the burrs formed under experimental conditions of Table 5.2 for Lc=200 μm.

SEM and laser microscope analysis of the burrs formed during experiments revealed that there is no specific correlation between burr height and burr width with the BUE height. However, burr height for lower cutting speed (28000 RPM) and lowest depth of cut (30 μm) tends to be minimum. Both burr height and burr width increases with increasing depth of cut independent from length of cut of the cutting tools. Therefore,

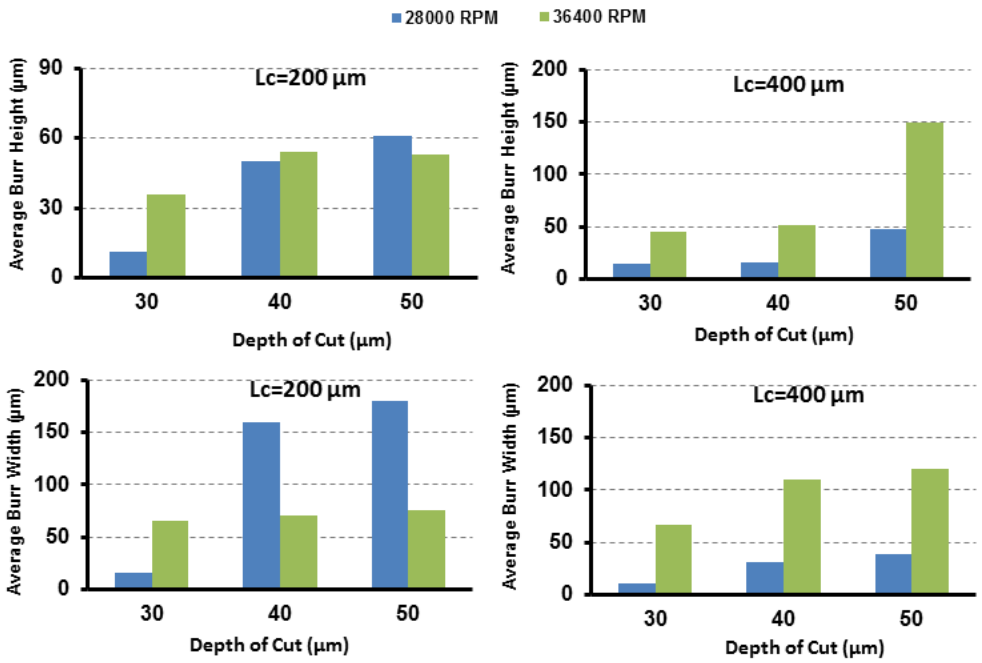

Figure 5.22: Measure burr height and width under experimental conditions of Table 5.2.

it can be said that burr parameters are independent form tool deflections.

5.8 Analysis of the Effect of Deflection on Surface Roughness

It is really difficult to isolate deflections in the machining process, since it is a very complex system with many constituents. However, in this study the use of tailored cutting tools made it possible to analyze the effect of tool deflection on surface roughness by changing length of cut of the micro end mills, knowing the fact that the longer tool will experience a larger deflection under the same machining conditions.

Two cutting tools having the same diameter (~ 400 µm) , clearance angles (7°), neck taper angle (45°), transition radius (0.075 µm) with different length of cuts of

0.2 mm and 0.6 mm are fabricated and used to investigate the effect of deflection on surface roughness. Both tools are fabricated under same μ-WEDM conditions to guarantee the dimensional equality, surface roughness and edge radius. Slot micromilling experiments are performed at 28000 RPM and constant depth of cut of 30 μm at a feed rates of (2, 3, 4, 5 and 6) μm/tooth. Figure 5.23 illustrates the results of surface roughness measurements.

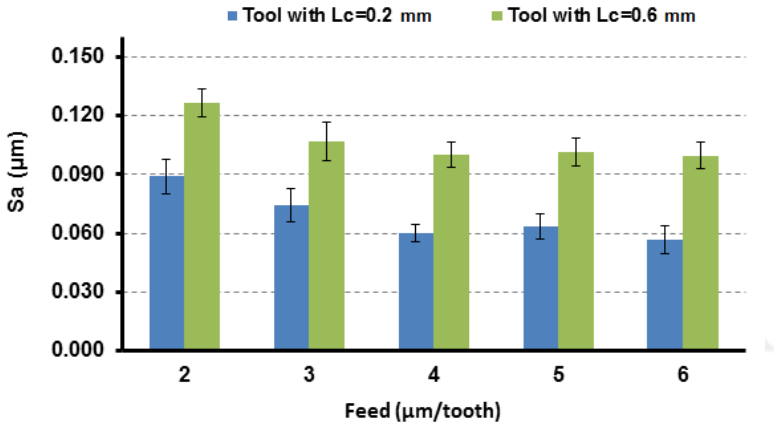

Figure 5.23: Effect of length of cut on surface roughness.

As it can be seen in Figure 5.23, at all feed rates the cutting tool with a shorter length of cut resulted in a better surface quality. From Figure 5.23, it can also be seen that for both cutting tools micromilling at an uncut chip thickness closer to the cutting edge radius resulted in the highest surface roughness. The surface roughness has improved by further increasing the feed rate. It should be mentioned that no significant difference in the microchannel depth has been observed, however, the microchannel width for shorter micro end mill was about 12 μm-18 μm larger than longer micro end mill. Tight manufacturing tolerances about ±2 μm guarantees that these differences are not due to the manufacturing error of the micro-tools, rather they are emanating from different deflections experienced by the tools due to different length of cuts.

The experimental results obtained in this section showed the effect of tool deflections on the dimensional accuracy and surface quality of the machined parts. Based on the results of this section, tool deflections need to be well understood and minimized

during micromilling operations to produce high precision parts with better surface finish. Therefore, the rest of this chapter is devoted to the study of tool deflections of tailored micro end mills.

5.9 Analytical Modeling of Tool Deflection for Tailored Micro-end Mills

This section aims to calculate tool deflections of tailored micro end mills by developing an analytical model of tool deflections. As it has been mentioned in chapter 3, the analytical models can be used to calculate instantaneous chip load including tool deflections and to improve cutting force predictions in micromilling operations.

Castigliano's second theorem is used to calculate the end deflection of tailored micro end mills in a similar way which has been discussed in chapter 3. Using this theory the deflection of a micro end mill (δ) can be related to the elastic strain energy stored in the micro end mills (U) under the action of machining forces (F) by using Castigliano's second theorem:

$$\delta = \frac{\partial U}{\partial F} \tag{5.1}$$

In order to use Castigliano's second theorem, the tool is partitioned into four sections as illustrated in Figure 5.24.

The following terminology is used during formulations:

- The subscript 't' is used for tangential direction and subscript 'r' is used for radial direction.
- The subscript 'C' is used for cutting portion of the tool which has a length of 'L_C' and extends from tool tip to the plane shown as end of cutting part in Figure 5.24.
- The subscript 'R' stands for the part with transition radius having a length of 'L_R' between end of cutting plane and end of transition radius plane.

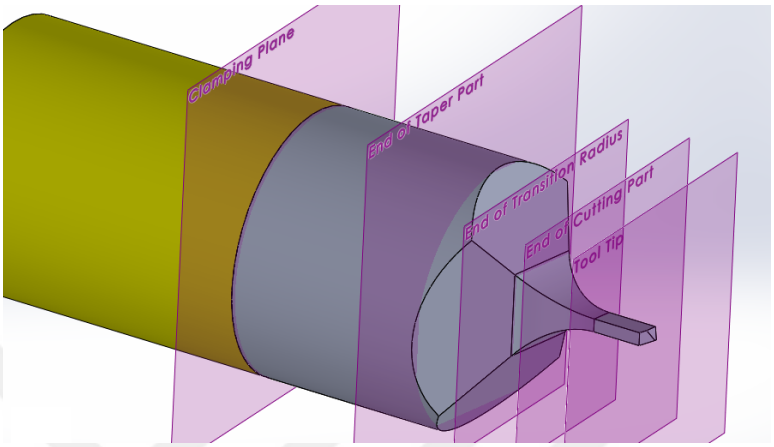

Figure 5.24: Tool partitioning for deflection calculations

- The subscript 'T' is used for the tapered part having a length of 'L_T' extending from end of transition radius plane to the end of tapered part.
- The subscript 'S' is used for the shank part having a length of 'L_S' extending from end of tapered part to the starting point of clamping.

The energy stored in the micro end mill as a result of different components of the machining forces (F_r: radial force and F_t: tangential force) can be expressed as:

$$U_t = \int_0^{L_C} \frac{M_{tC}^2}{2EI_{tC}}dx + \int_{L_C}^{L_R} \frac{M_{tR}^2}{2EI_{tR}}dx + \int_{L_R}^{L_T} \frac{M_{tT}^2}{2EI_{tT}}dx + \int_{L_T}^{L_S} \frac{M_{tS}^2}{2EI_{tS}}dx \tag{5.2}$$

$$U_r = \int_0^{L_C} \frac{M_{rC}^2}{2EI_{rC}}dx + \int_{L_C}^{L_R} \frac{M_{rR}^2}{2EI_{rR}}dx + \int_{L_R}^{L_T} \frac{M_{rT}^2}{2EI_{rT}}dx + \int_{L_T}^{L_S} \frac{M_{rS}^2}{2EI_{rS}}dx \tag{5.3}$$

Assuming that the forces are uniformly distributed over engagement depth (depth of cut (a_p)), the distributed uniform force can be replaced by a concentrated force acting in a position of '$\frac{a_p}{2}$' from tool tip, as depicted in Figure 5.25. Therefore at any point at a distance 'x' from tool tip, the moment can be written as:

$$M(x) = F.\left(x - \frac{a_p}{2}\right) \tag{5.4}$$

Since there is no other external force acting on the micro end mill, we have:

$$M_{tC} = M_{tR} = M_{tT} = M_{tS} = F_t.\left(x - \frac{a_p}{2}\right) \tag{5.5}$$

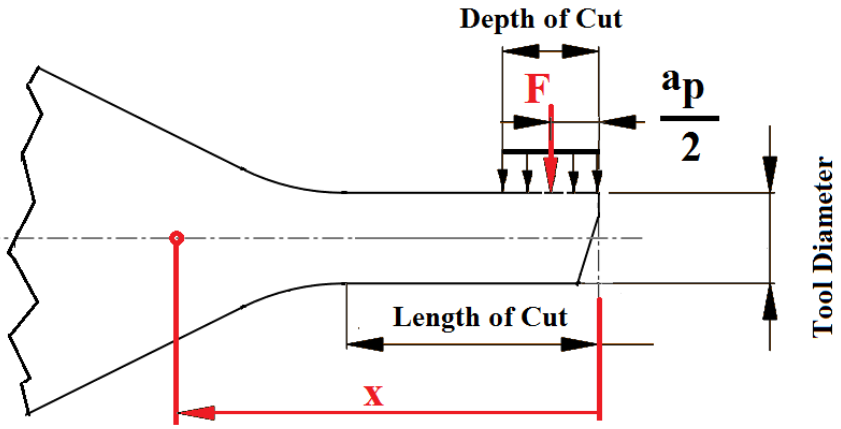

Figure 5.25: Concentrated force applied to a position of $\frac{a_p}{2}$ from tool tip.

$$M_{rC} = M_{rR} = M_{rT} = M_{rS} = F_r.\left(x - \frac{a_p}{2}\right) \tag{5.6}$$

Substituting equation 5.5 into equation 5.2 and Equation 5.6 into 5.3, and applying Equation 5.1, the end deflections in tangential and radial directions can be written as:

$$\delta_t = \frac{F_t}{E}\left(\int_0^{L_C} \frac{\left(x - \frac{a_p}{2}\right)^2}{I_{tC}}dx + \int_{L_C}^{L_R} \frac{\left(x - \frac{a_p}{2}\right)^2}{I_{tR}}dx + \int_{L_R}^{L_T} \frac{\left(x - \frac{a_p}{2}\right)^2}{I_{tT}}dx + \int_{L_T}^{L_S} \frac{\left(x - \frac{a_p}{2}\right)^2}{I_{tS}}dx\right) \tag{5.7}$$

$$\delta_r = \frac{F_r}{E}\left(\int_0^{L_C} \frac{\left(x - \frac{a_p}{2}\right)^2}{I_{rC}}dx + \int_{L_C}^{L_R} \frac{\left(x - \frac{a_p}{2}\right)^2}{I_{rR}}dx + \int_{L_R}^{L_T} \frac{\left(x - \frac{a_p}{2}\right)^2}{I_{rT}}dx + \int_{L_T}^{L_S} \frac{\left(x - \frac{a_p}{2}\right)^2}{I_{rS}}dx\right) \tag{5.8}$$

In order to calculate deflection components, it is necessary to determine the moment of inertia of each portion of the end mill depicted in Figure 5.24.

5.9.1 Moment of Inertia of the Cutting Portion

For cutting portion the cross sectional area is constant throughout its length. Considering the top view of the micro end mill (depicted in Figure 5.26), the cross-section is a parallelogram with side clearance angle α, therefore the moment of inertia in each

direction can be calculated as:

$$I_{rC} = \frac{1}{12}\left(\frac{D_C}{2\cos(\alpha)}\right)^3 D_C \cos^3(\alpha) = \frac{D_C^4}{96} \tag{5.9}$$

$$I_{tC} = \frac{D_C^4}{96}\left(4 + \tan^2(\alpha)\right) \tag{5.10}$$

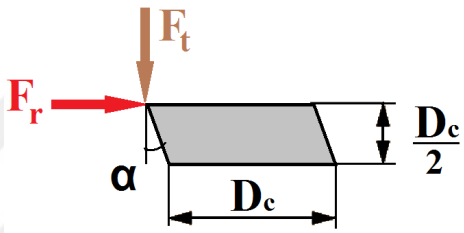

Figure 5.26: Cross-section of the cutting portion.

5.9.2 Moment of Inertia of the Transition Portion

For transition portion with radius 'R_{Tr}' , the cross-section varies with 'x'. Using dimensions given in Figure 5.27, the moment of inertia in the tangential and radial directions can be obtained as:

$$I_{tR}(x) = \frac{1}{12}\left[a_{Tr}(x)\, b_{Tr}(x) \cos(\alpha)\left(b_{Tr}^2(x) + a_{Tr}^2(x)\sin^2(\alpha)\right)\right] \tag{5.11}$$

$$I_{rR}(x) = \frac{1}{12} a_{Tr}^3(x)\, b_{Tr}(x) \cos^3(\alpha) \tag{5.12}$$

where

$$b_{Tr}(x) = D_c + 2R_{Tr}\left(1 - \sqrt{1 - \left(\frac{x}{R_{Tr}}\right)^2}\right) \tag{5.13}$$

$$a_{Tr}(x) = \frac{D_c}{2}\cos(\alpha) + 2R_{Tr}\left(1 - \sqrt{1 - \left(\frac{x}{R_{Tr}}\right)^2}\right) \tag{5.14}$$

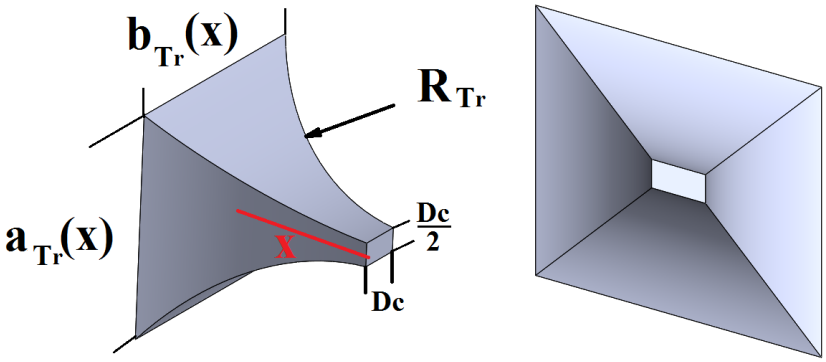

Figure 5.27: Cross-section of the transition portion.

5.9.3 Moment of Inertia of the Tapered Portion

For tapered portion with a neck taper angle of γ, the cross-section varies with 'x'. Using dimensions given in Figure 5.28, the moment of inertia in tangential and radial directions can be obtained as:

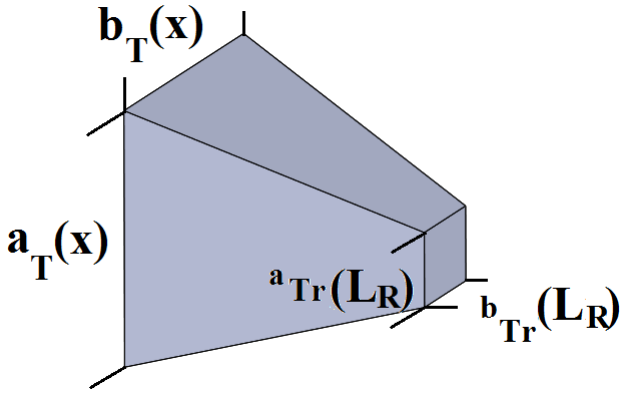

Figure 5.28: Cross-section of the tapered portion.

$$I_{tT}(x) = \frac{1}{12}\left[a_T(x)\, b_T(x) \cos(\alpha)\left(b_T^2(x) + a_T^2(x) \sin^2(\alpha)\right)\right] \tag{5.15}$$

$$I_{rT}(x) = \frac{1}{12} a_T^3(x)\, b_T(x) \cos^3(\alpha) \tag{5.16}$$

where

$$a_T(x) = a_{Tr}(L_R) + 2x\tan(\gamma) = \left(\frac{D_c}{2}\cos(\alpha) + 2R_{Tr}(1-\cos(\gamma))\right) + 2x\tan(\gamma) \quad (5.17)$$

$$b_T(x) = b_{Tr}(L_R) + 2x\tan(\gamma) = (D_c + 2R_{Tr}(1-\cos(\gamma))) + 2x\tan(\gamma) \quad (5.18)$$

5.9.4 Moment of Inertia of the Shank Portion

The shank portion has a constant circular cross-section of diameter 'D_s', therefore, its moment of inertia can be obtained as:

$$I_{rS} = I_{tS} = \frac{\pi(D_S)^4}{64} \quad (5.19)$$

5.10 Analytical Model of Tailored Micro End Mill Deflection

By substituting calculated moment of inertia into equations 5.7 and 5.8, tangential and radial deflections of tailored micro end mill can be calculated as:

$$\delta_t = \frac{96F_t\left(\left(\frac{a_p}{2}\right)\left(\frac{a_pL_C}{2} - L_C^2\right) + \frac{L_C^3}{3}\right)}{ED_C^4(4+\tan^2(\alpha))} + \frac{64F_t\left(\left(\frac{a_p}{2}\right)\left(\frac{a_p(L_S-L_T)}{2} - (L_S-L_T)^2\right) + \frac{(L_S-L_T)^3}{3}\right)}{\pi ED_S^4} +$$

$$\frac{12F_t}{\sin^2(\alpha)\cos(\alpha)E}\left(\int_{L_C}^{L_R} \frac{\left(x-\frac{a_p}{2}\right)^2}{\left(D_C-2R_{Tr}\left(\sqrt{1-\frac{x^2}{R_{Tr}^2}}-1\right)\right)^3\left(\frac{D_C}{2}\cos(\alpha)-2R_{Tr}\left(\sqrt{1-\frac{x^2}{R_{Tr}^2}}-1\right)\right)^3}dx\right. \quad (5.20)$$

$$\left. + \int_{L_R}^{L_T} \frac{\left(x-\frac{a_p}{2}\right)^2}{\left(\frac{D_c}{2}\cos(\alpha)+2R_{Tr}(1-\cos(\gamma))+2x\tan(\gamma)\right)^3(D_c+2R_{Tr}(1-\cos(\gamma))+2x\tan(\gamma))^3}dx\right)$$

similarly:

$$\delta_r = \frac{96F_r\left(\left(\frac{a_p}{2}\right)\left(\frac{a_pL_C}{2} - L_C^2\right) + \frac{L_C^3}{3}\right)}{ED_C^4} + \frac{64F_r\left(\left(\frac{a_p}{2}\right)\left(\frac{a_p(L_S-L_T)}{2} - (L_S-L_T)^2\right) + \frac{(L_S-L_T)^3}{3}\right)}{\pi ED_S^4} +$$

$$\frac{12F_r}{\cos^3(\alpha)\,E}\left(\int_{L_C}^{L_R}\frac{\left(x-\frac{a_p}{2}\right)^2}{\left(D_C-2R_{Tr}\left(\sqrt{1-\frac{x^2}{R_{Tr}^2}}-1\right)\right)\left(\frac{D_C}{2}\cos(\alpha)-2R_{Tr}\left(\sqrt{1-\frac{x^2}{R_{Tr}^2}}-1\right)\right)^3}dx+\right.$$
$$\left.\int_{L_R}^{L_T}\frac{\left(x-\frac{a_p}{2}\right)^2}{\left(\frac{D_c}{2}\cos(\alpha)+2R_{Tr}(1-\cos(\gamma))+2x\tan(\gamma)\right)^3(D_c+2R_{Tr}(1-\cos(\gamma))+2x\tan(\gamma))}dx\right) \tag{5.21}$$

It should be mentioned that due to the complex form of the integrals, closed form solution cannot be obtained. Therefore, in this study MATLAB built-in function '*quadgk*' is used to numerically evaluate integrals based on adaptive Gauss-Kronrod quadrature method. The total deflection is calculated as:

$$\delta_{total} = \sqrt{\delta_t^2+\delta_r^2} \tag{5.22}$$

As an example for the application of developed analytical tool deflection model, the deflection of a micro end mill with the specification of Table 5.3 is considered. A sample force with a magnitude of 8 (N) is applied in both directions. Total deflection calculated using analytical formulation for this tool is obtained as 25.69 μm.

Table 5.3: Micro end mill geometric specifications

Parameter	Value	Parameter	Value
Neck Taper Angle (deg.)	60	Clearance angle (deg)	14
Transition Radius (mm)	1.5	Overhang Length (mm)	7.7
Length of cut (mm)	0.8	Shank Diameter (mm)	4
Tip Diameter (mm)	0.4	Depth of Cut (mm)	0.05

5.11 Design Optimization of Tailored Micro End Mills Considering BUE Formation

As it has been shown in section 5.8, cutting tool deflections have a detrimental effect on the accuracy and surface quality of the machined parts. Therefore, minimizing tool deflections having stiffer micro end mills can be of significant importance in all micromilling applications. The aim of this section is to minimize tool deflections through optimizing design parameters of tailored micro end mills.

Considering the design of a single edge cutting tools with a geometry given in Figure 5.2, seven different design parameters i.e. tool diameter (D), bottom clearance angle (α_B), side clearance angle (α), length of cut (L_C), transition radius (R_{Tr}), cutting edge radius (r_e) and neck taper angle (γ) can be identified.

Different combinations of design parameters will result in different geometries, where each geometry will show different performances in terms of tool deflections and machining force induced stresses. Examples of different geometries are shown in Figure 5.29. The end mill already shown in Figure 5.5 has a transition radius of 1.8 mm, length of cut of 0.8 mm and a clearance angle of 7°. The neck taper angle in this case can be considered as 90°, however due to a larger transition radius the taper part has been vanished.

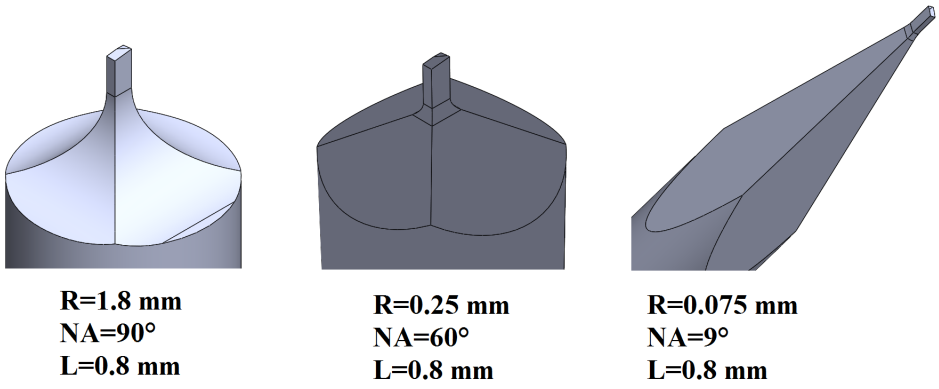

Figure 5.29: Geometry of the designed single edge cutting tools.

In this section, design optimization of tailored micro end mills using finite element method is discussed and a design optimization methodology has been proposed. This section aims to generalize the micro end mill design procedure under the framework of a design optimization methodology. Bottom clearance angle has been kept constant as 5°. It should be mentioned that cutting edge radius is controlled by the manufacturing process used for its fabrication and the length of cut (L_C) and tool diameter (D) are usually selected by the process planner depending on the machined part requirements.

5.11.1 Finite Element Modeling of Deflections and Stresses

Analysis of tool deflections and stresses are quite significant in designing proper micro end mills that could withstand harsh micromilling conditions. Understanding the effect of tool geometric parameters on machining induced deflections and stresses can be helpful in determining optimum geometric design parameters. To achieve this goal, finite element simulation has been used.

In order to have an insight into the performance of the fabricated micro tools and also to predict tool failure and deflections, a parametric solid model of the tools has been created in SolidWorks platform and is live linked into COMSOL Multiphysics to conduct finite element simulations. It should be mentioned that since it is not possible to model the rough surface using finite element model; all studies regarding finite element simulations are only valid for tools with a defect free surfaces machined under a well controlled low energy EDM regime.

The developed finite element model is used to predict tool failure using transverse rupture strength (TRS) as failure criterion. As discussed in chapter 3, a traverse rupture strength of ($TRS > 3.7$ GPa) is considered for ultra-fine grain tungsten carbide material [64] and is used as tool failure criterion. For comparison purposes the finite element model of the conventional micro end mill has been considered first. Figure 5.30 illustrates the finite element model of the conventional 0.4 mm tool (NS-tools, MSE230, L_C=0.8 mm, γ=9°, double flute, 30° helix angle, shank diameter of 4 mm).

Tetrahedral elements are used to mesh the model. The complete mesh consists of 64984 domain elements, 8942 boundary elements, and 555 edge elements. A fixed constraint has been applied into the clamping region shown in Figure 5.30. Material properties for the finite element analysis determined based on the EDS analysis of the cutting tool material which are shown in chapter 2.

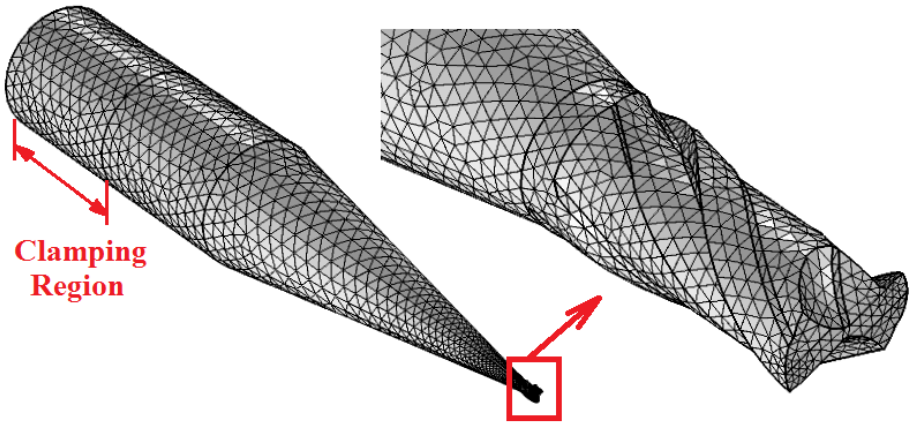

Figure 5.30: Finite element model of the conventional 0.4 mm cutting tool.

5.11.2 Verification of the Finite Element Model of Tool Failure

In order to verify the finite element models used in this study, a series of micromilling experiments are conducted on Ti6Al4V workpiece at a spindle speed of 25000 rpm and a depth of cut of 100 μm. In these tests, the feed rate is increased gradually in a stepwise manner until tool breakage occurred. In each step, the feed per tooth has been increased 1 μm/tooth and cutting forces are recorded. Figure 5.31 illustrates the recorded cutting forces for three different micro end mills.

Figure 5.31 (a) belongs to a conventional cutting tool with a nominal diameter of 0.4 mm. The feed per tooth value at the point of failure was 11 μm/tooth, where cutting tool experienced forces about 13 (N) and 10 (N) in X and Y directions, respectively. Figure 5.31 (b) illustrates the forces for a finish WEDMed tailored micro end mill. For this tool the feed per tooth value was 18 μm/tooth with a forces about 18 (N) and 17 (N) in X and Y directions, respectively. Recorded cutting forces for a rough WEDMed micro end mill with dimensions similar to finish WEDMed tool are shown in Figure 5.31 (c). This tool has been failed at a lower feed rate (6 μm/tooth) compare to other tools. The maximum X and Y forces in which micro end mill could be able to withstand during cutting, was about 8.8 (N) and 7.5 (N), respectively.

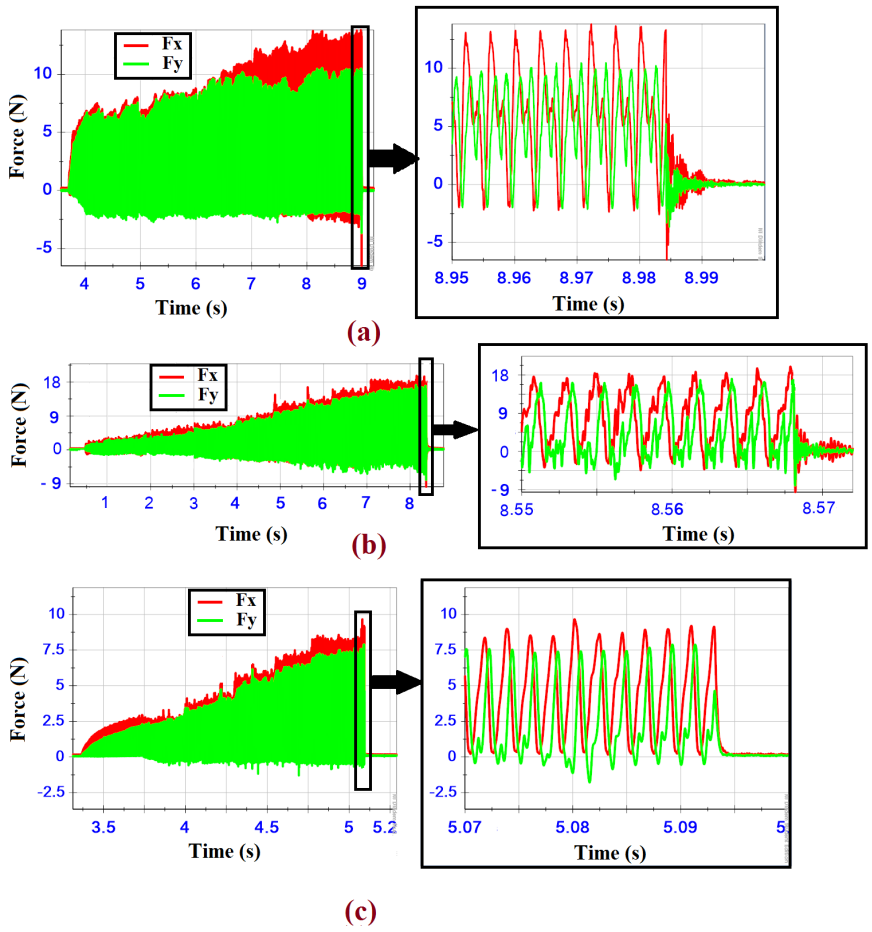

Figure 5.31: Cutting force data at the point of failure recorded for: (a) Conventional 0.4 mm micro end mill, (b) finish WEDMed, (c) rough WEDMed.

When comparing these three micro tools in terms of their stiffnesses, as it can be seen in Figures 5.31, a tool with a finished WEDMed surface having same length and effective diameter as the conventional micro end mill, can withstand larger forces before failure. This is mainly because of the geometry of the helical micro end mills. In conventional micro end mills, grinding of helical flutes highly reduces the stiffness of the micro tools. However, a tool with a rough WEDMed surface has lower stiffness compare to the conventional helical end mill. This low stiffness could be greatly attributed to the two facts; the first one is the existence of large craters on the surface of the micro end mill, which are produced due to the large WEDM energies. These large craters acts as stress risers. The second reason is due to a larger heat affected zone

and resolidified layer. Since in rough WEDMed tool, higher energies are used, the thickness of heat affected zone becomes larger and also the possibility of surface and subsurface cracks increases. Consequently, the core unaffected area of the tool reduces effectively, which significantly reduces the tool stiffness.

Figure 5.32 illustrates the maximum first principal stress and maximum deflection of the conventional micro end mill under the action of machining forces at the point of failure (Forces of Figure 5.31(a)). As it can be seen in Figure 5.32, considering a transverse rupture strength of 3.7 GPa, the finite element method is able to predict tool failure with a percent error of 4.6 % . The tool has experienced a deflection of 48.4 μm when failure occurred.

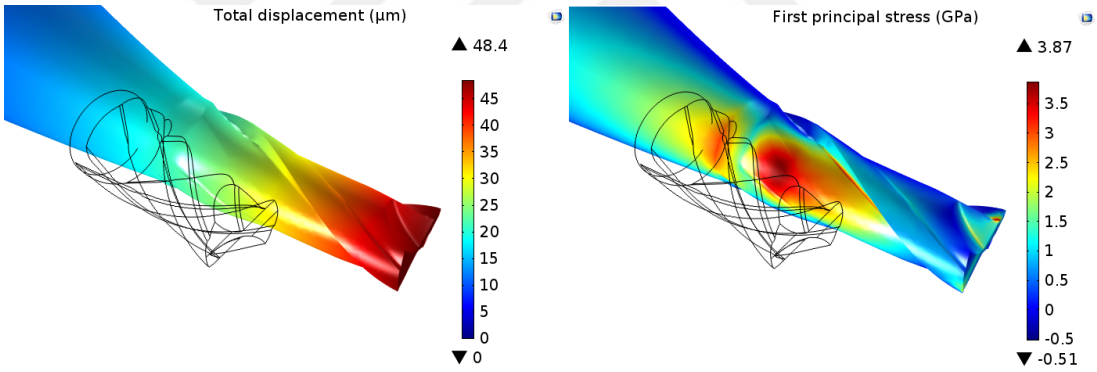

Figure 5.32: Results of first principal stress and tool deflection for a conventional 0.4 mm micro end mill.

A same procedure is used to predict the stresses and deflections of the tailored micro end mills. Figure 5.33 illustrates the finite element model of the single edge micro end mill with R_{Tr}=1.8 mm, L_C=0.8 mm. Complete mesh of the model consists of 18676 domain elements, 3514 boundary elements and 398 edge elements.

The results of finite element model can be seen in Figure 5.34. A broken micro end mill is also shown in Figure 5.34(c) for comparison. It can be seen in Figure 5.34 that using finite element method the developed stress can be estimated with 7.5% error, however since finite element predictions give a larger stress values, this can be considered as an additional factor of safety at the early stage of the micro end mill design.

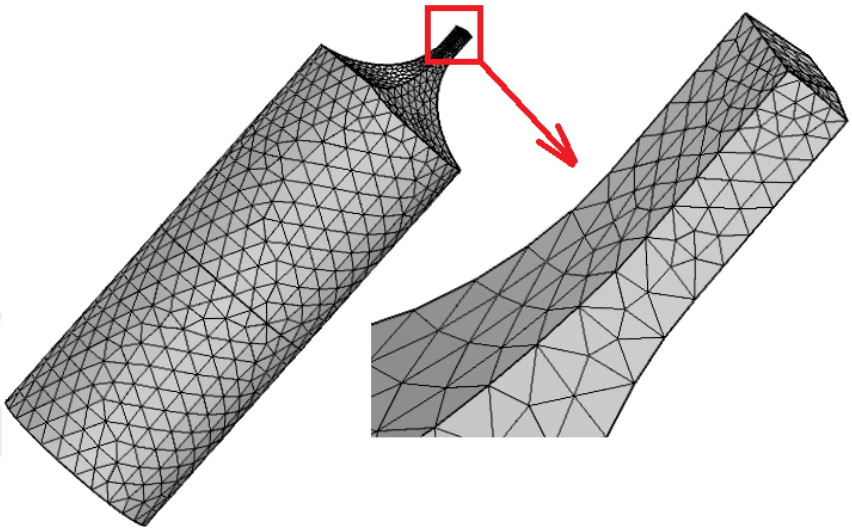

Figure 5.33: Finite element model of tailored micro end mill.

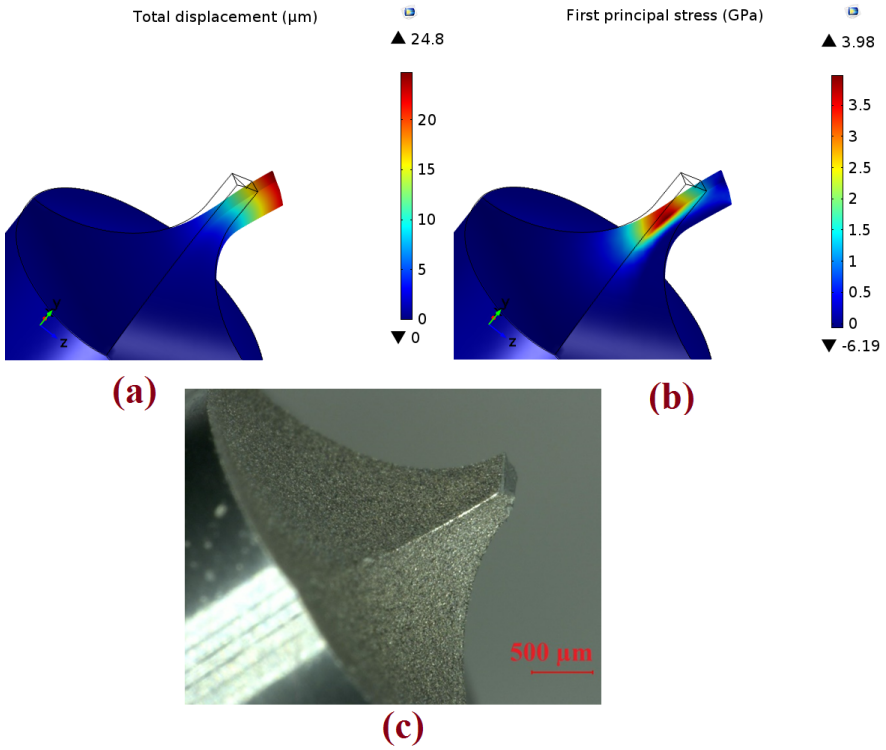

Figure 5.34: FEM results of tailored micro end mill: (a) deflection, (b) first principal stress, (c) broken micro end mill.

It is worth mentioning that, the discrepancy between FEM and experimental data is mainly because the finite element model used in this study is not capable of taking into account the side effects of WEDM process such as heat affected zone (HAZ), resolidified layer and the surface texture of the tools which is the superposition of very many craters produced as a result of sparking phenomenon.

5.11.3 Comparison between Finite Element and Analytical Model of Tailored Micro End Mill Deflection

In the previous section, finite element model is verified using experimental failure tests. In this section, a comparison is made between finite element predictions and developed analytical model to evaluate the accuracy of finite element predictions in modeling of tailored micro end mill deflections. In order to make comparison, a micro end mill with the specifications given in Table 5.3 is modeled in COMSOL Multiphysics and tool deflection is obtained for a sample force of 8 (N) in both directions. Figure 5.35 illustrates the deflection obtained by COMSOL Multiphysics.

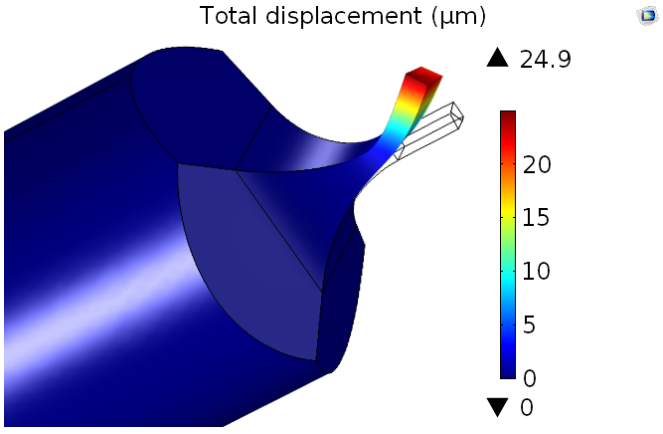

Figure 5.35: Calculated deflection for a cutting tool with specifications given in Table 5.3.

As it can be seen in Figure 5.35, the total deflection of the tool is 24.9 µm, which is in a good agreement with the results of analytical model, where a deflection of 25.69 µm is calculated.

Under similar loading condition and geometric parameters, a comparison is also made for different combinations of neck taper angle and transition radius. The results are shown in Table 5.4.

Table 5.4: A comparison between FEM and analytical model for different γ and R_{Tr} values.

Neck Taper Angle (deg.)	9	45	60	60	90
Transition Radius (mm)	0.07	1.5	0.07	1.8	1.8
FEM-Deflection (µm)	19.95	11.1	5.57	12.3	11.4
Analytical Model-Deflection (µm)	20.66	10.67	6.55	13	10.62

It can be seen in Table 5.4 that, there is a good agreement between analytical model and finite element predictions for different combinations of neck taper angle and transition radius values. A finite element model, which is verified using experimental tests and analytical model, can be used for the optimization of tailored micro end mills.

5.11.4 Graphical Optimization of Tailored Micro-End Mills Based on Finite Element Method

In order to optimize cutting tool geometry parameters, the response of different cutting tools are obtained for the forces of finish WEDMed tool at the point of failure which are depicted in Figure 5.31 (b). A safety factor of 1.25 is considered in terms of cutting forces, meaning that it is assumed that cutting forces for practical cutting conditions will be 25% lower than that of forces obtained at the point of failure.

Using finite element analysis, maximum deflection and maximum first principal stress are obtained for the full factorial combinations of neck taper angle (γ) (9°, 15°, 20°, 30°, 45°, 60°, 70°, 80° and 90°) and transition radius (R_{Tr}) (0.07, 0.15, 0.25, 0.5, 0.75, 1, 1.25, 1.5 and 1.8) mm. The length of cut has kept constant (0.8 mm). Total number of 81 finite element simulations is performed. For each neck taper angle, first principal stress and deflection curves are plotted as a function of transition radius. Figure 5.36 illustrates the results for neck taper angle of 9°.

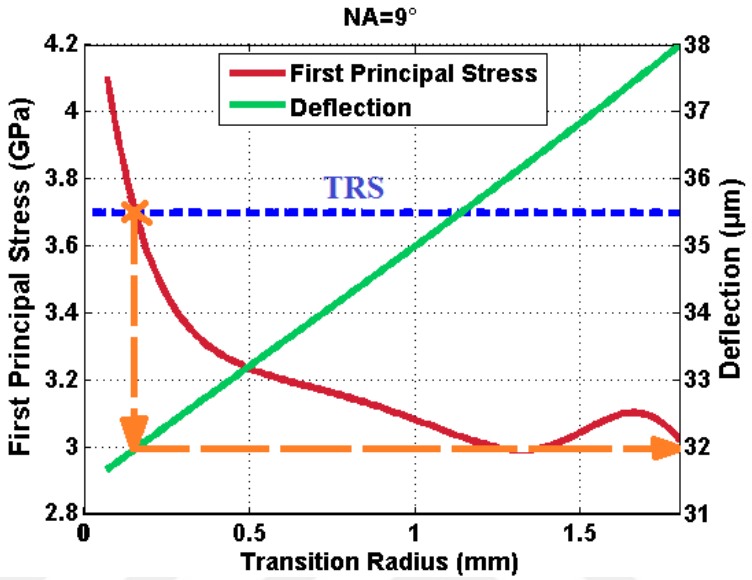

Figure 5.36: Calculation of critical transition radius and corresponding deflection.

As it is shown in Figure5.36, for each neck taper angle a critical transition radius is obtained by finding the transition radius at point of failure, where first principle stress is equal to the transverse rupture strength of the cutting tool material. For critical transition radius, corresponding deflection has been obtained. Figure5.37 illustrates the variation of deflection and first principal stress as a function of transition radius for different neck taper angles. Critical transition radii and corresponding deflections are given in Table 5.5.

Table 5.5: Critical transition radius and corresponding deflections for different neck taper angles (L_c=800 µm)

NA (deg.)	Critical Transition Radius (mm)	Deflection (µm)
9	0.1538	31.96
15	0.2487	16.76
20	0.2488	13.30
30	0.2614	11.12
45	0.2556	10.18
60	0.2632	10.03
70	0.2642	9.94
80	0.26	9.89
90	0.2765	9.99

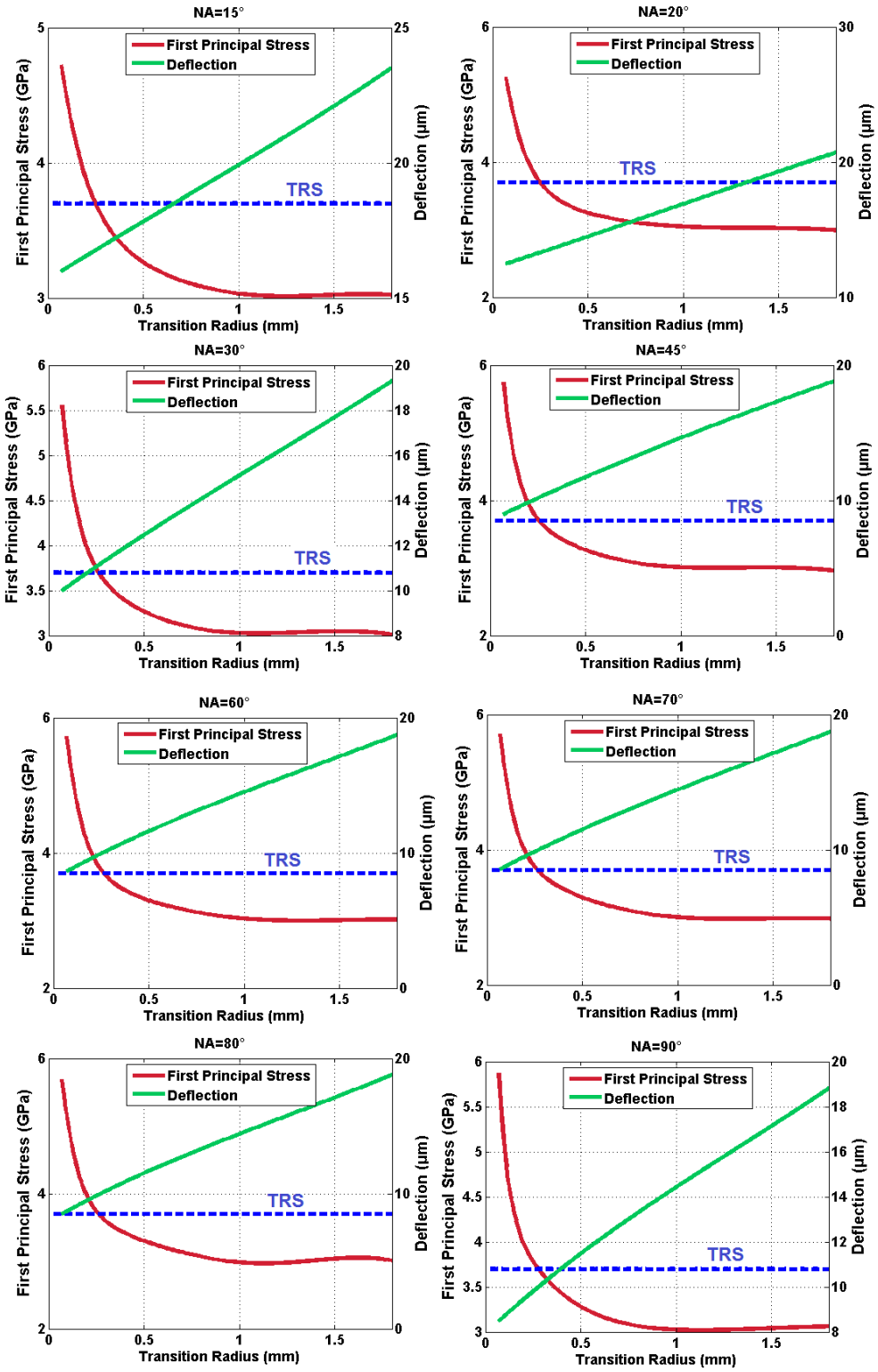

Figure 5.37: Variation of deflection and first principal stress as a function R_{Tr} for different γ values.

It can be seen from Table 5.5 that a tool with lowest deflection should have a neck taper angle between 60° and 80° with a transition radius close to 0.26 mm.

5.12 Analytical Optimization of Tailored Micro-End Mills Based on Finite Element Method

In previous section, a graphical method is used to determine the optimum micro end mill geometry. Analytical optimization of tailored micro end mill geometry can also be done by expressing deflections and stresses as a function of design parameters, i.e. transition radius and neck taper angle. This can be done by fitting a surface to the data obtained in previous section through finite element simulations. Figure 5.38 (a) and (b) illustrate the surfaces fitted to express the variation of tool deflection and first principal stresses as a function of neck taper angle and transition radius, respectively. The goodness of fit is decided based on R^2 values greater than 0.985.

The equation of tool deflection as a function of neck taper angle (γ) and transition radius (R_{Tr}) expressed as:

$$\begin{aligned}\text{def}\,(\gamma, R_{Tr}) = {} & p_{00} + p_{10}\gamma + p_{01}R_{Tr} + p_{20}\gamma^2 + p_{11}\gamma R_{Tr} + p_{02}{R_{Tr}}^2 + p_{30}\gamma^3 + p_{21}\gamma^2 R_{Tr} + \\ & p_{12}\gamma {R_{Tr}}^2 + p_{03}{R_{Tr}}^3 + p_{40}\gamma^4 + p_{31}\gamma^3 R_{Tr} + p_{22}\gamma^2 R_{Tr}^2 + p_{13}\gamma {R_{Tr}}^3 + p_{04}{R_{Tr}}^4 + p_{50}\gamma^5 + \\ & p_{41}\gamma^4 R_{Tr} + p_{32}\gamma^3 {R_{Tr}}^2 + p_{23}\gamma^2 {R_{Tr}}^3 + p_{14}\gamma {R_{Tr}}^4 + \\ & p_{05}{R_{Tr}}^5 + b \cdot \sin(m\pi\gamma R_{Tr}) + c \cdot \exp(-(wR_{Tr})^2)\end{aligned} \tag{5.23}$$

The coefficients in Equation 5.23 are given in Table 5.6. In a similar way, the equation for first principal stress can be written as follows:

$$\begin{aligned}1^{\text{st}}\,\text{P.S}\,(\gamma, R_{Tr}) = {} & p_{00} + p_{10}\gamma + p_{01}R_{Tr} + p_{20}\gamma^2 + p_{11}\gamma R_{Tr} + p_{02}{R_{Tr}}^2 + p_{30}\gamma^3 + \\ & p_{21}\gamma^2 R_{Tr} + p_{12}\gamma {R_{Tr}}^2 + p_{03}{R_{Tr}}^3 + p_{40}\gamma^4 + p_{31}\gamma^3 R_{Tr} + p_{22}\gamma^2 R_{Tr}^2 + p_{13}\gamma {R_t}^3 + \\ & p_{04}{R_{Tr}}^4 + p_{41}\gamma^4 R_{Tr} + p_{32}\gamma^3 {R_{Tr}}^2 + p_{23}\gamma^2 {R_{Tr}}^3 + p_{14}\gamma {R_{Tr}}^4 + p_{05}{R_{Tr}}^5\end{aligned} \tag{5.24}$$

The coefficients of Equation 5.24 are given in Table 5.7. Having determined the deflec-

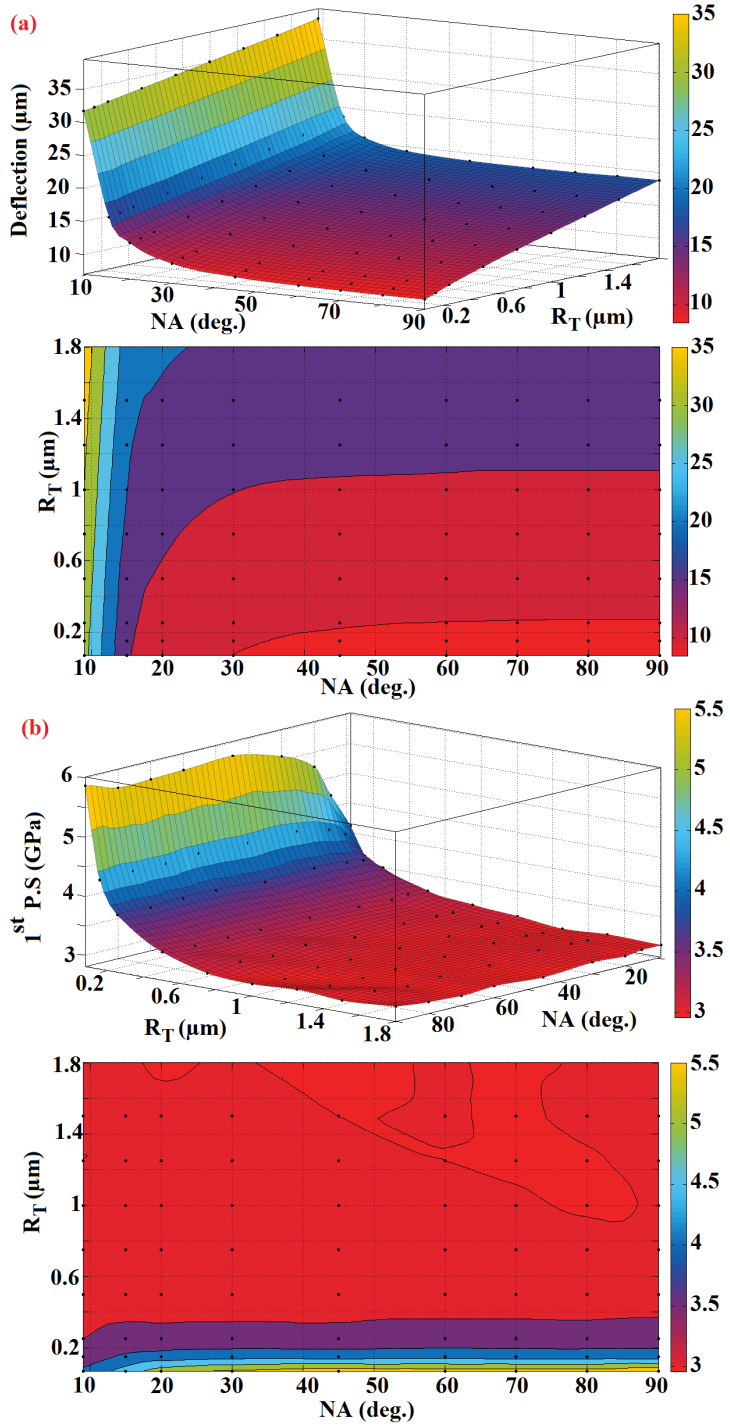

Figure 5.38: Variation of: (a) deflection and (b) first principal stress as a function R_{Tr} and γ.

Table 5.6: Coefficients for deflection equation.

Coefficient	p_{00}	p_{01}	p_{02}	p_{03}	p_{04}	p_{05}
Value	74.317	7.889	-3.704	3.303	-2.992	0.9174
Coefficient	p_{10}	p_{11}	p_{12}	p_{13}	p_{14}	p_{20}
Value	-7.688	0.4719	-0.2701	0.1209	-0.02289	0.3223
Coefficient	p_{21}	p_{22}	p_{23}	p_{30}	p_{31}	p_{32}
Value	-0.008221	0.001606	-0.0001821	-0.006389	7.865e-5	-5.677e-6
Coefficient	p_{40}	p_{41}	p_{50}	**w**	**b**	**c, (m)**
Value	5.99e-5	-2.979e-7	-2.138e-7	2.889	0.1585	3.42, (0.07748)

Table 5.7: Coefficient of the first principal stress equation.

Coefficient	p_{00}	p_{01}	p_{02}	p_{03}	p_{04}	p_{05}	p_{10}
Value	3.855	-11.91	38.6	-49.72	27.84	-5.651	0.1808
Coefficient	p_{11}	p_{12}	p_{13}	p_{14}	p_{20}	p_{21}	p_{22}
Value	-0.4385	0.4101	-0.1733	0.02775	-0.00391	0.006036	-0.003101
Coefficient	p_{23}	p_{30}	p_{31}	p_{32}	p_{40}	p_{41}	
Value	0.0005435	3.785e-5	-3.853e-5	8.587e-6	-1.359e-7	9.305e-8	

tion and first principal stresses as a function of neck taper angle and transition radius, the following optimization problem has been considered:

$$\begin{aligned}
&\text{minimize } def(\gamma, R_{Tr}) \\
&\text{subject to : } 1^{st} PS\ (\gamma, R_{Tr}) < 3.7 \\
&\text{where} \\
&9 < \gamma < 90 \\
&0.07 < R_{Tr} < 1.8
\end{aligned}$$

The optimization problem has been solved using MATLAB software, where the deflection function is minimized under the constraint of ($Induced\ Stress < TRS$). The optimum neck taper angle is obtained as 68° with a transition radius of 0.24 mm. The corresponding deflection is obtained as 8.9 µm. Using finish WEDM conditions, the tailored micro end mill with optimum parameters has been fabricated. The fabricated micro end mill is shown in Figure 5.39(a).

The tool with optimum geometry is used to machine 130 microchannels on Ti6Al4V (Figure 5.39(b)), and machining forces, surface roughness and edge condition are investigated.

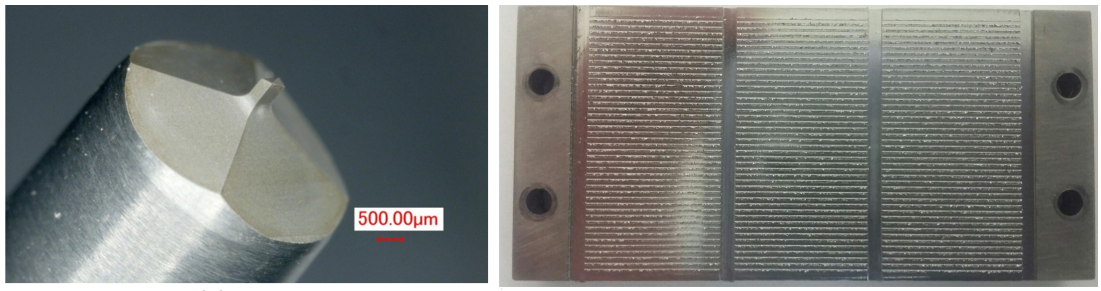

Figure 5.39: (a) Fabricated tailored micro end mill with optimum design parameters, (b) Machined microchannels using tailored micro end mill with optimum geometry.

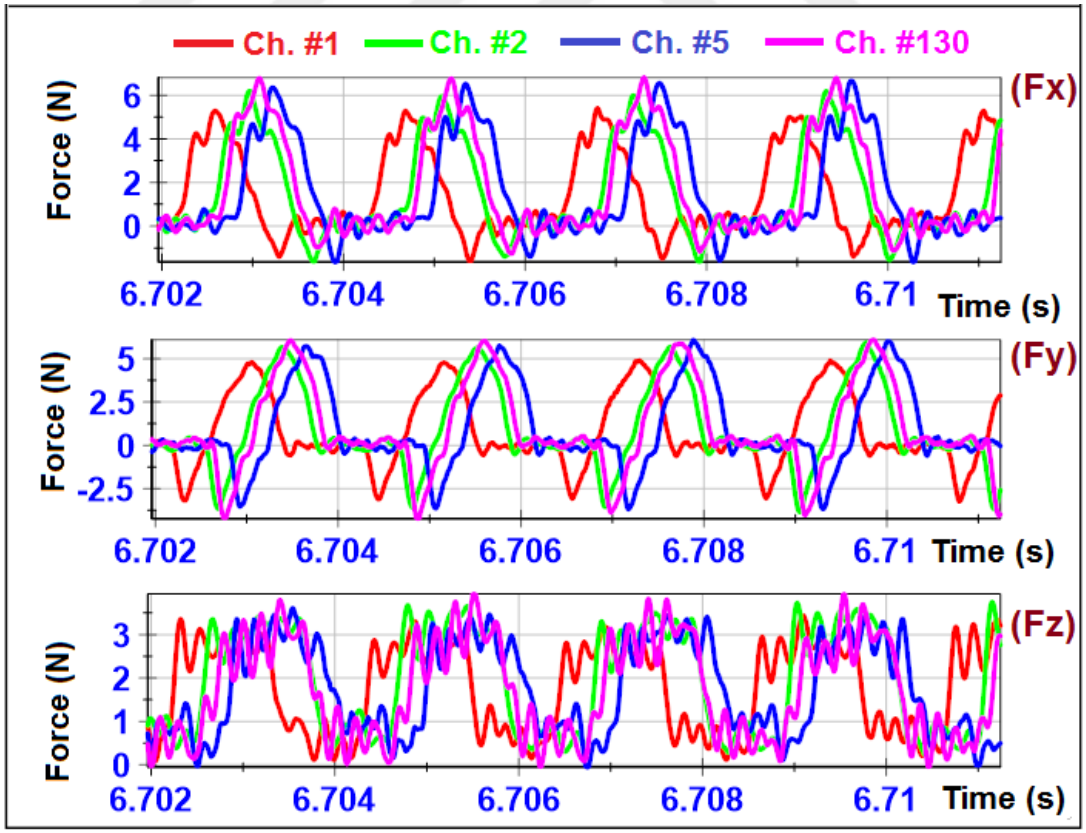

Figure 5.40: Micromilling forces for different microchannels machined by the tailored micro end mill with optimum geometry.

Figure 5.40 illustrates the micromilling forces for different microchannels. As it can be seen, at the beginning of micromilling, machining forces are relatively small, which is due to a sharper cutting edge. During break-in period, which lasts for five microchannels, the edge rounding occurs and BUE formation stabilizes. As a result, machining forces remain the same for the rest of microchannels. This situation can be seen in Figure 5.40, where the forces for channel #5 and channel #130 are in the same level, which is an indication of the protective effect of stable BUE.

Figure 5.41 illustrates the surface roughness measurements for the channel #1 and the channel #130. Both channels have almost the same surface roughness values. A stable BUE has been observed after machining 130 microchannels as depicted in Figure 5.42.

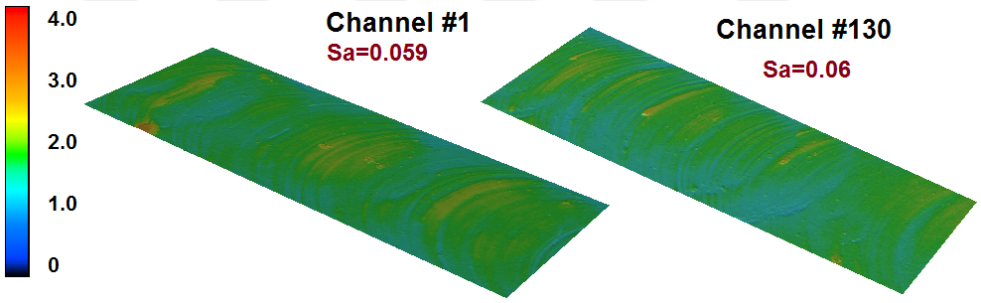

Figure 5.41: Surface roughness of the machined microchannels using tailored micro end mill with optimum geometry.

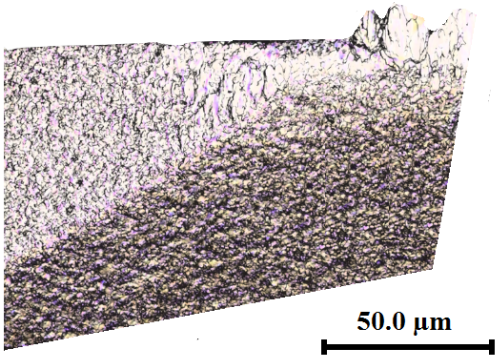

Figure 5.42: Stable BUE after micromilling for 130 microchannels.

Conclusions

In this chapter the effect of BUE on the process outputs of micromilling has been studied using tailored single edge micro end mills. A design methodology has been proposed for designing optimum tailored micro end mills through the use of finite element analysis. Analytical modeling of tailored micro end mills are also done in this chapter. The results of experimental phase can be summarized as follows:

- WEDM process parameters have a significant influence on the performance of tailored micro end mills.
- It has been observed that, in general larger BUE sizes resulted in larger resultant forces.
- It has been shown that BUE size largely depends on the selected depth of cut values. Under the conditions of this study, it has been found that independent from length of cut values, BUE height increases when changing depth of cut from 30 μm to 40 μm and it decreases by changing depth of cut from 40 μm to 50 μm.
- No correlation has been found between BUE and burr parameters, however it has been shown that by selecting proper micromilling process parameters burr height and width can be minimized.
- The positive impact of stable BUE formation on tool life of tailored micro end mills has been explored.
- By changing the length of cut of the micro end mills while using same geometric parameters, the effect of tool deflections on surface finish has been analyzed. It has been shown that increased tool deflections deteriorate surface quality of the machined parts.

The results of optimization and modeling phase of this chapter reveals that:

- An analytical model of the proposed tailored single edge micro end mills are developed and successfully used for the prediction of micro end mill deflection.

- A good agreement between finite element simulations and experimental failure tests are observed. Therefore, the finite element models of this study can be used for tool failure predictions at the initial steps of cutting tool design process.
- A good agreement between finite element simulations and proposed analytical model predictions has been observed in determining deflections of tailored micro end mills.
- A finite element based design optimization methodology of tailored micro end mills is proposed. Using this optimization methodology optimum values of neck taper angle and transition radius are determined based on minimum tool deflection criterion. For the geometry under consideration, a neck taper angle of 68° with a transition radius of 0.24 mm resulted in a minimum deflection of 8.9 μm.

Chapter 6

Fabrication of PCD Micro Tools for Ductile Mode Machining of Silicon

6.1 Introduction

Due to rapid growth in the electronics, optics, and biomedical industries, there is an increasing demand for components having ultra precision machined parts made from brittle materials such as different grades of ceramics, carbides, glasses, single crystal materials and semiconductors, because of their excellent and desirable engineering properties such as high hardness, high wear and corrosion resistance, thermal stability and etc. [189, 190, 191, 192, 38].

Among brittle materials, silicon is the material of choice for micro-electronic and micro-electro-mechanical systems (MEMS) because of its unique combinations of mechanical, chemical and electrical properties [193]. Various techniques have been developed to achieve features of different length scales on silicon. The ever increasing demand of MEMS industry for creating true 3D features with free-form surfaces in silicon is the main motivation for using mechanical micromachining processes for silicon micromachining.

In order to better understand the importance of application of mechanical micromachining on silicon processing, one can consider a construction of a diaphragm compressor. Generally, in these compressors the depth of the chamber 'x' is represented by an Nth order polynomial such as one proposed by Cabuz et al. [194] as:

$$\frac{x}{x_{\max}} = 1 - \left(\frac{r}{R}\right)^2 - 0.1\left(\frac{r}{R}\right)^3 + 0.1\left(\frac{r}{R}\right)^4 - 0.1\left(\frac{r}{R}\right)^5 + 0.1\left(\frac{r}{R}\right)^6 \tag{6.1}$$

where 'r' is the distance from the center of the chamber, 'R' is the radius of the chamber and '$x_{\max}$' is the maximum depth of the chamber.

There are many applications of these kinds that none of the MEMS based techniques can be used, because of the intrinsic limitation of these techniques as a 2.5D process. For such applications, mechanical micromachining can be considered as an enabling technology for fabricating true 3D features in silicon and other brittle materials. However, application of mechanical machining for creating complex features in brittle materials is a challenging task. Successful machining of these materials requires well designed cutting tool geometries and proper selection of machining process parameters to make ductile mode machining of these materials possible.

6.2 Ductile Mode Machining

Abrasive processes are the most commonly used processes for machining hard and brittle materials. However, due to their nondeterministic nature, high wear rates and self sharpening, it is more difficult to machine high precision parts by abrasive processes [189, 190]. In conventional grinding of optical glasses, it has been shown that grinding wheels with well-defined grain patterns known as engineered grinding tools (EGT) usually have advantages over randomly structured (stochastic) grinding wheels in terms of material removal predictability, lower grinding forces and power, and workpiece surface integrity [43]. Ductile mode machining using tools with defined cutting edge geometries, as a deterministic process can be a promising solution to have an acceptable surface quality while maintaining the contouring and form accuracy of the machined parts.

The idea of ductile mode machining came from the fact that brittleness is a scale dependent material characteristics, which means that all brittle materials can show some ductility when the scale of deformation became small enough. It was confirmed by Bifano et al. [195] that in brittle materials, as depth of cut decreases to a critical value known as critical depth of cut, a transition in deformation regime from brittle to ductile occurs. This transition has been described in terms of material removal energy, and it has been shown that for machining depth of cuts lower that critical depth of cut, plastic flow is energetically favorable material removal mechanism. The transition from ductile mode machining to brittle cutting schematically illustrated in Figure 6.1.

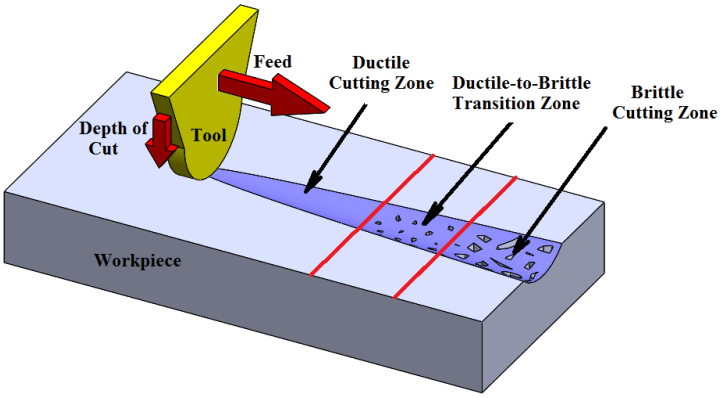

Figure 6.1: Schematic representation of ductile-to-brittle transition.

As it can be seen in Figure 6.1 as depth of cut increases when cutting tool moves from left to the right in the feed direction, three distinct zones can be identified as [196]: (i) ductile cutting zone, where material is removed in the form of chips produced through a plastic deformation. In this zone no surface and subsurface damage occurs. (ii) The second zone is a combination of ductile and brittle removal mechanisms, where as cutting tool further moves to the right, brittle fracture becomes dominant. This zone is called ductile-to-brittle transition zone. (iii) The third zone which is characterized by existence of large fractures, cracks and damaged surface, is the brittle cutting zone. It can also be seen in Figure 6.1 that, at a certain depth (known as critical depth of cut) ductile-to-brittle transition phenomenon occurs. This critical depth of cut depends on several parameters, including workpiece material properties, cutting tool geometry and machining process parameters.

Ductile mode machining has been studied by different researchers and successfully implemented to obtain crack-free surfaces on brittle materials. Blackley and Scattergood [197] proposed a relation for the critical chip thickness at the point of transition, where the critical chip thickness and surface damage depth is related to tool feed, tool nose radius and location of ductile-to-brittle transition.

Material removal energy has been used by Blake and Scattergood [198] to represent the concept of ductile-to-brittle transition. They mentioned that the ratio between energy of plastic flow and energy of brittle fracture is proportional to the undeformed chip thickness. The J-integral approach based on elastic-plastic fracture mechanics has been used by Ueda et al. [199] to analyze material removal mechanisms during micro cutting of ceramics. Using finite element method, they obtained J-integral values along several contours around the tip of the crack formed ahead of the cutting tool. The calculated J-integral values are compared to the critical value of J, which is a property of the material being cut. For J values greater than critical J value, material removal considered as brittle.

Recently, molecular dynamics simulations have been used to study the mechanism of material removal in ductile mode. Using MD simulations, Xiao and Zhang [200] studied atomic scale details of ductile deformation in the machining of silicon carbide, where the occurrence of phase transformation has been observed during cutting process.

Ductile regime machining has been experimented on different brittle materials. Engineered diamond wheels with defined and semi-defined diamond grain patterns has been developed by Heinzel and Rickens [190] and used for deterministic notch grinding of optical glass BK7. A minimum areal arithmetic mean height of Sa= 20 nm has been obtained. Zhang et al. [191] investigated the influence of microstructure and brittleness of RB-SiC/Si and WC/Co carbides in ultra-precision grinding. They obtained a surface roughness of 20 nm for SiC/Si under brittle material removal mode and 5 nm for WC/Co under ductile removal mode. Recently, Aurich et al. [192] conducted micro-grinding of mono-crystalline silicon [1 0 0] using their developed nano-grinding center by means of on-machine fabricated galvanic coated ultra-small micro pencil grinding tools with a diameter between 4-40 μm. They obtained a surface

roughness of 25 nm on silicon using 40 μm micro grinding tools. During mechanical micromachining of single crystal silicon, pitting damage may occur along special crystallographic orientations [201], which makes mechanical micromachining of silicon even more difficult.

6.3 Application of PCD Tools in Machining of Brittle Materials

Recently, polycrystalline diamond (PCD) is accepted as an excellent super hard tool material for machining of hard and brittle materials, especially at micro-scale. Several processing frameworks were developed for its fabrication, including liquid phase solvent-catalyst assisted sintering, encapsulation in refractory metal containers (normally tantalum), incorporation of a WC-Co substrates and diamond powder treatment prior to high-pressure/high temperature sintering [202]. Among these frameworks, infiltration from WC-Co substrates provides some advantages for tool fabrication purposes, because WC-Co gave a surface which could be readily joined to other materials.

Owing to its high hardness and strength, PCD is extremely difficult to be machined by mechanical methods, especially for feature sizes smaller than 100 μm [37]. Very low G-ratio (the ratio of the volume of material removed from PCD to the volume of material removed from the grinding wheel) is the characteristics of PCD grinding. EDM-based techniques can be considered as an alternative machining method for processing PCDs. The presence of cobalt as a PCD matrix, not only imparts in a significant degree to PCD toughness, but also makes it electro-discharge machinable. However, machining of PCD is still a challenging task for researchers and practicing engineers.

In an attempt for better machining of PCD, Yan et al. [203] developed a new pulse generator for μ-WEDM of PCD. They achieved a minimum surface roughness of Ra=0.6 μm in a PCD of 2 μm grain size. Chen and Jiang [38] fabricated a boron doped PCD tool having double sided negative back rake angle of -60° fabricated using WEDM process. They conducted force controlled grinding/milling of quartz glass. A

critical depth of cut of 1 μm is determined experimentally and they obtained a surface roughness of 25 nm. On-machine fabrication of PCD micro tools by block-EDM method has been done by Parveen et al. [204], and are used for machining three glass materials (BK7, Lithosil and N-SF14). A minimum average surface roughness of 12.79 nm is achieved on BK7.

Although silicon is a brittle material at room temperature, with proper controlling of micromachining process parameters and cutting tool characteristics, there is a possibility of complete ductile mode removal of materials. Therefore, it is necessary to have a systematic fundamental understanding of the effect of machining process parameters and tool specifications in ductile mode machining of brittle materials like silicon. To achieve this goal, a series of single edge micro end mills are designed and fabricated to conduct systematic studies on silicon micromachining. The results of this systematic investigations provide the required knowledge for optimizing PCD cutting tool geometry in order to achieve high productivity and better surface integrity. Based on this knowledge, novel micro end mill geometries are created on PCD and successfully used in ductile mode machining of silicon. The findings are also used to design novel mechanical planarization tools.

6.4 Defining PCD Micro End Mill Geometry

Square micro end mills can mainly produced by machining some radial grooves at the bottom face of a PCD rod, which results in having a radially patterned circular micro end mill. In some cases, the lateral surface of the PCD rod can also be machined to obtain a polygonal shape and to create cutting edges. The general definitions of two different micro end mill geometries considered in this thesis are shown in Figure 6.2.

The micro end mill geometry is mainly defined by its diameter (D), number of cutting edges (N_e), and distance between edges (W). The general geometry of the micro end mill (polygonal or circular) affects the rake angle (α) and the clearance angle (γ). Cutting edge radius (r) is defined by the grain size of the tool material and the process used to fabricate micro end mills. For the given tool designs, which both have six

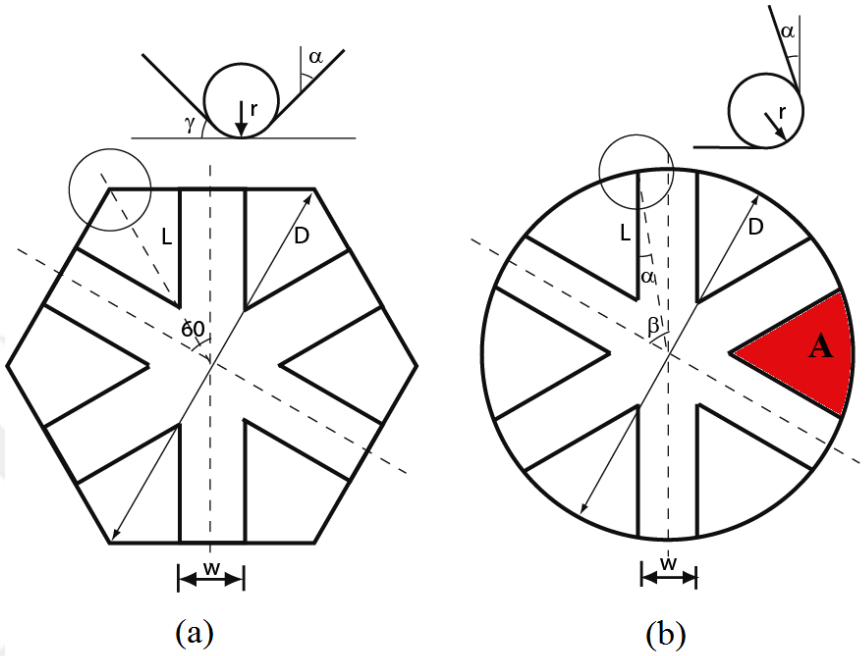

Figure 6.2: PCD micro end mill designs with 6 teeth: (a) Hexagonal, (b) Circular.

cutting edges, the hexagonal end mill has a negative rake angle of -30° and a clearance angle of 30°, while the circular end mill geometry has a positive rake angle and zero clearance angle. The rake angle of the circular geometry can be calculated as a function of tool diameter and the distance between edges as follows:

$$\alpha = \arcsin\left(\frac{W}{D}\right) \tag{6.2}$$

The positive rake angle helps evacuate the material debris towards the center of the tool to avoid accumulation of debris ploughed on the machined surface. Increasing positive rake angle also weakens the cutting edge. The clearance angle helps decrease the contact between the tool periphery and the workpiece. Increasing the number of edges decreases the contact area between workpiece surface and bottom of the tool. Increasing the distance between cutting edges also decreases the contact area between the tool and the workpiece surface. Considering low feed per tooth values used in silicon machining, cutting edge radius is larger than the feed value, therefore the effective rake angle becomes negative. It must also be noted that the diamond grains protrude from the surface of the tools and act like a grinding tool. PCD tools without an edge

geometry have been used as grinding tools to machine brittle materials with success [192].

The selection of tool geometry parameters are constrained with the strength of cutting edge and the stiffness of the tool [205]. Number of teeth and distance between edges can be changed to achieve different geometries as depicted in Figure 6.3.

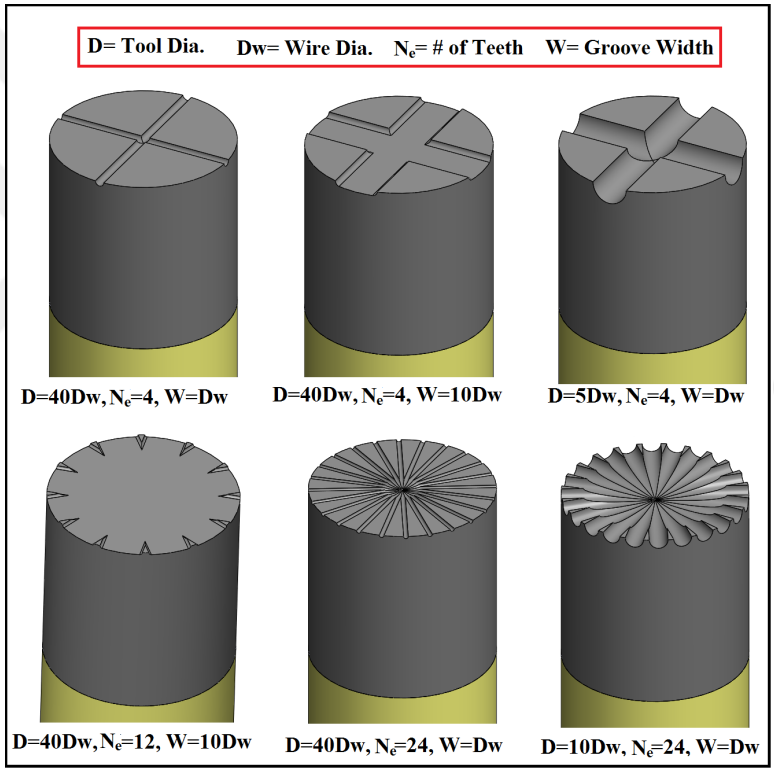

Figure 6.3: Different radially patterened PCD square end mills geometries.

The constraints associated with the design of these tools are: (i) distance between edges cannot be smaller than KERF, (ii) number of teeth should be always an even number because of limitations of the WEDM process, (iii) cutting tool diameter cannot be smaller than a minimum value determined by the constraints such as the system used for micro tool fabrication and edge strength. The reason is, as cutting tool diameter becomes smaller, it is not possible to create cutting edges which are able to withstand the cutting forces without breakage. Therefore, in order to obtain minimum diameter, a critical cross-sectional area of the cutting edges (A_{cr}) is always required.

As will be explained in detail in the subsequent section, single edge cutting tools are prepared having different edge sizes by varying distance between edges. The observations using 3D laser scanning microscope revealed that, under normal machining conditions, when the cross-sectional area becomes approximately 1300 μm^2 the edge breakage occurs. Considering a minimum safety factor of 1.5, the critical area can be set to 1950 μm^2. Hence, minimum theoretical tool diameter (D_{min}) can be obtained by making the area of circular sectors (A) shown in Figure 6.2 equal to (A_{cr}). From Figure 6.2, 'A' can be calculated as:

$$A = \frac{\pi}{N_e}\left(\frac{D}{2} - \frac{w}{2\sin\left(\frac{2\pi}{N_e}\right)}\right)^2 \tag{6.3}$$

for D =$D_{\min} \Rightarrow A = A_{cr}$ we have:

$$A_{cr} = \frac{\pi}{N_e}\left(\frac{D_{\min}}{2} - \frac{w}{2\sin\left(\frac{2\pi}{N_e}\right)}\right)^2 \rightarrow D_{\min} = \frac{2\sqrt{A_{cr}N_e} + \sqrt{\pi}w\csc\left(\frac{2\pi}{N_e}\right)}{\sqrt{\pi}} \tag{6.4}$$

In a similar way for a polygonal geometry the area can be calculated as:

$$A = \frac{1}{4}\left(D\sin\left(\frac{\pi}{N_e}\right) - w\right)\left(D\cos\left(\frac{\pi}{N_e}\right) - \frac{w}{\sin\left(\frac{\pi}{N_e}\right)}\right) \tag{6.5}$$

and for the conditions where $\cos\left(\frac{\pi}{N_e}\right) \neq 0$ and $\csc\left(\frac{\pi}{N_e}\right) \neq 0$, minimum diameter can be calculated as :

$$D_{\min} = \frac{1}{2}\sec\left(\frac{\pi}{N_e}\right)\left(w\left(\cot\left(\frac{\pi}{N_e}\right) + \csc\left(\frac{\pi}{N_e}\right)\right) + Q\right) \tag{6.6}$$

where $Q = \sqrt{4\cos\left(\frac{\pi}{N_e}\right)\left(4A_{cr}\csc\left(\frac{\pi}{N_e}\right) - w^2\csc^2\left(\frac{\pi}{N_e}\right)\right) + \left(w\cot\left(\frac{\pi}{N_e}\right) + w\csc\left(\frac{\pi}{N_e}\right)\right)^2}$

For Sodick AP250L WEDM, the minimum wire diameter is 30 µm with an approximate KERF of 50 µm. Therefore, setting minimum distance between edges to 50 µm, having 6 cutting edges and assuming $A_{cr} = 1950\mu m^2$, the theoretical minimum diameter for circular micro end mill will be 179 µm. Under the same conditions, the minimum diameter of hexagonal micro end mill will be 242 µm. It should be mentioned that, in practice errors due to tool setup and indexer runout, may limit the achievable minimum tool diameter. If smaller tools need to be machined, other techniques such FIB machining may be required.

6.5 Fabrication of PCD Micro End Mills by WEDM Process

6.5.1 Mechanism of Material Removal in EDM of PCD

Mechanism of material removal in electrical discharge machining of PCD is different than metallic materials. Discharge energy and the grain size of the PCD are two surface roughness controlling parameters in electrical discharge machining of PCD. Depending on the EDM energy used for machining of PCD, two different machining regimes can be identified as high energy EDM regime and low energy EDM regime as depicted in Figure 6.4.

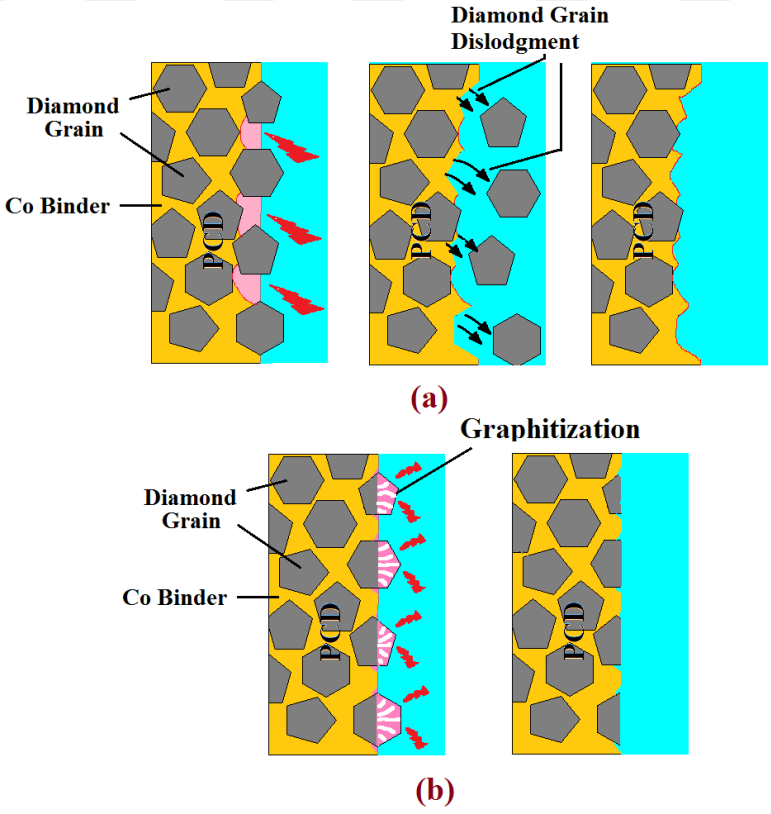

Figure 6.4: Schematic representation of material removal in EDM of PCD at: (a) High energy regime, (b) Low energy regime .

At high energy discharges the dominant material removal mechanism of PCD is believed to be the melting of binder (normally Cobalt or Nickel) and falling off of diamond grains (grain dislodgement) [43, 37]. This can be considered as the main reason why the craters on PCD tools are not like shallow bowl as can be observed in tungsten carbide tools [39]. However, when machining PCD at low discharge energies, gradual removal of diamond grains can occur as a result of microstructural changes through graphitization and thermo-mechanical reactions without falling off of diamond grains.

When using thin wires, WEDM energy level should be kept at a very low level to avoid wire breakage. This extremely low level of EDM energies makes it possible to obtain a lower surface roughness on PCD by switching the EDM process to low energy EDM regime. Figure 6.5 illustrates a PCD surface obtained using 30 µm wire. An average roughness of Ra=0.12 µm is achieved on PCD which is quite low compare to the value of Ra=0.6 µm reported by Yan et al [203].

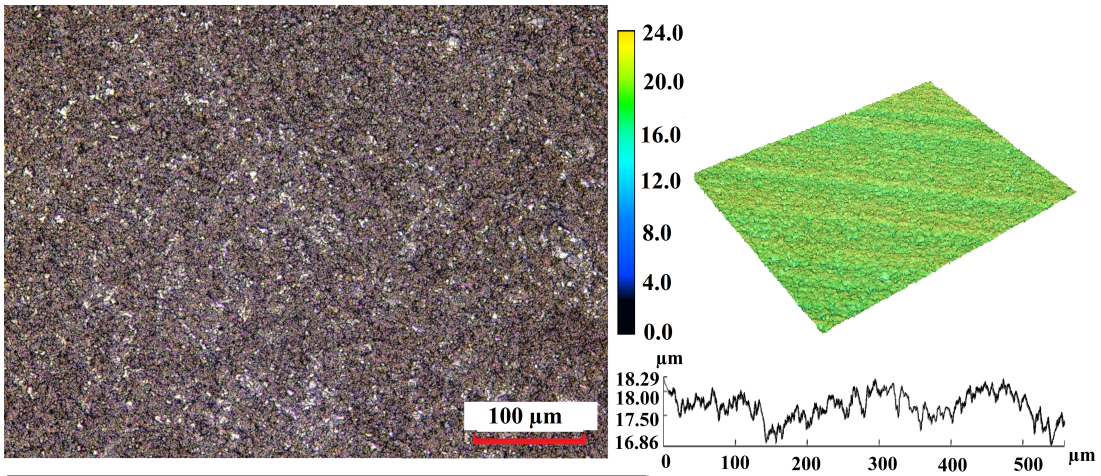

Objective lens	Standard Lens 50.0x	Intensity correction mode	Gamma correction
NA	0.800	Gamma correction value	0.45
Double scan	Auto(ON)	AI noise elimination	Auto(ON)

Rp	Rv	Rz(Rt)	Ra	Rq
0.554um	0.501um	1.055um	0.119um	0.150um

Figure 6.5: Surface roughness of PCD machined at low energy EDM regime.

6.5.2 Fabrication of PCD Tools

Micro end mills are fabricated using μ-WEDM process. A Sodick AP250L high precision WEDM machine was used to create circular array features on Sumitomo DA150 grade PCD rods with 5 μm grain size and 10-15% cobalt content. PCD rods of 500 μm diameter are mounted on the indexing spindle of the WEDM machine. A same setup explained in Chapter 5, is used for fabrication. The concentricity between PCD rod and rotational axis of the indexer is controlled using Mahr Federal Electronic lever type gauge as illustrated in Figure 6.6. Concentricity within ±2 μm is obtained by fine adjustments.

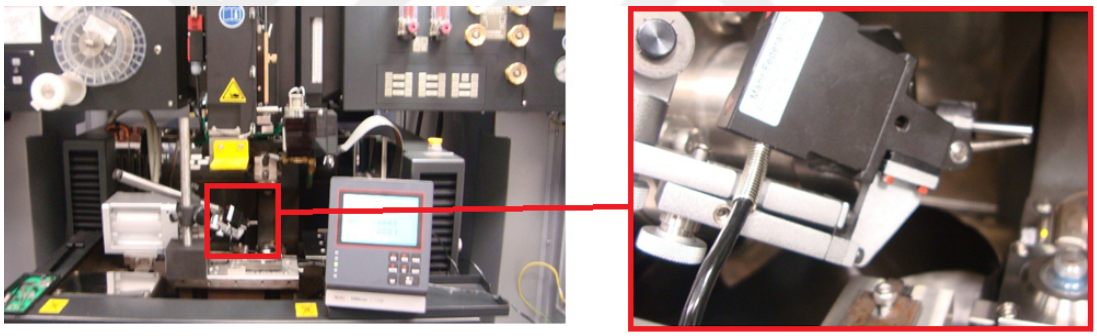

Figure 6.6: Setup used for testing concentricity of PCD tools.

Open contour machining with open nozzle positions is done to create cutting edges on PCD. μ-WEDM of the PCD is conducted by using 30 μm tungsten wire (TWS-30, 3330 N/mm^2 tensile strength).

In μ-WEDM process using thin wires machining parameters should be carefully selected to avoid wire breakage. Since automatic wire treading is not available yet for wires with diameters lower than 40 μm, manual threading should be done, which is tedious and time consuming and requires skilled operators. Therefore, for thin wires, wire breakage is an important factor which directly influences the economic feasibility of the process. To avoid wire breakage a very low level of EDM energies are selected. Table 6.1 illustrates the EDM parameters used for PCD micro tools fabrication.

One rough cutting and one finish cutting operations are done. EDMfluid 108 MP-S

is used as a dielectric fluid. The use of oil as a dielectric fluid eliminates electrolysis and minimizes KERF, recast layer and micro-cracking. This can be attributed to the lower cooling rate of oil compare to water. The cutting edge radii of the tools were measured to be around 2 µm using a laser scanning microscope (Keyence VK-X110) as shown in Figure 6.7.

Table 6.1: µ-WEDM parameters used for PCD tool fabrication

Parameters	**Roughing**	**Finishing**
Pulse On Time (µs)	2.5	2.5
Pulse Off Time (µs)	5	7.5
Reference Voltage (V)	+ 170.0	+120.0
Supply Voltage (V)	5.0	2.0
Peak Current (A)	3.6	0.6
Capacitance (nF)	200	200
Wire Speed (m/min)	3	5
Inverter Frequency (Hz)	20	12
Flushing (l/min)	2	2

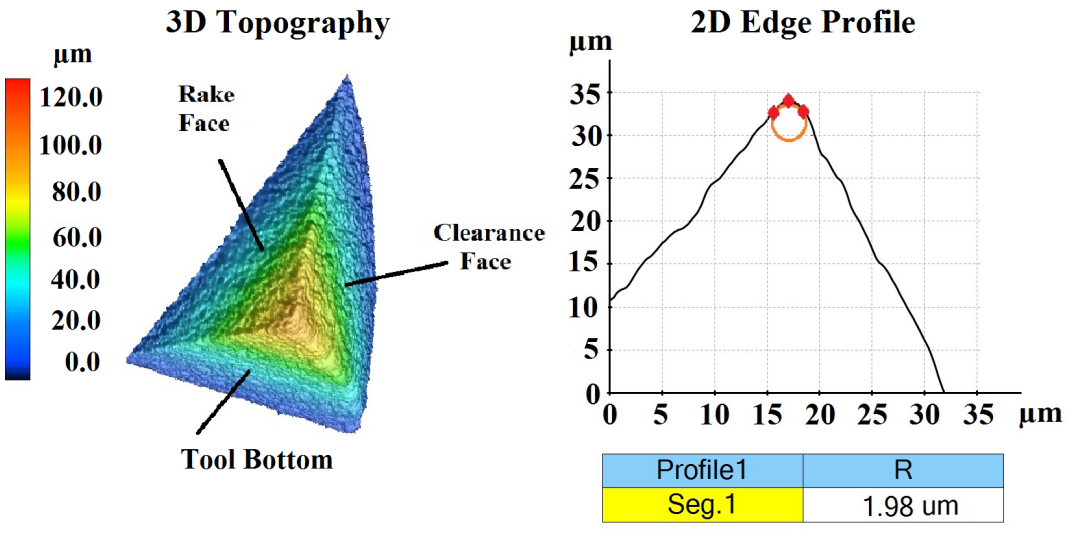

Figure 6.7: PCD cutting edge obtained at low discharge energies.

6.6 Experimental Setup and Plan for Micromilling Tests

Micromilling experiments were carried out on MIKROTOOLS DT-110 micromachining center as shown in Figure 6.8. Experiments were performed on a silicon window having 3 mm thickness at a spindle speed of 2000 RPM. The direction of machining is kept constant in the experiments. Topographies of the machined surface and the tools were obtained by using a laser scanning microscope (Keyence VK-X110). Machining forces were recorded using a Kistler (9256C1) mini dynamometer.

Two different sets of experiments were planned. In the first set of experiments, micro end mills with single edges were fabricated and tested under the same machining conditions. The edge geometries of the micro end mills were compared in terms of tool wear. In the second set of experiments, based on the findings of the first set of experiments, PCD end mills were fabricated and tested with a focus on surface quality.

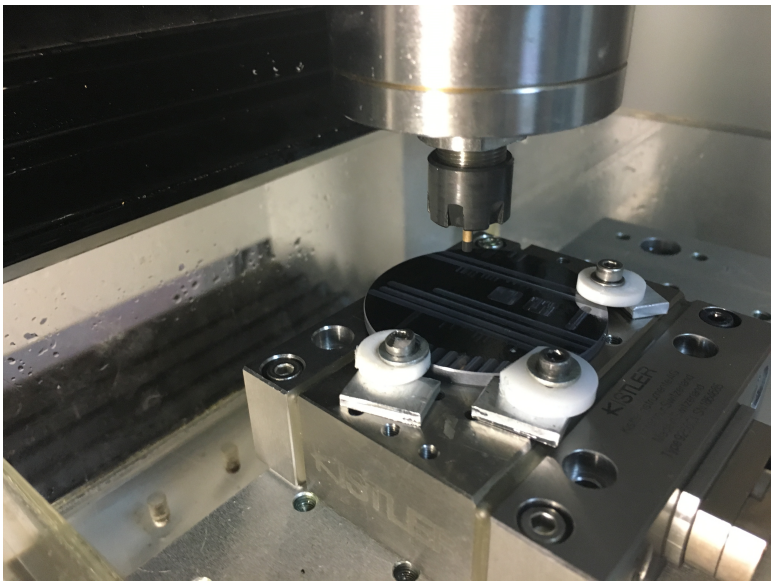

Figure 6.8: Micromilling experimental setup to test PCD micro end mills.

6.7 Influence of Tool Geometry on Tool Wear

The goal of these experiments is to understand the influence of edge geometry on tool wear. Single segments of hexagonal and circular tools having the same diameter and number of edges were produced. The distance between edges varied to change the rake angle for circular array tools and to change the contact area for both circular and hexagonal array tools.

Single edge tools allow the investigation of tool wear and ease the collection of force signals by eliminating the effect of runout and other potential problems of tools with multiple cutting edges. Machining tests were conducted under dry machining conditions in order to accelerate tool wear. For each tool, slots of 2 mm length and 1 µm depth were machined under three different feed values of 1, 1.3, and 1.5 µm/tooth. Experimental conditions were set to achieve an effective negative rake angle of -25° to -40° on the cutting edge. Each tool was cleaned after the tests using an ultrasonic cleaner and the cutting edges were investigated. Figure 6.9(a-d) shows the cutting edges of circular and hexagonal tools after the tests.

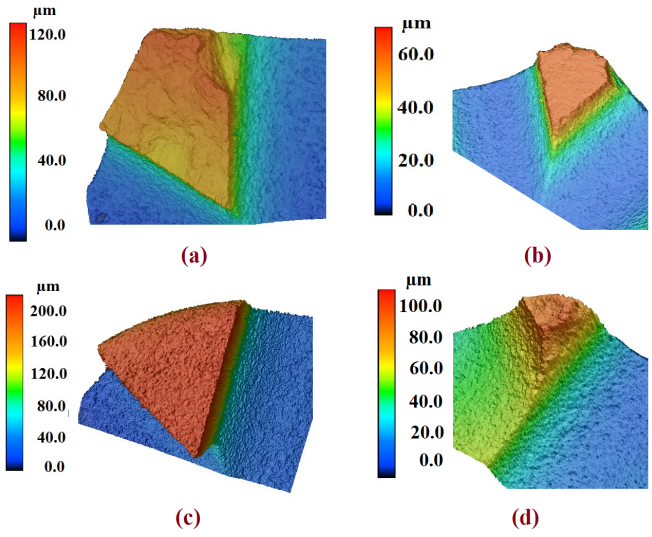

Figure 6.9: Tool wear of PCD observed at cutting edges: (a) Hexagonal edge with L=140 µm, (b) Hexagonal edge with L=80 µm, (c) Circular edge with L=140 µm, α = 20°, (d) Circular edge with L=50 µm, α = 30°.

The hexagonal edges both revealed significant tool wear after the tests. Interestingly, the worn section of the hexagonal edge as shown in Figure 6.9(a) is not the cutting edge but the end of the rake face. The circular tool with L=140 μm (rake angle of 20°) revealed less tool wear than the circular tool having L=50 μm (rake angle of 30°) as shown in Figure 6.9(c) and Figure 6.9(d). However, in Figure 6.9(b), the cutting edge of the tool was worn. These results indicate the importance of debris accumulation at the cutting edges during machining of silicon. Due to its positive rake angle, the circular edge tool performed better than the hexagonal tool in terms of tool wear under the conditions tested.

A common problem when machining silicon with PCD micro end mills is the adhesion of very small size chips to the surface which affects the chip formation process. Tool surface reconditioning techniques have been proposed to alleviate such problems [206].

Figure 6.10 shows the chips produced during machining experiments with circular and hexagonal edges. Figure 6.10(a) shows a long continuous chip formed during the experiments with circular array tools. Figure 6.10(b) shows chip flakes left at the surface after machining experiments using hexagonal geometry. The effective rake angle corresponding to the thickest chip segment was set to be equal to -40° during experiments.

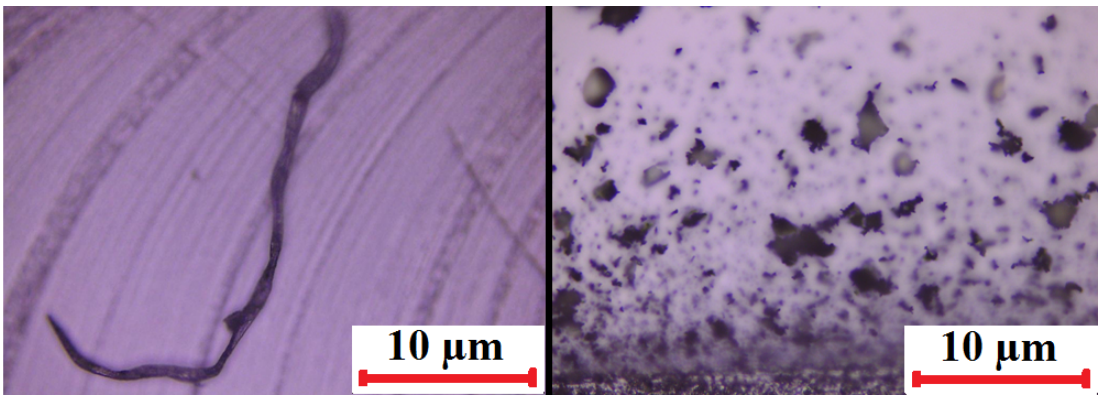

Figure 6.10: Chip formation during machining tests: (a) Circular edge (L=140 μm at 1 μm/tooth, (b) Hexagonal edge (L=140 μm at 1 μm/tooth).

Figure 6.11 compares the unfiltered forces measured with hexagonal and circular array edges. Measurements correspond to the beginning of the cut prior to any tool wear. Due to its larger contact length at the tool periphery, the circular edge yielded larger forces, especially in the 'Z' direction, compared to the hexagonal tool. Due to its clearance angle, forces in hexagonal cutting edge are observed to be smaller. The magnitude of forces measured in 'Z' direction are larger than in the direction of cut. These results show that a positive rake angle which will help to evacuate chips is preferable. Similarly, an edge geometry which maintains a smaller contact area at the tool periphery is also helpful in terms of decreasing forces in 'Z' direction. The forces in 'Z' direction are observed to be related to surface roughness during experiments.

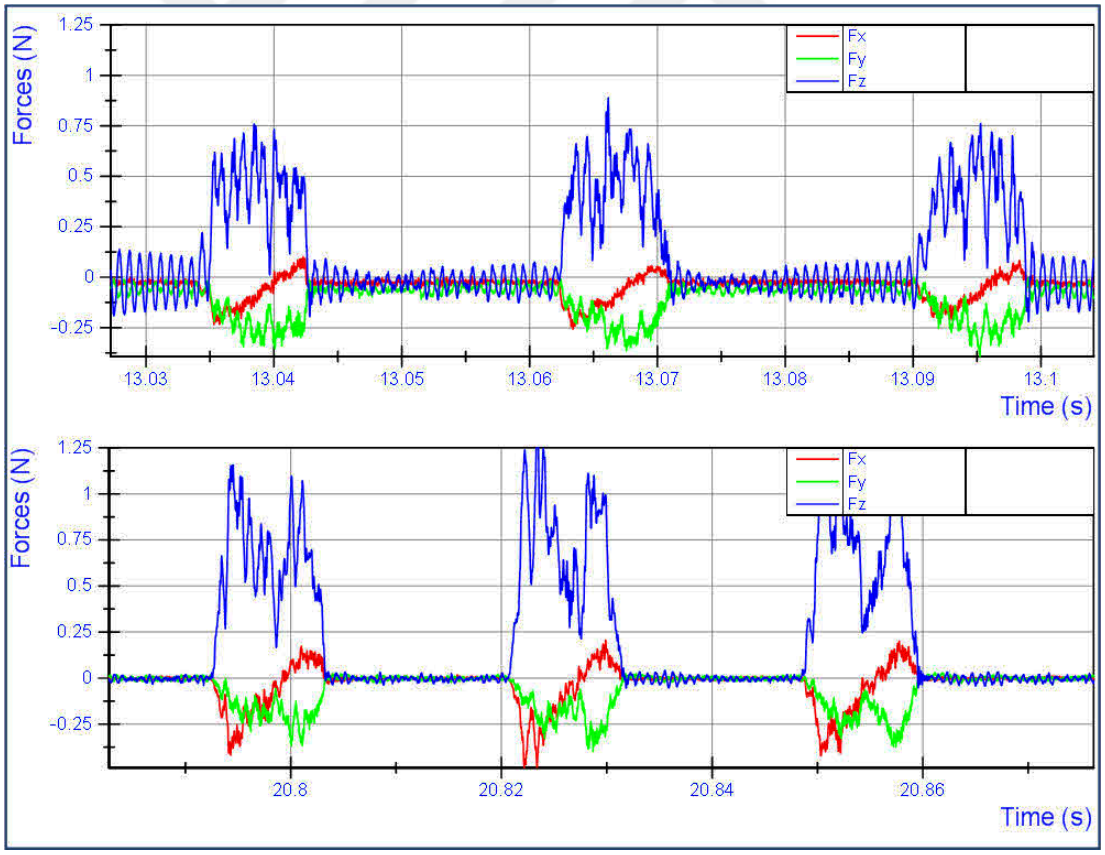

Figure 6.11: Measured forces during machining tests with 1.3 μm/tooth feed and 2 μm depth of cut: (Top) Hexagonal edge (L=140 μm), (Bottom) Circular edge (L=140 μm).

6.8 Design and Fabrication of Novel PCD Micro End Mill

Based on our findings with single edge cutting tools, in terms of tool wear, achievable surface finish and machining forces, a micro end mill with a novel geometry has been designed and fabricated. The aim of proposed design was to have a better swarf evacuation, reduced contact area and lower machining forces. In order to achieve these goals, a double relief angle at the bottom of the tool has been created for each individual edge, which helps in reducing contact area and provides enough space for swarf evacuation. Figure 6.12 illustrates the solid model of the proposed micro end mill and 3D topography of the fabricated micro end mill. An included angle of 130° used to provide a symmetric double relief angle at the bottom surface of the tool. The measured edge radius of the tool is about 2 µm.

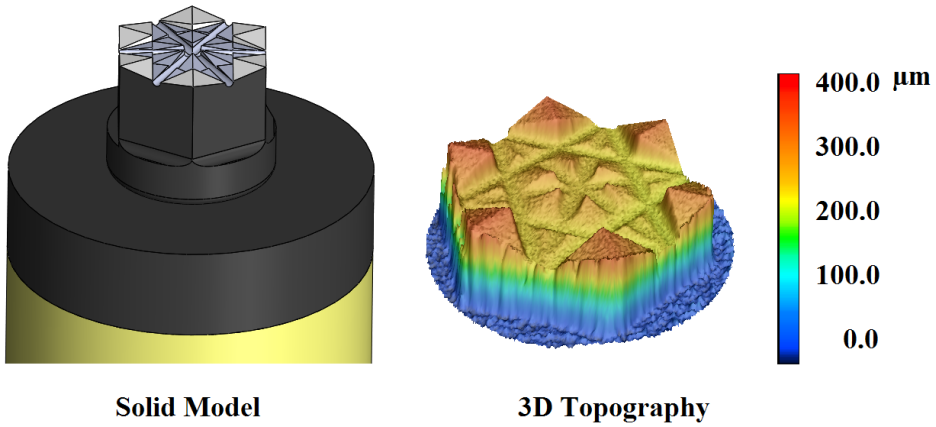

Figure 6.12: Solid model and 3D topography of the proposed micro end mill.

In order to analyze the performance of the proposed micro end mill, machining experiments are conducted using the same setup explained in section 6.6. In order to make comparisons, two micro end mills having same dimensions as proposed micro end mill with circular and hexagonal geometries are also fabricated.

The performance of these three different micro end mills in dry cutting of silicon is tested. Machining experiments are performed at two different depth of cut of 1 µm

and 2 μm at a feed rate of 1.2 μm/rev. After machining experiments tool conditions has been investigated using laser microscope to compare the swarf evacuation performance of the tools and silicon material clogging and accumulation.

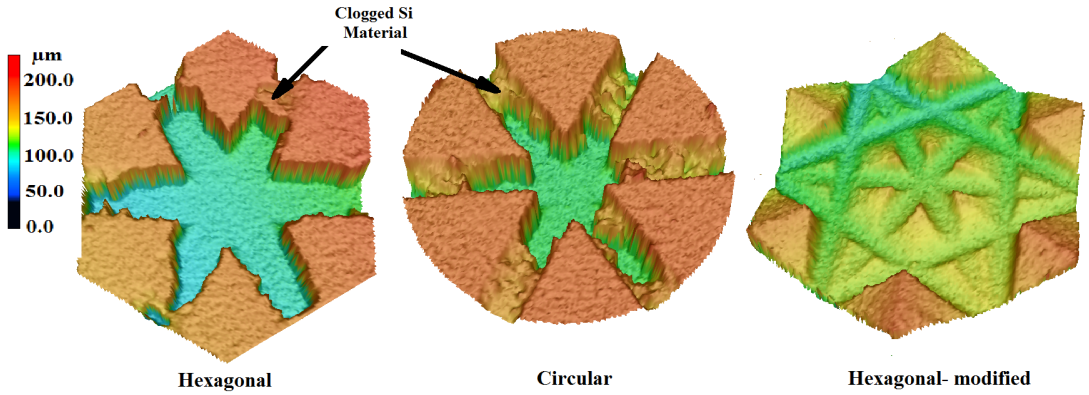

Figure 6.13: Micro end mill conditions after dry machining of silicon.

Figure 6.13 illustrates the conditions of three different geometries after dry cutting experiments. A large amount of accumulated silicon materials can be seen in circular and hexagonal geometries, however the proposed geometry was almost free of silicon material accumulation, which indicated its efficiency in the evacuation of machined materials.

A comparison has also made in terms of cutting forces generated during machining for three different geometries. The recorded cutting forces at a depth of cut of 2 μm and a feed rate of 1.2 μm/rev are shown in Figure 6.14.

As it can be seen in Figure 6.14, the circular geometry experiences larger forces along 'Z' direction and the magnitude of 'Z' force increases as length of cut increases. This results are completely in agreement with the findings of single edge experiments. The increase in the 'Z' component of the machining forces is mainly because as the machining process progresses, due to an inefficient evacuation, more martial will be accumulated in the machining zone. These materials, which are trapped between work-piece surface and bottom of the tool, will push the cutting tool upward and thereby together with the rubbing action of the flat bottom of the micro end mill will result in an increased forces.

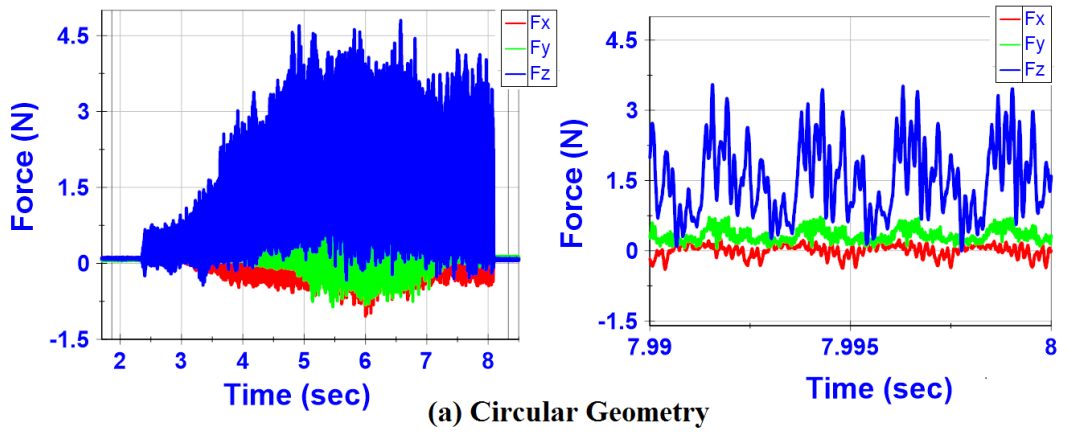

(a) Circular Geometry

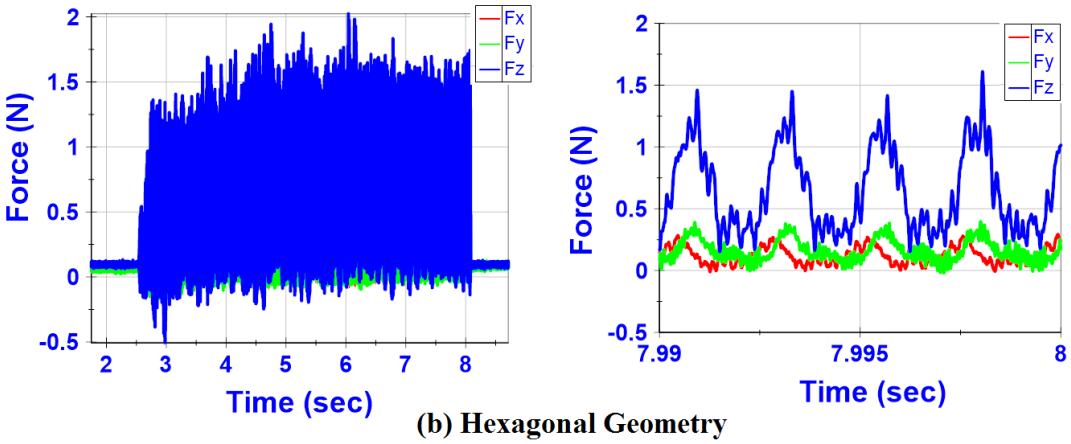

(b) Hexagonal Geometry

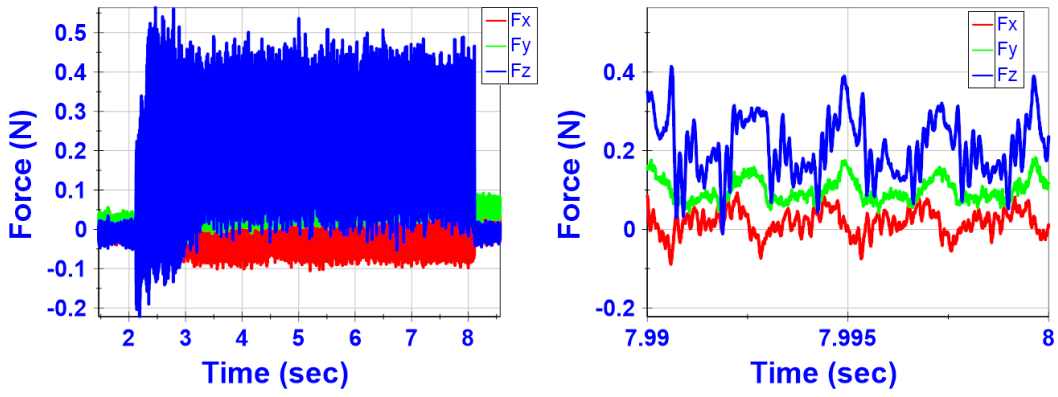

(c) Proposed Geometry

Figure 6.14: Cutting forces for three different micro end mill geometries.

Figure 6.15 illustrates the rubbing marks at the bottom of the circular micro end mill. Although, hexagonal geometry experiences lower 'Z' forces compare to the circular geometry, however 'Z' forces are three times larger than the proposed design, which demonstrates the better performance of the proposed micro end mill geometry. Similar to circular micro end mills, rubbing marks are also observed in hexagonal micro end mills.

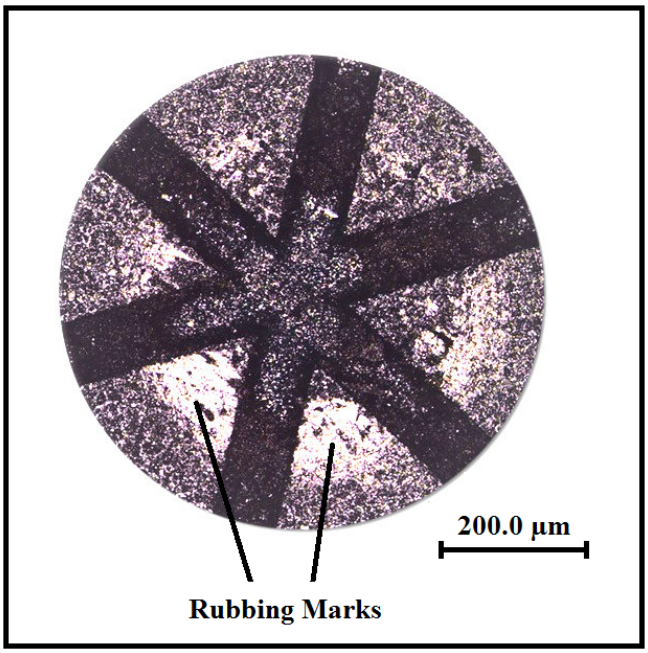

Figure 6.15: Rubbing marks observed at the bottom of circular micro end mill.

Surface roughness of the machined silicon channels (Figure 6.16) are also investigated as another performance measure for the cutting tools. As it can be seen in Figure 6.16 the proposed cutting tool resulted in a near mirror surface roughness of 32 nm. For hexagonal tool the color of the machined surface has been changed, which is an indication of high temperatures at the surface due to a large contact area. For circular tool, local fractures has been observed, which can be mainly attributed to the poor swarf evacuation. The large forces that pushes swarf clogged between tool and workpiece, to the surface can initiate local fractures at the surface.

Investigating tool condition after machining, surface roughness and machining

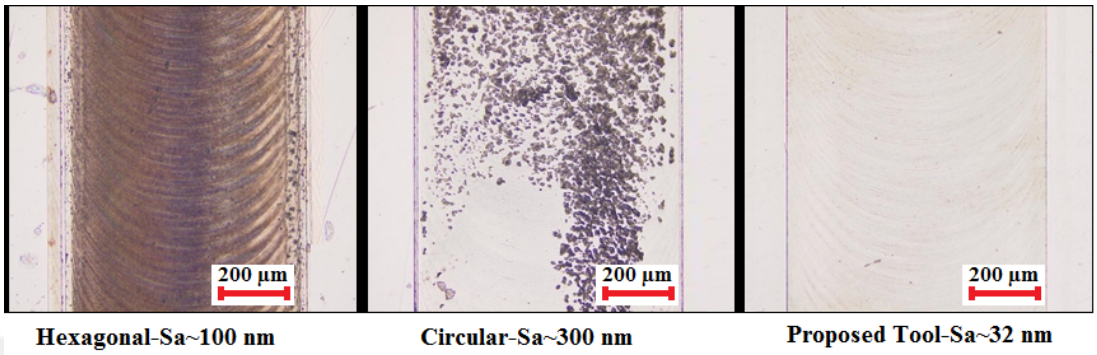

Figure 6.16: Micro end mill conditions after dry machining of silicon.

forces as three important performance indexes of the micro end mills, revealed that the proposed micro end mill shows a promising capability in ductile mode machining of silicon, being able to produce better surface finish while experiencing lower machining forces and having good chip evacuation capability.

In order to further investigate its performance in practical machining conditions in the presence of coolant, and to increasing material removal rate, a new setup has been prepared. Figure 6.17 illustrates the experimental setup used in wet machining of silicon. Machining tests are performed using NSK HES 510 spindle. A detailed specifications of the machine tool and spindle are given in chapter 3.

Micromachining experiments are performed at 25000 RPM and three different feed rates of 1.2 µm/rev, 1.6 µm/rev and 2 µm/rev. In order to achieve nanometer level depth of cut, silicon wafer has been mounted with a very small tilt of 10 µm/25 mm. After machining, the surface roughness corresponding to each depth of cut and feed rate has been measured using 3D laser scanning microscope and arithmetic mean roughness (Sa) is obtained. Figure 6.18 illustrates the measured 'Sa' values for different combinations of feed per tooth and depth of cut values.

It can be seen in Figure 6.18 that, at small feed rate and depth of cut values a better surface finish in the order of 20 nm can be achieved.

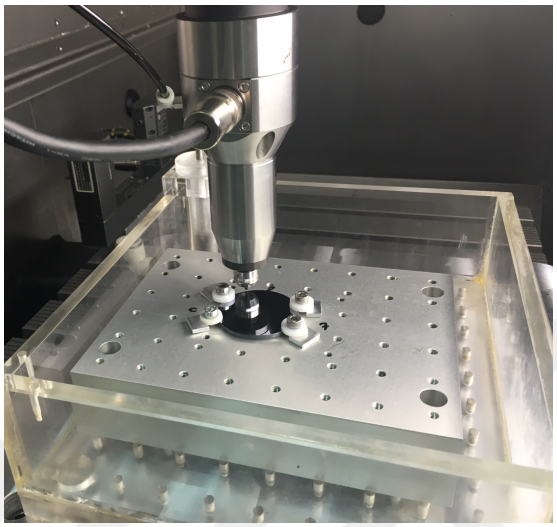

Figure 6.17: experimental setup used in wet machining of silicon.

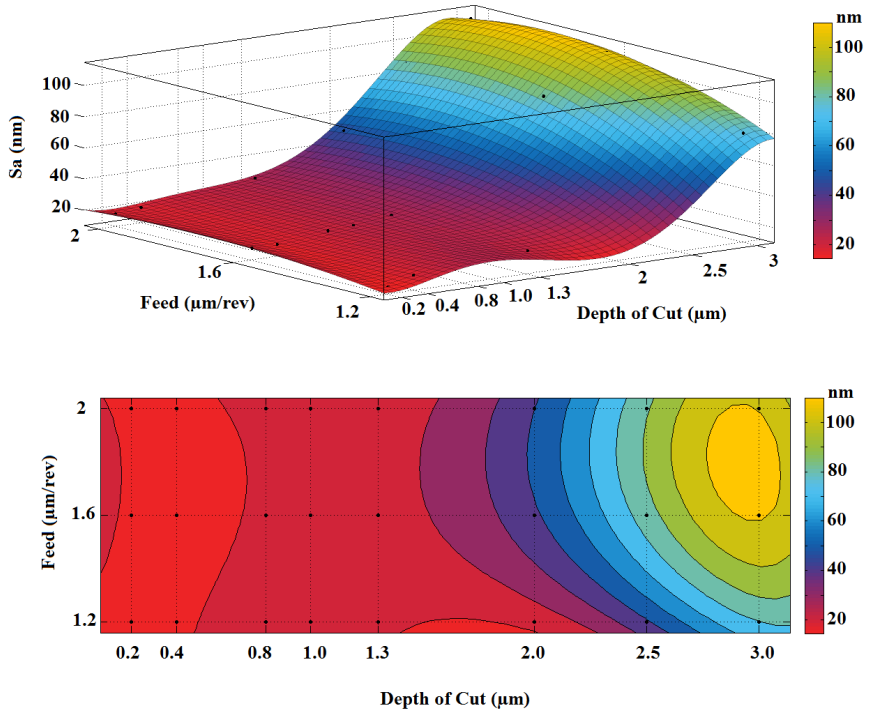

Figure 6.18: Variation of surface roughness as a function of feed rate and depth of cut for proposed geometry.

6.9 Fabrication of Mechanical Planarization Tools

It is already shown that, by changing design parameters of radially patterned end mills there is a possibility of obtaining different cutting tool geometries. One important application for these micro patterned tools can be in mechanical planarization operations. For this purpose the patterns are needed to be fabricated in larger diameters, to improve their material removal rate.

Mechanical planarization tools can be used as pre-processing tools before doing any precision machining operations on silicon or other brittle materials, because it is normally difficult to perfectly align the silicon surface with respect to the machine table. Knowing the fact that ductile mode machining is very sensitive to depth of cut variations, removing workpiece inclinations and misalignments arising from fixturing of the workpiece seems to be necessary. In addition to their applications for pre-processing, these tools can also be used to remove subsurface damage layers produced during precision machining of brittle materials. In these cases, process efficiency can be improved by first performing machining at a higher material removal rate which may induce some subsurface damages. These subsurface damages can be removed in a subsequent post-processing steps by performing ductile mode machining using developed mechanical planarization tools.

Two different mechanical planarization tools are considered. One design is based on the findings of the previous section, and the other geometry is based on an array of cutting edges in the form of micro-pyramids.

6.9.1 Radially Patterned Mechanical Planarization Tools

Radially patterned tools with different geometries can be achieved by generating number of radial grooves with different sizes on the bottom of a PCD rod. When these grooves are machined on larger diameters, they can be used for planarization purposes. Figure 6.19 illustrates examples of radially patterned fabricated mechanical planarization tools.

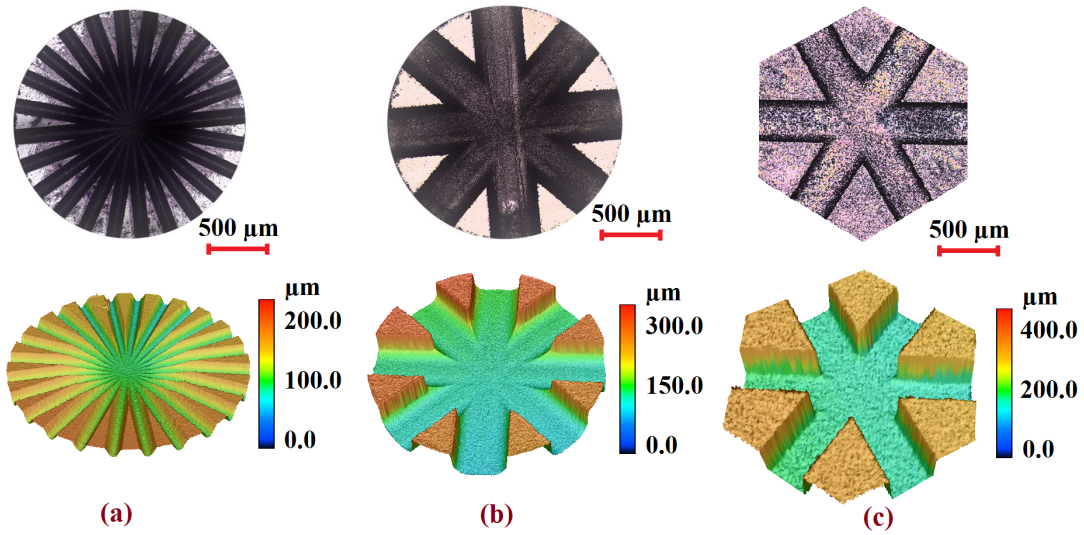

Figure 6.19: Radially patterned PCD mechanical planarization tools.

Although the tools shown in Figure 6.19 represent different geometries, however all of them suffer from the rubbing and silicon material accumulation. Therefore, attempt has been made to apply the findings in previous sections for fabricating larger diameter end mills for planarization purposes with better performances.

In order to decrease the area between the tool and the work material without introducing a negative rake angle, some changes have been made. Firstly, the number of edges are increased which, decreases the contact between the tool periphery and the workpiece. Secondly, the profile of the slots between edges is modified so that a V-shaped channel is produced. This modification further decreases the surface area between the tool and the workpiece at the bottom of the tool. Solid model of the proposed mechanical planarization tool is shown in Figure 6.20.

Figure 6.21 illustrates the fabricated mechanical planarization tool. The cutting edge radius is kept around 2 µm as in the previous set of experiments. Edge profile of the cutting tool can be seen in Figure 6.22. The increased diameter of the PCD end mill will result in an increased cutting speed, which in turn will result in a better debris evacuation.

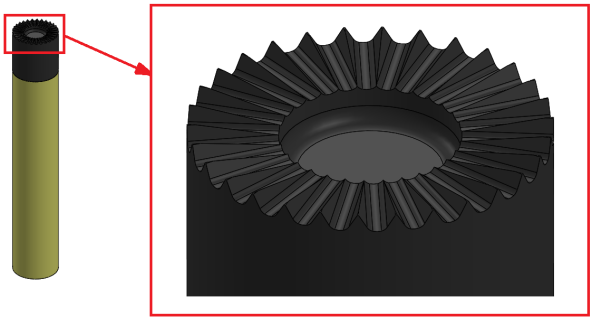

Figure 6.20: Solid model of the proposed radially patterned PCD mechanical planarization tools.

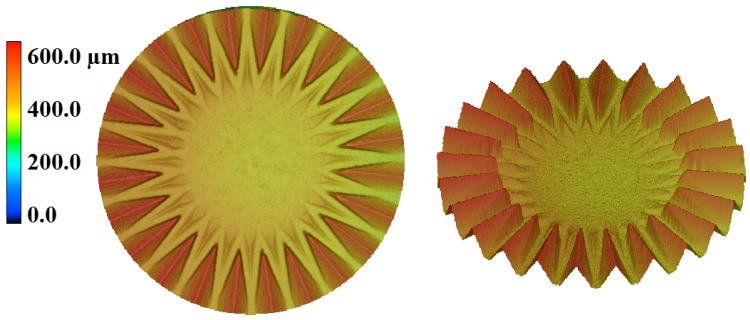

Figure 6.21: Fabricated radially patterned PCD mechanical planarization tools.

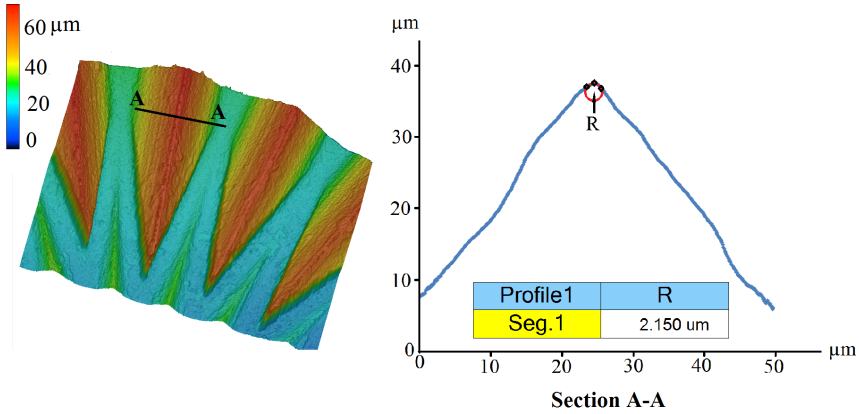

Figure 6.22: Edge radius of PCD mechanical planarization tool.

Using the experimental setup of Figure 6.17, square pockets (10×10 mm) are machined on silicon at a spindle speed of 15000 RPM, depth of cut of 2 μm and a feed rate of 2 μm/rev. For comparison purposes same experiments are conducted with fabricated circular geometries having flat lands at the bottom with 24 cutting edges (geometry depicted in Figure 6.19 (a)). Figure 6.23 illustrates square pockets machined by radially patterned tools. The pockets are machined using two different pocket milling strategies of true spiral and zigzag. A same radial immersion of 80% is used for both strategies.

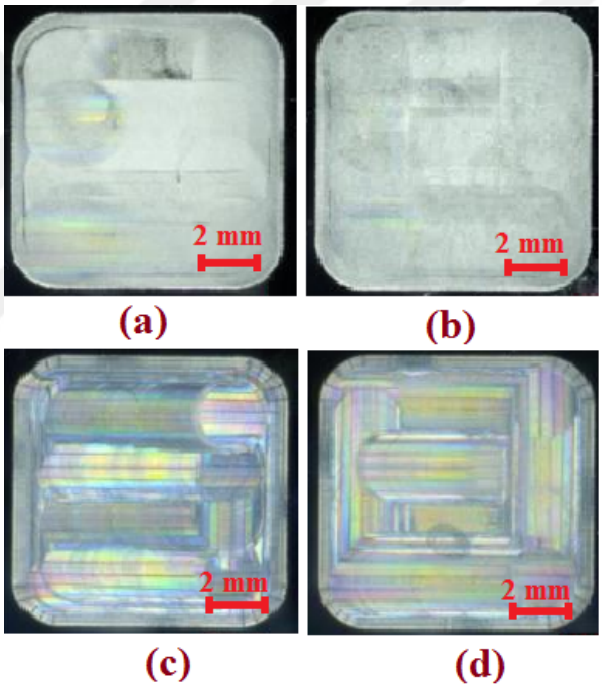

Figure 6.23: Machined pockets using different tools and different pocket milling strategies: Machined by a radially patterned tool with 24 cutting edges (a) Zigzag strategy, (b) True spiral strategy, Machined by proposed tool (c) Zigzag strategy, (d) True spiral strategy.

It can be seen in Figure 6.23 that, tool with flat lands at the bottom resulted in a poor quality surfaces. The measured 'Sa' values for the pockets machined by these tools were more than 0.2 μm due to the local fractures at the surface. These local fractures can be mainly characterized by the rubbing and friction of flat lands to the machined surface along with a possibility of pushing removed silicon materials to the

machined surface, which further deteriorate machined surfaces. However, for the proposed geometry a surface roughness below 35 nm is achieved using both strategies.

To further analyze the performance of the developed planarization tools, the influence of feed rate and depth of cut on the surface roughness is investigated during slot milling operations. Oil is used as coolant in these experiments. The depth of cut is varied between 0.7 and 5 µm, while the feed rate is selected between 0.5 and 2.5 µm/rev. The areal surface roughness (Sa) is measured as process output. The results are shown in Figure 6.24. It can be seen that, in ductile mode machining, areal surface roughness of 18 nm is achieved. The critical depth of cut is observed to be around 1 µm.

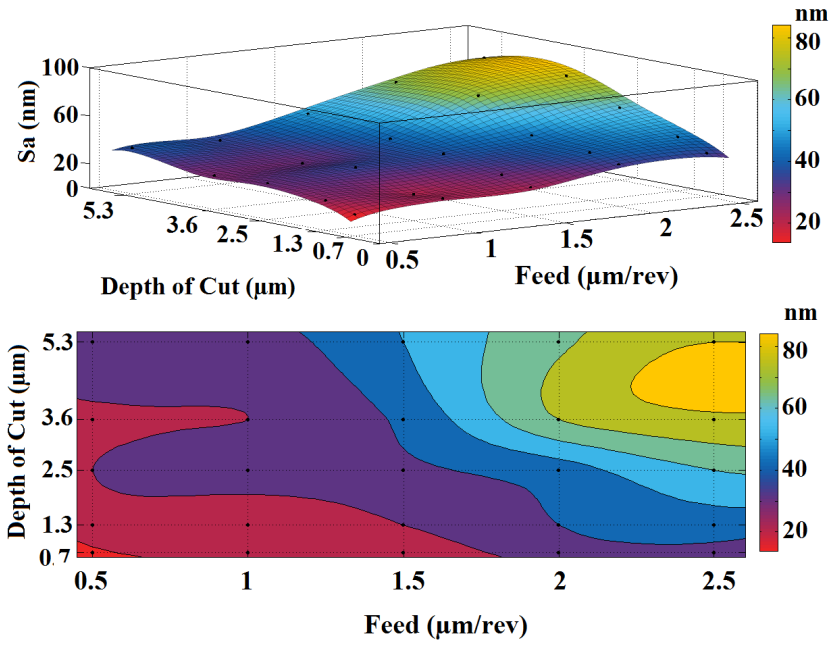

Figure 6.24: Surface roughness of machined silicon as a function of feed rate and depth of cut.

When surface roughness of the machined channels are analyzed, four different types of surfaces can be seen depending on the cutting conditions as depicted in Figure 6.25. At low feed and depth of cut values, the machining is done at ductile regime, which makes it possible to have a mirror like surface with a roughness value around 18 nm. When feed rate and/or depth of cut increases, grinding marks starts to appear on the

surface, however the machining mode is still ductile. The surfaces generated in this way normally have a roughness values up to 35 nm. When depth of cut and feed rate further increased, small fractures start to appear on the surface. The surface is characterized by a roughness values between 35 and 50 nm. The machining mode in this case is ductile-to-brittle transition. At higher feed and depth of cut values fracture becomes the dominant material removal mechanism and material removal becomes brittle with surface roughnesses larger than 50 nm.

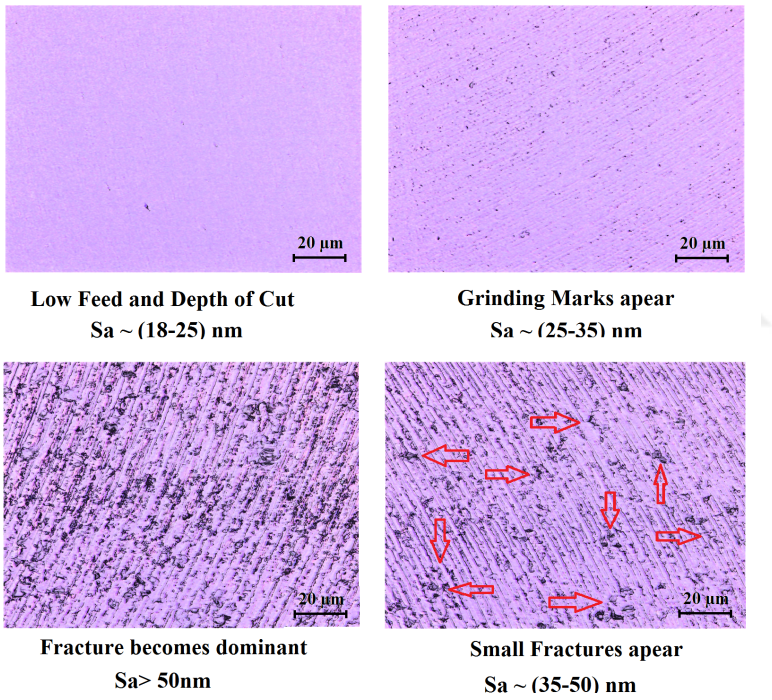

Figure 6.25: Surface roughness of silicon machined by PCD tools.

6.9.2 Mechanical Planarization Tools with Micro-pyramid Lattice Structure

Due to the importance of mechanical planarization tools in precision machining operations, in addition to radial patterning of PCD rods, another patterning scheme is also investigated. In the proposed design, an array of micro-pyramids are machined on a

PCD rod of 2 mm diameter. The performance of the tools are evaluated in terms of tool wear and achievable surface finish in ductile mode machining of silicon.

6.9.2.1 Fabrication of PCD Tools with Micro-pyramid Lattice Structure

PCD mechanical planarization tools are fabricated using the experimental setup explained in section 6.6. In order to obtain micro-pyramid lattice structures, an open contour WEDM operation with open nozzle positions is done in the form of cross cut (one cut at 0° and the other cut after 90° rotation). Figure 6.26 schematically illustrates the fabrication process of PCD tools with micro-pyramid lattice structure.

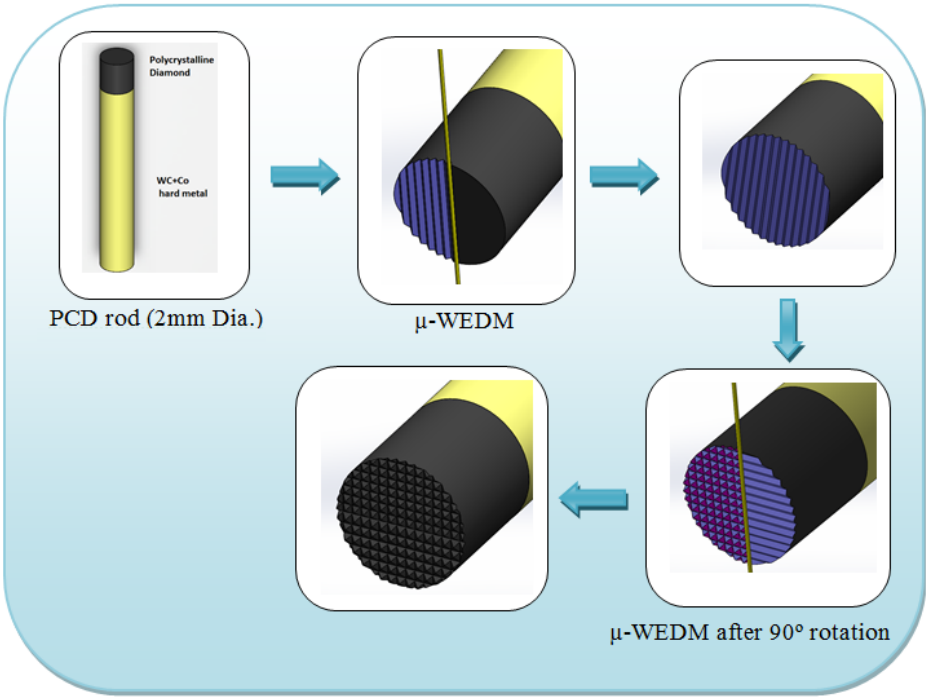

Figure 6.26: Fabrication steps for tools with micro-pyramid lattice structure.

In the fabrication process, an array of micro-pyramids with an apex angle of 60° are machined on a PCD rod of 2 mm with the specifications given in section 6.5. Depending on the spacing between pyramids, their height and base area, coarse patterned or fine patterned planarization tools can be fabricated. Figure 6.27 and 6.28 illustrate examples of fine patterned and coarse patterned planarization tools, respectively.

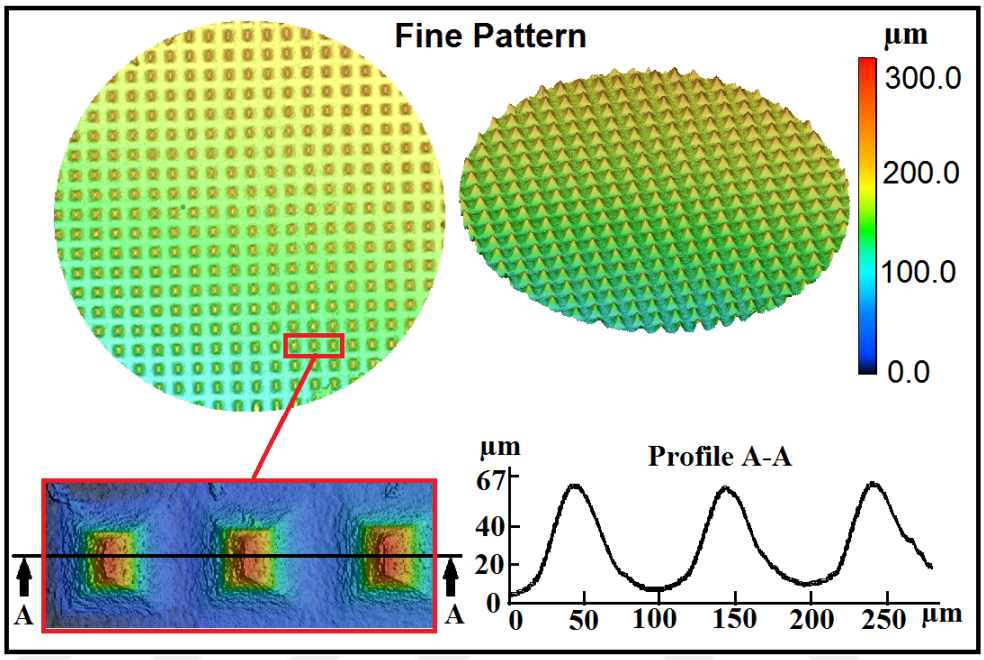

Figure 6.27: Fine patterned planarization tool.

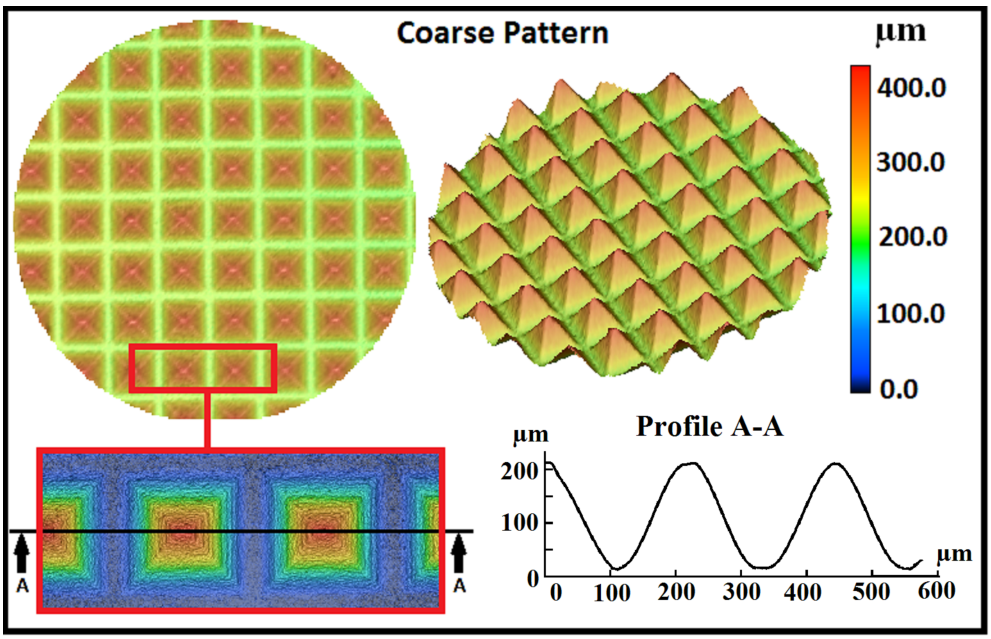

Figure 6.28: Coarse patterned planarization tool.

The fabricated planarization tools have been used for micromachining of silicon. It has been observed that some silicon material accumulated and clogged at the center of the tool (where the cutting velocity is zero). The accumulated material is shown in Figure 6.29(a). In this case due to the contact between the center of the tool and the machined surface, squeezing and rubbing of the silicon chips to the machined surface occurred, and as a result of increased friction and poor chip evacuation, the quality of the machined surface is deteriorated and some brittle fractures have been observed. As it can be seen in Figure 6.29(b), the surface finish is deteriorated at the middle of the tool path, while in outer sections a good surface roughness is achieved.

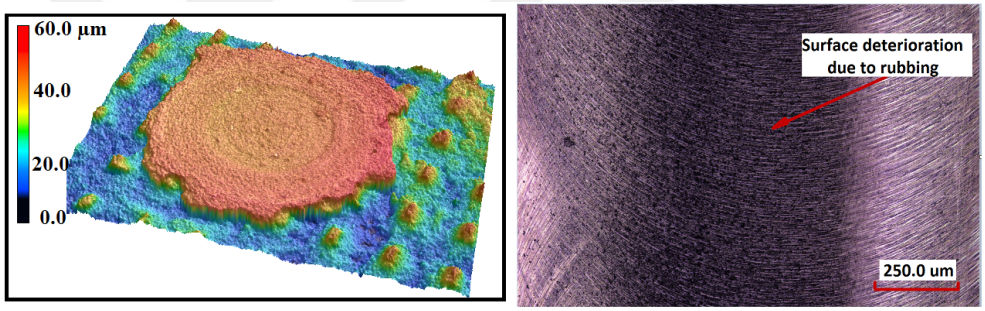

Figure 6.29: (a) Accumulation and clogging of silicon at the center of the cutting tool, (b) Surface deterioration due to the rubbing of clogged silicon material.

To overcome this problem a clearance should be created at the middle of the tool. It has been done by producing a µ-hole at the center of the tool. Therefore, an additional µ-EDM hole drilling step is added to the process of tool fabrication as depicted in Figure 6.30. Micro-EDM hole drilling were carried out using a graphite electrode of 500 µm diameter in a hybrid micro-machine tool (MIKROTOOLS DT-110). Table 3. shows the µ-EDM parameters. A 3D close up view of the planarization tool with a hole at the center is depicted in Figure 6.31.

Table 6.2: µ-EDM hole drilling parameters.

Spindle Speed	**Capacitance**	**Voltage**
1000 (RPM)	400 (nF)	100 (V)

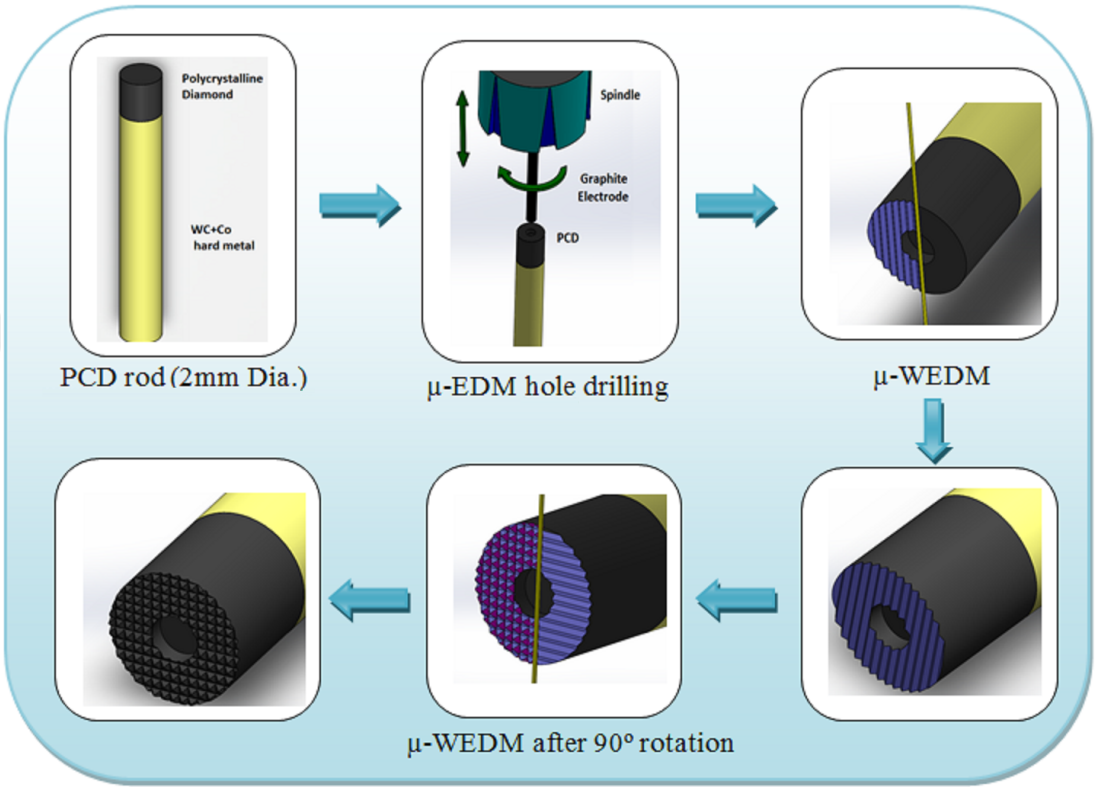

Figure 6.30: µ-EDM hole drilling of PCD tools.

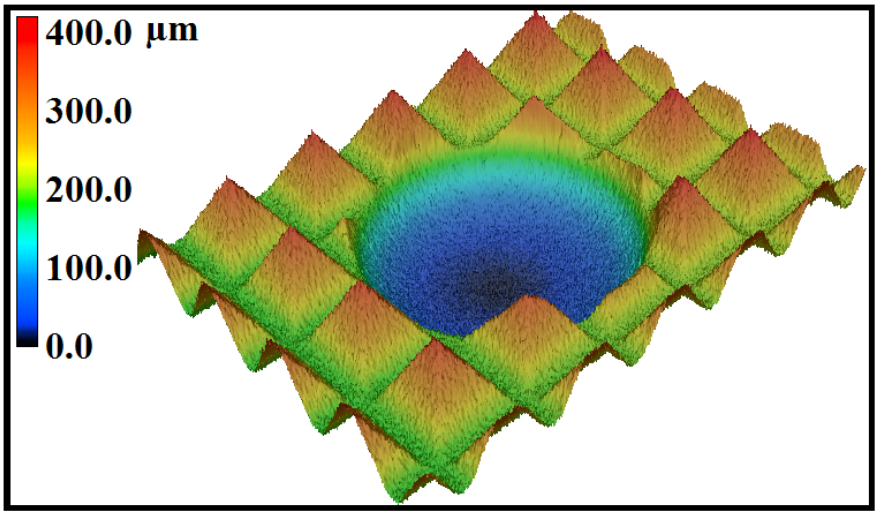

Figure 6.31: 3D close-up view of the hole drilled PCD tool.

6.9.2.2 Micromachining Experiments

The performance of the fabricated PCD mechanical planarization tools are tested by doing micro-grinding experiments on silicon. Micro-grinding experiments were carried out in MIKROTOOLS- DT-110 as can be seen in Figure 6.32 . All experiments were performed at a spindle speed of 2000 RPM.

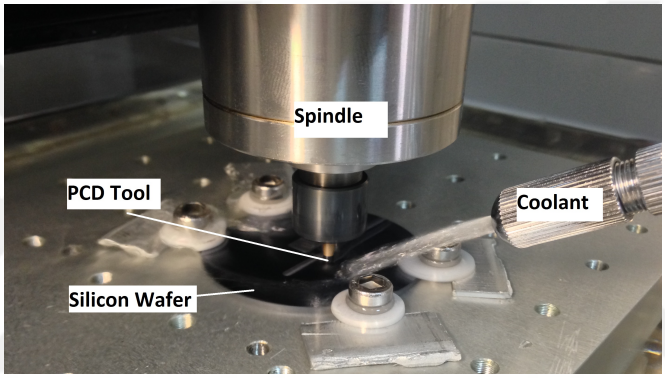

Figure 6.32: Micro-grinding experimental setup.

The performance of both fine patterned and coarse patterned tools are tested at various axial depth of cut and feed per revolutions. Table 6.3 shows the experimental conditions used for micro-grinding experiments. After each experiment, 3D topography of the machined surfaces is obtained.

Three different cutting regimes can be distinguished by analyzing machined surfaces; ductile mode machined surface, brittle mode machined surface and a transition surface. In ductile mode machining a nanometre surface roughness is achieved by removing material through plastic deformations rather than brittle fractures. Figure 6.33 illustrates silicon chips produced as a result of ductile mode machining of silicon.

In brittle mode machining, material is removed by brittle fractures and a completely damaged surface is achieved. The transition mode cutting regime is a combination of brittle fractures and ductile material removal. These three different cutting regimes are shown in Figure 6.34. The mode of machining for micro grinding experiments is given in Table 6.3.

Table 6.3: Silicon micro-grinding experimental conditions

Exp. #	Feed per revolution [μm]	Axial Depth of Cut (µm)	Machining Mode (F. P)	Machining Mode (C.P)
1	1	1	Brittle	Brittle
2	1	0.5	Ductile	Brittle
3	3	0.5	Transition	Brittle
4	3	0.2	Ductile	Ductile
5	3	0.1	Ductile	Ductile
6	6	0.1	Ductile	Ductile
7	6	0.2	Ductile	Ductile
8	10	0.1	Ductile	Ductile
9	10	0.2	Ductile	Transition
10	15	0.1	Transition	Brittle
11	15	0.2	Brittle	Brittle

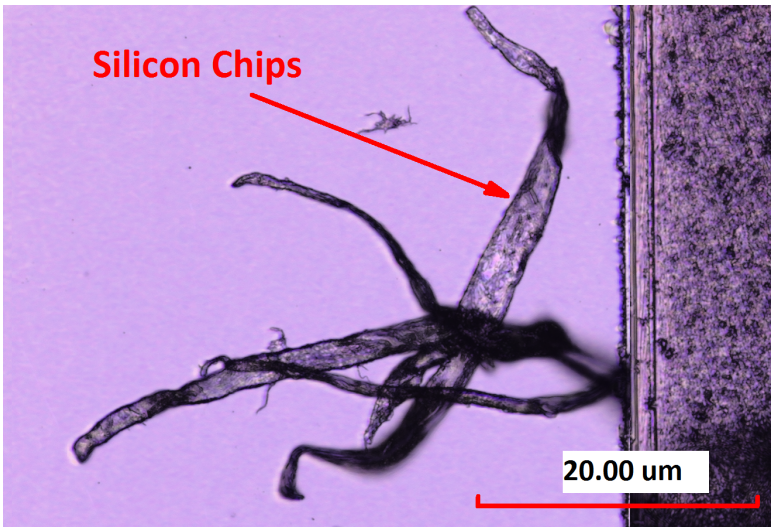

Figure 6.33: Chips produced as a result of ductile mode machining of silicon.

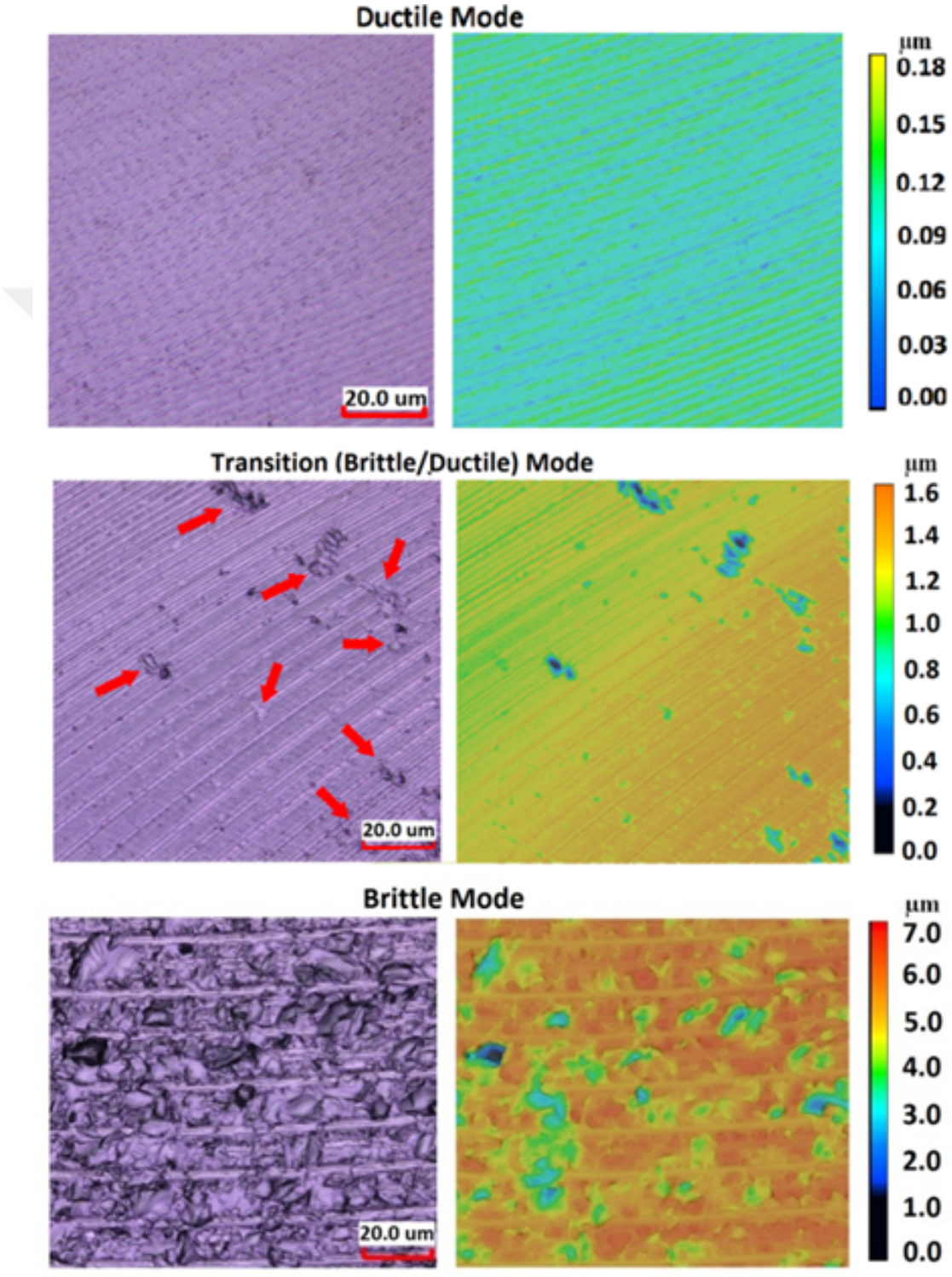

Figure 6.34: Different cutting regimes when machining silicon using different machining parameters.

For the experimental conditions of Table 6.3 'Sa' values are measured. The results of measurements for experimental cases which resulted in a ductile mode machining are shown in Figure 6.35. For transition mode machining the 'Sa' values varies between 0.12 μm and 0.18 μm, while for brittle mode machining 'Sa' values goes up to 2 μm.

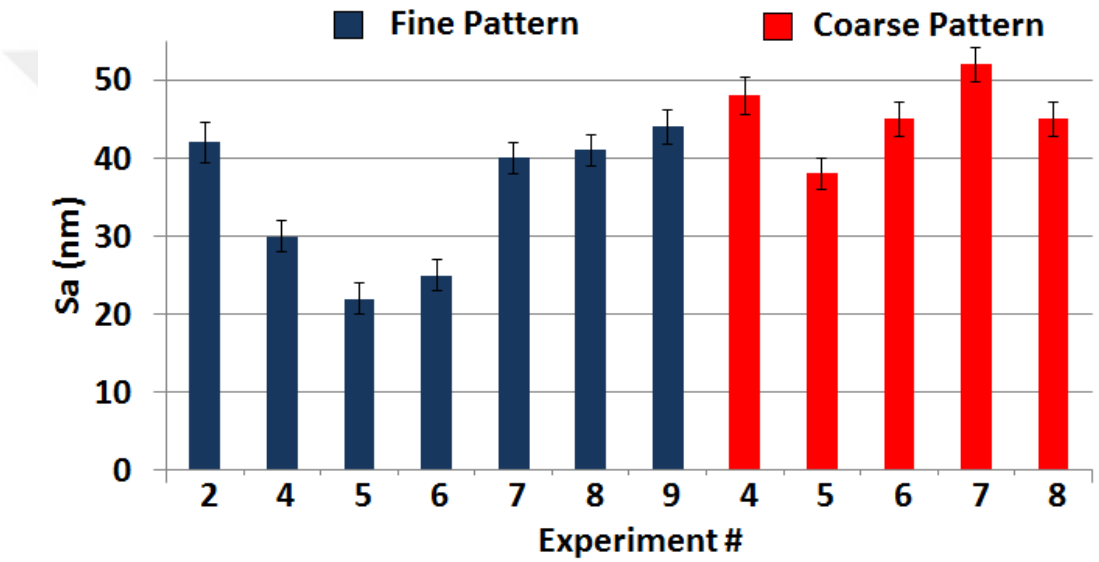

Figure 6.35: Measured Sa values for ductile mode machined silicon surfaces under different experimental conditions.

Figure 6.36 illustrates machined pockets of 10×10 mm using a fine patterned planarization tool on silicon. In this case two different radial immersions are used. Pocket of Figure 6.36(a) has been machined with 70% radial immersion, while the pocket shown in Figure 6.36(b) is machined with 5% radial immersion. It has been observed that radial immersion of 70% resulted in an arithmetic mean roughness of 25 nm, while a pocket machined at 5% radial immersion resulted in a surface with an 'Sa' value of 0.15 μm. The reason for obtaining such a poor surface quality at low radial immersions can be attributed to the excessive rubbing and increased friction between the cutting tool and workpiece surface, which causes excessive tool wear.

The mechanical planarization tools have also been examined for removing a damaged layer of the silicon. This post-processing method can be used to increase the

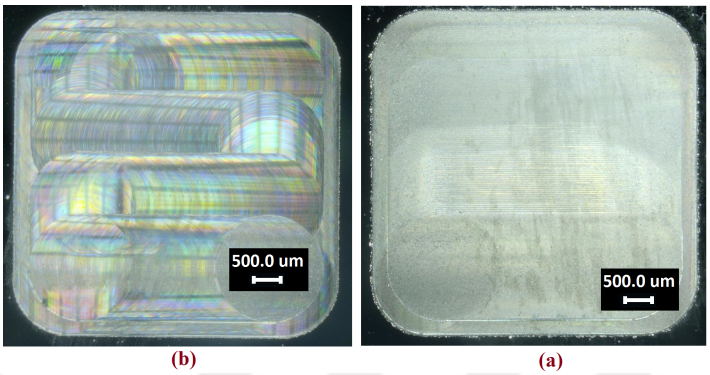

Figure 6.36: Machining of 10 × 10 mm area using a fine patterned planarization tool at: (a) 70% radial immersion, (b) 5% radial immersion.

productivity of the process, when machining deep features. In this case, as it can be seen in Figure 6.37, machining can be done at milling mode, where a larger depth of cut values are used. After bulk of the material being removed, a grinding mode machining can be used to remove sub-surface damage layer (SSD). Figure 6.38 illustrates the application of planarization tools for post-processing. It can be seen that, the damage layer resulted during brittle mode machining is removed by post-processing.

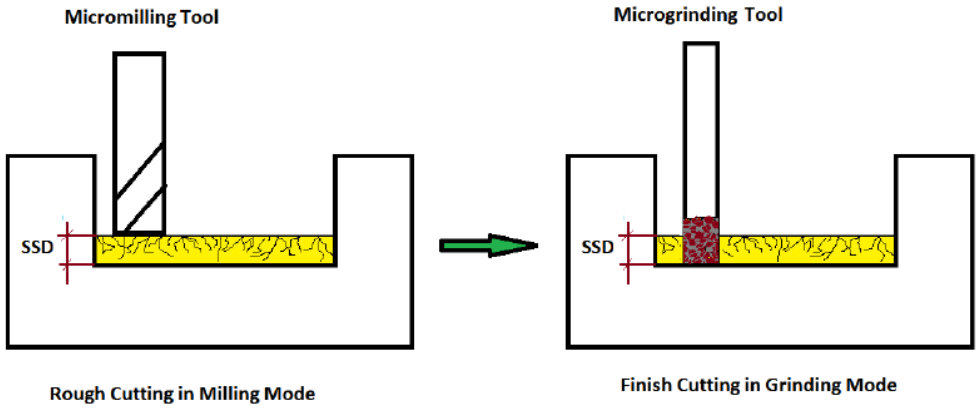

Figure 6.37: Schematic representation of post-processing using mechanical planarization tools to remove subsurface damage layer.

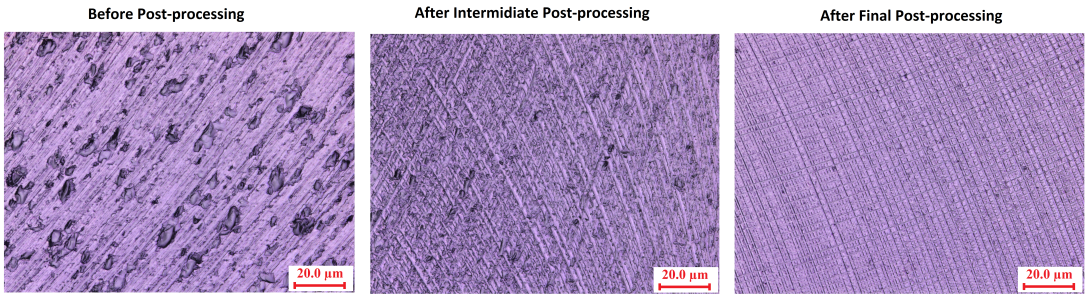

Figure 6.38: Post-processing using mechanical planarization tools to remove subsurface damage layer.

After long term cutting operations, 3D topography of the cutting tools has been obtained. For coarse patterned PCD tool only wear flats has been observed, but for fine patterned tools especially at higher feed and depth of cut values the breakage of the edges has been observed as depicted in Figure 6.39. It has been also observed that coarse patterned PCD planarization tools have a longer tool life compare to the fine patterned tools especially at larger feed and depth of cut values. This can be mainly due to smaller localized stresses of the coarse patterned tools because of their larger base area.

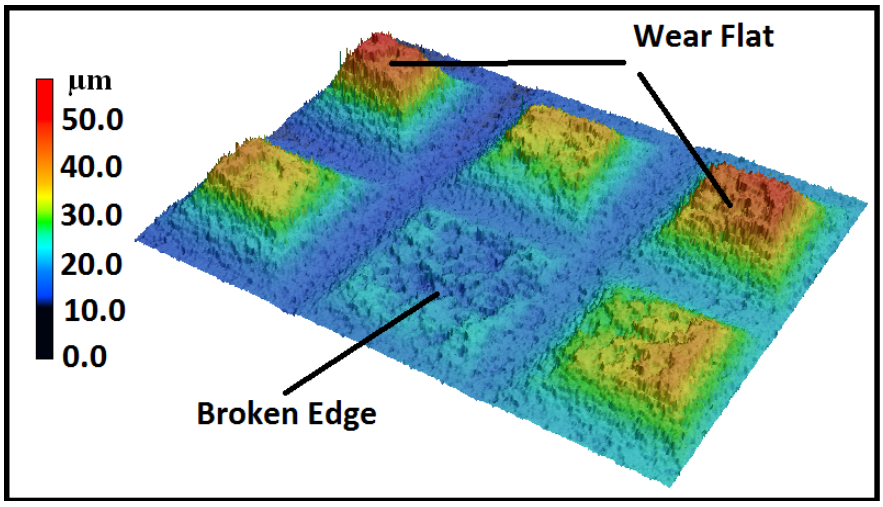

Figure 6.39: Wear and breakage of the edges of fine patterned PCD tool.

Conclusion

The influence of cutting edge micro geometry of PCD end mills on machining performance has been investigated by a systematic approach starting with single edge geometries. These single edge cutting tools having different geometries are implemented in machining of silicon and tool wear, swarf accumulation and adhesion, surface quality and machining forces are studied in detail.

The results indicated that a positive rake angle helps decreasing debris accumulation and hence improves tool wear performance of the cutting edges. Decreasing the contact area between the tool and the workpiece is shown to affect force measurements in the vertical direction which influences surface roughness.

Based on the outcomes of cutting tools with single edges, a novel PCD end mill is designed and fabricated. It is shown to be capable of producing nanometer level surface roughness while machining of silicon. A significant reduction in the cutting forces and material accumulation has been observed.

The geometry further extended to the design and fabrication of mechanical planarization tools, and novel planarization tools are designed and fabricated. For each tool, a combination of machining process parameters which can result in a ductile regime cutting are determined experimentally. In addition to radial patterning of the tools, a planarization tool with an array of fine and coarse micro-pyramids is also designed and fabricated. The conclusions can be summarized as follows:

- μ-WEDM process is successfully implemented for the fabrication of engineered micro-cutting tools from PCD.
- A systematic approach for designing high performance micro cutting tools from PCD for ductile mode machining of silicon is proposed.
- Fabricated micro cutting tools has been successfully implemented for ductile mode machining of silicon, and surfaces with nanometer roughness values are obtained.

- Fabricated tools have been employed successfully as a post-processing tool to remove subsurface damage layer of silicon.
- For cutting tools under investigation, combinations of machining parameters which resulted in ductile mode machining of silicon are determined.
- For tools with micro-pyramid lattice structure, tools with fine patterns can be employed in a wider range of machining conditions in terms of feed per revolution and depth of cut; however tool life issues must be taken into consideration when choosing machining process parameters. On the other hand, while coarse patterned tools have narrower machining parameter selection domain, they have a longer tool life.
- For radially patterned tools, tool wear in the form of increased edge radius is observed, while for tools with fine patterned micro-pyramids the progress of wear flat and breakage of pyramids are identified as tool life issues. For coarse patterned micro-pyramids, the tool life issue was the wear flat and no pyramid breakage is observed.

Chapter 7

Conclusions

Mechanical micromachining as an emerging method of fabricating micro components faces several challenges, especially when processing difficult-to-cut materials. Issues related to mechanism of cutting at micro scale, tool wear, tool deflection and surface quality requirements needs to be well addressed and understood in order for its successful implementation in producing high precision micro components. This study was set out to explore micromachining of difficult-to-cut materials emphasizing the interaction between cutting tool and workpiece at micro scale using engineered micro cutting tools. Both ductile materials (Stavax stainless steel and Ti6Al4V) and brittle materials (silicon) are studied. The reason for selecting various materials was their different behavior in the cutting process and existence of distinctive phenomena during their processing. Therefore, in this thesis a systematic approach for design and fabrication of micro cutting tools specific to a certain machining task is considered. The first phase of the research is devoted to micro tool fabrication and we arrived at the following conclusions:

- EDM-based techniques has been successfully implemented for fabrication of micro cutting tools with different geometries.
- A novel method for fabrication of ball end mills and lollipop end mills using modified block-EDG method is presented.

- The potential application of μ-WEDM as a flexible method for fabrication of high precision micro cutting tools with a controlled surface roughness has been investigated. The effect of nine WEDM process parameters (Pulse on time, Pulse off time, Peak current, voltage level for establishing machining stability criterion, Servo voltage, Gap voltage, Capacitance, Wire tension and Wire speed) on three performance measures of WEDM process (Width of cut (KERF), Surface roughness and material removal rate (MRR)) is studied using Taguchi's (L27) design of experiments. Analysis of Variance (ANOVA) and signal to noise (S/N) ratio are used to identify significant factors and to find a set of optimum parameters which result in a best surface finish, minimum KERF and maximum MRR.

- Servo voltage, Pulse off time, Wire tension and and MAO are identified as the most significant parameters in causing KERF variation, while Capacitance found to be the most dominant parameter affecting the surface roughness followed by Peak current and Gap voltage. For MRR, Servo voltage found to be the most significant process parameters followed by Pulse off time, Wire tension and MAO.

In the second phase of this research, in order to have an insight into the challenges of micromilling using conventional micro end mills, micromilling of two different ductile materials (Stavax ESR stainless steel and Ti6Al4V) are investigated. The influence of tool wear on micromilling forces, surface roughness, and tool deflections has been studied using experimental, analytical, and computational techniques. The tool wear and micromilling forces are used in the finite element simulation model of the micro end mill as inputs to analyze the tool deflections and tool breakage. The developed model is shown to produce results matching the experimental observations.

It has been shown that, while Stavax and Ti6Al4V are both ductile materials, however they show completely different characteristics in terms of the interaction between cutting tool and workpiece. Tool wear was identified as the major issue of micromilling of Stavax, while for Ti6Al4V built-up edge formation has been observed. The results of investigations in this phase can be summarized as follows:

- The influence of process parameters is investigated and suitable process parameters for circular pocketing operations of Stavax stainless steel are identified. Experimental results show the influence of plunging method on tool wear, which in turn affects micromilling forces and surface quality. The positive impact of not plunging the tool is also demonstrated.

- The relationship between radial immersion and feed per tooth is shown to affect tool wear. Areal surface roughness measurements revealed that low radial immersion yields lower surface roughness.

- Radial immersion and feed per tooth values must be selected in conjunction during the process planning stage of pocket micromilling. In our experiments, 60 % radial immersion yielded better tool performance compared to lower and higher radial immersion values.

- During circular pocket micromilling operation, tool wear is observed to evolve as edge rounding and flank wear increase. Relative tool diameter reduction, which is directly related to edge rounding of the tools, is considered as a measure of tool wear, which is relatively easy to monitor during the micromilling process.

- A proper selection of feed per tooth and radial immersion leads to a balanced edge rounding and flank wear development. In this wear case, feed per tooth may be increased in order to be able to conduct machining effectively as tool wear progresses. It must be noted that this is limited by the allowable tool deflections and stresses.

- Finite element models are developed, which are capable to predict tool deflections and stresses, which are in a very good agreement with experimental observations.

- An analytical model is developed to predict tool deflections of conventional micro end mills.

- Micromilling experiments on Ti6Al4V revealed that BUE formation is unavoidable in micromilling of this alloy. It has been observed that tool runout results in uneven tool wear and largely affects the cutting forces in micromilling process, specially at low feed per tooth values.

Based on our observations in the second phase this research, the study was set out to explore the influence of built-up edge on tool wear, forces, and surface roughness under micro scale machining conditions. The minimum uncut chip thickness is determined in the presence of BUE by conducting a well controlled micro scale orthogonal experiments. The uncut chip thickness, cutting speed, and clearance angle are considered as process variables. The outcomes of this phase can be summarized as follows:

- A stable BUE formation exists under micro scale machining conditions of the titanium alloy Ti6Al4V considered in this study.
- During break-in period, the cutting edge radius increases which promotes BUE formation, protecting the tools from crater and flank wear.
- The findings revealed the importance of predicting the size and shape of built-up edge formation during micro machining. A significant accumulation of BUE drastically affects the process.
- EDS analysis of the insert surface indicated a small change in the chemical analysis of the surface. But it is not as significant as those in macro-scale machining processes.
- Machining input conditions are shown to affect the size and shape of BUE, which affect machining forces and surface roughness values.
- Our findings confirm the influence of surface roughness on minimum uncut thickness. In the presence of BUE, the ratio of uncut chip thickness to edge radius is calculated to be around 10%.

Following experimental investigation of BUE formation, a finite element simulation model for micro scale machining of titanium alloy is developed. Built-up edge formation has been included in the simulation by modifying the cutting edge geometry based on experimental observations. The influence of friction conditions on finite element simulations has been investigated based on basic friction models. It is found that:

- Proposed finite element model is successful at predicting machining forces and chip shapes.
- A hybrid friction model where the rake face is modeled with shear friction factor of 0.8 and flank face is modeled with Coulomb friction of 0.2 yielded the best results.
- Finite element simulation predictions at uncut chip thickness of 0.4 μm significantly deviate from measurements in terms of cutting forces. This value was determined as the limit of transition from continuous to discontinuous chip formation. At this value, the surface roughness (Sz) and uncut chip thickness become almost equal, therefore machining is conducted through surface asperities. Beyond this value Finite element simulation predictions are improved.
- A material constitutive model, which was validated at macro scale conditions, is also shown to work at micro scale machining conditions under the identified friction conditions in this research.

Upon exploring the positive impact of BUE in orthogonal cutting tests, attempt has been made to extend these finding to micromilling operations. Based on this motivation, tailored micro end mills has been designed, fabricated and tested for micromilling of Ti6Al4V with geometries emanating from engineered tools used in orthogonal cutting experiments. The effect of BUE on the process outputs of micromilling has been studied using developed tailored single edge micro end mills. The results of this phase can be summarized as follows:

- Performance of tailored micro end mills are highly influence by their surface characteristics, which is a function of the WEDM process parameters used in their fabrication.
- A stable BUE formation has been observed when using tailored micro end mills in micromilling of Ti6Al4V.
- It has been observed that, in general larger BUE size resulted in a larger resultant forces.

- The findings revealed that BUE size largely depends on the selected depth of cut values. Under the conditions of this study, it has been observed that independent from length of cut values, BUE height increases when changing depth of cut from 30 μm to 40 μm and it decreases by changing depth of cut from 40 μm to 50 μm.

- No correlation has been found between BUE and burr parameters, however it has been shown that by selecting proper micromilling process parameters burr height and width can be minimized.

- By changing the length of cut of the micro end mills while using same geometric parameters, the effect of tool deflections on surface finish has been analyzed. It has been shown that increased tool deflections deteriorate surface quality of the machined parts.

- An analytical model of the proposed tailored single edge micro end mills are developed and successfully used for the prediction of micro end mill deflection.

- A finite element based design optimization methodology of tailored micro end mills is proposed. Using this optimization methodology optimum values of neck taper angle and transition radius are determined based on minimum tool deflection criterion.

The last phase of this thesis is devoted to the development of novel cutting tools for micromachining of silicon. In this phase the influence of cutting edge micro geometry of PCD end mills on machining performance has been investigated by a systematic approach starting with single edge geometries. This single edge cutting tools having different geometries are implemented in machining of silicon, and tool wear, swarf accumulation and adhesion, surface quality and machining forces are studied in detail.

The results indicated that a positive rake angle helps decreasing debris accumulation and hence improves tool wear performance of the cutting edges. Decreasing the contact area between the tool and the workpiece is shown to affect force measurements in the vertical direction which influences surface roughness. Based on the outcomes of cutting tools with single edges, a novel PCD end mill is designed and fabricated. It is

shown to be capable of producing nanometer level surface roughness while machining of silicon. A significant reduction in the cutting forces and material accumulation has been observed.

The geometry further extended to the design and fabrication of mechanical planarization tools and novel planarization tools are designed and fabricated. For each tool a combination of machining process parameters which can results in a ductile regime cutting are determined experimentally. In addition to radial patterning of the tools, a planarization tool with an array of fine and coarse micro-pyramids is also designed and fabricated. The conclusions of this phase can be summarized as:

- μ-WEDM process is successfully implemented for fabrication of engineered micro cutting tools from PCD.
- A systematic approach for designing high performance micro cutting tools from PCD for ductile mode machining of silicon is proposed.
- Fabricated micro cutting tools has been successfully implemented for ductile mode machining of silicon, and surfaces with nanometer level roughnesses are produced.
- Fabricated tools have been employed successfully as a post-processing tool to remove subsurface damage layer of silicon.
- For cutting tools under investigation, a combinations of machining parameters which resulted in ductile mode machining of silicon are determined.
- For tools with micro-pyramid structures, tools with fine patterns can be employed in a wider range of machining parameters in terms of feed per revolution and depth of cut; however tool life issues must be taken into consideration when choosing machining parameters. On the other hand, while coarse patterned tools have narrower machining parameter selection domain, they have a longer tool life
- For radially patterned tools, tool wear in the form of increased edge radius is observed, while for tools with fine patterned micro-pyramids the progress of wear

flat and breakage of pyramids are identified as tool life issues. For coarse patterned micro-pyramids tool life issue was the wear flat and no pyramid breakage is observed.

Recommendations for Future Works

- In this study the effect of WEDM process parameters on the arithmetic mean roughness of the machined surfaces has been studied in detail. Further investigations can be done by studying the effect of WEDM process parameters on other areal parameters such as Kurtosis, Skewness, Bearing area curve and etc. The effect of different surface morphologies of the micro end mills on their tribological behavior during machining of brittle materials can also be investigated.
- In this thesis BUE is included in the finite element model through its effect in the cutting edge geometry. One step forward to include BUE formation in the finite element simulation of machining processes including BUE formation can be the development of new damage models for the finite element simulation of micro scale cutting capable of modeling the BUE formation process.
- In this study PCD micro end mills are successfully used for ductile mode machining of silicon. Investigation of the performance of the developed micro cutting tools for machining other brittle materials, different grade of glasses and ceramics can also be investigated.
- In this thesis, analytical models of tool deflections are developed for tailored micro end mills. This models can be integrated into the cutting force models to increase accuracy of the cutting force predictions in modeling of micromilling forces using tailored micro end mills
- Modeling of grinding forces during machining of silicon using novel cutting tool geometries proposed in this thesis can also further investigated.

Bibliography

[1] K. F. Ehmann, D. Bourell, M. L. Culpepper, T. J. Hodgson, T. R. Kurfess, M. Madou, K. Rajurkar, and R. E. DeVor, "International assessment of research and development in micromanufacturing," tech. rep., DTIC Document, 2005.

[2] Y. Okazaki, N. Mishima, and K. Ashida, "Microfactoryconcept, history, and developments," *Journal of Manufacturing Science and Engineering*, vol. 126, no. 4, pp. 837–844, 2004.

[3] X. Liu, R. E. DeVor, S. Kapoor, and K. Ehmann, "The mechanics of machining at the microscale: assessment of the current state of the science," *Journal of manufacturing science and engineering*, vol. 126, no. 4, pp. 666–678, 2004.

[4] J. Chae, S. Park, and T. Freiheit, "Investigation of micro-cutting operations," *International Journal of Machine Tools and Manufacture*, vol. 46, no. 3, pp. 313–332, 2006.

[5] X. Lai, H. Li, C. Li, Z. Lin, and J. Ni, "Modelling and analysis of micro scale milling considering size effect, micro cutter edge radius and minimum chip thickness," *International Journal of Machine Tools and Manufacture*, vol. 48, no. 1, pp. 1–14, 2008.

[6] K. J. Maloney, K. D. Fink, T. A. Schaedler, J. A. Kolodziejska, A. J. Jacobsen, and C. S. Roper, "Multifunctional heat exchangers derived from three-dimensional micro-lattice structures," *International Journal of Heat and Mass Transfer*, vol. 55, no. 9, pp. 2486–2493, 2012.

[7] S. C. Terry, J. H. Jerman, and J. B. Angell, "A gas chromatographic air analyzer fabricated on a silicon wafer," *IEEE Transactions on Electron Devices*, vol. 26, no. 12, pp. 1880–1886, 1979.

[8] P. C. Garcia, R. Lozano, and A. E. Dzul, *Modelling and control of mini-flying machines*. Springer Science & Business Media, 2006.

[9] P. Fonda, K. Nakamoto, A. Heidari, H.-A. Yang, D. A. Horsley, L. Lin, and K. Yamazaki, "A study on the optimal fabrication method for micro-scale gyroscopes using a hybrid process consisting of electric discharge machining, chemical etching or micro-mechanical milling," *CIRP Annals-Manufacturing Technology*, vol. 62, no. 1, pp. 183–186, 2013.

[10] A. Rossetti, G. Pavesi, and G. Ardizzon, "A new two stage miniature pump: Design, experimental characterization and numerical analyses," *Sensors and Actuators A: Physical*, vol. 164, no. 1, pp. 74–87, 2010.

[11] M. Malekian, S. S. Park, and M. B. Jun, "Tool wear monitoring of micro-milling operations," *Journal of Materials Processing Technology*, vol. 209, no. 10, pp. 4903–4914, 2009.

[12] M. J. Jackson, *Micro-and Nanomanufacturing*. Springer, 2007.

[13] E. Brinksmeier, O. Riemer, and R. Stern, "Machining of precision parts and microstructures," in *Initiatives of Precision Engineering at the Beginning of a Millennium*, pp. 3–11, Springer, 2002.

[14] A. Asad, T. Masaki, M. Rahman, H. Lim, and Y. Wong, "Tool-based micromachining," *Journal of Materials Processing Technology*, vol. 192, pp. 204–211, 2007.

[15] S. Filiz, L. Xie, L. E. Weiss, and O. Ozdoganlar, "Micromilling of microbarbs for medical implants," *International Journal of Machine Tools and Manufacture*, vol. 48, no. 3, pp. 459–472, 2008.

[16] J. Aurich, J. Engmann, G. Schueler, and R. Haberland, "Micro grinding tool for manufacture of complex structures in brittle materials," *CIRP Annals-Manufacturing Technology*, vol. 58, no. 1, pp. 311–314, 2009.

[17] J.-J. Boy, M. Aiguille, A. Boulouize, and C. K. Malek, "Developments in micro ultrasonic machining (musm)," in *Proc. 2nd Int. Conf. on Multi-Material Micro Manufacture (4M), Grenoble, 20-22 sept. 2006*, pp. 123–126, Elsevier, 2006.

[18] G.-L. Chern and S.-D. Wang, "Punching of noncircular micro-holes and development of micro-forming," *Precision engineering*, vol. 31, no. 3, pp. 210–217, 2007.

[19] M. Geiger, M. Kleiner, R. Eckstein, N. Tiesler, and U. Engel, "Microforming," *CIRP Annals-Manufacturing Technology*, vol. 50, no. 2, pp. 445–462, 2001.

[20] W. Zhao, X. Li, and Z. Wang, "Study on micro electrochemical machining at micro to meso-scale," in *2006 1st IEEE International Conference on Nano/Micro Engineered and Molecular Systems*, pp. 325–329, IEEE, 2006.

[21] S. Lan, H.-J. Lee, E. Kim, J. Ni, S.-H. Lee, X. Lai, J.-H. Song, N. K. Lee, and M. G. Lee, "A parameter study on the micro hot-embossing process of glassy polymer for pattern replication," *Microelectronic Engineering*, vol. 86, no. 12, pp. 2369–2374, 2009.

[22] B. Sha, S. Dimov, C. Griffiths, and M. Packianather, "Investigation of micro-injection moulding: factors affecting the replication quality," *Journal of Materials Processing Technology*, vol. 183, no. 2, pp. 284–296, 2007.

[23] B. Duan, M. Wang, W. Y. Zhou, W. L. Cheung, Z. Y. Li, and W. W. Lu, "Three-dimensional nanocomposite scaffolds fabricated via selective laser sintering for bone tissue engineering," *Acta Biomaterialia*, vol. 6, no. 12, pp. 4495–4505, 2010.

[24] S. Ballandras, M. Calin, S. Zissi, A. Bertsch, J. André, and D. Hauden, "Microstereophotolithography and shape memory alloy for the fabrication of miniaturized actuators," *Sensors and Actuators A: Physical*, vol. 62, no. 1, pp. 741–747, 1997.

[25] K. Yamaguchi, K. Sakai, T. Yamanaka, and T. Hirayama, "Generation of three-dimensional micro structure using metal jet," *Precision Engineering*, vol. 24, no. 1, pp. 2–8, 2000.

[26] T. Masuzawa, "State of the art of micromachining," *CIRP Annals-Manufacturing Technology*, vol. 49, no. 2, pp. 473–488, 2000.

[27] Z. Zeng, Y. Wang, Z. Wang, D. Shan, and X. He, "A study of micro-edm and micro-ecm combined milling for 3d metallic micro-structures," *Precision Engineering*, vol. 36, no. 3, pp. 500–509, 2012.

[28] B. Yan, A. Wang, C. Huang, and F. Huang, "Study of precision micro-holes in borosilicate glass using micro edm combined with micro ultrasonic vibration machining," *International Journal of Machine Tools and Manufacture*, vol. 42, no. 10, pp. 1105–1112, 2002.

[29] U. Kunze, "Invited review nanoscale devices fabricated by dynamic ploughing with an atomic force microscope," *Superlattices and microstructures*, vol. 31, no. 1, pp. 3–17, 2002.

[30] D. Dornfeld, S. Min, and Y. Takeuchi, "Recent advances in mechanical micromachining," *CIRP Annals-Manufacturing Technology*, vol. 55, no. 2, pp. 745–768, 2006.

[31] M. Weck, S. Fischer, and M. Vos, "Fabrication of microcomponents using ultraprecision machine tools," *Nanotechnology*, vol. 8, no. 3, p. 145, 1997.

[32] L. Uriarte, A. Herrero, M. Zatarain, G. Santiso, L. L. de Lacalle, A. Lamikiz, and J. Albizuri, "Error budget and stiffness chain assessment in a micromilling machine equipped with tools less than 0.3 mm in diameter," *Precision Engineering*, vol. 31, no. 1, pp. 1–12, 2007.

[33] D. P. Adams, M. J. Vasile, G. Benavides, and A. N. Campbell, "Micromilling of metal alloys with focused ion beam–fabricated tools," *Precision Engineering*, vol. 25, no. 2, pp. 107–113, 2001.

[34] M. J. Vasile, C. R. Friedrich, B. Kikkeri, and R. McElhannon, "Micrometer-scale machining: tool fabrication and initial results," *Precision Engineering*, vol. 19, no. 2, pp. 180–186, 1996.

[35] D. Huo, *Micro-cutting: fundamentals and applications*. John Wiley & Sons, 2013.

[36] A. Perveen, W. Y. San, and M. Rahman, "Fabrication of different geometry cutting tools and their effect on the vertical micro-grinding of bk7 glass," *The International Journal of Advanced Manufacturing Technology*, vol. 61, no. 1-4, pp. 101–115, 2012.

[37] J. Yan, K. Watanabe, and T. Aoyama, "Micro-electrical discharge machining of polycrystalline diamond using rotary cupronickel electrode," *CIRP Annals-Manufacturing Technology*, vol. 63, no. 1, pp. 209–212, 2014.

[38] S.-T. Chen and Z.-H. Jiang, "A force controlled grinding-milling technique for quartz-glass micromachining," *Journal of Materials Processing Technology*, vol. 216, pp. 206–215, 2015.

[39] T. Masaki, T. Kuriyagawa, J. Yan, and N. Yoshihara, "Study on shaping spherical poly crystalline diamond tool by micro-electro-discharge machining and micro-grinding with the tool," *International Journal of Surface Science and Engineering*, vol. 1, no. 4, pp. 344–359, 2007.

[40] C. J. Morgan, R. R. Vallance, and E. R. Marsh, "Micro machining glass with polycrystalline diamond tools shaped by micro electro discharge machining," *Journal of Micromechanics and Microengineering*, vol. 14, no. 12, p. 1687, 2004.

[41] J. Fleischer, M. Deuchert, C. Ruhs, C. Kühlewein, G. Halvadjiysky, and C. Schmidt, "Design and manufacturing of micro milling tools," *Microsystem Technologies*, vol. 14, no. 9-11, pp. 1771–1775, 2008.

[42] J. Fleischer, T. Masuzawa, J. Schmidt, and M. Knoll, "New applications for micro-edm," *Journal of Materials Processing Technology*, vol. 149, no. 1, pp. 246–249, 2004.

[43] Z. Zhang, H. Peng, and J. Yan, "Micro-cutting characteristics of edm fabricated high-precision polycrystalline diamond tools," *International Journal of Machine Tools and Manufacture*, vol. 65, pp. 99–106, 2013.

[44] J. M. Meek and J. D. Craggs, "Electrical breakdown of gases," 1978.

[45] T. Lee, "T-f theory of electron emission in high-current arcs," *Journal of Applied Physics*, vol. 30, no. 2, pp. 166–171, 1959.

[46] M. Kunieda, B. Lauwers, K. P. Rajurkar, and B. Schumacher, "Advancing edm through fundamental insight into the process," *CIRP Annals-Manufacturing Technology*, vol. 54, no. 2, pp. 64–87, 2005.

[47] T. O. Hockenberry and E. M. Williams, "Dynamic evolution of events accompanying the low-voltage discharges employed in edm," *IEEE Transactions on Industry and General Applications*, no. 4, pp. 302–309, 1967.

[48] N. Ravi and H. Huang, "Fabrication of symmetrical section microfeatures using the electro-discharge machining block electrode method," *Journal of Micromechanics and Microengineering*, vol. 12, no. 6, p. 905, 2002.

[49] M. Rahman, H. Lim, K. Neo, A. S. Kumar, Y. Wong, and X. Li, "Tool-based nanofinishing and micromachining," *Journal of Materials Processing Technology*, vol. 185, no. 1, pp. 2–16, 2007.

[50] T. Masuzawa, M. Fujino, K. Kobayashi, T. Suzuki, and N. Kinoshita, "Wire electro-discharge grinding for micro-machining," *CIRP Annals-Manufacturing Technology*, vol. 34, no. 1, pp. 431–434, 1985.

[51] K. Egashira and K. Mizutani, "Micro-drilling of monocrystalline silicon using a cutting tool," *Precision Engineering*, vol. 26, no. 3, pp. 263–268, 2002.

[52] K.-T. Chiang and F.-P. Chang, "Optimization of the wedm process of particle-reinforced material with multiple performance characteristics using grey relational analysis," *Journal of Materials Processing Technology*, vol. 180, no. 1, pp. 96–101, 2006.

[53] B. Kuriachen, K. Somashekhar, and J. Mathew, "Multiresponse optimization of micro-wire electrical discharge machining process," *The International Journal of Advanced Manufacturing Technology*, vol. 76, no. 1-4, pp. 91–104, 2015.

[54] S. Assarzadeh and M. Ghoreishi, "Statistical modeling and optimization of process parameters in electro-discharge machining of cobalt-bonded tungsten carbide composite (wc/6% co)," *Procedia CIRP*, vol. 6, pp. 463–468, 2013.

[55] R. C. Weast, M. J. Astle, W. H. Beyer, *et al.*, *CRC handbook of chemistry and physics*, vol. 69. CRC press Boca Raton, FL, 1988.

[56] M. Sittig, "Handbook of toxic and hazardous chemicals," 1981.

[57] K. Liu, X. Li, M. Rahman, and X. Liu, "Cbn tool wear in ductile cutting of tungsten carbide," *Wear*, vol. 255, no. 7, pp. 1344–1351, 2003.

[58] P. Pandey and S. Jilani, "Electrical machining characteristics of cemented carbides," *Wear*, vol. 116, no. 1, pp. 77–88, 1987.

[59] M. Jahan, Y. Wong, and M. Rahman, "A study on the fine-finish die-sinking micro-edm of tungsten carbide using different electrode materials," *Journal of materials processing technology*, vol. 209, no. 8, pp. 3956–3967, 2009.

[60] S. Lee and X. Li, "Study of the effect of machining parameters on the machining characteristics in electrical discharge machining of tungsten carbide," *Journal of materials processing Technology*, vol. 115, no. 3, pp. 344–358, 2001.

[61] S. H. Lee and X. Li, "Study of the surface integrity of the machined workpiece in the edm of tungsten carbide," *Journal of materials processing technology*, vol. 139, no. 1, pp. 315–321, 2003.

[62] I. Puertas, C. Luis, and L. Alvarez, "Analysis of the influence of edm parameters on surface quality, mrr and ew of wc–co," *Journal of Materials Processing Technology*, vol. 153, pp. 1026–1032, 2004.

[63] G. S. Upadhyaya, *Cemented tungsten carbides: production, properties and testing*. William Andrew, 1998.

[64] Z. Z. Fang, "Correlation of transverse rupture strength of wc–co with hardness," *International Journal of Refractory Metals and Hard Materials*, vol. 23, no. 2, pp. 119–127, 2005.

[65] A. Ikram, N. A. Mufti, M. Q. Saleem, and A. R. Khan, "Parametric optimization for surface roughness, kerf and mrr in wire electrical discharge machining (wedm) using taguchi design of experiment," *Journal of Mechanical Science and Technology*, vol. 27, no. 7, pp. 2133–2141, 2013.

[66] S. Di, X. Chu, D. Wei, Z. Wang, G. Chi, and Y. Liu, "Analysis of kerf width in micro-wedm," *International Journal of Machine Tools and Manufacture*, vol. 49, no. 10, pp. 788–792, 2009.

[67] P. J. P. J. Ross, *Taguchi techniques for quality engineering: loss function, orthogonal experiments, parameter and tolerance design*. 1996.

[68] N. Tosun, C. Cogun, and G. Tosun, "A study on kerf and material removal rate in wire electrical discharge machining based on taguchi method," *Journal of Materials Processing Technology*, vol. 152, no. 3, pp. 316–322, 2004.

[69] R. Leach, *Characterisation of areal surface texture*. Springer, 2013.

[70] C. L. Giusca, R. K. Leach, F. Helary, T. Gutauskas, and L. Nimishakavi, "Calibration of the scales of areal surface topography-measuring instruments: part 1. measurement noise and residual flatness," *Measurement Science and Technology*, vol. 23, no. 3, p. 035008, 2012.

[71] B. Muralikrishnan and J. Raja, *Computational surface and roundness metrology*. Springer Science & Business Media, 2008.

[72] L. Blunt and X. Jiang, *Advanced techniques for assessment surface topography: development of a basis for 3D surface texture standards" surfstand"*. Elsevier, 2003.

[73] F. Koenigsberger, *Design Principles of Metal-Cutting Machine Tools*. Elsevier, 2013.

[74] M. P. Vogler, R. E. DeVor, and S. G. Kapoor, "Microstructure-level force prediction model for micro-milling of multi-phase materials," *Journal of Manufacturing Science and Engineering*, vol. 125, no. 2, pp. 202–209, 2003.

[75] G. Bissacco, H. N. Hansen, and L. De Chiffre, "Size effects on surface generation in micro milling of hardened tool steel," *CIRP Annals-Manufacturing Technology*, vol. 55, no. 1, pp. 593–596, 2006.

[76] H.-J. Kang and S.-H. Ahn, "Fabrication and characterization of microparts by mechanical micromachining: precision and cost estimation," *Proceedings of the*

Institution of Mechanical Engineers, Part B: Journal of Engineering Manufacture, vol. 221, no. 2, pp. 231–240, 2007.

[77] S. N. B. Oliaei and Y. Karpat, "Influence of tool wear on machining forces and tool deflections during micro milling," *The International Journal of Advanced Manufacturing Technology*, pp. 1–18, 2015.

[78] H. Li, X. Lai, C. Li, J. Feng, and J. Ni, "Modelling and experimental analysis of the effects of tool wear, minimum chip thickness and micro tool geometry on the surface roughness in micro-end-milling," *Journal of Micromechanics and Microengineering*, vol. 18, no. 2, p. 025006, 2007.

[79] A. Aramcharoen and P. Mativenga, "Size effect and tool geometry in micromilling of tool steel," *Precision Engineering*, vol. 33, no. 4, pp. 402–407, 2009.

[80] Y. Karpat, "Investigation of the effect of cutting tool edge radius on material separation due to ductile fracture in machining," *International Journal of Mechanical Sciences*, vol. 51, no. 7, pp. 541–546, 2009.

[81] R. E. DeVor and S. G. Kapoor, "On the modeling and analysis of machining performance in micro-endmilling, part i: Surface generation," *J. Manuf. Sci. Eng*, vol. 126, no. 4, pp. 685–694, 2004.

[82] A. A. Elkaseer, S. Dimov, K. Popov, and R. Minev, "Tool wear in micro-endmilling: Material microstructure effects, modeling, and experimental validation," *Journal of Micro and Nano-Manufacturing*, vol. 2, no. 4, p. 044502, 2014.

[83] C.-J. Kim, M. Bono, J. Ni, *et al.*, "Experimental analysis of chip formation in micro-milling," *TECHNICAL PAPERS-SOCIETY OF MANUFACTURING ENGINEERS-ALL SERIES-*, 2002.

[84] C. Li, X. Lai, H. Li, and J. Ni, "Modeling of three-dimensional cutting forces in micro-end-milling," *Journal of Micromechanics and Microengineering*, vol. 17, no. 4, p. 671, 2007.

[85] A. Mamedov, I. Lazoglu, *et al.*, "Instantaneous tool deflection model for micro milling," *The International Journal of Advanced Manufacturing Technology*, vol. 79, no. 5-8, pp. 769–777, 2015.

[86] P. Rodríguez and J. Labarga, "Tool deflection model for micromilling processes," *The International Journal of Advanced Manufacturing Technology*, vol. 76, no. 1-4, pp. 199–207, 2015.

[87] G. Mijušković, P. Krajnik, and J. Kopač, "Analysis of tool deflection in micro milling of graphite electrodes," *The International Journal of Advanced Manufacturing Technology*, vol. 76, no. 1-4, pp. 209–217, 2015.

[88] W. Bao and I. Tansel, "Modeling micro-end-milling operations. part iii: influence of tool wear," *International Journal of Machine Tools and Manufacture*, vol. 40, no. 15, pp. 2193–2211, 2000.

[89] M. Câmara, J. C. Rubio, A. Abrão, and J. Davim, "State of the art on micromilling of materials, a review," *Journal of Materials Science & Technology*, vol. 28, no. 8, pp. 673–685, 2012.

[90] V. Kovvuri, Z. Wang, A. Araujo, M. da Silva, S. Bukkapatnam, and W. Hung, "Built-up-edge formation in micromilling," in *ASME 2015 International Mechanical Engineering Congress and Exposition*, pp. V02AT02A057–V02AT02A057, American Society of Mechanical Engineers, 2015.

[91] Z. Wang, V. Kovvuri, A. Araujo, M. Bacci, W. Hung, and S. Bukkapatnam, "Built-up-edge effects on surface deterioration in micromilling processes," *Journal of Manufacturing Processes*, 2016.

[92] F. Vollertsen, "Categories of size effects," *Production Engineering*, vol. 2, no. 4, pp. 377–383, 2008.

[93] M. Abouridouane, F. Klocke, and D. Lung, "Microstructure-based 3d fe modeling for micro cutting ferritic-pearlitic carbon steels," in *ASME 2014 International Manufacturing Science and Engineering Conference collocated with the JSME 2014 International Conference on Materials and Processing and the 42nd North American Manufacturing Research Conference*, pp. V001T01A008–V001T01A008, American Society of Mechanical Engineers, 2014.

[94] N. Moronuki, Y. Liang, and Y. Furukawa, "Experiments on the effect of material properties on microcutting processes," *Precision engineering*, vol. 16, no. 2, pp. 124–131, 1994.

[95] D. Lucca, Y. Seo, and R. Komanduri, "Effect of tool edge geometry on energy dissipation in ultraprecision machining," *CIRP Annals-Manufacturing Technology*, vol. 42, no. 1, pp. 83–86, 1993.

[96] Z. Yuan, M. Zhou, and S. Dong, "Effect of diamond tool sharpness on minimum cutting thickness and cutting surface integrity in ultraprecision machining," *Journal of Materials Processing Technology*, vol. 62, no. 4, pp. 327–330, 1996.

[97] A. Bayoumi, G. Yücesan, and D. Hutton, "On the closed form mechanistic modeling of milling: Specific cutting energy, torque, and power," *Journal of materials engineering and performance*, vol. 3, no. 1, pp. 151–158, 1994.

[98] F. Vollertsen, D. Biermann, H. N. Hansen, I. Jawahir, and K. Kuzman, "Size effects in manufacturing of metallic components," *CIRP Annals-Manufacturing Technology*, vol. 58, no. 2, pp. 566–587, 2009.

[99] E. Armarego and R. Brown, "On the size effect in metal cutting," *THE INTERNATIONAL JOURNAL OF PRODUCTION RESEARCH*, vol. 1, no. 3, pp. 75–99, 1961.

[100] D. Lucca, R. Rhorer, and R. Komanduri, "Energy dissipation in the ultraprecision machining of copper," *CIRP Annals-Manufacturing Technology*, vol. 40, no. 1, pp. 69–72, 1991.

[101] W. Backer, E. Marshall, and M. Shaw, "The size effect in metal cutting," *Trans. Asme*, vol. 74, no. 1, p. 61, 1952.

[102] S. Filiz, C. M. Conley, M. B. Wasserman, and O. B. Ozdoganlar, "An experimental investigation of micro-machinability of copper 101 using tungsten carbide micro-endmills," *International Journal of Machine Tools and Manufacture*, vol. 47, no. 7, pp. 1088–1100, 2007.

[103] M. C. Shaw, "The size effect in metal cutting," *Sadhana*, vol. 28, no. 5, pp. 875–896, 2003.

[104] J. Larsen-Basse and P. Oxley, "Effect of strain-rate sensitivity on scale phenomena in chip formation," in *Proceedings of the Thirteenth International Machine Tool Design and Research Conference*, pp. 209–216, Springer, 1973.

[105] J. Takadoum, *Materials and surface engineering in tribology*. John Wiley & Sons, 2013.

[106] N. Ikawa, S. Shimada, and H. Tanaka, "Minimum thickness of cut in micromachining," *Nanotechnology*, vol. 3, no. 1, p. 6, 1992.

[107] J. Saedon, A. H. A. Halim, H. Husain, M. Meon, and M. F. Othman, "Influence of cutting edge radius in micromachining aisi d2," in *Applied Mechanics and Materials*, vol. 393, pp. 253–258, Trans Tech Publ, 2013.

[108] H. Weule, V. Hüntrup, and H. Tritschler, "Micro-cutting of steel to meet new requirements in miniaturization," *CIRP Annals-Manufacturing Technology*, vol. 50, no. 1, pp. 61–64, 2001.

[109] S. M. Son, H. S. Lim, and J. H. Ahn, "Effects of the friction coefficient on the minimum cutting thickness in micro cutting," *International Journal of Machine Tools and Manufacture*, vol. 45, no. 4, pp. 529–535, 2005.

[110] D. Biermann, A. Baschin, E. Krebs, and J. Schlenker, "Manufacturing of dies from hardened tool steels by 3-axis micromilling," *Production Engineering*, vol. 5, no. 2, pp. 209–217, 2011.

[111] K. Lee and D. A. Dornfeld, "A study of surface roughness in the micro-end-milling process," *Laboratory for Manufacturing and Sustainability*, 2004.

[112] U. Natarajan, P. Periyanan, and S. Yang, "Multiple-response optimization for micro-endmilling process using response surface methodology," *The International Journal of Advanced Manufacturing Technology*, vol. 56, no. 1-4, pp. 177–185, 2011.

[113] M. Rahman, A. S. Kumar, and J. Prakash, "Micro milling of pure copper," *Journal of Materials Processing Technology*, vol. 116, no. 1, pp. 39–43, 2001.

[114] E. Uhlmann, S. Piltz, and K. Schauer, "Micro milling of sintered tungsten–copper composite materials," *Journal of Materials Processing Technology*, vol. 167, no. 2, pp. 402–407, 2005.

[115] E. Vázquez, C. A. Rodríguez, A. Elías-Zúñiga, and J. Ciurana, "An experimental analysis of process parameters to manufacture metallic micro-channels by micro-milling," *The International Journal of Advanced Manufacturing Technology*, vol. 51, no. 9-12, pp. 945–955, 2010.

[116] W. Wang, S. Kweon, and S. Yang, "A study on roughness of the micro-end-milled surface produced by a miniatured machine tool," *Journal of Materials Processing Technology*, vol. 162, pp. 702–708, 2005.

[117] K. Weinert and V. Petzoldt, "Machining niti micro-parts by micro-milling," *Materials Science and Engineering: A*, vol. 481, pp. 672–675, 2008.

[118] T. Thepsonthi and T. Özel, "Multi-objective process optimization for micro-end milling of ti-6al-4v titanium alloy," *The International Journal of Advanced Manufacturing Technology*, vol. 63, no. 9-12, pp. 903–914, 2012.

[119] T. Thepsonthi and T. Özel, "An integrated toolpath and process parameter optimization for high-performance micro-milling process of ti–6al–4v titanium alloy," *The International Journal of Advanced Manufacturing Technology*, vol. 75, no. 1-4, pp. 57–75, 2014.

[120] H. Li, X. Lai, C. Li, J. Feng, and J. Ni, "Modelling and experimental analysis of the effects of tool wear, minimum chip thickness and micro tool geometry on the surface roughness in micro-end-milling," *Journal of Micromechanics and Microengineering*, vol. 18, no. 2, p. 025006, 2007.

[121] A. Aramcharoen, P. Mativenga, S. Yang, K. Cooke, and D. Teer, "Evaluation and selection of hard coatings for micro milling of hardened tool steel," *International Journal of Machine Tools and Manufacture*, vol. 48, no. 14, pp. 1578–1584, 2008.

[122] J. Saedon, S. Soo, D. Aspinwall, A. Barnacle, and N. Saad, "Prediction and optimization of tool life in micromilling aisi d2 (62 hrc) hardened steel," *Procedia Engineering*, vol. 41, pp. 1674–1683, 2012.

[123] P. Cardoso and J. P. Davim, "Optimization of surface roughness in micromilling," *Materials and Manufacturing Processes*, vol. 25, no. 10, pp. 1115–1119, 2010.

[124] H. Liu, Y. Sun, Y. Geng, and D. Shan, "Experimental research of milling force and surface quality for tc4 titanium alloy of micro-milling," *The International Journal of Advanced Manufacturing Technology*, vol. 79, no. 1-4, pp. 705–716, 2015.

[125] M. Jun, R. Devor, S. Kapoor, and F. Englert, "Experimental investigation of machinability and tool wear in micro-endmilling," *Trans of NAMRI/SME*, vol. 36, pp. 201–208, 2008.

[126] E. Ezugwu, "Key improvements in the machining of difficult-to-cut aerospace superalloys," *International Journal of Machine Tools and Manufacture*, vol. 45, no. 12, pp. 1353–1367, 2005.

[127] M. Otkur and I. Lazoglu, "Trochoidal milling," *International Journal of Machine Tools and Manufacture*, vol. 47, no. 9, pp. 1324–1332, 2007.

[128] Keyence, "Technical Document: Introduction to Surface Roughness Measurement." `http://www.keyence.com/products/microscope/lasermicroscope/vk-x100_x200/`.

[129] M. Arizmendi, F. Campa, J. Fernández, L. L. de Lacalle, A. Gil, E. Bilbao, F. Veiga, and A. Lamikiz, "Model for surface topography prediction in peripheral milling considering tool vibration," *CIRP Annals-Manufacturing Technology*, vol. 58, no. 1, pp. 93–96, 2009.

[130] M. Arizmendi, J. Fernández, L. L. de Lacalle, A. Lamikiz, A. Gil, J. Sánchez, F. Campa, and F. Veiga, "Model development for the prediction of surface topography generated by ball-end mills taking into account the tool parallel axis offset. experimental validation," *CIRP Annals-Manufacturing Technology*, vol. 57, no. 1, pp. 101–104, 2008.

[131] Y. S. Liao and C. L. Huang, "An approach to improve machined surface finish in micro milling," in *Advanced Materials Research*, vol. 797, pp. 649–654, Trans Tech Publ, 2013.

[132] Y. Altintas, *Manufacturing automation: metal cutting mechanics, machine tool vibrations, and CNC design*. Cambridge university press, 2012.

[133] L. Zhou, F. Peng, R. Yan, P. Yao, C. Yang, and B. Li, "Analytical modeling and experimental validation of micro end-milling cutting forces considering edge radius and material strengthening effects," *International Journal of Machine Tools and Manufacture*, vol. 97, pp. 29–41, 2015.

[134] M. Salgado, L. L. De Lacalle, A. Lamikiz, J. Muñoa, and J. Sánchez, "Evaluation of the stiffness chain on the deflection of end-mills under cutting forces," *International Journal of Machine Tools and Manufacture*, vol. 45, no. 6, pp. 727–739, 2005.

[135] C.-J. Kim, J. R. Mayor, and J. Ni, "A static model of chip formation in microscale milling," *Journal of manufacturing science and engineering*, vol. 126, no. 4, pp. 710–718, 2004.

[136] H.-Y. Feng and C.-H. Menq, "A flexible ball-end milling system model for cutting force and machining error prediction," *Journal of Manufacturing Science and Engineering*, vol. 118, no. 4, pp. 461–469, 1996.

[137] W. Kline, R. DeVor, and I. Shareef, "The prediction of surface accuracy in end milling," *Journal of Engineering for Industry*, vol. 104, no. 3, pp. 272–278, 1982.

[138] G. Kim, B. Kim, and C. Chu, "Estimation of cutter deflection and form error in ball-end milling processes," *International Journal of Machine Tools and Manufacture*, vol. 43, no. 9, pp. 917–924, 2003.

[139] T. A. Dow, E. L. Miller, and K. Garrard, "Tool force and deflection compensation for small milling tools," *Precision Engineering*, vol. 28, no. 1, pp. 31–45, 2004.

[140] E. Ezugwu and Z. Wang, "Titanium alloys and their machinabilitya review," *Journal of materials processing technology*, vol. 68, no. 3, pp. 262–274, 1997.

[141] H. Hong, A. Riga, J. Gahoon, and C. Scott, "Machinability of steels and titanium alloys under lubrication," *Wear*, vol. 162, pp. 34–39, 1993.

[142] E. Paul, C. J. Evans, A. Mangamelli, M. L. McGlauflin, and R. S. Polvani, "Chemical aspects of tool wear in single point diamond turning," *Precision Engineering*, vol. 18, no. 1, pp. 4–19, 1996.

[143] N. Baltzer and T. Copponnex, *Precious Metals for Biomedical Applications*. Elsevier, 2014.

[144] R. Boyer, "Titanium for aerospace: rationale and applications," *Advanced Performance Materials*, vol. 2, no. 4, pp. 349–368, 1995.

[145] H. J. Siekmann, "How to machine titanium," *The Tool Engineer*, vol. 34, no. 1, pp. 78–82, 1955.

[146] X. Zhao, W. Ke, S. Zhang, and W. Zheng, "Potential failure cause analysis of tungsten carbide end mills for titanium alloy machining," *Engineering Failure Analysis*, vol. 66, pp. 321–327, 2016.

[147] A. Shokrani, V. Dhokia, and S. T. Newman, "Investigation of the effects of cryogenic machining on surface integrity in cnc end milling of ti–6al–4v titanium alloy," *Journal of Manufacturing Processes*, vol. 21, pp. 172–179, 2016.

[148] S. Kalpakjian, S. Schmid, *et al.*, *Manufacturing, Engineering and Technology SI 6th Edition-Serope Kalpakjian and Stephen Schmid: Manufacturing, Engineering and Technology*. Digital Designs, 2006.

[149] K. Woon, M. Rahman, K. Neo, and K. Liu, "The effect of tool edge radius on the contact phenomenon of tool-based micromachining," *International Journal of Machine Tools and Manufacture*, vol. 48, no. 12, pp. 1395–1407, 2008.

[150] D. J. Waldorf, R. E. DeVor, and S. G. Kapoor, "An evaluation of ploughing models for orthogonal machining," *Journal of manufacturing science and engineering*, vol. 121, no. 4, pp. 550–558, 1999.

[151] N. Fang and P. Dewhurst, "Slip-line modeling of built-up edge formation in machining," *International Journal of Mechanical Sciences*, vol. 47, no. 7, pp. 1079–1098, 2005.

[152] Y. Karpat and T. Özel, "Mechanics of high speed cutting with curvilinear edge tools," *International Journal of Machine Tools and Manufacture*, vol. 48, no. 2, pp. 195–208, 2008.

[153] T. Childs, "Ductile shear failure damage modelling and predicting built-up edge in steel machining," *Journal of Materials Processing Technology*, vol. 213, no. 11, pp. 1954–1969, 2013.

[154] M. B. Jun, R. E. DeVor, and S. G. Kapoor, "Investigation of the dynamics of microend millingpart ii: model validation and interpretation," *Journal of manufacturing science and engineering*, vol. 128, no. 4, pp. 901–912, 2006.

[155] M. Malekian, M. Mostofa, S. Park, and M. Jun, "Modeling of minimum uncut chip thickness in micro machining of aluminum," *Journal of Materials Processing Technology*, vol. 212, no. 3, pp. 553–559, 2012.

[156] A. C. Ramos, H. Autenrieth, T. Strauß, M. Deuchert, J. Hoffmeister, and V. Schulze, "Characterization of the transition from ploughing to cutting in micro machining and evaluation of the minimum thickness of cut," *Journal of Materials Processing Technology*, vol. 212, no. 3, pp. 594–600, 2012.

[157] M. Armendia, A. Garay, L.-M. Iriarte, and P.-J. Arrazola, "Comparison of the machinabilities of ti6al4v and timetal® 54m using uncoated wc–co tools," *Journal of Materials Processing Technology*, vol. 210, no. 2, pp. 197–203, 2010.

[158] A. Pramanik and G. Littlefair, "Machining of titanium alloy (ti-6al-4v)theory to application," *Machining Science and Technology*, vol. 19, no. 1, pp. 1–49, 2015.

[159] T. Thepsonthi and T. Özel, "3-d finite element process simulation of micro-end milling ti-6al-4v titanium alloy: Experimental validations on chip flow and tool wear," *Journal of Materials Processing Technology*, vol. 221, pp. 128–145, 2015.

[160] P. D. Hartung, B. Kramer, and B. Von Turkovich, "Tool wear in titanium machining," *CIRP Annals-Manufacturing Technology*, vol. 31, no. 1, pp. 75–80, 1982.

[161] J. Kümmel, J. Gibmeier, E. Müller, R. Schneider, V. Schulze, and A. Wanner, "Detailed analysis of microstructure of intentionally formed built-up edges for improving wear behaviour in dry metal cutting process of steel," *Wear*, vol. 311, no. 1, pp. 21–30, 2014.

[162] J. Kümmel, D. Braun, J. Gibmeier, J. Schneider, C. Greiner, V. Schulze, and A. Wanner, "Study on micro texturing of uncoated cemented carbide cutting tools for wear improvement and built-up edge stabilisation," *Journal of Materials Processing Technology*, vol. 215, pp. 62–70, 2015.

[163] N. Yussefian, P. Koshy, S. Buchholz, and F. Klocke, "Electro-erosion edge honing of cutting tools," *CIRP Annals-Manufacturing Technology*, vol. 59, no. 1, pp. 215–218, 2010.

[164] B. Denkena and D. Biermann, "Cutting edge geometries," *CIRP Annals-Manufacturing Technology*, vol. 63, no. 2, pp. 631–653, 2014.

[165] A. Attanasio, M. Gelfi, A. Pola, E. Ceretti, and C. Giardini, "Influence of material microstructures in micromilling of ti6al4v alloy," *Materials*, vol. 6, no. 9, pp. 4268–4283, 2013.

[166] A. Ikuta, K. Shinozaki, H. Masuda, Y. Yamane, H. Kuroki, and Y. Fukaya, "Consideration of the adhesion mechanism of ti alloys using a cemented carbide tool during the cutting process," *Journal of materials processing technology*, vol. 127, no. 2, pp. 251–255, 2002.

[167] J. Gerez, M. Sanchez-Carrilero, J. Salguero, M. Batista, and M. Marcos, "A sem and eds based study of the microstructural modifications of turning inserts in the dry machining of ti6al4v alloy," in *THIRD MANUFACTURING ENGINEERING SOCIETY INTERNATIONAL CONFERENCE: MESIC-09*, vol. 1181, pp. 567–574, AIP Publishing, 2009.

[168] P.-J. Arrazola, A. Garay, L.-M. Iriarte, M. Armendia, S. Marya, and F. Le Maitre, "Machinability of titanium alloys (ti6al4v and ti555. 3)," *Journal of materials processing technology*, vol. 209, no. 5, pp. 2223–2230, 2009.

[169] V. P. Astakhov and J. C. Outeiro, "Metal cutting mechanics, finite element modelling," in *Machining*, pp. 1–27, Springer, 2008.

[170] J. C. Outeiro, D. Umbrello, R. M'Saoubi, and I. Jawahir, "Evaluation of present numerical models for predicting metal cutting performance and residual stresses," *Machining Science and Technology*, vol. 19, no. 2, pp. 183–216, 2015.

[171] V. P. Astakhov, *Tribology of metal cutting*, vol. 52. Elsevier, 2006.

[172] N. Nzorev, "Interrelationship between shear processes occurring along tool face and on shear in metal cutting e," *International Research in Production Engineering, New York: Anler. Soc. Mech. Engrs*, 1993.

[173] E. Usui and T. Shirakashi, "Mechanics of machiningfrom descriptive to predictive theory," *ASME Publication PED*, vol. 7, pp. 13–35, 1982.

[174] M. Dirikolu, T. Childs, and K. Maekawa, "Finite element simulation of chip flow in metal machining," *International Journal of Mechanical Sciences*, vol. 43, no. 11, pp. 2699–2713, 2001.

[175] P. Arrazola, T. Özel, D. Umbrello, M. Davies, and I. Jawahir, "Recent advances in modelling of metal machining processes," *CIRP Annals-Manufacturing Technology*, vol. 62, no. 2, pp. 695–718, 2013.

[176] T. Thepsonthi and T. Özel, "Experimental and finite element simulation based investigations on micro-milling ti-6al-4v titanium alloy: Effects of cbn coating on tool wear," *Journal of Materials Processing Technology*, vol. 213, no. 4, pp. 532–542, 2013.

[177] X. Jin and Y. Altintas, "Prediction of micro-milling forces with finite element method," *Journal of Materials Processing Technology*, vol. 212, no. 3, pp. 542–552, 2012.

[178] S. Afazov, S. Ratchev, and J. Segal, "Modelling and simulation of micro-milling cutting forces," *Journal of Materials Processing Technology*, vol. 210, no. 15, pp. 2154–2162, 2010.

[179] K. G. Budinski, "Tribological properties of titanium alloys," *Wear*, vol. 151, no. 2, pp. 203–217, 1991.

[180] L. Zhang and H. Tanaka, "Towards a deeper understanding of wear and friction on the atomic scalea molecular dynamics analysis," *Wear*, vol. 211, no. 1, pp. 44–53, 1997.

[181] S. Venkatachalam and S. Y. Liang, "Effects of ploughing forces and friction coefficient in microscale machining," *Journal of manufacturing science and engineering*, vol. 129, no. 2, pp. 274–280, 2007.

[182] M. Calamaz, D. Coupard, and F. Girot, "A new material model for 2d numerical simulation of serrated chip formation when machining titanium alloy ti–6al–4v," *International Journal of Machine Tools and Manufacture*, vol. 48, no. 3, pp. 275–288, 2008.

[183] M. Sima and T. Özel, "Modified material constitutive models for serrated chip formation simulations and experimental validation in machining of titanium alloy ti–6al–4v," *International Journal of Machine Tools and Manufacture*, vol. 50, no. 11, pp. 943–960, 2010.

[184] R. Liu, S. Melkote, R. Pucha, J. Morehouse, X. Man, and T. Marusich, "An enhanced constitutive material model for machining of ti–6al–4v alloy," *Journal of Materials Processing Technology*, vol. 213, no. 12, pp. 2238–2246, 2013.

[185] X. Zhang, R. Shivpuri, and A. Srivastava, "Role of phase transformation in chip segmentation during high speed machining of dual phase titanium alloys," *Journal of Materials Processing Technology*, vol. 214, no. 12, pp. 3048–3066, 2014.

[186] Y. Karpat, "Temperature dependent flow softening of titanium alloy ti6al4v: An investigation using finite element simulation of machining," *Journal of Materials Processing Technology*, vol. 211, no. 4, pp. 737–749, 2011.

[187] J. P. Davim, *Machining of hard materials*. Springer Science & Business Media, 2011.

[188] R. Lekkala, V. Bajpai, R. K. Singh, and S. S. Joshi, "Characterization and modeling of burr formation in micro-end milling," *Precision Engineering*, vol. 35, no. 4, pp. 625–637, 2011.

[189] E. Brinksmeier, Y. Mutlugünes, F. Klocke, J. Aurich, P. Shore, and H. Ohmori, "Ultra-precision grinding," *CIRP Annals-Manufacturing Technology*, vol. 59, no. 2, pp. 652–671, 2010.

[190] C. Heinzel and K. Rickens, "Engineered wheels for grinding of optical glass," *CIRP Annals-Manufacturing Technology*, vol. 58, no. 1, pp. 315–318, 2009.

[191] Q. Zhang, S. To, Q. Zhao, B. Guo, and G. Zhang, "Impact of material microstructure and diamond grit wear on surface finish in micro-grinding of rb-sic/si and wc/co carbides," *International Journal of Refractory Metals and Hard Materials*, vol. 51, pp. 258–263, 2015.

[192] J. C. Aurich, M. Carrella, and M. Walk, "Micro grinding with ultra small micro pencil grinding tools using an integrated machine tool," *CIRP Annals-Manufacturing Technology*, vol. 64, no. 1, pp. 325–328, 2015.

[193] M. Tilli and A. Haapalinna, "Properties of silicon," *Handbook of Silicon Based MEMS Materials and Technologies*, p. 3, 2009.

[194] C. Cabuz, W. R. Herb, E. I. Cabuz, and S. T. Lu, "The dual diaphragm pump," in *Micro Electro Mechanical Systems, 2001. MEMS 2001. The 14th IEEE International Conference on*, pp. 519–522, IEEE, 2001.

[195] T. G. Bifano, T. Dow, and R. Scattergood, "Ductile-regime grinding: a new technology for machining brittle materials," *Journal of engineering for industry*, vol. 113, no. 2, pp. 184–189, 1991.

[196] K. Liu, X. Li, M. Rahman, and X. Liu, "A study of the cutting modes in the grooving of tungsten carbide," *The International Journal of Advanced Manufacturing Technology*, vol. 24, no. 5-6, pp. 321–326, 2004.

[197] W. Blackley and R. Scattergood, "Ductile-regime machining model for diamond turning of brittle materials," *Precision engineering*, vol. 13, no. 2, pp. 95–103, 1991.

[198] P. N. Blake and R. O. Scattergood, "Ductile-regime machining of germanium and silicon," *Journal of the American ceramic society*, vol. 73, no. 4, pp. 949–957, 1990.

[199] K. Ueda, T. Sugita, H. Hiraga, and K. Iwata, "A j-integral approach to material removal mechanisms in microcutting of ceramics," *CIRP Annals-Manufacturing Technology*, vol. 40, no. 1, pp. 61–64, 1991.

[200] G. Xiao, S. To, and G. Zhang, "The mechanism of ductile deformation in ductile regime machining of 6h sic," *Computational Materials Science*, vol. 98, pp. 178–188, 2015.

[201] T. Shibata, S. Fujii, E. Makino, and M. Ikeda, "Ductile-regime turning mechanism of single-crystal silicon," *Precision Engineering*, vol. 18, no. 2, pp. 129–137, 1996.

[202] Z. Fang, *Sintering of advanced materials fundamentals and processes*. Oxford Philadelphia, PA: Woodhead Pub, 2010.

[203] M.-T. Yan, G.-R. Fang, and Y.-T. Liu, "An experimental study on micro wire-edm of polycrystalline diamond using a novel pulse generator," *The International Journal of Advanced Manufacturing Technology*, vol. 66, no. 9-12, pp. 1633–1640, 2013.

[204] A. Perveen, M. Jahan, M. Rahman, and Y. Wong, "A study on microgrinding of brittle and difficult-to-cut glasses using on-machine fabricated poly crystalline diamond (pcd) tool," *Journal of Materials Processing Technology*, vol. 212, no. 3, pp. 580–593, 2012.

[205] X. Cheng, K. Nakamoto, M. Sugai, S. Matsumoto, Z. Wang, and K. Yamazaki, "Development of ultra-precision machining system with unique wire edm tool fabrication system for micro/nano-machining," *CIRP Annals-Manufacturing Technology*, vol. 57, no. 1, pp. 415–420, 2008.

[206] K. Katahira, S. Takesue, J. Komotori, and K. Yamazaki, "Micromilling characteristics and electrochemically assisted reconditioning of polycrystalline diamond tool surfaces for ultra-precision machining of high-purity sic," *CIRP Annals-Manufacturing Technology*, vol. 63, no. 1, pp. 329–332, 2014.